# Nouveaux diagnostiques pour l'étude de la matière dense et chaude : application aux cibles comprimées par choc laser.

Alessandra Ravasio

# THESE

présentée à l'Ecole Polytechnique

pour obtenir le grade de

## DOCTEUR DE L'ECOLE POLYTECHNIQUE

**Spécialité : Physique**

par

Alessandra RAVASIO

# Novel diagnostics for Warm Dense Matter : Application to shock compressed target

Soutenue publiquement le 1 Mars 2007
devant le Jury composé de :

Mme Alessandra BENUZZI-MOUNAIX
M. Marco BORGHESI
M. Jean Claude GAUTHIER, Rapporteur
M. François GUYOT
M. Thomas HALL, Rapporteur
M. Michel KŒNIG, Directeur de thèse
M. Daniel VANDERHÆGEN

# Remerciements

Je remercie d'abord Monsieur François Amiranoff pour m'avoir accueillie dans son laboratoire où j'ai pu travailler dans d'excellentes conditions. Je remercie également les membres du jury : Messieurs les rapporteurs Jean Claude Gauthier et Thomas Hall, ainsi que M. Marco Borghesi, M. François Guyot et M. Daniel Vanderhægen pour l'attention qu'ils ont porté au manuscript.

Je tiens à remercier Michel Koenig, mon directeur de thèse, dont j'ai particulièrement apprecié la rigeur et l'honnêteté intellectuelle. Grace à lui j'ai été introduite dans la communauté scientifique et j'ai pu travailler dans les meilleurs laboratoires du monde parmi lequels le LLNL (*Lawrence Livermore National Laboratory*) aux Etats-Unis, ILE (*Institute of Laser Engineering*) à Osaka et le RAL(*Rutherford Appleton Laboratory*) dans les landes perdues de l'Oxfordshire. Je le remercie aussi pour m'avoir fait confiance dans la conduite de ce projet, pour lequel il m'a laissé la complete autonomie.

Un grand merci va à Alessandra Benuzzi Mounaix, pour sa disponibilité et ses conseils, toujours très précieux.

Tengo particolarmente a ringraziare Gianluca Gregori, per avermi guidato nei meandri dell' X-Ray Thomson Scattering e per la pazienza con la quale ha sempre risposto alle mie domande. La sua disponibilità e il suo aiuto sono stati indispensabili per la riuscita di questa (difficile) parte della mia tesi.

L'aide d'Erik Brambrink et Lorenzo Romagnani a également été indispensable pour "sympatiser" avec les protons et leur bizarreries. Je remercie Erik pour les longues et fructueuses discussions, aussi bien que pour les cocktails du samedi soir. La comprensione e la fiducia dimostratami da Lorenzo mi ha aiutato in alcuni dei momenti più bui dell'analisi dei dati.

Merci à Laurent Gremillet pour les simulations concernant les électrons et leur propagation dans notre étrange configuration.

Merci aussi a tous les post-docs et thesards avec qui j'ai passé au moins une partie de mes trois années de thèse : Norimasa, Tommaso, Seb, Emeric, Gael, Berenice (eh bien oui!!), Perceval, Ludovic et Benjamin.

Ce travail n'aurait pu etre terminé sans l'aide essentielle (plus unique que rare) de Marc Rabec-le-Gloahec, toujours present avec ses immenses competences, sa gentillesse et son calme. Je garde un trés plaisant souvenir des

journees que nous avons passées à travailler ensemble, efficacement au point de pouvoir prendre le temps de rigoler ou d'aller a la piscine ! Merci de même à Christophe Godinho et à ses synchros, à l'equipe laser du LULI2000 et à l'equipe technique : Alain Michard, Jean-Michel Boudenne et Pascal Guehennec (pas seulement pour ses pieces toujours parfaites, mais aussi pour les crumbles au pommes...délicieuses !).

Je remercie également les nombreuses personnes que ont participé aux differentes experiences : Carlo Cecchetti, Angelo Schiavi, Prav Patel, Hye Sook Park, Damien Hicks, Dimitri Batani, Tom Boehly, Riccardo Dezulian, Rob Clark, Margareth Notley e Sujit Banyopadyay au RAL, Dave Ryley et Alice Delserieys à la manip XRTS au LULI et Sigfried Glenzer pour m'avoir invité a LLNL.

Merci aussi à Patrick Audebert pour les inmombrables conseils, à Jean-Raph, Jean-Philippe et Mathieu, pour avoir su me distraire de Paris.

Il più sentito dei miei ringraziamenti va ai miei genitori e a Fede, senza il loro affetto e il loro costante sostegno non avrei mai terminato questa tesi, lontano da casa (e dalle montagne !).

Enfin, merci á celui qui, avec sa nature un peu "zen", a su maîtriser et calmer les orages de mon esprit pendant les journées et les longues (noires) soirées de redaction.

# Contents

# Chapter 1

# Introduction

## WDM contexts

This thesis aims at the development of novel diagnostics for the investigation of Warm Dense Matter (WDM). WDM is part of the so-called *High Energy Density Physics* [1], lying at the frontiers between condensed matter and plasma physics. It is characterized by temperatures in the range 0.1-100 eV and densities varying between 0.1-10 the solid density. Our knowledge of the matter properties in these regimes is extremely poor while its understanding is of primary importance in different branches of science. In particular the precise knowledge of the relation between pressure, density and temperature, which defines the *Equation Of State* (EOS), is a key issue in important domains, such as Inertial Confinement Fusion (ICF), geophysics, astrophysics, including planetology.

**Inertial Confinement Fusion (ICF)** Notwithstanding the improvement of exploration and extraction technologies, the availability of conventional fuel sources is rapidly decreasing and the development of new energy resources becomes more and more urgent. Controlled thermonuclear fusion represents one of the most promising alternative, being a clean and abundant energy source which, in particular, allows overcoming the problem of radioactive wastes. Fusion energy research has thus motivated the founding of large scale projects, like ITER (International Thermonuclear Experimental Reactor) in Cadarache south of France [2], LMJ (Laser Mega Joule) in Bordeaux [3] and NIF (National Ignition Facility) at Livermore, USA [4].

Among the different possibilities to reach controlled thermonuclear fusion in laboratory, the most promising involves the use of deuterium (D) and tritium (T) atoms which are fused together, producing an $\alpha$ particle and a neutron. Since the final state of the reaction is more tightly bound than the initial one, a large amount of energy is released in the form of kinetic energy of the two products: 3.5 MeV for the $\alpha$ particle

and 14 MeV for the neutron. The neutron kinetic energy can then be captured in the form of heat and then converted into electric power by a suitable thermal cycle. This simple basic principle is in reality not easy to accomplish, since the two nuclei must be sufficiently energetic to overcome the Coulomb potential barrier and the number of reactions adequate to produce a self-sustaining process (*the ignition*). These requirements imply extremely high temperatures (the nuclei kinetic energy must be of the order of $\sim$ 10-20 keV). Under these conditions, matter appears in form of plasma and tends to fly apart unless constrained in some way. One of the greatest difficulties in fusion research consists indeed in confining this plasma in such a way that high temperatures and densities are maintained simultaneously for sufficiently long time [5].

Two different approaches have been proposed in order to realize the fusion. A first scheme is represented by the *magnetic confinement fusion* (MCF), whose realization is delegate to ITER project. In this case the basic idea is to confine the fuel to relatively low densities ($n \sim 10^{14} cm^{-3}$) during a long time ($\tau \sim 1s$) by means of magnetic fields. The second scheme, the *inertial confinement fusion* (ICF), exploits the inertia of the process ($\sim 10^{-10}$ s) to confine the fuel, which then needs to be brought to very high densities. Under these conditions, the created plasmas do not behave like a perfect gas, as coupling and degeneracy effects become important. These are the main characteristics typical of WD plasmas.

In the standard ICF scenario, a few milligrams of cryogenic DT fuel ($\rho \sim 0.2 g/cm^3$) are contained in millimeter spherical capsule (the pellet), which is symmetrically irradiated with intense laser beams (typically $10^{14} - 10^{15} W/cm^2$). Ignition conditions are not attained in the whole volume, too exigent from the energetic point of view, but in a small central region of the target, the *hot spot*. The energy carried by the $\alpha$ particles of these initial reactions is then absorbed in the rest of the fuel, leading to the ignition of the whole capsule.

The fuel ignition via the hot spot is realized through following steps. First, the fuel is compressed by means of the laser beams which heat and ionize the outer capsule layers. The created plasma radially expands in the vacuum and, as a reaction, an inward movement of the shell towards the pellet center is generated together with a radial shock wave, which strongly compresses the target. In this case, a knowledge of WD EOS and of WD transport coefficients is essential as they dominate the implosion dynamics. In order to create the hot spot, the compression is optimized by adjusting the laser intensity so to generate a sequence of shocks, converging at the same time at the capsule center. Here, a temperature of 5-10 keV is created and the first thermonuclear reactions can occur. In the last phase, the $\alpha$ particles produced in these reactions,

can successively transfer their energy to the near compressed regions, leading to a burn wave propagation and ensuring the self-sustaining of the reaction. Ignition is in this way obtained.

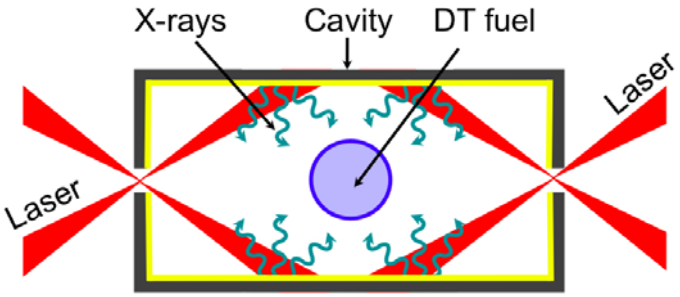


**Figure 1.1:** *Indirect drive scheme in ICF. The fuel is compressed by an intense x-ray flux.*

Two alternatives are used to compress the target by means of laser beams: the direct and indirect drive.
In the indirect drive, fig.1.1 the fuel is placed at the centre of a cavity, made of a high Z material, most of the time gold. The laser beams enter the cavity and hit its walls, which emit an intense x-ray flux, ensuring the fuel compression. This approach guarantees a uniform compression of the pellet, but it has a limited conversion efficiency.

In the direct drive approach, the laser beams directly compress the fuel, as shown

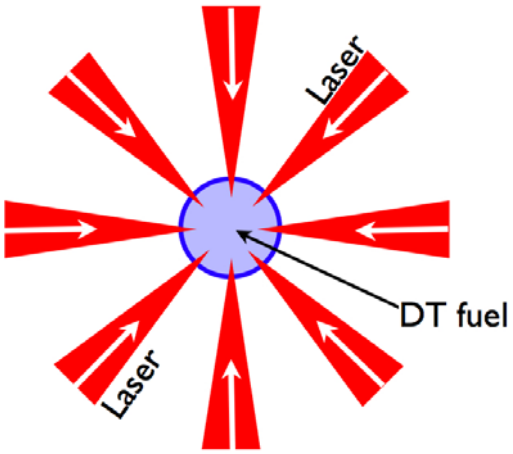


**Figure 1.2:** *Direct drive scheme for fuel compression in ICF approach.*

in fig.1.2. Even if much more efficient, the direct drive approach presents some issues regarding the symmetry of the implosion, which requires a high uniformity of the implosion velocity (better than 1%). Defects arise because of the capsule manufacture,

the quality of its surface and the spatial and temporal non-uniformity of the laser irradiation. Small initial perturbations give rise to hydrodynamic instabilities, which further degrade of the implosion symmetry. In order to overcome these difficulties, a new scheme, the *fast ignition* (FI), was recently proposed, [6]. In this case, the idea is to separate the compression phase from the heating process. The fuel is initially compressed in the "traditional" scheme. At the moment of maximum compression a first short pulse high intensity laser beam ($I \sim 10^{19} W/cm^2$) is focused on a side of the pellet and bores a channel in the ablated plasma. Finally a second short pulse laser, perfectly aligned with the first one, propagates in the created channel and transfer its energy to the fuel via the supra-thermal electrons, which are created in the laser matter interaction at these high intensities regimes.

So far, ignition has not been achieved yet. Overcoming the difficulties encountered requires, besides the employment of bigger facilities, a deeper knowledge of the involved process. Accurate calculations for targets design and optimisation must also carried on in order to facilitate the accomplishment of the goal. In this context, the characterisation of WDM is essential.

**Astrophysics** In giant planets, as Jupiter, Saturn, Uranus and Neptune, the inwardly directed pressure strongly compresses their constituent matter, creating extremely high temperatures and densities. The knowledge of the EOS of materials under these extreme conditions are necessary in order to validate planetary formation models and, more generally, to determine their structure [7].

High pressures EOS of Hydrogen and Helium are particularly interesting as they represent the most abundant elements among Jupiter and Saturn constituents [8],[9]. While these two planets are well characterized on the surface, basic questions regarding their interior are still open. In particular, it is controversial whether Jupiter has a rocky core. The detection of a rocky core in this planet is a live debate as it would allow to discriminate between the standard model of giant planet formation via nucleated capture of nebular hydrogen and the alternative scenario involving spiral instabilities in protostellar disks [10].
Moreover, the observed Saturn luminosity is $\sim 50\%$ more intense than what is predicted by theoretical work [11], the emitted light being much more important than the amount received by the sun. This implies the existence of an internal heat source which was suggested to be associated to the phase separation of Helium and Hydrogen. The study of hydrogen-helium mixtures behavior under extreme conditions is therefore necessary to verify this hypothesis and well understand Saturn evolution [9].
An adequate description of Uranus and Neptune is even more difficult, as it requires

the characterization of the EOS of all their components, including a large fraction of heavy elements. Their density profiles suggest that these two planets do have a rocky core, a hydrogen gas atmosphere and a mantle rich in water, methane and ammonia. EOS of all these materials need to be known along the planet isentrope, lying in a pressure range from 1-8 Mbar and at temperatures of 0.15-0.6 eV, i.e. in WDM regimes.

EOS are also important in the comprehension of star evolution. White dwarf cosmochronology is a powerful tool to determine the ages of ancient stellar population, important clues for the understanding of spiral galaxy formation. Modeling the atmosphere of a cool white dwarf requires an accurate knowledge of optical properties and equation of state of hydrogen-helium mixtures [12]. Moreover warm dense degenerate electron plasmas, (see section 2.1), characterize white dwarf interior, counterbalancing the gravity force.
A similar situation holds for brown dwarfs. They have a little masse and their interior is not hot enough for the hydrogen to burn. Their internal structure and their cooling rate depends on the EOS of matter at densities close to solid one and at temperature of $\sim eV$ [12].

**Geophysics** As in the case of the giant planets, the knowledge of the equation of state in the WDM regime, allows to infer information of the earth internal structure.One of the most important element in geophysics is iron: earth's core is composed by solid iron covered by a liquid Fe layer. The heat released by the Fe crystallization in the core is responsible of the convective motion in the liquid core, explaining the dynamo phenomena which are responsible for the earth magnetic field. In order to well estimate the energy rate produced in this process, it is necessary to well characterize the iron fusion temperature at the pressure of 3.3 Mbar, corresponding to the liquid-solid core boundary, known as the $IOB$ for "Inner-Outer core Boundary".

# Why do we need to develop novel diagnostics?

In each of these areas, the inaccurate knowledge of matter properties is at the origin of unresolved debates, like the ones mentioned before. This is the reason why so many efforts are done in developing new diagnostics of WDM. Both warm dense states and diagnostic tools can be generated in laboratory. Moreover, the experimental approach is of particular importance in this context, as a satisfying theoretical description of WDM states is still missing.
So far, EOS measurements have been mainly performed by means of optical or low energy x-ray diagnostics. Despite being an useful tool which has allowed the investigation of the behavior of different materials under extreme conditions, these techniques

present some issues that must be overcome in order to reach a complete understanding of WDM. In particular the information obtained with these "standard" diagnostics is indirect, leading to big concerns in the measurements precision, often not sufficient to discriminate between different theoretical models. In addition, more energetic sources are necessary for the investigation of high Z plasmas.
The issues related to these "standard" diagnostics affect our understanding of WDM states, leaving many crucial open questions. In order to well illustrate this point, we discuss as examples the state of art for hydrogen and iron, two materials of fundamental interest in various physical areas whose characterization is still unsatisfactory.

**Hydrogen** Hydrogen is by far the most abundant element present in the universe. While at standard conditions it behaves essentially like a light perfect gas, its behavior is comparable to that of a dense fluid under astrophysical conditions. At low temperatures, hydrogen is a non conductive molecular solid, with the molecules placed on a lattice able to rotate (*phase I*) or oscillate (*phase II*). A third conductive phase was then predicted at 0 K [13], but still never observed. At normal pressure, the solid transforms in a non conductive liquid at 20 K, a phase that can be kept up to 800 K when a pressure of 1 Mbar is applied. At still higher temperature, ionization effects occur and a conductive plasma is created. This transition, between the non conductive molecular fluid to the conductive plasma state, occurs in the WDM regime and it is still not completely understood.

Up to 1996 only one equation of state was available for the hydrogen and its isotopes deuterium and tritium: the equation of state SESAME [14]-[16]. It was validated by gas gun experiments in 1983 [17],[18], whose results showed optimal agreement with the model. It was in 1997 that a Lawrence Livermore National Laboratory (LLNL) team published the data from laser driven shock compressed targets [19],[20] which were in complete disagreement with the results of gas gun experiments and thus with SESAME EOS. The compressibility measured in the LLNL experiment, resulted 50% higher than the one predicted by SESAME, increasing the value of the maximum compressibility $\rho/\rho_0$ limit from 4.4 predicted by SESAME up to $\sim 6$. These results were confirmed by later experiments where new interferometry techniques have been employed [21]. This scenario was again challenged in 2000, when new data, obtained on Z-pinch machines, were presented by a group from Sandia National Laborarory (SNL) [22]. These results are in good agreement with SESAME EOS and in full contradiction with those obtained by LLNL, opening a vive debate. At present, new experiments from Sandia Z machine [23], from spherical compression [24],[25], [26] and from laser driven shock compression [27] have been obtained. However, the situation is far from been settled, [28],[29], as well evidenced in fig.1.3 which summarises the results.

Even if SESAME EOS seems to be the most accredited hypothesis, a new set of absolute measurements is necessary to conclude this debate.
From the theoretical point of view, the situation is not much clearer. There are various models of high-pressure hydrogen which can be compared with the experimental measurements. *Ab initio* calculations seem to be in general agreement with stiffer EOS data. On the other hand, empirical EOS model [30] and Saumon-Chabrier-Van Horne model [31] favour a softer EOS, i.e. a higher compressibility.

In planetology, the details of the $H_2$ (including its isotopes such as $D_2$) EOS have

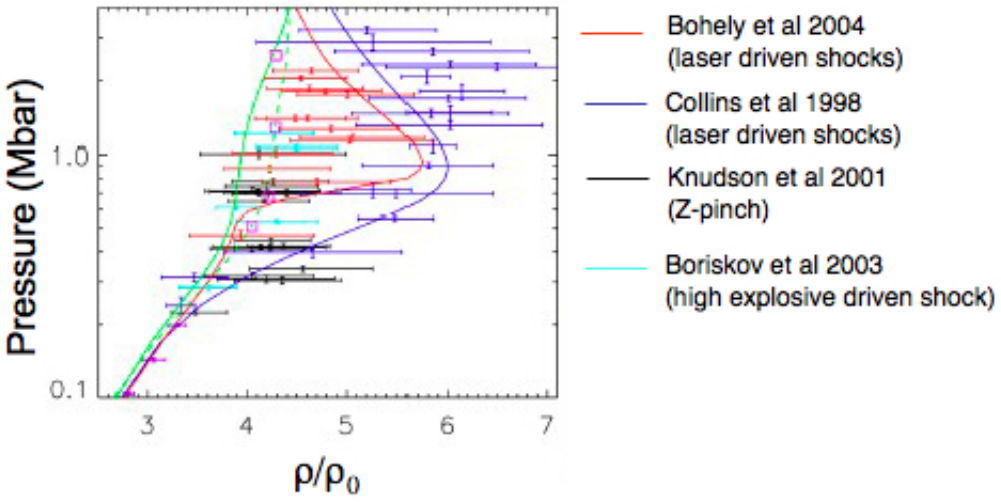


**Figure 1.3:** *Deuterium pressure-density compression Hugoniots, together with theoretical models and experimental results. In particular Sesame theoretical model is represented with green solid line, while Ross model is the blue line. The solid red line results form ab-initio calculations. Dots are the experimental data from the indicated references.*

strong impacts, on giant planets core characterization [32] for example, as we have previously mentioned. Since there is no a direct way to detect their interior, the description refers to indirect measurements and to theoretical models which rely on the EOS. The internal structure description is therefore highly affected by the uncertainties on high-pressure hydrogen EOS and the debate on giant planet formation is still unresolved. A high compression value as predicted by LLNL data is consistent with the existence of a large core, $\sim$ 15 earth masses. Jupiter, instead, would have an insignificant core if the compression limit is the one predicted by SESAME and Z-pinches experiments.
In ICF the detailed knowledge of deuterium EOS is necessary for the target design and

the calculations for its optimization.

**Iron** As we have previously mentioned, iron is one of the fundamental earth constituents. Its behavior at Mbar pressures is of crucial importance in the description of Earth's core. The application of standard techniques on high Z materials is complicated by the fact that they are generally opaque to optical and low energy x-ray probes. Moreover, at high pressures, the use of these techniques imposes the necessity of performing relative measurements, where the deduced information depends on other materials EOS, which is considered well known and taken as reference. In this case, the measurement precision is strongly linked to the confidence degree in the reference material characterization. The resulting scenario for iron is quite complex, with

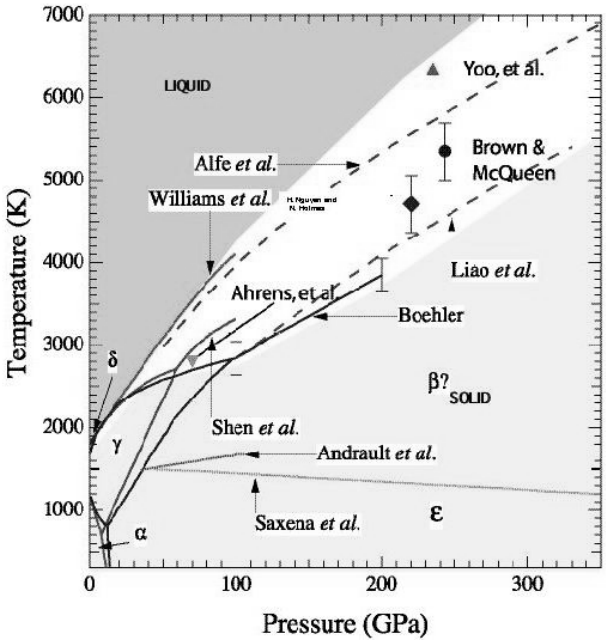


**Figure 1.4:** *Phase diagram of Iron.*

a sharp disagreement between different experimental measurements at high pressures. This is well evidenced in the iron phase diagram, complicated and contradictory as pressure exceeds $\sim 1$ Mbar (fig.1.4). In particular, the melting temperature at the IOB is still at the center of a long standing controversy. Indeed, temperature is generally a delicate parameter to measure; its characterization becomes even more difficult when opaque materials are involved since it is typically based on optical emission pyrometry. Recently, visible emission and reflectivity diagnostics were applied to iron release states in a transparent LiF window [33] in order to obtain temperature measurements. Although, precise results were obtained only up to 1.5 Mbar. It was shown that for

higher pressures, these measurements were strongly dependent on LiF optical properties, which still need a better characterization. Therefore, temperature at IOB could not be directly accessed, but deduced from data extrapolation.

## Goals and plan of the thesis

It is now clear that the development of new techniques is necessary in order to make a real breakthrough in the understanding of WDM properties.
In this work, we will present three novel diagnostics for warm dense plasma investigations: hard x-ray radiography, proton radiography and x-ray Thomson scattering. Each of these techniques is applied in shock compression experiments. The main objective consists in accessing a new parameter, in addition to shock and particle velocity, for EOS measurements (see section 3.1).

In the first chapter we will give a deep description of WDM states as strongly coupled and Fermi degenerate states. We will then introduce how we have generated a WDM state in our experiment: *the shock wave*. We will, in particular, illustrate its formation in the classical laser-matter interaction regime.

In the second chapter the principles of standard probing techniques will be presented. This will allow us to deeper understand the main issues related to these measurements. We will see that energetic probe sources are necessary to investigate high Z dense plasmas and introduce *proton and hard x-ray beams*, our probing tools. The principles of each new diagnostic will be discussed and illustrated.

The third chapter is dedicated to x-ray radiography results. We will report on a first direct density measurement of a shock compressed high Z target using K$\alpha$ hard x-ray radiation. These results are of great interests as they allow an *in situ* characterization of high Z material, impossible with standard techniques. We will show that probing a well known material as Al will allow the comparison between our data and the results from already validated simulations. In this way, we will be able to isolate the main problems to be overcome in future experiments.

In the fourth chapter, we will present the results obtained from proton radiography on low density carbon foam. The data analysis will require the development of a specific Montecarlo code to simulate the proton propagation through the shocked target. A brief description of this code will be given. The comparison of the simulations with the experimental data will show a low dependency on density. However, this technique will reveal a good sensitivity to the density gradient details.

The fifth chapter will be devoted to x-ray Thomson scattering results. This technique was the only one that we have tested in more than one experiment, allowing an improvement on the experimental design. For the first time, we have performed collective x-ray Thomson scattering measurement from a shock compressed target, accessing to electron density and temperature. The obtained results will be compared with simulated x-ray scattered spectra. A good knowledge of the plasma state achieved via optical techniques together with the use of a well known material (Al), will provide a validation of this diagnostic. The novel technique will then be used in the investigation of less characterised materials (LiH samples). In addition, from the obtained data, we will be able to evidence the effects of strong coupled ion dynamics in dense plasmas.

Finally, in the conclusion we will resume the results we have obtained and we will present some of the future perspectives for WDM research.

# Bibliography


[1] *Frontiers in high energy density physics*, N.R.Concil, The national academy press (2003)

[2] http://www.iter.gouv.fr

[3] http://www-lmj.cea.fr/html/cea.htm

[4] http://www.llnl.gov/nif

[5] Lawson J.D. Proc. Royal Soc. (London) **70B**, 6 (1957)

[6] M Tabak, *et al.* Phys. Plasmas **1**, 1626 (1994)

[7] Annual Review of Earth and Planetary Sciences, **33**, p.493-530 (2005)

[8] T.Guillot, Science **286** 72-77 (1999)

[9] G.Chabrier, D. Saumon, W.B. Hubbard and I. J. Lunine, Astrophysical Journal, Part 1, **391**, 2, 817-826 (1992)

[10] R.Hueso, Ricardo, T. Guillot, Space Science Reviews, **106**, 1, 105-120 (2003)

[11] R.Smoluchowski, Nature **215**, 691-695 (1967)

[12] D. Saumon, W.B. Hubbard, G. Chabrier, H.M. van Horn, Astrophysical Journal, Part 1, **391**, 2, 827-831 (1992)

[13] E.Wigner, H.B.Huntington, J. Chem.Phys, **3**, 764 (1939)

[14] T4 Group LANL, No. LALP-83-4 (1983)

[15] B. I. Bennett, J. D. Johnson, G. I. Kerley and G. T. Rood, LANL, No. LA-7130-UC- 34 (1978)

[16] K. S. Holian, LANL, No. LA-10160-MS UC-34 (1984)

[17] W.J.Nellis, *et al.*, J. Chem.Phys, **79**, 1480 (1983)

[18] N.Holmes, *et al.*, Phys. Rev. B, **52**, 15835 (1995)

[19] L.B.DaSilva, P.Celliers, G.W.Collins, *et al.*, Phys. Rev.Lett., **78**, 483 (1997)

[20] G. W. Collins, L. B. Da Silva, P. Celliers, *et al.* Science **281**, 1178 (1998).

[21] P.Celliers, G.W.Collins, P.Celliers, *et al.*, Phys. Rev.Lett., **84**, 5564 (2000)

[22] M. D. Knudson *et al.*, Phys. Rev. Lett. **87**, 225501 (2001)

[23] M. D. Knudson, D.L.Hanson, J.E.Bailey, *et al.*, Phys. Rev. Lett. **90**, 035505 (2003)

[24] S. I. Belov, G. V. Boriskov, A. I. Bykov, *et al.*, JETP Lett. **76**, 433 (2002)

[25] G. V. Boriskov, A. I. Bykov, R. I. Ilkaev, *et al*, Dokl. Phys. **48**, 553 (2003)

[26] G. V. Boriskov, A. I. Bykov, R. I. Ilkaev, *et al*, Phys. Rev. B, **71** 092104 (2005)

[27] T.Boehly *et al.*, Phys. Plasmas **11** L49 (2004)

[28] A.N.Mostovych, *et al.*, Phys. Plasmas **8** 2281 (2001)

[29] W.J. Nellis, *et al.* Phys. Rev. Lett. **89** 165502 (2002)

[30] M.Ross, Phys. Rev. B **58** 669-677 (1998)

[31] D.Saumon and G.Chabrier, Phys. Rev. A. **46** 2084 (1992)

[32] D.Saumon and T. Guillot, The Astrophysical Journal, **609** 1170-1180 (2004)

[33] G.Huser, M.Koenig, A.Benuzzi-Mounaix, *et al.* Phys. Plasmas **12** 060701(2005)

# Chapter 2

# Warm Dense Matter and its generation

In this opening chapter we will first introduce Warm Dense Matter. We will characterize strongly coupled and Fermi degenerate states, typical of warm dense plasmas which make their description particularly challenging. We will then introduce the method that we have used to create WDM conditions in our experiments: the shock wave compression. The description of the shock wave generation will be done through a quick overview of the laser-matter interaction in the classical regime. The link between shock compression and equation of state will conclude the chapter.

## 2.1 WDM, Fermi degenerate and strongly coupled plasmas

The so called Warm Dense Matter (WDM) regime is a state of matter which lies at the frontiers between condensed matter and plasma physics. While there is no exact boundary, for convenience WDM is generally considered to be the region of the phase diagram characterized by temperatures in the range 1 to 100 eV and densities varying between the 0.1 to 10 times the solid density.

The interest in warm dense matter states comes from their wide occurrence in many physical environments: in astrophysics, WDM is what cool stars and giant planets are made of, in geophysics, as WDM characterizes the center of rocky planets including earth, in ICF research, where a correct description of WDM is necessary for a good characterization of capsules compression and their performances optimization.

Besides its great importance, the description of WDM is a big challenge from both theoretical and experimental point of view. Indeed, WDM regimes are characterized

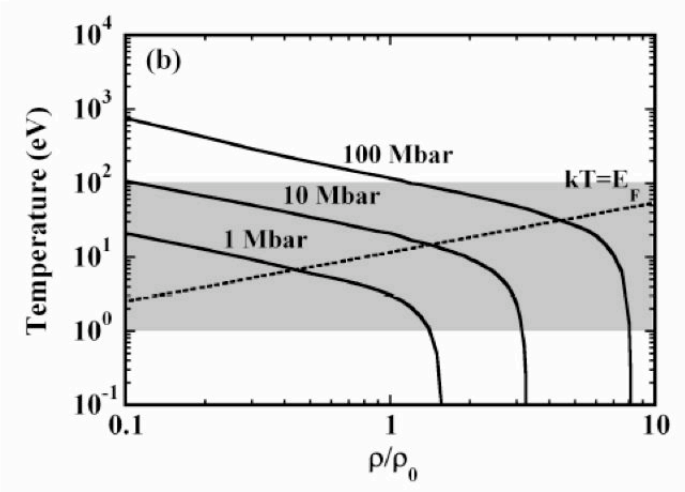


**Figure 2.1:** *WDM regimes are here represented in the gray region. They are generally considered to be characterized by temperatures in the range 0.1 to 100eV and densities varying between the 0.1 and 10 times the solid density.*

by thermal energies comparable with Coulomb energies and appear as strongly coupled plasmas. In such conditions, short and long correlation effects on the electrons and ions cannot be neglected anymore and the description of the atoms based on their isolated behavior is no longer correct.

Most of the difficulties in the theoretical picture of these regimes arise from the impossibility to use the usual Debye screening and perturbation expansions, commonly applied to the description of classical plasmas. In addition, density-dependent effects, such as pressure ionization, begin to gain a strong importance, as the surrounding starts to impinge on the internal ion structure. Viewed as a high temperature condensed state, the system appears disordered and its description requires detailed knowledge of excited states, structure factors and of the complex dynamics of strongly interacting electrons and ions. As a consequence of this complex scenario, experiments represent the only valid way to discriminate between the different theories.
Nevertheless, the experimental investigation of these extreme conditions is not an easy task neither. The first great challenge is to create an uniform, well defined WDM state. Once created in laboratory, warm dense matter does not remain in a steady specific thermodynamic state, but it evolves rapidly, making its characterization extremely difficult. Probing these states, then, is also non trivial. Due to the high density, most of the methods employed for the characterization of under-dense plasmas are not applicable and one has to deal with higher energy probes. This means that high power sources

able to deliver high energy fluxes must be developed and employed.
Because of all these raisons WDM is an extremely stimulating field whose investigation is gaining more and more attention.

In order to better understand the properties that make WDM plasmas a real challenge, we will introduce strongly coupled and Fermi degenerate plasmas. This classification will then be useful to characterize our plasmas.

### 2.1.1 Strongly coupled and Fermi degenerate plasmas

The study of plasmas may be divided into two large categories: classical and quantum (degenerate) plasmas. A further classification regards the degree of coupling between one or more species. These domains are characterized by nondimensional parameters:

**i)** The plasma parameter, $\Gamma$, allows to distinguish between classical strongly and weakly coupled plasmas. The definition of this parameter is extended in the quantum regime to $\Gamma_Q$.

**ii)** The quantum degeneracy parameter, $\Lambda$, which discriminates between classical and degenerate plasmas

#### 2.1.1.1 The Plasma parameter $\Gamma$

The distinction between weakly and strongly coupled plasmas is given in terms of the plasma parameter:

$$\Gamma \equiv \frac{1}{4\pi n \lambda_D^3} \tag{2.1}$$

where n is the charge density number and $\lambda_D = \left(\frac{\epsilon_0 k_B T}{4\pi n e^2}\right)^{1/2}$ is the Debye shielding distance. For simplicity we will consider coupling between electrons, the same treatment can be done for ions. Electron and ion coupling can also be considered. The physical interpretation of this parameter becomes clear when we consider the mean two-particle potential energy:

$$< V >= \frac{e^2}{4\pi\epsilon_0 d} \tag{2.2}$$

where d is the mean sphere radius $d = (3/4\pi n)^{1/3}$. The mean kinetic energy is:

$$< E_K > \simeq k_B T \tag{2.3}$$

Coupling between particles is small if the ratio between these two energies satisfies:

$$\frac{< V >}{< E_K >} = \frac{e^2}{4\pi\epsilon_0 k_B T d} \simeq \frac{e^2 n^{1/3}}{k_B T} \simeq \Gamma^{2/3} \ll 1 \tag{2.4}$$

Thus, we have the following criteria:

$\Gamma \ll 1$, weakly coupled plasmas

$\Gamma \gtrsim 1$, strongly coupled plasmas

In weak coupling limit, thermal energy dominates over potential energy and the plasma can be described classically, in term of a one-particle distribution function. In the opposite limit of strong coupled plasma, the dynamics involves at least the two-particle distribution function. Coulomb interactions have strong consequences on macroscopic properties. In particular, correlations decrease both the total energy and the pressure of the ideal gas.

#### 2.1.1.2 Quantum degeneracy parameter $\Lambda$

The criterion used to distinguish between a classical or a quantum degenerate plasma is expressed in terms of the deBroglie wavelength:

$$\lambda_{dB}^2 = \frac{\hbar}{2\pi m k_B T} \tag{2.5}$$

where m is the mass of the particles considered. If $\lambda_{dB} < n^{1/3}$, the interparticle spacing is large compared to the thermal deBroglie wavelength and the plasma acts as a classical gas. In the opposite case, the fluid becomes degenerate. In terms of the dimensionless variable

$$\Lambda \equiv \lambda_{dB} n^{1/3} \tag{2.6}$$

the criteria is expressed as:

$\Lambda \ll 1$, classical plasmas

$\Lambda \gtrsim 1$, degenerate plasmas

If we introduce the explicit expression of the deBroglie wavelength in eq.2.6 we find:

$$\Lambda^2 = \frac{2\pi\hbar^2}{m} \frac{n^{2/3}}{k_B T} \tag{2.7}$$

which shows that quantum behavior may be expected at high densities and low temperatures. [1] For typical conditions of our plasmas, the ions are always non-degenerate, while electrons may show different degrees of degeneracy. In the case of high degeneracy, the electrons are described by the Fermi-Dirac distribution. One of the direct consequences of degeneracy is pressure ionization phenomena. The free electrons are pushed into bound electrons orbitals, which undergo a reduction of their binding energy.

For degenerate plasmas, a new definition of the coupling parameter $\Gamma$ is necessary and given by considering the kinetic energy associated to the uncertainty momentum:

$$< E_Q >= \frac{(\Delta p)^2}{2m} \simeq \frac{\hbar^2}{2m}\frac{1}{(\Delta x)^2} \simeq \frac{\hbar^2}{2m} n^{2/3} \tag{2.8}$$

where p is the momentum and $x$ the displacement. The ratio between the mean potential energy 2.2 and the quantum uncertainty energy appears as:

$$r_s \equiv \frac{< V >}{< E_Q >} = \left(\frac{3}{4\pi}\right)^{1/3} \frac{e^2 m}{\epsilon_0 \hbar^2 n^{1/3}} = \frac{3\pi}{2^{5/3}} \frac{< V >}{E_F} \simeq \frac{e^2}{4\pi\epsilon_0 E_F d} \tag{2.9}$$

where $E_F = \dfrac{\hbar^2}{2m}(3\pi^2 n)^{2/3}$ is the Fermi energy. Thus, condition for weakly coupled degenerate plasmas translates in $r_s \ll 1$. If, on the contrary, $r_s \gtrsim 1$ we are in the strongly coupled degenerate regime. We can remark that in this case, in contrast with a classical plasma, by increasing the density the coupling parameter decreases, as it is $\sim n^{-1/3}$.

The natural extension of the classical plasma parameter $\Gamma$ to the quantum domain is found replacing the Debye length $\lambda_D$ with its quantum analogue, the Thomas-Fermi length:

$$\lambda_{TF} = \left(\frac{2\epsilon_0 E_F}{3ne^2}\right)^{1/2} \tag{2.10}$$

finding that

$$\Gamma_Q^2 \sim \left(\frac{1}{n\lambda_{TF}^3}\right)^2 \sim r_s^3 \tag{2.11}$$

Therefore, we find that the criterion for a weak coupled classical plasma, $\Gamma \ll 1$, has a natural extension to the criterion of weakly coupled degenerate plasma, $\Gamma_Q < 1$.

[1] Since the particle density n is directly linked to the Fermi energy $E_F = \frac{\hbar^2}{2m}(3\pi^2 n)^{2/3}$, some times it is more practical to consider the ratio $k_B T_e/E_F$ instead of $\Lambda$. In this case, the plasma is degenerate if $k_B T_e/E_F \ll 1$.

## 2.2 How we have created WD plasmas: the shock wave

The starting point of all our experiments is the generation of WDM conditions to be probed. Most of the time, warm dense plasmas are generated via strong compressions. In this case, two main techniques can be used: *static* or *dynamic* compressions.

The modern static compression technology traces its origin back to the first pioneering work done by Bridgman ([1]-[3]), who was actively engaged in high pressure research from 1906 to his death. Nowadays, the most important static high pressure technique is the Diamond Anvil Cell (DAC), based on isothermal compression. The interesting properties of this cell come not only from the diamond hardness but also from its transparency to both x-ray and visible light, which allows a large variety of measurements. Accurate measurements of the achieved pressure can be done by inserting a ruby crystal in the cell and by recording its fluorescence line shift, already calibrated ([4]). The pressures achievable by this approach are though limited to few ($\sim$3) Mbar.

Dynamic methods of compression, on the other hand, came into play during and immediately after World War II, when shock wave research was developed independently by United States and Russia. Its development was closely related to nuclear weapons research. The pressures attainable by means of dynamic methods are much higher ($\sim$750 Mbar [5]), even if they allow the investigation of a restricted region of the phase diagram, as we will see in section 2.2.3. Different possibilities are offered to generate a shock wave: from chemical (and now banned nuclear [6]) explosions to gas guns, Sandia Z-pinch machines or high power lasers.
We must mention that recently static and dynamic techniques were coupled together [7],[8] accessing a much larger part of the phase diagram, which was up to now inaccessible and opening new perspectives.

Finally, WDM can also be created via "isochoric heating", i.e. depositing the energy in a short time scale before heating-induced expansion decreases the density of the heated matter. In this way, in principle it is possible to reach a unique high-temperature and high-pressure state. Attempts to achieve isochoric heating have been pursued either using short-pulses lasers [10] or short pulse laser produced x-rays [9]. Recently, a new and original approach using high energy proton beams has been proposed by Patel *et al.* [11].

In all our experiments, warm dense plasmas were obtained through laser generated shock waves. This choice was mainly motivated by the high pressures accessible through

this method, the highest reachable nowadays. Moreover, in the last few years, several works [12]-[14] have demonstrated the validity of this technique as a tool for EOS studies.

In this approach, a shock wave is generated by irradiating a solid target with a laser beam at moderate-high intensities ($I\lambda^2 < 10^{15} W cm^{-2} \mu m^2$), where the absorption mechanisms mainly occur through collisional processes. In the following sections we will illustrate the most important features of the laser-plasma interaction in this classical regime and we will discuss the shock wave generation.

### 2.2.1 Laser plasma interaction in the ns regime

In the interaction between an intense laser ($I > 10^{12} W/cm^2$) and a solid target, its surface is rapidly ionized and a hot plasma is created. The laser has hence to propagate in an electron density gradient. The dispersion relation of an electromagnetic wave of angular frequency $\omega$, wavelength $\lambda$ and wave vector k is:

$$c^2 k^2 = \omega^2 - \omega_p^2 \tag{2.12}$$

where c is the speed of light[2] and $\omega_p$ is the plasma frequency and depends on the electron density $N_e$ through:

$$\omega_p^2 = \frac{N_e e^2}{\epsilon_0 m_e} \tag{2.13}$$

When $\omega^2 = \omega_p^2$ the wave vector $k = 0$ and the wave does not propagate anymore. This condition puts a limit on the maximum electron density the laser can propagate through. This limits is called the *critical density* $N_c$ and is set to:

$$N_c = \omega^2 \frac{\epsilon_0 m_e}{e^2} = \frac{1.11485 \cdot 10^{21}}{(\lambda[\mu m])^2} cm^{-3} \tag{2.14}$$

In our conditions the laser wavelength $\lambda$=0.527 $\mu m$ and $N_c = 4 \cdot 10^{21}$ $cm^{-3}$.
Accounting for different electronic densities, we can naturally characterize three main regions in the created plasma, fig.2.2:

- The interaction region, called *corona*, with a density less than $N_c$, is the region where the absorption mechanisms occur. Its temperature is nearly uniform and $\sim$ keV for a ns pulse duration and a typical intensity of $I \sim 10^{13}$ $W/cm^3$.
- In the *conduction region*, where the electron density is included between $N_c$ and the solid density $N_s$, the laser energy absorbed in the corona is transported towards denser regions. The main transport processes are different according to the target

[2] in the whole work, when not indicated differently, c indicates the speed of light

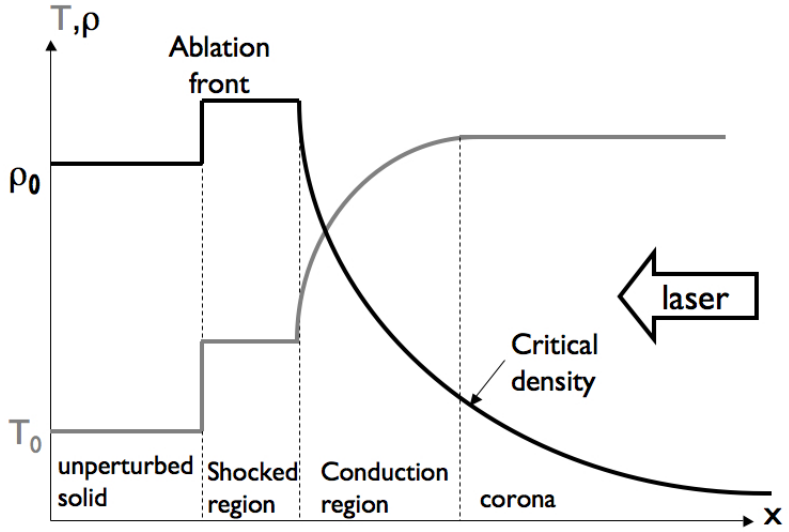


**Figure 2.2:** *Characteristic temperature (gray line) and density (black line) profile for a low Z plasma created with a ns pulse laser beam.*

atomic number. For light materials, where $Z < 10$, the energy transfer is ensured by heat transport of thermal electrons. For $Z > 10$ x-ray emission and absorption processes also contribute. This region is characterized by a temperature in the range between 10 eV and 1 keV.

- The third region is the *shocked region*, characterized by densities larger than $N_s$ and temperatures of the order of $\sim$ 1-10 eV.

#### 2.2.1.1 Absorption mechanisms

There are two main mechanisms of laser absorption in the corona: resonant and collisional absorption. The first one is relevant only for intensities $I > \frac{10^{14}}{\lambda^2[\mu m]}$, a condition not verified with the ns laser pulse we have used in our experiments. Nevertheless, it will be the most efficient process when we will consider short pulse laser- matter interaction. We will thus postpone the discussion in that context, in section 3.2.1.1.

**Collisional absorption** Collisional absorption, also called inverse Bremsstrahlung, involves a photon absorption in the collision between an electron and an ion. The laser absorption is described by:

$$\frac{dI}{dx} = -\alpha I \tag{2.15}$$

where $\alpha$ is the absorption coefficient expressed in $m^{-1}$. In the Drude-Lorentz classical model

$$\alpha = \frac{\nu_{ei}\omega_p^2}{\omega^2 c\Re(n)[1+(\nu_{ei}/\omega)^2]}, \tag{2.16}$$

where $\Re(n)$ is the real part of the refractive index ($n = \sqrt{1-N_e/N_c}$) and $\nu_{ei}$ is the electron-ion collisional frequency. We can obtain the value for $\nu_{ei}$ from the Fokker-Plank equation :

$$\nu_{ei} = 3.6Z^2 N_i \frac{log\Lambda}{T_e^{3/2}} \tag{2.17}$$

with $T_e$ the electron temperature and log$\Lambda$ the Coulomb logarithm:

$$log\Lambda = log\frac{\lambda_D}{b_0} \tag{2.18}$$

Here $\lambda_D$ is the Debye length et $b_0$ the impact parameter for a 90° deflection. For laser generated plasma, the Coulomb logarithm is in the range between 5-10.
In our conditions $\nu_{ei} \ll \omega$ and the absorption coefficient can be expressed as:

$$\alpha = \frac{3.6Z^2 N_i \omega_p^2 log\Lambda}{T_e^{3/2}\omega^2 c\sqrt{1-N_e/N_c}} \tag{2.19}$$

We can notice that this coefficient is a decreasing function of the temperature $T_e$ but it increases with electron density $N_e$. Indeed, it presents a narrow maximum in the vicinity of $N_c$, which induces the absorption to occur mainly at the critical density.

#### 2.2.1.2 Ablation process

The ablation process is at the base of the shock wave generation. In the interaction between an intense laser and a solid target, a hot plasma is created at the target surface. When this plasma relaxes into the vacuum, as a reaction, a shock wave is generated and launched into the target, strongly compressing it.
Scaling laws are available for the ablation pressure as a function of the laser wavelength $\lambda$, pulse length $\tau$, the material atomic number Z and its ionization degree $Z^*$. It can be demonstrated [15] that for intensities weaker than the critical value

$$I_c[W/cm^2] \approx 2\cdot 10^{13}\lambda^{-5}[\mu m]\left(\frac{Z^*}{3.5}\right)^{3/2}\left(\frac{A}{2Z}\right)^{5/4}\tau^{3/2}[ns], \tag{2.20}$$

the ablation rate $\dot{m}_a$ and and ablation pressure $p_a$ can be written as:

$$p_a(Mbar) = 11.6(I(10^{14}W/cm^2))^{3/4}(\lambda(\mu m))^{-1/4}\left(\frac{A}{2Z}\right)^{7/16}\left(\frac{Z^*\tau(ns)}{3.5}\right)^{-1/8}$$

$$\dot{m}_a(kg/s.cm^2) = 143(I(10^{14}W/cm^2))^{3/4}(\lambda(\mu m))^{-4/3}\left(\frac{A}{2Z}\right)^{2/8}\left(\frac{Z^*\tau(ns)}{3.5}\right)^{-1/4}$$

In all our experiments we have used plastic as ablator, for which we can suppose $Z^* = 3.5$, a laser of wavelength $\lambda = 0.527\ \mu m$ and temporal length $\tau = 1 - 2$ ns, so that $I_c \approx 4.4 \cdot 10^{14} - 1.2 \cdot 10^{15} W/cm^2$. The intensities we have reached were much lower that this value ($< 10^{14} W/cm^2$ in all the experiments) so that the presented scaling law can be used to calculate the ablation pressure, which is found $< 13 Mbar$.

### 2.2.2 The shock wave

In the previous section, we have given a generic characterization of the shock wave as a sudden and rapid compression of the target, consequent to the ablation process. We can now describe the shock from a more formal point of view, as the result of the development of non linear effects in fluid dynamics. When a large pressure is suddenly applied to a fluid system, the linear regime of the sound waves breaks down and a shock wave is formed. We shall hence begin from the analysis of the sound waves.

A sound wave is the propagation of a small perturbation of one of the thermodynamic quantities of the medium, such as temperature T, density $\rho$ pressure P or a quantity related to its movement. The equations for the conservation of the mass, momentum and energy of a perfect fluid can be written as:

$$\frac{\partial \rho}{\partial t} + \frac{\partial}{\partial x}(\rho u) = 0 \tag{2.21}$$

$$\frac{\partial}{\partial t}(\rho u) + \frac{\partial}{\partial x}(P + \rho u^2) = 0 \tag{2.22}$$

$$\frac{\partial}{\partial t}\left[\rho(\epsilon + \frac{1}{2}u^2)\right] = -\frac{\partial}{\partial x}\left[\rho u(\epsilon + \frac{1}{2}u^2) + Pu\right] \tag{2.23}$$

In the case where the perturbation of the density $\Delta\rho$ and pressure $\Delta P$ are considerably small in comparison with the average equilibrium values $\rho_0$ and $P_0$ and the flow velocity u is small comparing to the sound speed (see below), we can consider the solutions of these equations in the linear approximation. Small oscillations around the equilibrium values are called "sound waves". The density and the pressure can be written respectively $\rho = \rho_0 + \Delta\rho$ and $P = P_0 + \Delta P$, with $\frac{\Delta\rho}{\rho_0} \ll 1$ and $\frac{\Delta P}{P_0} \ll 1$ while the fluid velocity can be expressed as $u = u_0 + \Delta u$.
Neglecting the second order terms and considering the case of a planar uniform fluid initially at rest ($u_0 = 0$), we can rewrite eq.2.21-2.22 as:

$$\frac{\partial \Delta\rho}{\partial t} + \rho_0 \frac{\partial \Delta u}{\partial x} = 0 \tag{2.24}$$

$$\frac{\partial \Delta u}{\partial t} + \frac{1}{\rho_0}\frac{\partial \Delta P}{\partial x} = 0 \tag{2.25}$$

We can use the fact that in a perfect fluid the particle motion in the sound wave is adiabatic and a small change in pressure is related to a small change in density by the isentropic relation:

$$\Delta P = \left(\frac{\partial P}{\partial \rho}\right)_S \Delta\rho = c^2 \Delta\rho \tag{2.26}$$

where we have introduced the sound speed $c = \left(\frac{\partial P}{\partial \rho}\right)_S^{\frac{1}{2}}$. From eq.2.24-2.26 we obtain a wave equation for the perturbation:

$$\frac{\partial^2 \Delta\phi}{\partial t^2} = c^2 \frac{\partial^2 \Delta\phi}{\partial x^2} \tag{2.27}$$

where $\phi$ can be one of the variables $\Delta\rho, \Delta P, \Delta u$. A wave equation 2.27 allows two families of solutions: $\Delta\phi = \Delta\phi(x - t)$ and $\Delta\phi = \Delta\phi(x + t)$. If c is the positive root $c = +\sqrt{\left(\frac{\partial P}{\partial \rho}\right)_S}$, the first solution describes a disturbance that propagates in the positive x direction, while the second describes the similar motion but in the opposite direction. The general solution is made up from two particular solutions, corresponding to waves propagating in the positive and negative x directions.

If now the small perturbation conditions are not verified, the linear approximation cannot be applied anymore. In this case, the acoustic wave profile is distorted, leading to the formation of a discontinuity, the shock wave. We will give a more qualitative explanation of the phenomena rather than an analytic solution. Let's go back to the equations describing the dynamic of the fluid. The equation for the mass and momentum conservation are equation 2.21 and 2.22. Still considering the isentropic hypothesis and introducing the sound speed, eq.2.21 can be written as :

$$\frac{1}{\rho c}\frac{\partial P}{\partial t} + \frac{u}{\rho c}\frac{\partial P}{\partial x} + c\frac{\partial u}{\partial x} = 0 \tag{2.28}$$

Adding this equation to eq.2.22, we have:

$$\left[\frac{\partial u}{\partial t} + (u + c)\frac{\partial u}{\partial x}\right] + \frac{1}{\rho c}\left[\frac{\partial P}{\partial t} + (u + c)\frac{\partial P}{\partial x}\right] = 0 \tag{2.29}$$

Similarly, subtracting one equation to the other we obtain

$$\left[\frac{\partial u}{\partial t} + (u - c)\frac{\partial u}{\partial x}\right] - \frac{1}{\rho c}\left[\frac{\partial P}{\partial t} + (u - c)\frac{\partial P}{\partial x}\right] = 0 \tag{2.30}$$

We can demonstrate that these two equations are exact differentials $du + dp/\rho c$ and $du - dp/\rho c$ along some particular curves, called the characteristics, respectively:

$$C^+ : \frac{dx}{dt} = u(x,t) + c(x,t) \tag{2.31}$$

and

$$C^- : \frac{dx}{dt} = u(x,t) - c(x,t) \tag{2.32}$$

Along these curves:

$$\int_{C^+} du + \frac{dP}{\rho c} = u + \int_{C^+} c\frac{d\rho}{\rho} = const \equiv J^+ \tag{2.33}$$

$$\int_{C^-} du - \frac{dP}{\rho c} = u - \int_{C^-} c\frac{d\rho}{\rho} = const \equiv J^- \tag{2.34}$$

The constants of motion $J^+$ and $J^-$ are called the Riemann invariants. Resolving eq.2.33 or eq.2.34 we obtain an expression of $\rho$ as a function of $u$. The isentropic condition then allows to express any of the thermodynamic parameters, including the sound speed, as a function of $\rho$. Combining these two observations, we can finally write any of the thermodynamic variable as a function of $u$ only. In particular, we can express the sound speed $c = g(u)$.
Eq.2.31 can then be integrated into:

$$x = [u + c(u)]t + F(u) \tag{2.35}$$

This equation determines u as an implicit function of x and t. The solution is a wave travelling in the positive x direction:

$$u = f\{x - [u + c(u)]t\} \tag{2.36}$$

$$c = g \circ f^{-1}\{x - [u + c(u)]t\} \tag{2.37}$$

A wave travelling in the opposite direction with velocity $c(u) - u$ can be obtained in a similar manner. The most important remark can now be made: in contrast to the case of a travelling wave of small amplitude, here the propagation velocity is not constant, but depends on the wave amplitude. As a result, the wave crests travel relatively faster due to a higher sound speed and higher gas velocity, so that the initial profile is distorted. The wave distortion increases with time, as shown in fig.2.3, until the final profile, characterized by a discontinuity, is reached. It can be mathematically demonstrated that this is the only possible final configuration for the system 2.21-2.23. Such a discontinuity is a mathematic point of view; in reality the shock wave has a thickness which is typically of the order of some mean free paths in a gas or of some cell sizes of the crystal lattice in a solid. If we consider a sufficiently long period, we could in principle obtain an "overshooting" of the wave, like shown in fig.2.3(d). This picture, though, has no physical meaning since it does not give a unique solution.

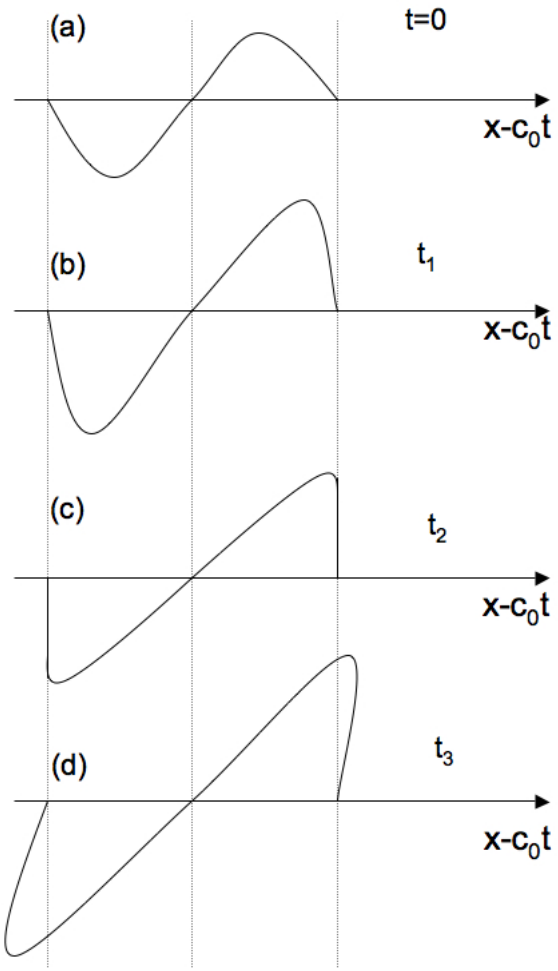


**Figure 2.3:** *As a result of the non linearity of the gas dynamics an initial wave profile is distorted.*

### 2.2.3 Hugoniot-Rankine Relations

The conservation laws across the shock discontinuity are known as Hugoniot-Rankine equations. They relate the thermodynamic quantities to the dynamics of the shocked and unshocked fluid.
We consider a fluid in which a shock wave propagates. We will choose the "shock wave" as the reference frame, in which the shock is at rest. An upstream flow, the unperturbed fluid, will then approach the shock with a velocity $u_0$, while there will be an outgoing flow moving with a velocity $u_1$. An integration of the conservation equations 2.21-2.23 over a small region across the discontinuity leads, for the mass conservation for instance, to:

$$\int_{x_1}^{x_0} \frac{\partial \rho}{\partial t} dx' = -\int_{x_1}^{x_0} \frac{\partial}{\partial x}(\rho u) dx' = \rho u|_{x_1} - \rho u|_{x_0} \tag{2.38}$$

As $x_0 - x_1$ approaches zero, the first term on the left of eq.2.38 becomes infinitesimal and we end up with:

$$\rho_1 u_1 = \rho_0 u_0 \tag{2.39}$$

Doing the same for all the other equations 2.22-2.23, we obtain:

$$P_1 + \rho_1 u_1^2 = P_0 + \rho_0 u_0^2 \tag{2.40}$$

$$E_1 + \frac{P_1}{\rho_1} + \frac{u_1^2}{2} = E_0 + \frac{P_0}{\rho_0} + \frac{u_0^2}{2} \tag{2.41}$$

Equations 2.39-2.41 are called the *Hugoniot-Rankine* equations. As experiments are done in the inertial frame of the laboratory, it is useful to rewrite the same equations in the laboratory frame where the upstream fluid is at rest. In such a reference frame the shock propagates with a velocity $U_s = -u_0$, while the shocked fluid has a velocity: $U_P = u_1 - u_0 = u_1 + U_s$. In this reference, equations 2.39-2.41 take the form:

$$\rho_0 U_s = \rho_1 (U_s - U_P) \tag{2.42}$$

$$P_1 - P_0 = \rho_0 U_s U_P \tag{2.43}$$

$$E_1 - E_0 = \frac{U_P^2}{2} + \frac{P_0 U_P}{\rho_0 U_s} \tag{2.44}$$

These equations are fundamental from an experimental point of view, as they represent the starting point for the equation of state measurement.

## 2.3 Shock compression and Equation of State

In deriving the Hugoniot-Rankine relations in section 2.2.3, no assumption was done on the thermodynamic state of the shocked material. Indeed, the three quantities P, $\rho$ and E are not independent but they are related to each other via a relation called the *Equation Of State* (EOS) of the material:

$$f(P, \rho, E) = 0 \tag{2.45}$$

If the equation of state is known, we have four equations (the three Hugoniot-Rankine relations+ EOS) with five parameters $(P_1, \rho_1, E_1, U_s, U_P)$: the measurement of only one of them allows to infer the values of all the others. In this case, rewriting the equation of the energy conservation as:

$$E_1 - E_0 = \frac{1}{2}(P_1 + P_0)(V_0 - V_1) \tag{2.46}$$

where V is the specific value (V=$1/\rho$), we can define a curve on the (P,V) plane which is called the *Hugoniot curve*:

$$P = P_H(V, P_0, V_0) \tag{2.47}$$

This curve is of extreme importance in the shock wave physics as it represents all the final states that can be reached by a single shock, starting from a well defined initial state. Indeed, the Hugoniot curve is a function of two parameters, the initial pressure $P_0$ and the initial volume $V_0$ and differs from ordinary isentropes, which belong to one-parameter family of curves $P = P_S(V, S)$. It is worth noting that the shock compression is highly dissipative. The process is hence irreversible and the path followed to reach the final state does not lie on the surface defined by 2.45. The entropy increase strongly modifies the system. As a consequence, the final state achieved by a compression with a single strong shock will differ by the one reached by multiple shocks. If starting from the same initial state, a single and a multiple shock compression lead to the same pressure, the final density will be different (fig.2.4). By generating a series of multiple shocks, one can achieve a nearly isentropic transformation, where the compression is maximum. A shock compresses less than an isentropic transformation, as part of its energy is used to heat the material.

Indeed, there is a limit on the compression achievable with a single shock. This is determined by the specific heat ratio $\gamma$. If $\gamma$ is supposed to be constant along the Hugoniot, we can determine this limit through the equation of state for a polytropic gas. The polytropic gas EOS is a useful approximation under many circumstances, particularly at high temperatures, where any material behaves like an ideal gas. In this case the internal energy is:

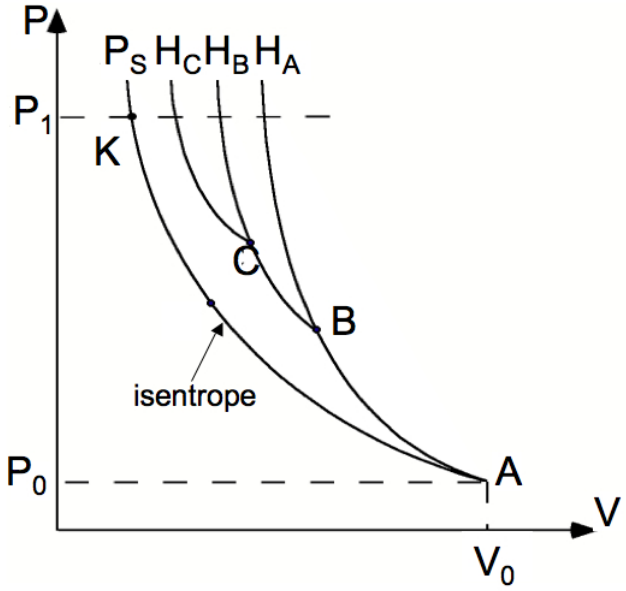


**Figure 2.4:** *The compression state reached with a single strong shock differs by the one reached by multiple shocks. Here $H_A, H_B, H_C$ represent the Hugoniot curves from the initial states A,B,C respectively. $P_S$ is the isentrope with initial state A. A series of shocks approaches the isentrope compression.*

$$E = \frac{1}{\gamma - 1} PV \tag{2.48}$$

Solving eq.2.39-2.40 for $u_0$ and $u_1$ we obtain:

$$u_0^2 = V_0^2 \left(\frac{P_1 - P_0}{V_0 - V_1}\right) \tag{2.49}$$

and

$$u_1^2 = V_1^2 \left(\frac{P_1 - P_0}{V_0 - V_1}\right) \tag{2.50}$$

Using now eq.2.48 and the conservation of the energy (eq.2.46), we can explicitly write the ratio of the specific volumes, which is given by:

$$\frac{V_1}{V_0} = \frac{(\gamma - 1)P_1 + (\gamma + 1)P_0}{(\gamma + 1)P_1 + (\gamma - 1)P_0} \tag{2.51}$$

It is clear from this equation that for a very strong shock, where the pressure behind the front is much higher than the initial pressure ($P_1 \gg P_0$), the density ratio does not increase indefinitely with pressure but reaches a well known fixed value:

$$\frac{\rho_1}{\rho_0} = \frac{V_0}{V_1} = \frac{\gamma+1}{\gamma-1} \tag{2.52}$$

Consequently, the compression limit in a perfect monoatomic gas with $\gamma = 5/3$ is 4, and it is 6 in a diatomic gas ($\gamma = 7/5$).
Remaining in the context of a polytropic gas EOS, we can also make some important considerations on the shock wave dynamics by comparing the fluid velocities on both sides of the discontinuity with the corresponding sound speeds. For $P_1 \gg P_0$ using eq.2.48, equations 2.49 and 2.50 we have the relations:

$$u_0 = \left(\frac{\gamma+1}{2} P_1 V_0\right)^{1/2} \tag{2.53}$$

and

$$u_1 = \left(\frac{(\gamma-1)^2}{2(\gamma+1)} P_1 V_0\right)^{1/2} \tag{2.54}$$

while the sound speed is:

$$c^2 = \gamma \frac{P}{\rho} = \gamma P V \tag{2.55}$$

The ratio $\left(\frac{u}{c}\right)$, called the *Mach Number*, is then given by:

$$\left(\frac{u_0}{c_0}\right)^2 = \frac{(\gamma-1) + (\gamma+1)P_1/P_0}{2\gamma} \tag{2.56}$$

and

$$\left(\frac{u_1}{c_1}\right)^2 = \frac{(\gamma-1) + (\gamma+1)P_0/P_1}{2\gamma} \tag{2.57}$$

in the downstream and upstream flows respectively. We can observe that in the case of a weak shock, where $P_1 \approx P_0$, the density increase is also small (eq.2.51), implying that $c_1 \approx c_0$. From eq.2.56-2.57, is then obvious that $u_0 \approx c_0 \approx c_1 \approx u_1$ which expresses the fact that a weak shock wave is an acoustic compression wave. Equations 2.56-2.57 also show that in the shock wave reference frame, the gas flows in the discontinuity with a supersonic velocity $u_0 > c_0$ and flows out with a subsonic velocity $u_1 < c_1$. Said in a different way, the shock propagates at a supersonic velocity with respect to the unperturbed gas while it moves at a subsonic velocity with respect to the compressed gas behind it.

### 2.3.1 Shock propagation at interfaces

The analysis of the shock propagation across the interface of two materials is the best way to understand the impedance mismatch technique, widely used for EOS measurement experiments.
When a shock wave travels from one material A to another material B, the interface has to remain at equilibrium during and after the shock propagation. This means that on both sides of the discontinuity the fluid velocity $U_P$ and pressure P are equal. The other thermodynamic quantities can have different values, given by the equation of state.

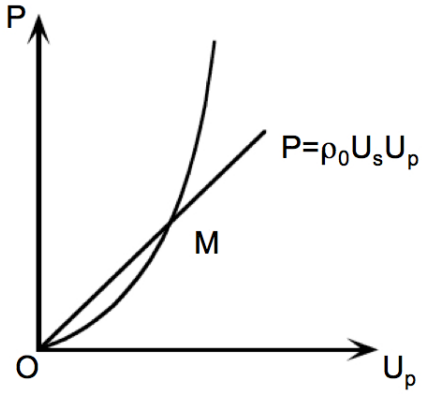


**Figure 2.5:** *Hugoniot curve with initial state O. The slope of the line OM is the shock impedance.*

The curve describing the final states achievable with a shock compression in the plain $(P, U_P)$ is called Hugoniot curve. If M is the final state reached by a single shock, we call shock impedance the slope of the straight line OM (fig.2.5) which, from eq.2.43, takes the value

$$Z = \rho_0 U_S$$

When the shock crosses the interface between A and B two different cases occur:

- If $Z_A < Z_B$: a higher pressure shock is transmitted in B and a shock of the same pressure is reflected in A.
- If $Z_A > Z_B$: a weaker shock is transmitted in B while a relaxation wave propagates in A.

$Z_A < Z_B$

At the interface, the shock wave brings the material A to a state represented by the point A in the plane $(P - U_P)$ (fig.2.6). From this point a shock is reflected in A, described by the curve $H'_{AC}$ which is the symmetric of $H_{AC}$. It is called hot Hugoniot

curve because its starting point A lies on the already compressed Hugoniot curve $H_A$. In B, a shock wave of the same pressure is transmitted. The value of this common pressure is given by the intersection of $H'_{AC}$ and $H_B$

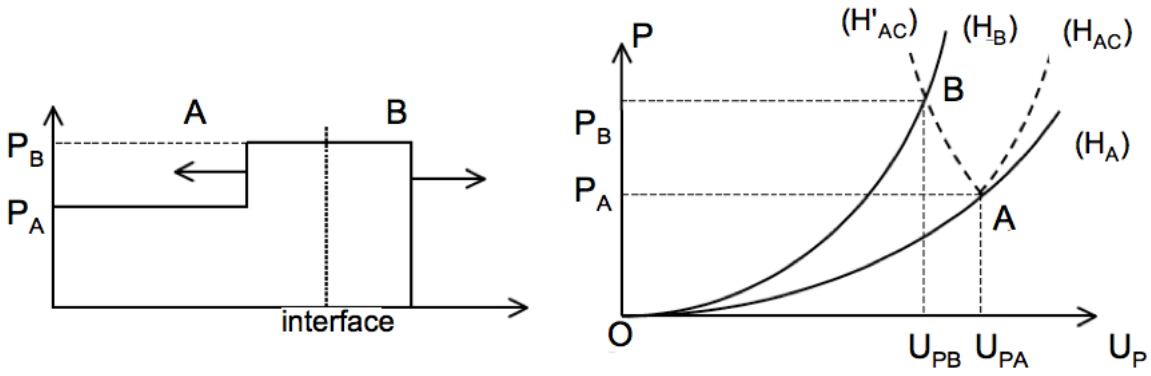


**Figure 2.6:** *Pressure profile after the shock has crossed the interface between material A and B when* $Z_A < Z_B$.

$Z_A > Z_B$

A relaxation wave propagates in A, while a weaker shock is transmitted in B. Here, the final pressure is given by the intersection of the isentrope curve starting from the state A and the shock Hugoniot for material B, $H_B$ fig.2.7.

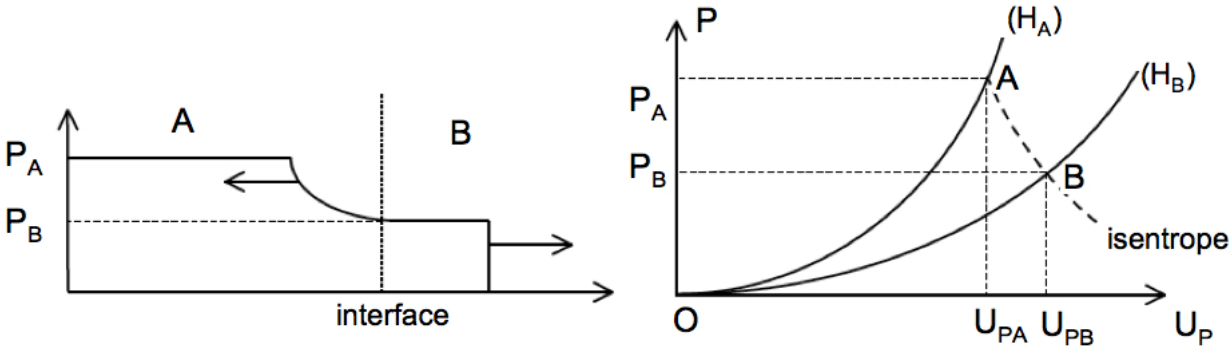


**Figure 2.7:** *Pressure profile after the shock has crossed the interface between material A and B when* $Z_A > Z_B$.

The relaxation wave induces a pressure decrease in A and the released wave propagates at a speed given by:

$$v = \int_{P_a}^{P_B} \left(-\frac{\partial V}{\partial P}\right)_S^{1/2} dP + U_{PA} \tag{2.58}$$

# Bibliography


[1] The physics of High Pressure (London: G. Bell and Sons) 1931, reprinted 1970 (New York: Dover)

[2] Collected Experimental Papers (Cambridge, MA: Harvard University Press) 1964

[3] C. E. Weir, E. R. Lippincott, A. Van Valkenburg, and E. N. Bunting , J. Res. Natl. Bur. Stand **63A**, 55-62 (1959)

[4] Mao H.K.,Bell P.M., Shaner J.W. and Steinberg D.J., J. Appl. Phys **89**, 3276-83 (1978)

[5] R.Cauble, D.W. Phillion, T.J. Hoover, *et al.*, Phys. Rev. Lett. **70**, 4, 2102 (1993)

[6] C.E. Ragan, Phys. Rev. A **49**, 1391-1402 (1984); R.F. Trunin, Sov. Phys. Usp. **37**, 1123-1145 (1994)

[7] E.Henry, *Équation d'état et métallisation de l'eau comprimée par choc laser* , Thèse de doctorat de l'école polytechnique (2003)

[8] S.Brygoo, Chocs laser sur le diamant, l'hélium et l'hydrogène : une étude expérimentale de la « Warm Dense Matter », Thèse de doctorat CEA (2006)

[9] A.Saemenn, K.Eidmann, I.E.Golovkin, *et al.*, Phys. Rev. Lett. **82**, 4843 (1999)

[10] P.Audebert, R.Shephered, K.B.Fournier, *et al.*, Phys. Rev. Lett. **63**, 265001 (2002)

[11] P.K.Patel, A.J.Mackinnon, *et al.*, Phys. Rev. Lett. **91**, 125004 (2003)

[12] T. Löwer, R. Sigel, K. Eidmann, Phys. Rev. Lett, **72**, 20, 3186 (1994)

[13] M.Koenig, B. Faral, J.M. Boudenne, *et al.*, Phys. Rev. Lett., **74**, 12, 2260 (1995)

[14] A. Benuzzi-Mounaix, T. Löwer, M.Koenig, *et al.*, Phys. Rev. E., **54**, 2, 2162 (1996)

[15] R. Fabbro, B. Faral, J,Virmont, *et al.*, Phys. of Fluids **28**, 3414-3423 (1985)

# Chapter 3

# How to probe Warm Dense Matter

After having introduced how to generate WDM, we shall describe the various methods available to probe it, in order to obtain quantitative information. In this section, we will shortly remind the basic principles of equation of state measurements by shock compression. We will see how to determine a point on the EOS of a material and we will describe "standard" equation of state experiments. These techniques are widely used and did allowed several detailed studies of materials behavior under extreme conditions. Unfortunately, we will also see that the indirect approach they are mostly based on, leads to several issues on the data precision, a key point necessary to distinguish between models. In this context, the main objective of this thesis is to develop new diagnostics suitable for the measurement of other parameters than the hydrodynamic ones. In particular, we will investigate new methods to directly access the density, temperature and electronic density of highly compressed plasmas. Energetic probes, such as MeV proton beams and high energy K$\alpha$ radiation, will be employed. The laser-plasma interaction regimes required for their generation will be discussed. A presentation of the general principles of each new technique as well as the basic physical processes involved will conclude this long chapter.

## 3.1 How dense plasmas are usually probed

In the previous chapter, we have seen that WDM can be generated by shock compression. The possibility to produce high quality shocks to be effectively used for equation of state measurements was demonstrated in the 90's ([1],[2],[3],...). The principle of these experiments are directly based on the Hugoniot-Rankine relations. We have seen that the thermodynamic quantities of the shocked material, P, E, and $\rho$ are related to the shock velocities $U_s$ and $U_P$ via the Rankine-Hugoniot equations (par.2.2.3).
If the equation of state is known[1], the measurement of only one parameter is suffi-

[1] we recall that the EOS is the law relating the pressure, density and temperature

cient to determine all the other quantities. If, instead, we want to determine the EOS, the measurement of two parameters is necessary in order to close the system of the Hugoniot-Rankine equations. If these two parameters can directly be inferred for the test material, an *absolute measurement* is performed.
The shock velocity $U_s$ is one of the easiest parameter that we can experimentally access to. The choice of the second quantity, though, is in general more delicate and represents one of the key points of this work. In "standard" absolute EOS measurement experiments, the choice is usually addressed to the particle velocity $U_P$. In the particular case of a low Z material which under shock compression remains transparent to visible light, optical interferometry techniques can be used to directly monitor $U_P$. The same measurement can be done for opaque materials, but in the only limit of weak shocks [10]. Nevertheless, in a general case accessing to $U_P$ is not an easy task, and often a *relative measurement* is carried on. The relative approach is generally easier as it consists in measuring the shock velocity simultaneously in two materials, one of which is known and used as reference. Using its EOS, it is possible to identify the state of the reference material and, from it, to deduce the state of the sample.

### 3.1.1 Absolute EOS measurement

Some of absolute EOS experiments on low Z materials like deuterium, beryllium and polystyrene were done using time resolved x-ray radiography. In [4] a plasma x-ray source was used to infer simultaneous $U_s - U_P$ measurement from streaked radiography of shocked deuterium. The targets were composed by an Al pusher and a cryogenic cell containing liquid $D_2$. The use of this kind of targets allowed to follow the $Al/D_2$ interface trajectory, the pusher being opaque to the x-ray radiation, while the liquid $D_2$ remains transparent (fig.3.1). The $Al/D_2$ interface correspond to the boundary between

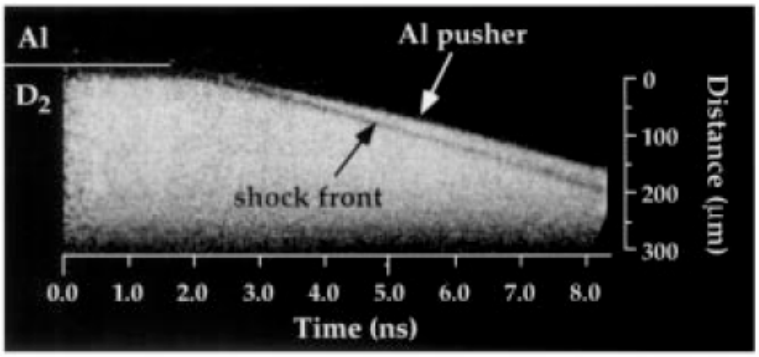


**Figure 3.1:** *From [4]. Time resolved side-on radiograph on a $D_2$ cell. The bright area shows the D2 through beryllium windows with the x-ray-opaque aluminum pusher above. The shock is the dark line in front, moving faster than the pushery/D2 interface.*

the dark and light regions. When the shock breaks into the $D_2$, the pusher moves at the particle velocity. The shock front moving ahead the interface appears as a black line because of the refraction of the x-rays at the density jump across the shock front. X-rays grazing the shock front interface are refracted to angular deflections greater than the angular field of view. The shock velocity and the particle velocity are then inferred from the slopes of the pusher and shock trajectories. In [9] the same technique was used to probe compressed polystyrene and beryllium in an indirect drive configuration. In this case the different transmission between the cold and compressed part of the target was used to monitor the shock trajectory, while again the use of an opaque pusher enabled to measure the fluid velocity from the pusher/transparent sample interface. The intrinsic nature of these measurements requires a perfect shock wave steadiness. Often, though, the shock decelerates in its propagation and the slopes are not constant. This technique cannot be easily applied to probe high Z material, as they are opaque to "soft" x-ray radiation ($h\nu < 10$ keV). The first absolute measurement of a high Z material EOS was done in [10], where optical techniques were used to probe iron samples. In this case optical interferometry diagnostic (VISAR) coupled to a stepped target structure were used to obtain simultaneous fluid and shock velocity (fig.3.2). The

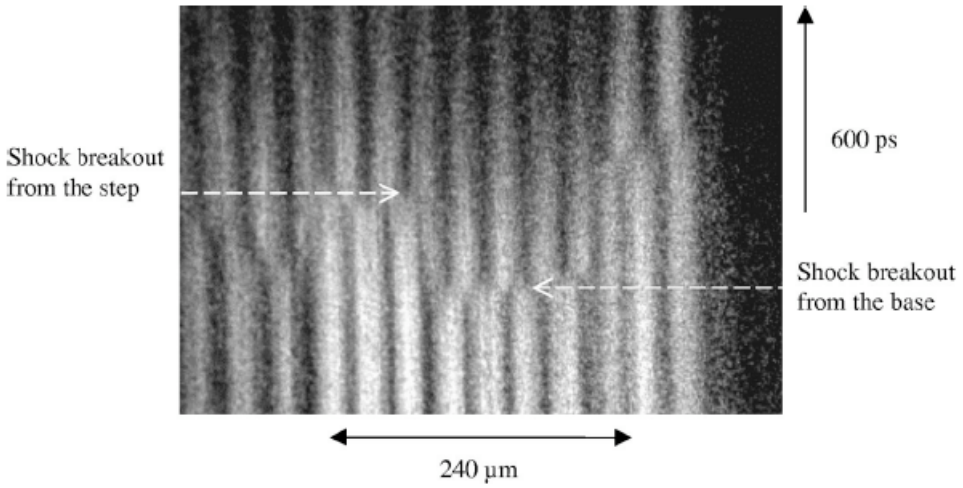


**Figure 3.2:** *From [10]. VISAR image from a stepped Fe target. From the fringe shift after the shock breakout the fluid velocity can be determined. Shock velocity is inferred from the time delay between breakouts at the base and at the step.*

VISAR working principle will be explained in more details in section 6.1.1.2. Here we just mention that it is an interferometric diagnostic able to determine the velocity of a reflecting surface. The variation in the wavelength due to the Doppler effect, directly linked to the velocity, is detectable from the interferometry pattern as a fringe shift.

Temporally resolving the interferometric pattern also allowed to obtain the shock transit time in the step. This was determined from the shock break out at the base and at the end of the step, recorded as two distinguished fringe shifts (fig.3.2). Knowing the step thickness, it is then possible to deduce the mean shock velocity $U_S$. However, the method used to measure $U_S$ leads to mean values and requires the shock to be steady during the measurement. In this context, relative measurements represent the only way to probe high Z materials under higher pressures.
The free surface velocity after these breakouts could also be determined with the VISAR. This information can be obtained as far as the shock does not lead to a vaporization of the target and for materials which have high melting temperature under compressions, such as iron. In this case, the rear side of the target still reflects the probe beam even after the shock breakout (fig.3.2).
The "weak" shock regime is then necessary to infer $U_P$ from the free expansion velocity $u$. Indeed in this regime the fluid velocity is comparable to the sound velocity of the compressed material and the simple relation, $u = 2U_P$ holds. This approach to the absolute equation of state of a high Z material is therefore restricted to a low pressure regime, $P < 4$ Mbar for iron.

### 3.1.2 Relative EOS measurement

Since the measurement of a second parameter is often impossible, most of the time a relative approach is used. This alternative procedure is based on the *impedance mismatch* technique. It involves the simultaneous measurement of the shock velocity in two different materials and it is based on the conservation relations across the materials interface, illustrated in section 2.3.1. One of the two materials must be well known to be used as reference (A) while the other one is the material to be studied (B). The two experimental shock velocities $U_{SA}$ and $U_{SB}$ give two straight lines in the $(P, U_P)$ plane ($P = \rho_0 U_S U_P$). We can determine the state of the material A just behind the shock front by considering the intersection point between the known Hugoniot curve of A and the straight line determined by $U_S A$. This represents the starting point for the reflected shock, if $Z_A < Z_B$, or release wave, if $Z_B < Z_A$, in the reference material A (see section 2.3.1). From the transmission conditions at the two materials boundary, then, the intersection between the reflected wave and the straight line given by $U_S B$ gives a point on the EOS of test material. The procedure is schematically represented in fig.3.3.

Most of time the measurement of the two shock velocities needs a particular target geometry. In these measurements, the targets are usually composed by a common base made of the reference material with two steps: one made of the same reference material and the other one made by the test material. The thicknesses of the steps are accurately measured in such a way that the shock velocity can be deduced by recording the

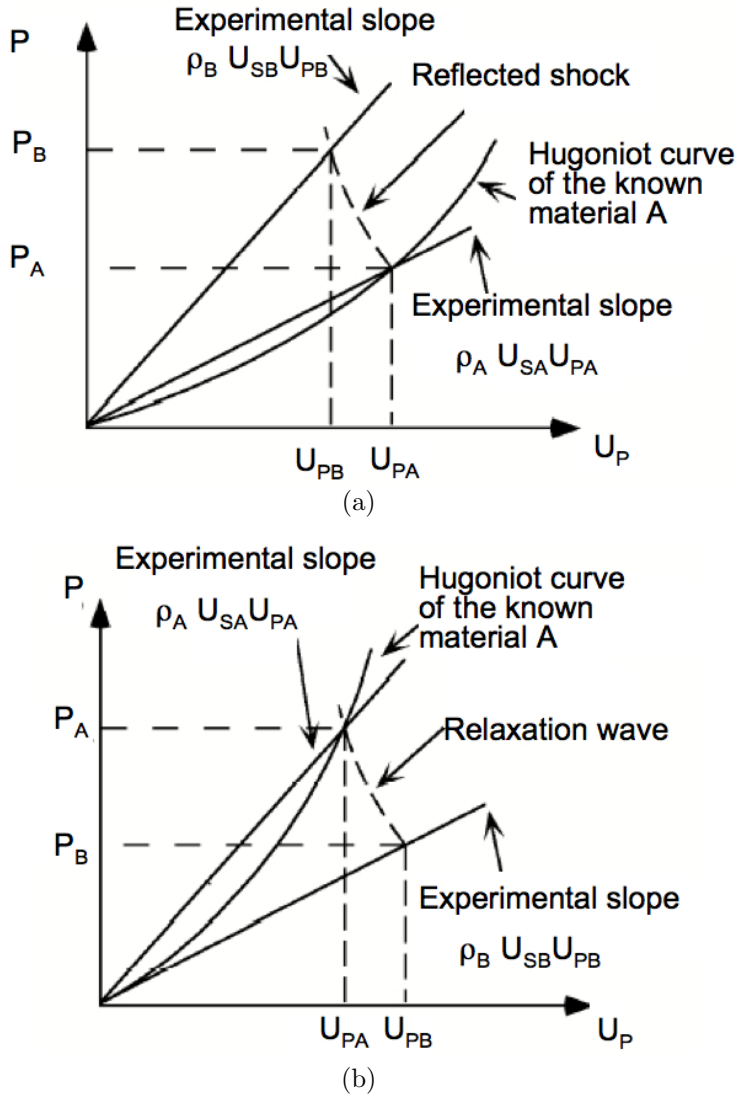


**Figure 3.3:** *Schematic representation of the impedance matching technique for the relative measurement of equation of state. Material A is the reference material while B is the material to be studied. In 3.3(a)* $Z_A < Z_B$*, in 3.3(b)* $Z_A > Z_B$

transit time in each of them. Different diagnostics can be used for this purpose. Beside the VISAR as mentioned before, the easiest way consists in recording the temporal evolution of the target rear side self emission. As the shock breaks out, the rear side temperature is suddenly increased and thermal radiation is emitted in the a spectral domain which extends from IR to X-UV regions. By collecting the emitted light and focusing it on a streak camera slit, it is possible to record the shock breakout from the base and from the two steps, obtaining the shock transit time through each step. Again, the measured velocities are mean values and their precision is affected by shock steadiness and step thickness measurements issues. In addition, by deducing the shock

breakout at two spatially distinguished points, one also requires a good uniformity of the shock wave. Good shock planarity involves the employment of high quality phase plates, like Phase Zone Plates (PZP), Continuous Phase-Plates (CPP), Kinoform Phase Plate (KPP) or Distributed Phase Plates (DPP).
We must mention that the use of quartz as reference material has recently been proposed in order to [12] significantly improve the impedance-matching technique. The substitution of aluminum with quartz allows the use of VISAR for a much more accurate velocity measurement. Indeed, the quartz becomes reflective at relatively low pressures ($\sim$ 2 Mbar) [13] and instantaneous velocity can be accessed. In this case the measurement is not affected by indecision on the step thickness and precisions of 1% can be achieved.
Uncertainties due to the degree of confidence on the reference material still remain. At high pressures, even for most studied and well known materials, as Aluminum above 20 Mbar, the principal Hugoniot is uncertain. This introduces a limit in the use of relative measurements at very high pressures, at least at present time. Recently, new experiments were performed at ILE Osaka combining x-ray radiography for $U_P$ measurement and self emission-Visar diagnostic for $U_S$ measurement in order to obtain an absolute EOS for aluminum at high pressures [11].
In addition, preheating effects could affect the VISAR measurements, leading to a further indecision on the reference material state.

### 3.1.3 Measurement precision

The errors induced in the velocities measurements have different origins, according to the diagnostic used. The main problem general arises from the shock steadiness, which induces an error when the mean velocity is measured. Concerning the temporally resolved x-ray radiography data, the main issue consists in accurately inferring the velocity from a trajectory. In the relative measurements further errors are induced from the step thickness.
Whatever the cause of the experimental uncertainty on the velocity is, the crucial point to be underlined here is that it is amplified when considering important parameter such as density. This is a consequence of the error propagation through Hugoniot-Rankine relations. Form these equations, $\rho/\rho_0 = U_S/(U_S - U_P)$, so that the error on the density can be written as:

$$\frac{\delta\rho}{\rho} = \left(\frac{\rho}{\rho_0} - 1\right)\sqrt{\left(\frac{\delta U_S}{U_S}\right)^2 + \left(\frac{\delta U_P}{U_P}\right)^2} \tag{3.1}$$

We can notice that for highly compressible materials, a small uncertainty in the measurement of the two velocities lead to large errors on compression. To better understand

this key point we can consider the hydrogen case. In the introduction we have briefly discussed the confused situation presented in both experimental and theoretical contexts. In particular it is possible to identify two trends in complete disagreement between themselves (which we report in fig.3.4(a)). The discrepancy on the compression values is obvious. It is interesting, though, to consider the same data on the ($U_S$, $U_P$) plane (fig.3.4(b)). Here the disagreement is much less evident. Therefore, can conclude that the large incompatibilities on compression measurements come from relative small differences in the $U_S$, $U_P$ values. It is thus clear that extremely accurate measurements are needed to solve this controversy.

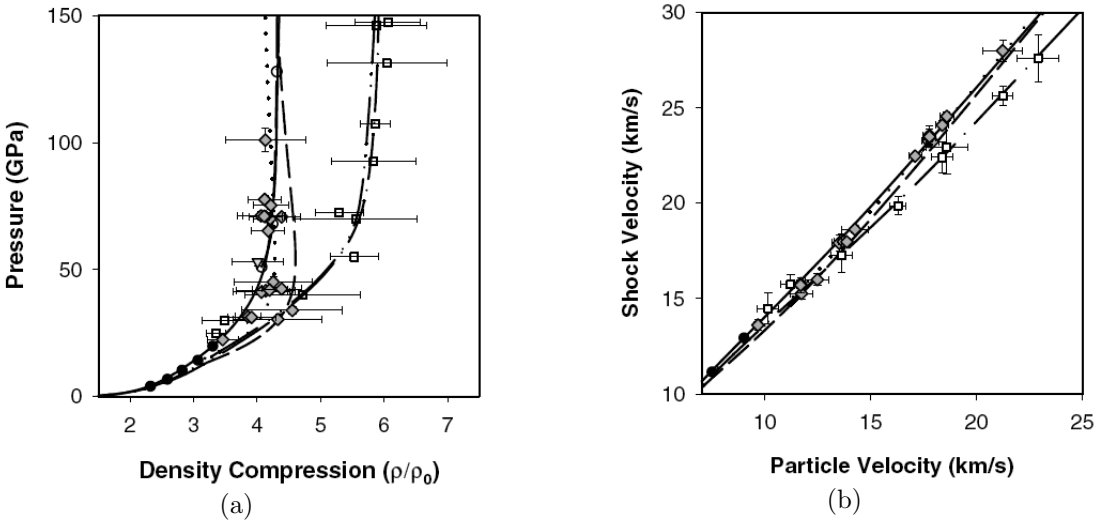


(a) (b)

**Figure 3.4:** *From [5], Deuterium pressure-density compression Hugoniots, together with theoretical models and experimental results. In particular Sesame theoretical model is represented with solid line, while Ross model is the dot-dot-dashed line. Experimental results: Gas gun [6] as filled circles, laser driven [4] as open squared, magnetically driven flyer plates [7] gray diamonds, convergent geometry [8] gray triangles. The same data on the $U_s$ $U_p$ plane (b).*

## 3.2 New probes for Warm Dense Matter: protons and hard x-rays

From what we have discussed so far, it emerges an urgent necessity of developing new diagnostics for a real and substantial breakthrough in the investigation of WDM states. Moreover, energetic probes are necessary to investigate high Z dense plasmas. The novel diagnostics developed in this thesis employ energetic protons beams and hard x-rays generated by $K\alpha$ radiation. Both energetic particles and high energy radiation are generated in laser-plasma interaction, but in an extremely different regime from the one presented in the previous chapter. Here the characteristic energy fluxes are considerably

higher ($> 10^{17} W/cm^2$) and they are obtained with ultra short pulse beams. These characteristics strongly affect the physics of the interaction, leading to considerably different phenomena.
In this section, we will present the main processes of the laser-plasma interaction at high intensity, underlying the differences with the already considered classical ns regime. It will allow to understand the generation of the hot electron population, fundamental for the protons acceleration and $K\alpha$ generation mechanisms. These two processes will also be discussed.

### 3.2.1 Laser plasma interaction at high intensity

After the invention of the laser in the 60's a big challenge has been producing more and more powerful lasers allowing to reach higher and higher intensities. It was soon clear that this goal would have been reached only through the development of ultra short laser pulses, rather than the implementation of very high energy lasers, which have become a distinguished challenge. The main difficulty was represented by the fact that short pulse beams could not be directly amplified as the amplifying medium would have been damaged. The break through came only in the middle of 80's when a new technique able to overcome this limitation was proposed, [14], the so-called *Chirped Pulse Amplification* (CPA). As a short laser pulse has a significantly large bandwidth, the idea consists in stretching it in time allowing its amplification at low irradiance. The pulse is then re-compressed to reach high irradiances. This technique is now at the base of all the high intensity laser systems.With chirped pulse amplification, irradiances of $10^{21}$ $W/cm^2$ are achievable, as in existing PW laser, [15] as an example. These extremely high intensities give rise to completely new laser matter interaction regimes.

The differences between laser matter interaction at high intensity ($I \sim 10^{16-21} W cm^{-2}$) and the "traditional" ns regime mainly are:

- the high electromagnetic fields associated to the laser wave

- the short pulse duration

Due to the high intensity, the interaction between matter and the electromagnetic field associated to the laser wave is non-linear and relativistic effects arise. The electric field associated to the laser can be expressed in term of the intensity as:

$$E = 2.7 \cdot 10^{12} \left( \frac{I(W cm^{-2})}{10^{18}} \right)^{1/2} V m^{-1} \tag{3.2}$$

In the traditional ns regime, the intensity values typically lie of $10^{13-15} W cm^{-2}$ so that the electric field is of the order of $10^{9-10} V/m$, one order of magnitude less than

the Coulomb electric field (in the hydrogen atom ($E_H \sim 5 \cdot 10^{11} V m^{-1}$). For intensities of $10^{16-20}$ $W \cdot cm^{-2}$, characteristic of the femtosecond regime, the electric field values vary between $3 \cdot 10^{11} V/m$ and $3 \cdot 10^{13} V/m$, becoming comparable or even greater that the coulomb atomic field. A direct consequence is a rapid ionization of the atoms via nonlinear phenomena (such as multi-photon or tunnel ionization [16],[17]). In such a high field, the electron quiver velocities can reach values close to the speed of light and relativistic effects, related to the electron mass variation, can become important. A reduction in the plasma frequency can be associated to the increment in the electron mass by the $\gamma$ factor, (eq.2.13 ). As a first consequence, the critical density is shifted to higher values and the laser can penetrate to higher density regions, normally not allowed to classical regimes (self-induced transparency [18] ). Another typical relativistic effect is explicit in the index of refraction increase:

$$n_{rel} = \left(1 - \frac{1}{\gamma}\left(\frac{\omega_{pe}}{\omega_{laser}}\right)^2\right)^{1/2} \tag{3.3}$$

The spatial modulation in the laser intensity is reflected in the spatial dependence of $n_{rel}(r)$ which acts as a convergent lens for the laser radiation (self-focusing [19] ).

The main effect associated to the short duration of the laser pulse is a considerably weak expansion (10 nm-1 $\mu m$) of the plasma during the interaction. The under-dense coronal plasma, typical of the ns-interaction regime, does not have time to form and the conditions for the shock wave generation are missed. The energy deposition, thus, occurs in a steep gradient, at high densities (from the critical to the solid density), i.e. in extremely different conditions from the classical regime. In these conditions, the plasma kinetic properties dominate the fluid aspects and the plasma is no more at thermal equilibrium. While the electron temperature can be raised very quickly by the laser field, the electron-ion thermalisation time (of $\sim 10ps$) is longer than the laser pulse, preventing the ions to be efficiently heated. A significant part of the laser energy is transferred to the electrons by non collisional mechanisms and they are strongly accelerated. For intensities higher than $10^{15}$ $W/cm^2$, the quiver velocity and kinetic energy that an electron can gain in one cycle can be so high that an efficient thermalisation cannot be established. In such a way a population of supra-thermal (hot) electrons is generated in the interaction region and it can propagate through the target over long distances, up to hundreds microns.
In order to better illustrate the absorption mechanisms responsible for the acceleration of the electrons, it is useful to quickly describe the main structure of the interaction region and its characteristics.

- The expansion zone, characterized by densities lower than the critical density, $N_c$. This zone is formed by the plasma relaxing towards the vacuum in front

of the target. The plasma expands at the ablation velocity $v_{abl}$ for a time $\tau$, comparable with the laser pulse duration. The typical length of this region is thus characterized by the gradient length, $L_{grad} = \tau \cdot v_{abl}$; at high intensity $L_{grad}$ is of the order of 10 nm-1 $\mu m$, much smaller than the typical dimensions of the corona region in the ns regime, typically of some hundreds microns.

- The skin layer corresponds to the laser penetration depth. In this layer the laser energy absorption takes place. Its dimension is $L_{skin} = \frac{c}{\omega_{pe}}$. For very steep gradients, the skin layer lies at very high densities, close to the solid density, $N_s$.

- Conduction layer, which represents the zone where the energy is transferred deeply inside the target by thermal electrons. In the classical limit, the heat conduction is described by the Spitzer theory, which considers that the electron mean free path is smaller than the typical thermal gradient length. At high intensities, $I > 10^{17} W/cm^2$, this theory is no more valid since non local effects come into play as a consequence of the large electrons mean free path. New approaches must hence be considered [20],[21]

#### 3.2.1.1 Absorption mechanisms: the supra-thermal electrons generation

There are various energy absorption mechanisms that play a role in the electrons acceleration processes. At high intensities, many collisionless processes become important; these include skin-layer heating, resonance absorption, vacuum heating and $J \times B$ heating. The collisional mechanisms, that are the principal cause of the laser energy absorption in the ns regime, are strongly damped in the high flux regime. As we have seen, the collisional mechanisms efficiency is directly proportional to the electron-ion collision frequency and inversely proportional to the electron temperature. Besides, collisional absorption increases as the ratio $L_{grad}/\lambda$ increases, the number of collisions being greater. In high intensity regimes, the electron temperature at the critical density can be extremely high, the density gradient steep and the thermal velocity much lower than the oscillation velocity. All these reasons make the collisional absorption inefficient, although present in the skin layer.

**Resonant absorption** Resonance absorption [22] is a non collisional absorption mechanism that takes place at the critical surface. It involves a first excitation of an electron plasma wave which then accelerates a small population of fast electrons. For a P polarized laser beam at an oblique incidence, there is a component of the electric field which is parallel to the density gradient. This longitudinal component can penetrate only up to the density $n = n_c cos^2\theta$ and can not reach the critical surface. However, it is possible to demonstrate that the electric field can tunnel evanescently up to the critical surface, [22], making the electrons resonantly oscillate in the direction

of the gradient and thus producing charge density fluctuation. In this way, part of the laser energy is transferred to an electrostatic oscillation (an electronic plasma wave) at the laser frequency. It is worth mentioning that even at normal incident there can be an electric field component parallel to the density gradient, due, for example, to the roughness of the target. The absorption has its maximum when the distance between the reflection region and the critical density, given by $L_{grad}sin^2\theta$, is equal to the laser penetration depth. This condition fixes an optimum angle: $\theta = arcsin\frac{\lambda}{2\cdot\pi L_{grad}}$. It is the best compromise between two processes occurring when the angle of incidence increases. On one hand, the component of the electric field along the plasma wave propagation direction increases as well. On the other hand, the density at which the radiation is reflected back decreases ($n = n_c cos^2\theta$) and the electric field has to tunnel through a larger distance, reducing the absorption efficiency.

The second step in the resonance absorption involves the transfer of the energy to the plasma itself. This process takes place via the damping of the plasma wave. There are many possibilities for the plasma wave to be damped, but only one is responsible for the fast electron population. In this case, the resonant wave reaches such a high amplitude that the trajectories of different electrons can cross ("wave breaking"). In this way some electrons undergo to a sudden change in the electric field and the fastest can escape from the wave restoring force, carrying with them a high kinetic energy. As a result, the electrons can be separated in a high number of non energetic (or cold) electrons and in a small population of fast (or hot) electrons. The two populations are described by Maxwellians at two different temperatures.

The resonant absorption efficiency is bound to the steepness of the density gradient. It becomes less important for very steep gradient, as the amplitude of the electron fluctuations can be larger than the gradient length itself. In this way the plasma wave would be destroyed at each cycle. On the other hand, for very smooth gradients the optimum angle decreases, also reducing the electric field component responsible for the phenomenon.

**Vacuum heating** For strongly steep gradients, the laser wave cannot penetrate deep inside the target and resonant absorption may not be possible. In this case, another collisionless absorption mechanism known as "Vacuum heating" or "Brunel heating" can occur. If the the gradient is very steep the laser interacts just with the surface of the solid. The P component of the laser electric field ionizes the target surface and accelerates the electrons through the vacuum. When the laser field changes its sign, they are re-injected into the target with an energy equal to the oscillation energy in the vacuum. As the laser can penetrate into the target only up to the skin depth, the electrons do not feel any restoring force and are irreversibly accelerated into the target.

As the electrons are accelerated at each laser cycle, Brunel heating leads to packets of electrons injected into the target with a frequency equal to the laser frequency.
The fraction of the energy which is absorbed is written:

$$f = \frac{\eta}{2\pi} \frac{v_{osc}^2}{v_{las}^2 ccos\theta} \tag{3.4}$$

where $\theta$ is the incident angle, $v_{las} = eE_{las}/m\omega_{las}$ et $\eta \approx 1.75(1+2v_{th}/v_{osc})$. At very high energies the importance of this mechanism decreases due to the magnetic contribution of the Lorentz force which deviates the electrons trajectories. A deeper treatment of the vacuum heating can be found in [25]

**J×B heating** At high laser irradiances the longitudinal motion of the electrons in the laser field, due to the $\mathbf{J} \times \mathbf{B}$ component of the Lorentz force, becomes comparable to the transverse motion associated to the electric field. The acceleration process is directly related to the electromagnetic field of the incident laser pulse. At high densities, the radiation pressure associated to the laser wave becomes comparable or even stronger than the thermic plasma pressure. Non linear effects related to the spatial gradients of the laser irradiation occur, resulting in a macroscopic movement of matter deep into the target and a strong acceleration of the plasma electrons.
A direct consequence of the radiation pressure is a non-linear force acting on the plasma electrons. For a linear polarized plasma wave, the non linear force can be expressed as:

$$\mathbf{F_{NL}} = m_e \left(\frac{dv}{dt}\right) = -\frac{e^2}{4m_e\omega_{las}} [\nabla(|\mathbf{E_0}|^\mathbf{2}) + \nabla(|\mathbf{E_0}|^\mathbf{2}) cos2\omega_{las}t] \tag{3.5}$$

The first term in eq.3.5 varies slowly with the laser frequency $\omega_{las}$ and its temporal mean value over a laser period is called the ponderomotive force:

$$\langle \mathbf{F_p} \rangle = \frac{e^2}{4m_e\omega las} \frac{1}{2c} \nabla I_{las} \tag{3.6}$$

The direct consequence of this term is to steepen the density gradient as its effect is to push the electrons towards the weak intensity regions. In a laser pulse, a spatial gradient is present both in the transverse direction and the longitudinal direction, in this last case because of the temporal profile and the wave damping further beyond the critical density. Therefore, the electrons are accelerated both towards the edges and towards the interior of the target. The ions do not respond directly to the ponderomotive force because of their higher inertia, but they follow the electrons on a temporal scale of some ps, longer than the pulse duration.
The second term in eq.3.5 is responsible for the electrons acceleration process in the skin layer. The heating mechanism is called "$J \times B$ heating" as it raises from the magnetic term of the Lorentz force. The absorption mechanism is similar to the Brunel's one,

where the electrons are driven across the vacuum plasma interface by the magnetic field rather than the electric field. A detailed description of this heating mechanism can be found in [23] and [24]. The process has its best efficiency at position, $\sim 4n_c$, where both the oscillating force and the number of electrons involved in the process are maximized.

**Normal and anomalous skin effects** These absorption mechanisms require extremely steep plasma profiles and become important in the interaction of ultra-short, high contrast laser pulse with solid targets. In normal skin effect, the laser energy can be absorbed in the skin layer through classical collision mechanisms as soon as the electronic mean free path is smaller than the skin layer. These conditions requires relatively low laser intensities, $\lesssim 10^{16} W/cm^2$. As the intensity rises, the electrons become less collisional and their mean free path can exceed the skin depth so that local thermalization can not occur anymore. A collisionless absorption mechanism can then take place, the anomalous skin effect. In this case the electrons, which are accelerated by the laser field within the skin layer, can penetrate beyond the skin depth and transfer their energy deeper in the target. A more accurate theory applicable in this regime can be found in [20].

### 3.2.2 Proton beams

Fast ion production from laser irradiated targets have been observed and measured in experiments since 1960's [26]. The coupling of the laser energy to the fast ion population occurs via the hot electrons we have discussed above. The proton generation and acceleration process is mainly due to charge separation electrostatic fields built up by fast electrons at the target-vacuum interfaces. These extremely intense fields interact with hydrocarbons contaminants, ionize them and accelerate the resulting ions. The discovery of the major role played by contaminants was soon realized when Gitometer *et al.*[27] first collected data from laser solid interaction in different conditions of target geometries and laser pulses. It was observed that most of the ions detected from their spectrometers were protons, regardless the target material. This fact suggested that most of the signal came from a thin layer of hydrocarbon contaminants. This layer, of typical thickness of $\sim$ 20 Å, is always present on the target surface because of preparation procedure, handling or pump vacuum oil. The protons response to the accelerating field is quicker than other ions' because of the higher charge to mass ratio. Therefore, the proton population depletes the available energy and the heavier ions cannot be significantly accelerated. This interpretation has been tested by removing the contaminant layer before the laser irradiation, by resistive heating for example [28]. In this case the proton signal is lowered and the ions from the target constituents are accelerated to higher energies. In the following, we shall always refer to proton beams, as they are the particles we used in our experiments. It should be stressed anyway that

the same treatment can be applied to ion beams, accounting for their mass and charge. We shall focus on the acceleration mechanisms of a small population of energetic ions propagating axially, along the laser direction.

In [29] and [30] two main processes have been proposed to describe the accelerating mechanism. They are used to describe the properties of protons originated respectively at the front surface of the target, i.e. where the laser is focused onto, and at the target rear side. Indeed, until some years ago there was an open controversy on which was the most efficient accelerating mechanism. Some experiments, [31]-[32], seemed to evidence that the observed protons were mainly originated at the front of the target, in disagreement with other experimental works [33]-[34], indicating that most of the detected signal was due to protons from the rear side. At present, the rear surface acceleration seems to be the most efficient scenario. Several experiments have confirmed this picture, as demonstrated in [35]-[37]. We will quickly present both mechanisms.

**Hole-boring effect** Proton acceleration at the front of the target is done via the charge separation induced by the laser ponderomotive force. As we have seen before, the ponderomotive force acts on the electrons and push them into the target until it is balanced by the electrostatic field induced by the charge separation. This field $E_s$ is estimated to be:

$$E_s \approx \frac{m_e c \omega_{las}}{2e} \frac{a_0^2}{\sqrt{1+\frac{a_0^2}{2}}} \tag{3.7}$$

where $a_0$ is the dimensionless laser amplitude defined as $a_0 = \frac{eE}{m_e c \omega_{las}}$

The maximum energy for the protons accelerated at the front surface is, [29],

$$E_{max}^{front} \sim 2\sqrt{2}{a_0}^2 \cdot 0.511 MeV \tag{3.8}$$

For typical irradiances of $10^{19}\ W \cdot cm^{-2}$ protons reach maximum energy of $E_{max}^{front} \sim 2.8$ MeV. We have to point out that in this treatment no assumption on the target properties (material or thickness) is made, in contrast with experimental observations.

**Plasma expansion into a vacuum** According to this picture, protons are accelerated from the electrostatic field built up at the target rear side. As we have previously discussed, hot electrons propagate through the target. Typically, the hot electrons mean free path is larger than the target thickness used in these experiments. Nonetheless, only few electrons can escape from the rear side before that the target is substantially

[2] If ions are considered, $E_{max}^{front} \sim 2\sqrt{2}a_0 Z \cdot 0.511$, where Z is the ion charge.

charged up, preventing further escaping. The electrons are thus confined forming a Debye sheath. Intense electrostatic fields are hence built up by charge separation. The Debye sheath thickness is of the order of 1 $\mu m$ so that the generated electrostatic fields are sufficiently intense (of the order of a teravolt per meter) to ionize the atoms and accelerate the protons in a direction normal to the target surface. After this phase, the protons stream freely into the vacuum, being charge neutralized by the co-moving electrons.
This acceleration mechanism is described by many authors as a plasma expansion in the vacuum, see [30] for more details. Due to the isothermal assumption made, this model predicts an unlimited value of the ion expanding velocity, which in reality saturates.
Figure 3.5, taken from [34], shows a schematic representation of this acceleration mechanism.

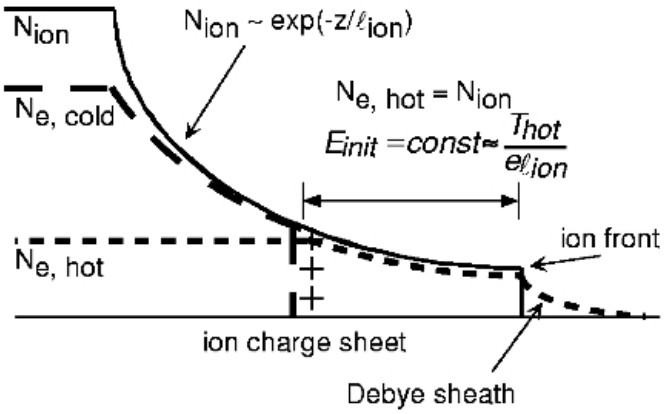


**Figure 3.5:** *Schematic representation of the rear side acceleration mechanism from [34].*

The validity of this sheath model is confirmed by different experiments. In [35] it was found that the accelerating mechanism was drastically reduced when a plasma with scale length of 100 $\mu m$ was produced on the back of the foil. In that case, the maximum proton energy was $< 5$ MeV, while $> 20$ MeV protons were easily observed with unperturbed foils. These results are consistent with the accelerating field solutions predicted by the model, $E_s = \dfrac{k_B T_e}{e L_s}$, where $T_e$ is the electron temperature and $L_s$ is the proton density scale length at the rear side. In addition, in [36] the acceleration efficiency was investigated as a function of the initial target thickness. The data show a reduction in both proton signal and maximum energy for thicker targets, which is a clear evidence of the principal role played by the electrostatic sheath in the acceleration process. Indeed, the temporal dynamics of the hot electrons changes by varying the target thickness, affecting the sheath electron density and hence the sheath electric

field. The electrons that are accelerated into the target are reflected at the rear side by the Debye sheath, go back towards the front side where they are again reflected from the front Debye sheath and so on. In targets where the double transit time is much less than the pulse duration, the electron density at the rear side is a superposition of the electrons directly accelerated by the laser pulse and those reentering the target. In thinner targets, the hot electron density at the rear side is therefore larger. Finally, in [37] the efficiency of both the front and rear face acceleration is measured under identical conditions. It was found that higher energy particles with smaller divergence are generated at the target rear side.

### 3.2.3 K-$\alpha$ generation

The propagation of the fast electron population through the target is also responsible for the x-ray $K\alpha$ emission. During their propagation into matter the hot electrons undergo numerous collisions with the medium atoms. This results in an energy transfer from the electrons to the atoms via different mechanisms (ionization, excitation, radiative damping, etc...).
In particular, K-shell ionization is induced by electron impact if the electron energy is larger than the K-shell ionization threshold. The atom is thus left in an unstable state and an outer shell electron drops to the ground state in order to reestablish the equilibrium. The energy released in this electron transition can be emitted in the form of x-ray radiation or transferred to another atomic electron, which is then ejected from the atom (Auger effect).
The probability that radiative emission takes place is given by the fluorescence yield $W_K$. It is expressed as a function of the atomic number Z as:

$$W_K = \frac{Z^4}{Z^4 + 1.12 \cdot 10^6} \tag{3.9}$$

In the case of a radiative transition following the ionization of the K shell, the most probable transitions are shown in fig.3.6. Among them, the $K\alpha$ transition ($2p \rightarrow 1s$) is the most probable and gives rise to the most intense line. The probability that an electron of energy E knocks out an electron of the K shell, whose binding energy is $E_K$, depends on the internal shell (K,L,M,...) ionization cross section, given by [38]:

$$\sigma_K = \frac{\pi e^4}{E E_K} 2 b_K ln \frac{4E}{c_K E_K} \tag{3.10}$$

where $b_K$ and $c_K$ are empirical parameters which depend on the material properies. The cross section has its maximum for electron energies slightly higher than the shell binding energy and rapidly decreases. The intensity of the $K\alpha$ signal will then be particularly sensitive to the low energy tail of the electron distribution.

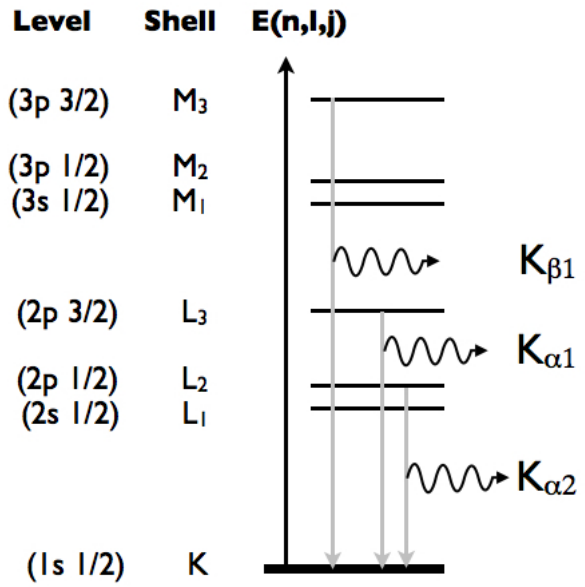


**Figure 3.6:** *Schematic representation of the radiative disexcitation transitions for an ionized atom in the K shell. An upper shell electron drops to the ground state to re-establish the equilibrium. The $K\alpha$ transition is the most probable.*

The number of $K\alpha$ photons emitted when a material of thickness $dx$ is crossed by $n$ electrons of energy E is given by:

$$N_{ph} = n\sigma_K(E)W_K N_i dx \tag{3.11}$$

$N_i$ being the atomic density. K$\alpha$ photons are uniformly emitted and the formula gives the total value in a solid angle $\Omega = 4\pi$ .
Another characteristic of the K$\alpha$ emission, which is particularly interesting in its application to shock radiography, is represented by its short temporal duration. As we are concerned by the K$\alpha$ emission generated by the hot electron population, its duration is directly related to the typical electron thermalisation time in the solid. Since, the hot electrons are generated during the laser pulse duration, it is reasonable to consider the K$\alpha$ emission not sensibly longer than the laser pulse.
In our experiment, high energy K$\alpha$ x-rays are employed in the radiography of a shock compressed material. The CPA laser used in the x-ray source generation had a 1 ps pulse, so that we can suppose almost the same duration for the K$\alpha$ emission. This is of considerable importance in our experiment, as it allows probing a well defined plasma state, given that the hydrodynamic evolution is $\gtrsim$ 100 ps.

## 3.3 New diagnostics for Warm Dense Matter

Having introduced the proton and K$\alpha$ beams, we can now discuss how they can be used in WDM probing. In particular, we will investigate their application in measurements of density and temperature, as these are two of the most important parameters involved in several controversies. Accessing to a third parameter, other than shock and particle velocity, is fundamental since it allows to reach higher accuracy in EOS measurements. In this thesis we have investigated three novel techniques, being successfully applied to shock compression experiments. *Hard x-ray radiography* and *high energy proton radiography* are proposed as diagnostic tools for direct density measurements, while collective *x-ray thomson scattering* allows to access electron temperature, electron density and collective effects of dense plasmas.
The experimental results obtained with each technique will be discussed in the next three chapters. Here we will shortly present the basic principles of each measurement.

### 3.3.1 X-ray radiography

X-ray backlighters are often used in high energy density experiments as standard techniques to diagnose hydrodynamic evolutions. In particular precise informations on shock trajectories, interface motion and instability growths can be obtained with time resolved radiography. In inertial confinement research this is an useful technique to study the capsule implosion and Rayleigh-Taylor instabilities, while in the astrophysical context, it can be suitably applied to the investigation of jets hydrodynamics or radiative shocks, for instance.

While most of times time-resolved x-ray radiography is used in indirect compression measurements ([4]-[9] for example), a direct approach was followed by Hammel *et al.* in [39]. Here, Fe K-shell emission at $\sim 6.7$ keV was used to probe shock compressed CH targets. By using a slit pinhole coupled to a streak camera, the x-ray transmission was obtained as a function of time. The 1D measurement, though, could not allow to take the details of the shock front shape into account, necessary to correctly determine the actual x-ray path through the shocked material. In particular, neglecting the shock curvature leads to an underestimate of the linear density in the shock compressed region. The measurement, thus, results in a lower limit of the compression.
Since that work, it has been clear that a 2D shock image is essential in order to obtain high precision density measurements from x-ray radiography.

Different techniques are generally used to obtain 2D x-ray images. Most of the time, these diagnostics include reflective-optics systems, metal mirror Kirkpatrick−Baez (KB) microscopes [40], multi-layer coated KB microscopes [42], x-ray framed microscope [41],

bent crystal KB microscopes, single spherical [43] or toroidal crystal microscopes [44] or more complex compound grazing incident systems as Wölter microscopes [45]. Many of these methods can be well adapted to the x-ray radiography technique; their use is nevertheless limited to a few keV. If hard x-rays need to be used, the most practical way to obtain a 2D x-ray image relies on the point projection configuration.

In a point projection configuration, a x-ray source produces a flash of radiation. The

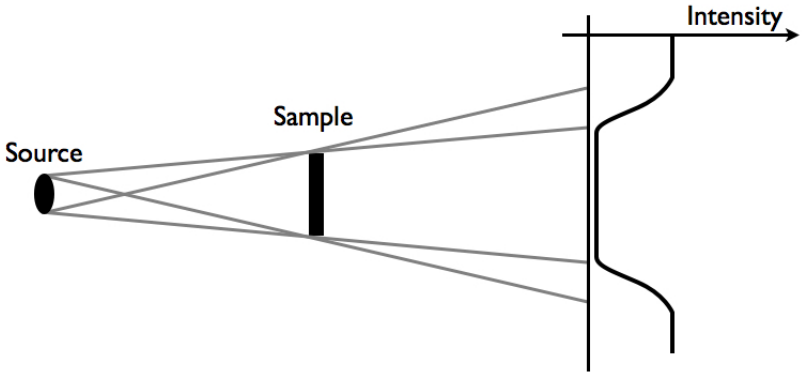


**Figure 3.7:** *Schematic representation of the point projection technique.*

x-rays are then used to backlight the sample and are recorded on a x-ray sensitive detector (see fig.3.7). In this way, an imaging system is combined with information on the absorption from the sample. Therefore, point projection imaging can be used to obtain direct density measurements.

#### 3.3.1.1 Principle of the measurement

In shock compression contexts, the idea is to obtain a snapshot of a spherical shock. The 2D image is then "inverted" to extract the density profile behind the shock front. This technique overcomes a lot of concerns previously discussed. First of all, the measurement being done on a snapshot, it does not require steady shocks, which are instead of crucial importance in many of the standard measurements described before. The spherical approach, then, does not require the use of high quality phase plates for the planarity.

This technique can be implemented to standard velocity diagnostics, providing absolute EOS measurements. Its first application was tested on the OMEGA laser [46], where shock compressed polystyrene was radiographed (fig.3.8) to obtain EOS hugoniot data. In that experiment, the x-ray source was generated in the interaction of a ns laser with a backlighter target. The source size was artificially reduced by means of a 10 $\mu m$ pinhole and the transmitted radiation was collected on a x-ray framing camera. The density

change associated to the shock compression causes a difference in the x-ray absorption. A high transmission is related to weakly compressed regions, while the darker parts of the image correspond to higher densities. Therefore, recording the transmitted signal from the whole target allows to obtain a density map.

In order to get quantitative measurements, the detector must show a good contrast

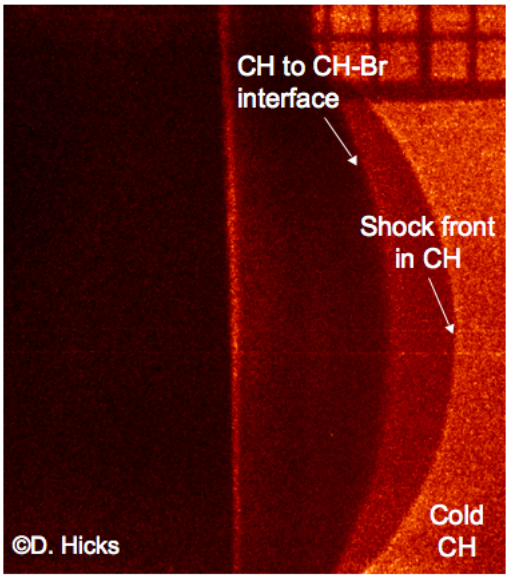


**Figure 3.8:** *Radiograph of a shock compressed polystyrene.*

between the shocked and unshocked part of the target, which induces strict limits on the choice of the x-ray source. The photon energy must not only account for the target density, thickness and Z, but also for the expected compression. In [46] a $\sim$ 5 keV x-ray backlighter source generated with a long (ns) pulse laser was well adapted to probe CH targets (see fig.3.8). However, in order to investigate higher Z materials, one needs to employ more energetic radiation. In this case, thermal x-ray are no more suitable, as they cannot exceed few keV. A two to four contrast ratio is usually well adapted to obtain high quality radiographs. For high Z plasmas this condition requires x-rays of $\sim$13 keV, as shown in fig.3.9, where we plot the x-ray transmission from 400 $\mu m$ thick Al at normal density and for a typical 2.0 fold compression.

In order to achieve such energies, K$\alpha$ emission generated by ultraintense laser beams ($I_L > 10^{17} W/cm^2$) represents a promising candidate. We have discussed the K$\alpha$ generation mechanism in 3.2.3, underlining two other important advantages: its short temporal duration and its high monochromaticity. During the $K\alpha$ emission (almost coincident with the laser pulse), there are no considerable changes in the plasma hydrodynamics (occurring on $\sim$100 ps scales) and a precise state of matter can be probed. Moreover, a highly monochromatic beam simplifies the data analysis, allowing to reach a much

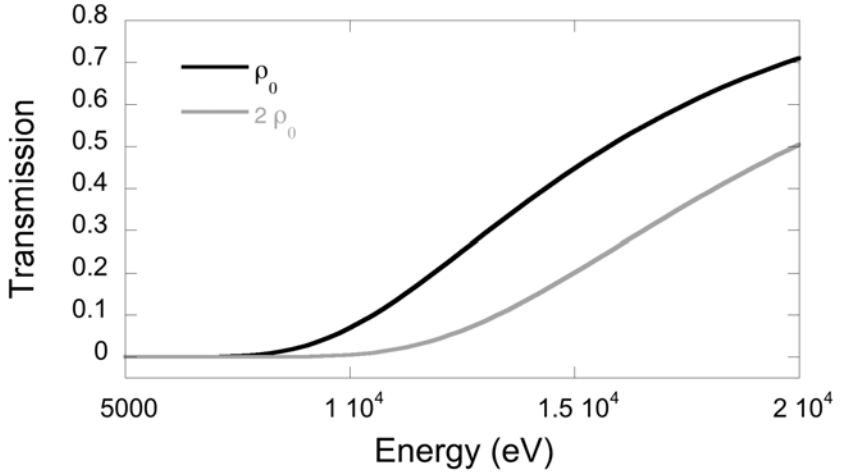


**Figure 3.9:** *∼2 contrast ratio is expected between shocked and unshocked aluminum in a* $400\mu m$ *sliver with ∼ 13 keV x-rays.*

higher precision on the density measurement. The importance of the total radiation spectrum emitted by the backlighter target will appear clear in the section dedicated to the data analysis. In the experiment we used a Molybdenum K$\alpha$ at 17.5 keV, which was the best compromise between energy requirements and easiness of practical handling. In this case we expect a contrast of ∼1.8

To extract the density from the acquired radiographs, one needs to consider that the obtained absorption values come from a line integral of the local absorption. This means that each point on the image accounts for the absorption obtained along the whole line of sight. The projection of the transmission onto the image plane is hence proportional to the corresponding line integral over the density $\rho(r)$. If the shock front has a spherical, cylindrical or a more general azimuthal symmetry, it is possible to use Abel inversion to directly extract the local density.
The general Abel transform may be written as:

$$S(y) = 2\int_y^R \frac{f(r)r}{\sqrt{r^2-y^2}}dr \tag{3.12}$$

where $S(y)$ represents the observed data and $f(r)$ is the function to be determined. The inversion formula is given by :

$$f(r) = -\frac{1}{\pi}\int_r^R \frac{dS(y)}{dy}\frac{dy}{\sqrt{y^2-r^2}} \tag{3.13}$$

In our analysis we can obtain an equation equivalent to eq.3.12, where the observed data $S(y)$ are represented by the experimental transmissions. To come to the suited

formula we must consider the areal density in the radiograph direction.

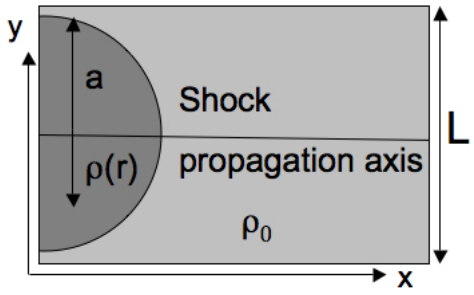


**Figure 3.10:** *Azimuthal symmetry to perform Abel inversion*

If azimuthal symmetry about the shock propagation axis is considered (fig.3.10) the areal density in the radiograph direction can be written as:

$$\overline{\rho z} = 2\int_y^a \frac{\rho(r)rdr}{\sqrt{r^2-y^2}} + \rho_0(L - 2\sqrt{a^2-y^2}) \tag{3.14}$$

Here, the first term refers to the shocked region, while the second term accounts for contributions from the unshocked part of the target. If we define $\beta(r) = \frac{\rho}{\rho_0} - 1$, eq.3.14 can be expressed as:

$$\overline{\rho z} = \rho_0 \left( 2\int_y^a \frac{\beta(r)rdr}{\sqrt{r^2-y^2}} + L \right) \tag{3.15}$$

We need then to relate the areal density encountered by the photons in their propagation through the target to the recorded transmission. This is done in the easiest case by the Beer-Lambert law, $I = I_0 exp(-\mu\overline{\rho z})$, which expresses the transmitted x-ray intensity after propagation in a layer of density $\rho$ and thickness $z$. The quantity $\mu$ is the mass attenuation coefficient and it will be discussed in the next section. From this equation we can easily extract $\overline{\rho z} = -\frac{1}{\mu} ln\left(\frac{I}{I_0}\right)$. When we insert this expression in eq.3.15 we end up with:

$$-\frac{1}{\rho_0\mu} ln\left(\frac{I}{I_0}\right) - L = 2\int_y^a \frac{\beta(r)rdr}{\sqrt{r^2-y^2}} \equiv F(y) \tag{3.16}$$

which has exactly the form of eq.3.12. Its inversion is given by eq.3.13 and it can be explicitly written as:

$$\beta(r) = -\frac{1}{\pi\rho_0\mu}\int_r^a \frac{dF}{dy}\frac{dy}{\sqrt{y^2-r^2}} \tag{3.17}$$

From our experimental transmission data we can thus directly infer the compression factor $\rho/\rho_0$ by Abel inversion.

When writing the Beer-Lambert law as $I = I_0 exp(-\mu\overline{\rho z})$ one must keep in mind that it is valid for a monochromatic radiation. If the radiation is "quasi monochromatic", i.e. the spectrum is a narrow band around a precise wavelength, we can define a "mean mass coefficient", still using eq.3.17 as a good approximation. If, on the other hand, a broad-band component contributes to the emission, one must account for the attenuation of the whole spectrum. Therefore, it appears crucial to have a precise knowledge of the incident spectrum in order to obtain a correct evaluation of the absorption and, hence, of the density.

In this analysis another assumption is made by considering that the mass absorption coefficient remains constant with temperature. This assumption is valid for incident x-ray energies $h\nu$ well above the K-edge in the sample material and for low sample temperatures, when $h\nu/kT \gg 1$. To better understand the absorption mechanisms as well as how the shock compression can influenced it, it is worth recalling the basic principles of the x-ray interaction with matter.

#### 3.3.1.2 X rays interaction with matter

The interaction between x-rays and cold matter involves elastic, inelastic scattering and photo-electric absorption. The cross section for each of these processes is wavelength and material dependent. Elastic scattering contribution comes mostly from tightly bound electrons (Rayleigh). Inelastic scattering occurs when x-rays can transfer energy to the free or loosely bound electrons (Compton). In the photoelectric process, the photon transfers its energy to a bound atomic electron, ionizing the atom. The cross sections for this phenomenon are characterized by a sequence of jumps at absorption edges, where x-rays have enough energy to remove the electron from a particular shell. For soft x-rays, incoherent scattering is negligible while the coherent scattering accounts for less than 1% so that the most important process is the photoelectric absorption. At higher energies, scattering prevails and the photoelectric cross section decreases very sharply with energy. The interaction of a x-ray photon of energy E with an atom is described by the complex amplitude

$$A(E,\theta) = A_\theta[f_1(E) + if_2(E)] \tag{3.18}$$

where $A_\theta$ is the amplitude resulting from the scattering on a free electron and $\theta$ is the scattering angle. The atomic scattering factors $f_1(E)$ and $f_2(E)$ describe respectively the overall scattering and photon absorption by the atom. They can be considered being $\theta$ independent as the x-ray wavelength is larger than the atomic electron distribution

size. Relativistic quantum dispersion theory can be used to obtain the values of $f_1(E)$ and $f_2(E)$, leading to:

$$f_1(E) = Z + \frac{4\epsilon_0 m_e c}{he^2}\int_0^\infty \frac{W^2\sigma(W)}{E^2 - W"}dW - \Delta_{rel} \tag{3.19}$$

$$f_2(E) = \frac{2\epsilon_0 m_e c}{h}E\sigma(E) \tag{3.20}$$

where Z is the atomic number of the scatterer, $\sigma(E)$ is the photoabsorption cross section and $\Delta_{rel}$ a relativistic correction factor that can be ignored except near the absorption edges.
The macroscopic x-rays matter interaction can be described through the complex refractive index:

$$\widetilde{n} = 1 - \delta - i\beta \tag{3.21}$$

The amplitude of the electromagnetic wave after propagation on a distance s through the material is:

$$A = A_0 exp(-\frac{2\pi\beta s}{\lambda})exp(\frac{i2\pi\delta s}{\lambda}) \tag{3.22}$$

and as a consequence the intensity is:

$$I = |A|^2 = I_0 exp(-\frac{4\pi\beta s}{\lambda}) \tag{3.23}$$

where $A_0$ and $I_0$ are respectively the amplitude and the intensity of the incident electromagnetic wave. Thus the phase change is $2\pi\delta s/\lambda$ and the absorption is $exp(-\mu' s)$ where

$$\mu' = \frac{4\pi\beta}{\lambda} \tag{3.24}$$

is the linear attenuation coefficient.
The macroscopic quantities $\delta$ and $\beta$ are related to the atomic scattering factors $f_1$ and $f_2$ via: $\delta = Kf_1, \beta = Kf_2$ with K:

$$K = \frac{r_e\lambda^2}{2\pi}\frac{N_A}{A}\rho \tag{3.25}$$

where $r_e = \frac{e^2}{mc^2}$ is the classical electron radius, $N_A$ the Avogadro number, A the atomic weight and $\rho$ the density of the material. We can define the mass attenuation coefficient $\mu = \mu'/\rho$ so that $I_0 exp(-\mu\rho s)$ is the intensity transmitted through a material layer of thickness $s$.

The values of the mass attenuation coefficient as function of the incident x-ray energy for aluminium are plotted in fig. 3.11.

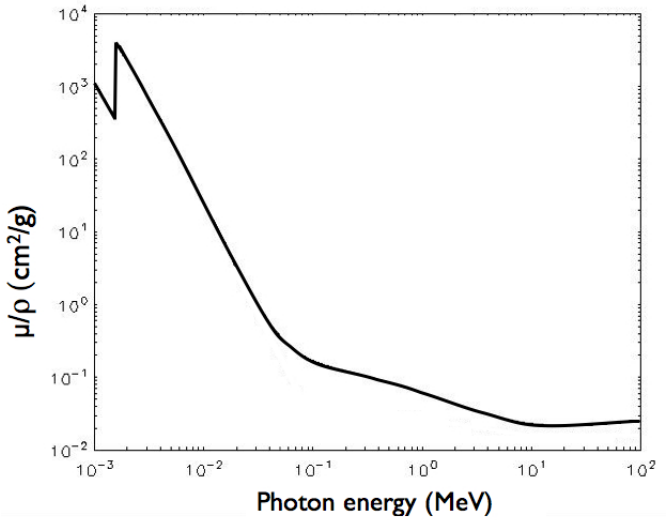


**Figure 3.11:** *Mass attenuation coefficient values for Al from NIST.*

The mass attenuation coefficient depends on the energy of the incident radiation. For a polychromatic X-ray beam eq.3.23 needs to be applied to each component of the spectrum:

$$I(\nu)d\nu = I_0(\nu)exp(-\rho\mu(\nu)s)d\nu \tag{3.26}$$

The shock wave changes the atomic layers due both to compression and heating. In this way it has impacts on the photoelectric absorption cross section. As we will see later, though, for our typical conditions these effects are negligible and the cold mass attenuation coefficient values can be used even for the shocked target.

### 3.3.2 Proton radiography

The idea to use protons as a radiographic source has circulated for several years [47],[48]. Their use for biomedical applications was also proposed [49],[50] for example. Ion beams from accelerators have also been used to probe electric fields [51]. In [52], bursts of 800 MeV protons from accelerators were successfully employed to radiograph objects with integrated areal densities near 50 $g/cm^2$. However, practical difficulties exist in coupling particle beams from conventional accelerators to laser-plasma experiments. As a consequence, their application in these contexts is highly limited. Moreover, the spatial and temporal resolutions achieved with these sources are typically of $\sim$200 $\mu m$ and 50 ns respectively, which are far too low for laser-plasma physics.
On the other hand, protons from high-intensity laser-matter interaction present unique properties that make them more suitable for warm dense matter experiments. In par-

ticular, the high temporal and spatial resolution required in such experiments can easily be obtained due to their specific properties [53].
So far, the main application of proton probing concerns its unique capability to detect electromagnetic fields. Direct information on electric fields generated in the laser-plasma interaction has be obtained in various experiments [53]-[57]. The high temporal resolution is here of fundamental importance, as it allows to detect highly transient fields, typical of ICF plasmas.
Several radiographic applications of laser-produced protons have then been reported. Proton radiography of thick targets in [58]-[59] have allowed to reach direct information on their areal density, underlying the possibility to reach micron spatial resolution. Radiography of thin objects, i.e. with an areal density smaller than the proton range, has also been studied, in [60],[57] for instance.
However the possibility to use proton radiography as diagnostic for dense plasmas generated in laser-driven shock compression, has not been deeply investigated yet. Laser driven implosion of plastic microballoon was for the first time studied in [61],[57],[62]. In this case information on the compression ratio was obtained with the aid of Monte-Carlo simulations. In [63] a first attempt to study shock compressed targets is presented. In that experiment, though, the important scattering prevented the shock to be probed. In our experiment we wanted to investigate in more details the feasibility of this technique.
In the following sections, as done for the x-ray radiography, we will present the principle of the measurement as well as the major physical processes involved in the interaction of proton beams with matter. The experimental results will be presented and discussed in chapter 4.

#### 3.3.2.1 Principle of the measurement

The density measurement from proton radiography is not as straightforward as for x-rays. The interaction of charged particles with matter includes several processes which have important effects on the imaging mechanism. The mutual dependence of these processes makes it difficult to establish a functional relation between the target density and the radiograph. As a counterpart, high energy protons have a greater ability to penetrate thick materials than x-rays and they can give a higher signal to noise ratio. Besides, protons are sensitive to the materials composition, which can then be distinguished, while density is the only relevant parameter when dealing with x-rays. Finally, protons can easily provide views from multiple angles, which is a challenge for X-ray beams. For these reasons, proton radiography is worth investigating as a new diagnostic tool.

Proton propagation into matter is mainly affected by two important processes: multiple Coulomb scattering and energy losses.
Coulomb collisions causes the protons to be scattered at small angles. Therefore the trajectory has a random character which prevents a direct estimation of the sample density via the Abel inversion, as it was done in the case of X-rays. Moreover, small angle scattering can have an undesirable blurring effect on proton radiographs, when dealing with low energy protons.

The energy losses of a proton beam propagating through matter depend on the initial protons energy and on the material density. As a consequence, if we consider the case of a monochromatic proton beam going through a density gradient, the energy losses differ for different parts of the beam, depending on the path followed in the propagation. When using a radiochromic film (RCF) stack as detector, each layer selects a narrow range of proton energies (we will discuss this point in details in paragraph 5.3). As a consequence, different layers account for protons with different energies. A deep analysis of the whole RCF stack is thus required to achieve a complete information on the energy losses. The phenomenon gets more complex when using laser produced protons as they have a wide energy spectrum. Each film can then contain contributions from protons with different initial energies which become equal after propagation in the density gradient. Low energy protons that have gone through weak densities and high energy protons passed through higher density regions can end with the same energy and can then be stopped in the same film. In this case a good knowledge of the incident proton spectrum is also necessary to estimate the energy losses.

Due to the complexity of the involved processes, density measurements from proton radiography are obtained with the aide of statistical simulations, such as Monte-Carlo methods, which describe the proton propagation through matter. The proton beam properties (spreading, energy, etc...) are strongly affected by the density profile they are propagating through. Therefore, the idea is to estimate the correct target density by evaluating the effects it has inferred to the beam. In particular, we can consider the spatial and spectral proton distribution after propagation. The proper density profile is assumed to be the one that gives the same experimental proton profile on the detector. This is an iterative process (fig.3.12): from an initial density profile, the Monte-Carlo simulation gives a corresponding proton distribution on the detector; the comparison with the experimental data indicates a correction for the density profile to be inserted in a new simulation. The process is repeated until a good agreement between experimental and simulated profiles is obtained.

In our experiment, the density gradient was associated to shock compression. We can hence use the density profile obtained from 1D or 2D hydrodynamic simulations as

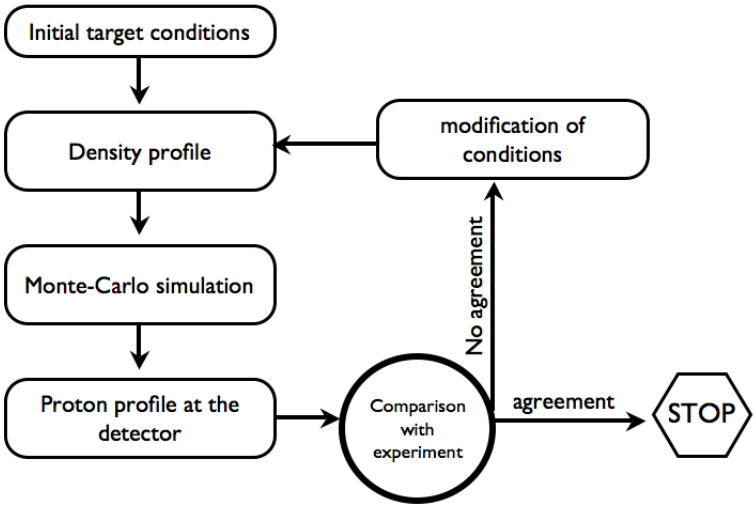


**Figure 3.12:** *The correct density of the radiographed object can be estimated through an iterative process involving Monte-Carlo simulations for a description of the proton propagation in matter.*

input parameter in the Monte-Carlo code.
A deeper description of the Monte-Carlo code will be given in section 5.6; here we will describe the main physical processes involved, included in the code: the proton stopping power and the multiple Coulomb scattering. Imaging via small angles scattering will also be discussed, as the principal imaging mechanism in our experiment.

#### 3.3.2.2 Proton stopping Power

When a particle propagates through matter, it loses energy trough interactions with the material constituents. Heavy particles at moderately relativistic energy deposit their energy mainly through ionization, while emission of radiation is the most important process for light ultra-relativistic particles energy losses.
The total stopping power can be divided into two contributions: the nuclear stopping power and the electron stopping power. The nuclear stopping power takes into account the energy transfer between the incident particle and the atomic nucleus. It contributes at very low incident particle energy: for 20keV protons hitting an aluminum atom, the nuclear stopping is less than 1%. As we will deal with MeV protons, nuclear stopping power will be neglected. Electronic stopping power accounts for the interactions of the incident particle with medium's electrons. There is not an unique theory able to describe electronic stopping power, as the processes involved are different according to the incident particle energy. Therefore, distinguished approaches are used to calculate its contribution over three different energy ranges, as shown in table 3.1. From the same table, we also observe that for proton energies typical of our experiment (1-20 MeV),

the stopping power can be described within the Lindhard and Bethe-Bloch frameworks.

| **Energy (MeV/amu)** | **gamma factor** | **Framework** |
|---|---|---|
| $< 10$ | $< 1.01$ | Lindhard |
| $10 - 10^6$ | 1.01-1000 | Bethe-Bloch |
| $> 10^6$ | $> 1000$ | Radiative Losses |

**Table 3.1:** *Different approaches are used to describe the proton stopping power according to the incident particle's energy. Here we show the theoretical framework applied to each of the three main regimes.*

**Lindhard's approach** This picture is used when the incident particle velocity is comparable or smaller than the mean velocity of the target electrons. In this case, the atomic electrons have time to propagate the effects of the interaction around and ahead the particle track. As a consequence, the interaction is best described as the one occurring between a charged particle with a gas of free electrons [64]. Energy transfer to collective processes are included, as this model naturally accounts for both electron polarization by the charged particles and plasma density fluctuation. The target is described as a zero-temperature gas of free electrons on a fixed uniform positive background. The initial electron plasma is of constant density, and the interaction of an incident charged particle is described as a perturbation on the electron gas. The total electronic stopping $S_e$ may be formulated as:

$$S_e = \int I(v, N_e) Z_{inc}^2 N_e dV \tag{3.27}$$

where $I$ is the stopping interaction function of a particle of unit charge with velocity $v$ in a plasma of electronic density $N_e$. $Z_{inc}$ is the charge of the incident particle and the integral is performed over the whole volume V of the target.

**Bethe-Bloch theory** When the incident particle velocity is "fast" with respect to the mean orbital velocity of atomic electrons, energy losses are mostly related to the interaction with bound electrons. In this formulation, the interaction can be considered as impulsive, i.e. a small and sudden perturbation of the atom. The atom is treated as a collection of harmonic oscillators. Starting from Bohr's treatment in 1913, a modern expression of the electronic stopping power in this regime can be written as:

$$S = K \frac{Z_{inc}^2}{\beta^2} \frac{Z_2}{A} \left[ ln \frac{2mc^2\beta^2}{(1-\beta^2) - \langle I \rangle} - \beta^2 \right] \tag{3.28}$$

Here $Z_2$ and A are the atomic number and atomic weight of the target material, $Z_{inc}$ is the charge of the incident particle and $\beta$ the relativistic parameter. I is the mean

excitation potential of the material which takes into account the total contribution of the bound electrons. It is given by:

$$Z_b lnI = \sum_n f_n lnE_n$$

where $Z_b$ is the number of bound electrons in state n with binding energy $E_n$ and oscillator strength $f_n$. Averaged ionization potential were obtained experimentally for different materials and they are tabulated by Andersen and Ziegler [65]. The constant K in eq.3.28 is 0.307 MeVmol$^{-1}$cm$^2$; the units are chosen so that the stopping power is expressed in MeV/g cm$^{-2}$. Eq.3.28 is accurate to about 1% for protons in solids in the energy range of 1-100MeV. Correction terms can be added as shown in [66].

#### 3.3.2.3 Coulomb scattering

We have seen that the dominant source of energy loss for heavy charged particles is the inelastic excitation and ionization of atomic electrons. In the Coulomb interactions with these electrons, the incident particle is deflected and its trajectory departs from a straight line during its propagation through matter.

Let's consider a particle of mass M, charge $Z_1 e$ and velocity $v$ incident on a material whose particles have mass m, charge $Z_2 e$ and are at rest. Due to the interaction between the Coulomb field of the incident particle and the charged particle in the target, the incident particle is given a perpendicular momentum $p_\perp$:

$$p_\perp = \frac{2Z_1 Z_2 e^2}{bv} \tag{3.29}$$

where b is the impact parameter. It will then be deflected by a small angle given by

$$\varpi \simeq \frac{p_\perp}{p} = \frac{2Z_1 Z_2 e^2}{bvp} \tag{3.30}$$

where $p = Mv$ is its momentum. The differential cross section for scattering with an impact parameter between b and $b + db$ is $2\pi bdb$, which can be related to the cross section between $\varpi$ and $\varpi + d\varpi$. For a Coulomb potential the exact form of the scattering differential cross section is given by the Rutherford scattering formula:

$$\frac{d\sigma(\varpi)}{d\Omega} = \frac{1}{4} Z_1^2 Z_2^2 r_e^2 \left(\frac{mc}{\beta p}\right)^2 \frac{1}{sin^4(\varpi/2)} \tag{3.31}$$

Here $r_e = \frac{e^2}{mc^2}$ is the classical electron radius and $\beta = v/c$ the relativistic parameter. The $sin^{-4}(\varpi/2)$ dependence of the cross section shows that small angles scattering is more probable than large ones. The Z and $v$ dependence, then, implies that the diffusion

is more efficient for low energy particles propagating in a high Z solids. The Rutherford scattering formula, though, is not valid at very small or very large angles. At small angles, corresponding to large impact parameters, the Coulomb potential of the nucleus is screened by the atomic electrons, so that the cross section can be written as [67]:

$$\frac{d\sigma(\varpi)}{d\Omega} = 4Z_1^2 Z_2^2 r_e^2 \left(\frac{mc}{\beta p}\right)^2 \frac{1}{(\varpi^2 + \varpi_{min}^2)^2} \tag{3.32}$$

Eq.3.32 avoids the divergence at $\varpi = 0$, having a minimum value for the angle $\varpi_{min}$. $\varpi_{min}$ is estimated as the minimum between the classical calculation of eq.3.30 using the atomic radius $r_a = \frac{a_0}{Z_2^{1/3}}$ (with $a_0$ the Bohr radius) as impact parameter or by the quantum mechanical limit coming from the uncertainty principle.

For our conditions, the quantum limit leads to a smaller value and that is what we have used in the code. The expression for the minimum angle is then given by:

$$\varpi_{min} = \alpha Z_2^{1/3} \frac{mc}{p} \tag{3.33}$$

where $\alpha = e^2/\hbar c \cong 1/137$.

#### 3.3.2.4 Imaging via multiple scattering

The proton stopping power is the basic mechanism involved in the proton radiography when the beam interacts with an object whose thickness is much greater than their stopping range. Significant changes in the beam intensity are observed even when protons propagate through thin objects, i.e. with an areal density much smaller than the stopping range. Thin objects images were initially attributed to electrical charge-up of the object itself due to hot electrons preceding the proton beam [53]: the image was then attributed to by proton pile up due to the electric field deflection.

In fact, this effect is not necessary to explain the observations, as small angles scattering alone can reproduce the experimental data [68]. When the protons propagate into the material they undergo several collisions with the nuclei and they are subjected to a larger lateral spread than the protons going through vacuum. At the edges of the object, the differences in the lateral spreads produces a perturbation in the beam intensity profile, while far away from them the beam remains unperturbed, provided that the object is thinner than the proton stopping range.
The process is outlined in fig.3.13, where the protons are represented as a divergent beam 3.13a. The effect of scattering is to change the divergence of the beam itself 3.13b, which translates into a different particle areal density. At the edge of the object, the intersection of the two parts of the beam creates a modulation. Particularly protons accumulate in a small region in the vacuum (or more generally in the region at weaker

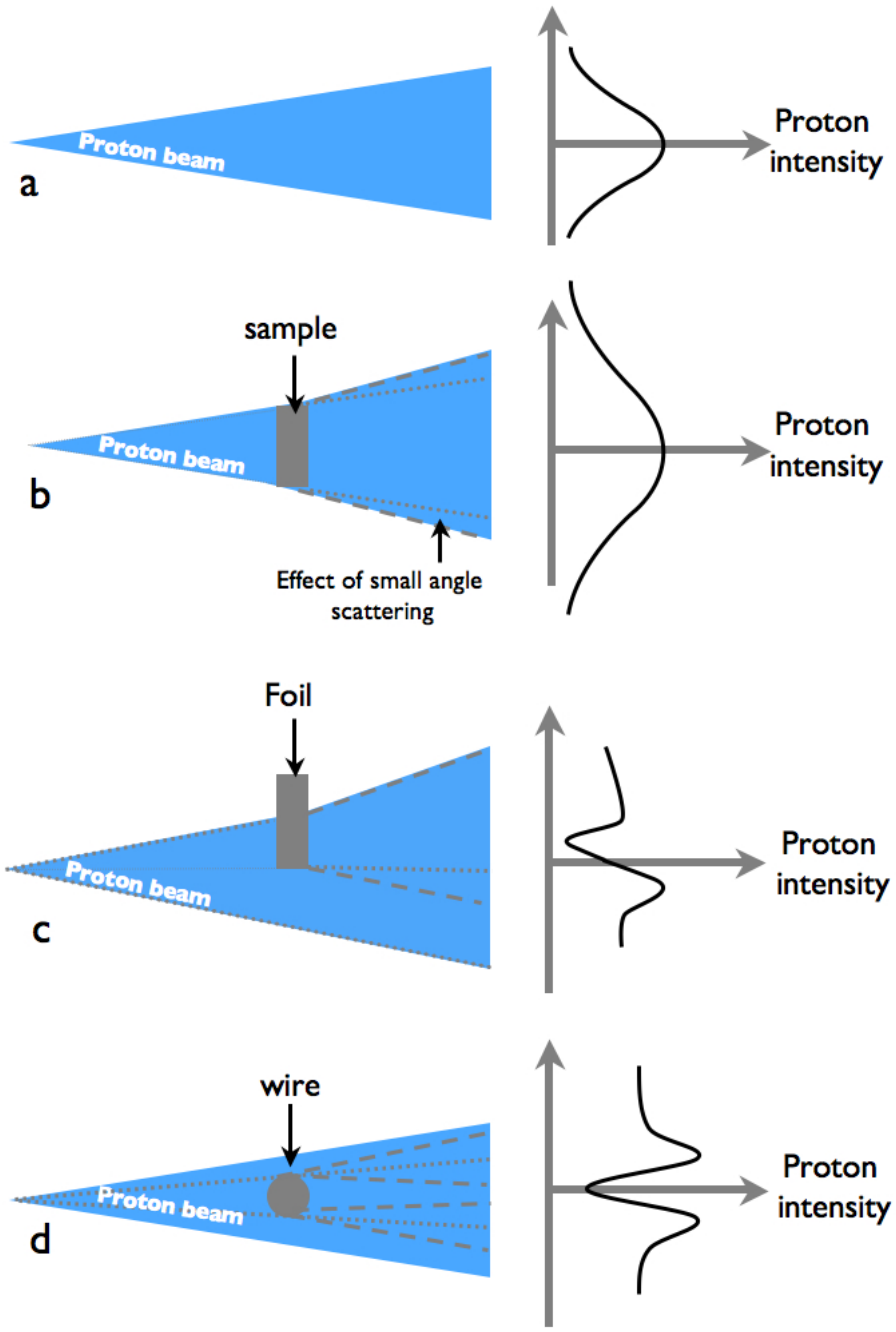


**Figure 3.13:** *Protons that propagate through matter are subjected to a larger lateral spread than those propagating through vacuum. At an object edges the difference in the spread produces a perturbation of the beam intensity.*

densities) 3.13c-d, resulting in the observed pile up. The conservation of the mass then, induces a minimum next to the higher density region.
In the case that the transverse size of the object is larger than the perturbation width, only the edge of the object is visible, fig.3.13c. As we will see, this is the case of our target edges, fig.5.10. If, on the contrary, the transverse size of the object is smaller than the perturbation's width, as typically in the case of a thin wire, then the perturbations due to two adjacent edges can superimpose, producing deeper effects in the intensity profile, 3.13d. The two proton accumulations can be observable at each side of the wire, while the depletion regions are superimposed in a deep minimum in the intensity profile.

### 3.3.3 X-ray scattering

Before describing x-ray scattering from dense plasmas, we think it can be useful to review some basic aspects of light scattering. After a quick review of scattering on single electrons, we will briefly illustrate the use of optical Thomson scattering as a low-density plasma diagnostic. In this way we will introduce some general scattering concepts, like the collective and incoherent regimes, furnishing the necessary background to understand the scattering process in the x-ray regime. In the end of the chapter, we will finally describe how dense plasma temperatures and electron densities can be obtained through x-ray Thomson scattering.

#### 3.3.3.1 Scattering from single electrons

Soon after he discovered the electron, for which he was awarded the nobel price in 1906, J.J.Thomson presented a theory for the scattering of electromagnetic radiation from free electrons, a process that still carries his name. The principle of Thomson theory is based on a quite simple picture: the oscillating field of an incident planar electromagnetic wave causes the free electron to oscillate at the wave frequency inducing a dipole radiation due to the charge acceleration.
Let's consider an electric field $\mathbf{E}= \mathbf{E}_0 e^{i\omega t}$ incident on an atom. In the limit of low incident energies, as for visible light, the momentum transfer from the photon to the electron of mass m is considerably small, $\hbar k << mc$, and quantum corrections can be neglected. In response to E, an electron of the atom will vibrate with oscillations of amplitude:

$$\mathbf{x} = \frac{e\mathbf{E}_0}{m(\omega_0^2 - \omega^2)} \tag{3.34}$$

where for simplicity we have considered just one oscillator of natural frequency $\omega_0$ and we have neglected any damping. The power $P_s$ scattered by an atom in all directions

can be found by considering the power emitted from an accelerated charge $P = \frac{2}{3}\frac{e^2a^2}{c^3}$, where $a$ is the acceleration. In the case of an oscillator, the acceleration can be expressed as $a = -\omega^2 x e^{i\omega t}$ so, using eq.3.34:

$$P_s = \frac{e^2E_0^2}{3m^2c^3}\frac{\omega^4}{(\omega^2-\omega_0^2)^2} \tag{3.35}$$

Dividing this equation by the time averaged Poynting vector $< S >= (c/8\pi)E_0^2$, we obtain the cross section for the scattering process as function of frequency:

$$\sigma(\omega) = \frac{8\pi}{3}\left(\frac{e^2}{mc^2}\right)^2\frac{\omega^4}{(\omega^2-\omega_0^2)^2} \tag{3.36}$$

If any of the natural frequency of the system is higher than the frequency of the incident light $\omega_0 \gg \omega$, in first approximation the scattering is proportional to the forth power of the frequency and we find the usual Rayleigh scattering responsible for the blue color of the sky.
On the other hand, in the limit of small natural frequencies $\omega_0 \sim 0$ or for completely unbound electrons, the cross section tends to a constant value, called the Thomson scattering cross section given by:

$$\sigma = \frac{8\pi}{3}\left(\frac{e^2}{mc^2}\right)^2 = 6.65210^{-25}cm^2 \tag{3.37}$$

In these regimes the scattered light is emitted at nearly the incident frequency and it is broadened by Doppler shifts because of electrons motion. The observation of Thomson scattering in the laboratory had to wait for fifty years until the lasers could furnish a strong enough source to produce a detectable scattered signal.

#### 3.3.3.2 Scattering from particle ensembles

The first experimental results of scattering from electrons were, however, obtained with radar waves in 1958, when Bowles, under the suggestion of W.E.Gordon, first observed 41 MHz microwaves backscattered from the earth's ionosphere [69]. In this case the radiation was scattered by a whole ensemble of particles and the obtained results led to important theoretical conclusions. From these experimental data, theorists [70]-[74] realized that scattering is intimately connected to the spectrum of density fluctuations of the particles in the system. In the following, we will consider a collection of electrons, which is the most usual scatterering system. The scattered spectrum is then determined not simply by the Doppler broadening due to thermal motion of the individual electrons, but by the character of the density fluctuations. In particular, the net scattered power depends on the amplitude of the density fluctuations. The total power scattered from a uniform distribution of particles in the scattering volume would be almost zero, as a

result of the interference between contributions of opposite phase.
In the general form, the scattered power from the electron gas can be expressed as:

$$P_s(\omega)d\omega = \sigma_T I_0 N_e V S(\mathbf{k},\omega)d\omega \tag{3.38}$$

where V is the scattering volume, $N_e$ the electron density, $I_0$ the incident radiation intensity and $\sigma_T$ is the Thomson cross section defined in 3.37. $S(\mathbf{k},\omega)$ contains the information on the frequency spectrum of the fluctuations at a given wavevector $\mathbf{k}$ and it is called the dynamic structure factor. Its physical meaning can be understood in the context of a microscopic description of a fluid. The dynamic structure factor is indeed directly related to the Van Hove function, which describes the equilibrium local density-density time correlation function. In a general formulation, for a number of particles $N$, it can be written as:

$$G(\mathbf{r},t) = \frac{1}{N}\left\langle \sum_{i=1}^{N}\sum_{j=1}^{N}\int \delta[\mathbf{r}' + \mathbf{r} - \mathbf{r}_i(t)]\delta[\mathbf{r} - \mathbf{r}_j(0)]d\mathbf{r}' \right\rangle \tag{3.39}$$

where $\mathbf{r}_i(t)$ and $\mathbf{r}_j(t)$ are the vector positions at time t of the particles $i$ and $j$ respectively. The physical interpretation of the van Hove correlation function is that $G(r,t)dr$ is proportional to the probability of finding a particle i in the region d$\mathbf{r}$ at time t, given that there was a particle j at the origin at time 0. Rather than considering the density-density correlations in real space, it is often convenient to focus on their Fourier components, $F(\mathbf{k},t) = \int G(\mathbf{r},t)e^{-i\mathbf{k}r}d\mathbf{r}$, where $F(\mathbf{k},t)$ is often called the *intermediate scattering function*. Its spectrum:

$$S(\mathbf{k},\omega) = \frac{1}{2\pi}\int_{-\infty}^{\infty} F(\mathbf{k},t)e^{i\omega t}dt \tag{3.40}$$

is the *Dynamic Structure Factor*. It immediately follows that:

$$S(\mathbf{k},\omega) = \frac{1}{2\pi}\int_{-\infty}^{\infty} e^{i\omega t}dt \int_{-\infty}^{\infty} G(\mathbf{r},t)exp(-i\mathbf{k}\cdot\mathbf{r})d\mathbf{r} \tag{3.41}$$

As we will see later (eq.3.46), a direct proportionality exists between the scattering cross section and the dynamic structure factor. It thus follows that a measurement of the scattering cross section is equivalent to determine the van Hove function $G(\mathbf{r},t)$. A deeper treatment of $S(\mathbf{k},\omega)$, directly related to the fluid dynamics, as well as its other important properties can be found in [75].

The Dynamic Structure Factor is related to the *static structure factor* $S(k)$:

$$S(\mathbf{k}) = \int_{-\infty}^{\infty} S(\mathbf{k},\omega)d\omega \tag{3.42}$$

S(k) is an extremely interesting quantity as it is experimentally accessible.
In particular, for systems where the atoms interact through pairwise-additive forces, all the thermodynamic macroscopic quantities can be written as integrals over the pair distribution function $g(\mathbf{r})$. The pair distribution function measures the density probability that a particle is separated by a distance r from another one. In this case the static structure factor can be express as:

$$S(\mathbf{k}) = 1 + n \int d\mathbf{r}[g(\mathbf{r}) - 1]exp(i\mathbf{k} \cdot \mathbf{r}) \tag{3.43}$$

where we have introduced the quantity n, the local particle density.

#### 3.3.3.3 Scattering from classical plasmas

In a plasma, electrons are the only important scattering particles, as ions, due to their higher mass, suffer little acceleration in an electromagnetic wave field. Their contribution to the total scattered power can be neglected. Therefore the spectrum of the scattered light is only determined by the electron density fluctuations.
The wavelength of the density fluctuation that yields scattering depends on the wavelength of the incident radiation as well as on the angle at which scattered light is measured. Let's consider again the same monochromatic wave incident on the plasma in a given direction. The energy and momentum conservation require that: $\omega = \omega_0 - \omega_1$ and $\mathbf{k} = \mathbf{k}_0 - \mathbf{k}_1$, where $\omega_0$ and $\omega_1$ represent now the frequency of the incident and scattered radiation and $\omega$ the one of the plasma density fluctuation. Similarly, $\mathbf{k}_0$ is the wave number of the incident radiation, $\mathbf{k}_1$ the wave number of the scattered radiation and their difference $\mathbf{k}$ represents the wave number of the electron density fluctuation. If $\theta$ is the scattering angle,

$$k = |\mathbf{k}| = \frac{4\pi}{\lambda_0} sin(\theta/2) \tag{3.44}$$

with $\lambda_0$ the probe wavelength.
The character of the plasma density fluctuations depends on whether the fluctuation wavelength is larger or smaller than the Debye length $\lambda_D$. The classification of the scattering process is usually given in term of the dimensionless parameter $\alpha = (k\lambda_D)^{-1}$.

When $\alpha \ll 1$, the probe wavelength is much smaller than $\lambda_D$ and the individual electrons act as free particles, fig.3.14. The scattered spectrum, thus, is determined by the electron velocity distribution function: it is often gaussian in shape with FWHM $\Delta\omega$ given by

$$\frac{\Delta\omega}{\omega_0} = 4sin\left(\frac{\theta}{2}\right)\left(\frac{2k_B T_e}{m_e c^2} ln2\right)^{1/2}$$

It reflects the Doppler shift that is due to scattering from individual uncorrelated electrons. For this reason, this type of scattering is often called *incoherent* and the scatter

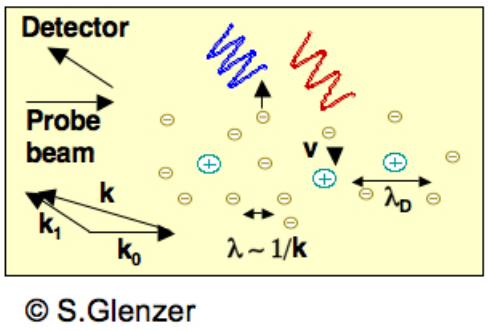


**Figure 3.14:** *When $\alpha \ll 1$ the probe wavelength is much smaller than $\lambda_D$ and the individual electrons act as free particles.*

power is in this case proportional to the number of electrons.

As $\alpha$ increases, the wavelength of the probe approaches or becomes bigger than the Debye length, fig.3.15. In this case, the density fluctuations reflect a collective

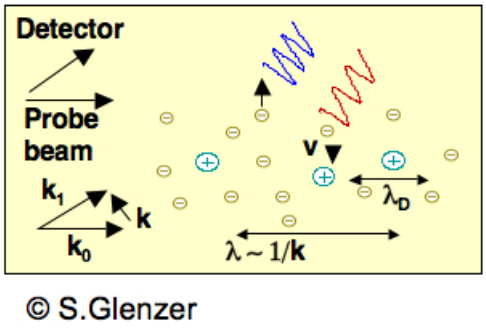


**Figure 3.15:** *When $\alpha \gtrsim 1$ the scattering reflects collective behavior.*

behaviour and the scattering is often referred as *collective* or *coherent* scattering. In thermal plasmas, resonances start to appear at low frequency near the ion acoustic wave $\omega_{ia} = \sqrt{\frac{Zk_BT_ek^2}{M}}$, where $M$ is the ion mass and $Z$ the ionization level, and at high frequency near the Bohm-Gross frequency of the electron plasma waves $\omega_{BG} = \sqrt{\omega_p^2 + 3\frac{k_BT_e}{m_e}k^2}$, see fig.3.16. The scattered spectrum, thus, presents two pairs of peaks symmetric about the probe frequency and shifted by $\pm\omega_{BG}$ (the electron satellites) and $\pm\omega_{ia}$ (the ion feature). The intensities and widths of these peaks are determined by the damping of the associated plasma waves.

Today optical Thomson scattering is currently used to probe low density plasmas ([76] as an example), giving relevant information of plasma temperatures, density, ionization stage [77] or even dispersion of ion acoustic thermal fluctuations [78] with extremely high degree of accuracy.

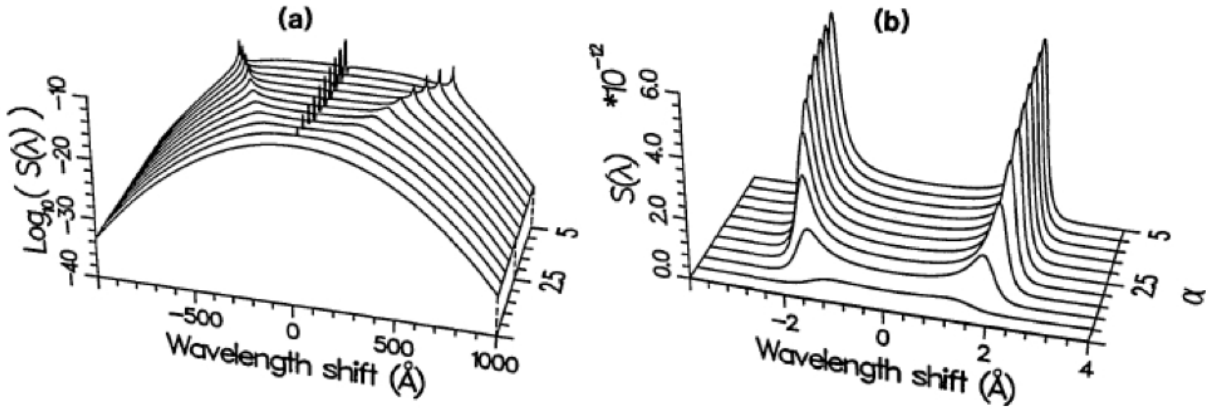


**Figure 3.16:** *From [76]. Theoretical visible scattered spectra ($k = 1.7 \cdot 10^7 m^{-1}$). Plasma conditions are Te=Ti=100 eV, Z=6 while the electron density is varied to obtain different $\alpha$ regimes. The central ion feature and the two electrons satellites are shown in (a), while (b) contains the details of the ion feature.*

#### 3.3.3.4 Scattering from dense plasmas

The application of this powerful diagnostic to solid density plasmas is limited by the simple fact that they are opaque to optical and UV light. The investigation of plasma with density $> 10^{21} cm^{-3}$ implies the use of different sources. Recently x-ray Thomson scattering was proposed as a new tool for WDM plasmas probing [79]. Direct measurements of density, temperature and ionisation state in a dense plasma can be obtained from spectrally resolved x-ray Thomson scattering [79]. The big advantage of employing x-ray radiation instead of visible light is that, in a same scattering configuration, it is possible to probe plasmas whose density is more than 6 order of magnitude higher. This is evidenced in fig.3.17, where the regimes accessible by Thomson scattering for Beryllium plasmas are shown. In the electronic density-temperature representation, the upper-left dark grey region represents Fermi degenerate states while the middle light grey region is typical of strongly coupled plasma regimes. The solid lines indicate the regimes accessible with a constant $\alpha$ of 0.1-0.3 for a 2400Å UV and 2.4Å X-ray source. We can notice that with an x-ray source, strongly coupled and Fermi degenerate states become directly accessible. Collective scattering can be achieved with smaller angles and/or longer wavelength probes.

#### 3.3.3.5 X-ray Thomson scattering

In dealing with x-ray scattering, the main difference from the usual optical scattering lies in the higher energy associated with the incident radiation. As a first consequence both free and bound electrons in the plasma contribute to the scattering process. Another relevant effect is associated with an important amount of energy transferred from the

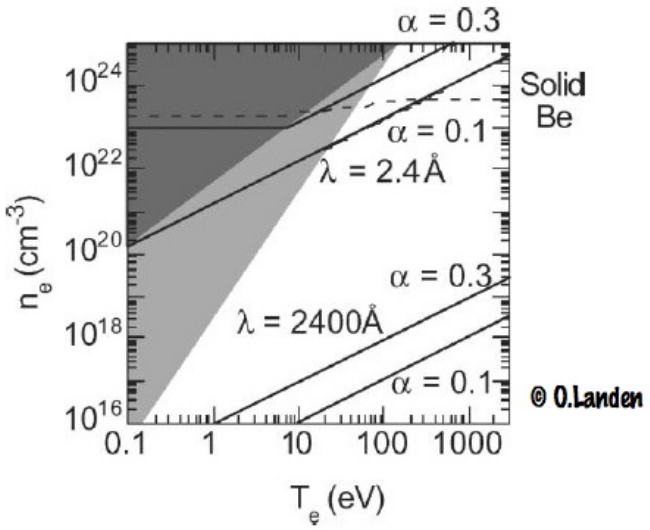


**Figure 3.17:** *Regimes accessible by Thomson scattering with $\alpha = 0.1 - 0.3$ for a UV and X-ray probe. Solid density regimes for Beryllium are accessible with a 2.4Å probe.*

photon to the electron which is large compared to the electron's kinetic energy. The scattered photons are thus downshifted in energy by the Compton effect, which is expressed, in terms of wavelength, as:

$$\Delta\lambda = \frac{h}{mc}(1 - cos\theta) \sim 24.3(1 - cos\theta)m\mathring{A} \tag{3.45}$$

where $\frac{h}{mc}$ is called the Compton wavelength and $m$ is the electron mass. Moreover the scattered spectrum is broadened by the thermal motion of the electrons.
A detailed description of the x-ray scattering theory is given in [80],[81]. This treatment can be applied to the description of scattering from degenerate to weakly coupled plasmas; corrections for strongly coupling effects can instead be found in [82]. Here we will just limit ourselves to present the main features necessary to understand the principle of the experimental measurement. Following recent works [80],[81],[82], the sample is considered as a uniform plasma containing N ions per unit volume. We shall label the nuclear charge of the ion as $Z_A$, the number of electrons, including bound and free ones, being $Z_A$N. We will consider that the probe frequency $\omega_0$ is such that $\hbar\omega_0 \gg E_I$, where $E_I$ is the ionisation energy of any bound electrons. This means that we can neglect photon-absorption, the incident frequency being much greater than any natural resonance frequency of the atom. It is useful to distinguish the electrons that are kinematically free with respect to the scattering process and core electrons that are tightly bound to the ions. For free electrons, the binding energy is less than the energy transferred in the scattering process, while the opposite condition apply to the core

electrons. If $Z_f$ is the number of free electrons and $Z_c$ the number of the core ones, $Z_A = Z_c + Z_f$. It should be underlined here that $Z_f$ can differ from the true ionisation state of the atom as it accounts for both truly free electrons (i.e. truly removed from the atom) and the valence or conduction electrons.
It has been demonstrated [83] that the total x-ray scattering cross section can be written as:

$$\frac{d^2\sigma}{d\Omega d\omega} = \sigma_T \frac{k_1}{k_0} S(k,\omega) \tag{3.46}$$

where $S(k,\omega)$ is the total dynamic structure factor of the plasma. In the treatment of the x-ray scattering from a plasma we can follow the approach proposed [83] and [84] where the free and core electrons contributions are separated. For isotropic cases, as in the case of liquid metals or plasmas, the dynamic structure factor depends only on the magnitude of **k**, $|k|$. The general expression for the dynamic structure factor can be then written as, [80]:

$$S(k,\omega) = |f_I(k) + q(k)|^2 S_{ii}(k,\omega) + Z_f S^0_{ee}(k,\omega) + Z_c \int \tilde{S_{ce}}(k,\omega-\omega') S_s(k,\omega') d\omega' \tag{3.47}$$

The first term in eq.3.47 accounts for electrons that dynamically follow the ion motion, $S_{ii}(k,\omega)$ representing the ion-ion density correlation function. This term includes both core electrons, represented by the ion form factor $f_I(k)$, and screening free and valence electrons, represented by q(k). The second term corresponds to the contribution from the density fluctuations of the free electrons that are not correlated to the ion motion. Inelastic scattering by core electrons is included in the last term of eq.3.47. It comes from Raman transition to the continuum of core electrons within an ion, $\tilde{S_{ce}}$, modulated by the ions motion, $S_s(k,\omega)$.
The different terms in eq.3.47 give rise to signals at different frequencies. By resolving the scattered spectrum, it is possible to evaluate the different contributions from the electrons of the plasma, giving the opportunity to access temperature, densities and ionisation state measurements.

It is then clear that a good knowledge of the three partial structure factors is of extreme importance in the analysis of the x-ray scattered spectrum. In the following sections, we will establish the basic concepts necessary to calculate each partial structure factor. In particular, we will focus on the method they were implemented in the code we have used to simulate our scattered spectra.

**The Ion Feature** The Ion feature is representative of the ion-ion correlations, which reflect the ion motion. These are density fluctuations at low frequency which are actually not accessible experimentally. The dynamic structure factor in the cross section

calculation can thus be approximate as $S_{ii}(k,\omega) = S_{ii}(k)\delta(\omega)$ and the static structure factor is the only quantity that we need to calculate. As a consequence, the scattered spectrum appears as a unique unshifted component at the same frequency of the incident radiation, often called elastic or Rayleigh component. The observed width of this feature is solely determined by the instrumental resolution.
In simple liquids, S(k) is mainly determined by considering convenient reference systems and developing then variational approaches for the investigation of the considered fluid. In treating our plasmas, a considerable help comes from the theories of simple liquid metals, characterized by the presence of conduction electrons, which require a quantum-mechanical treatment.

Theories of the structure and thermodynamics of simple liquid metals have developed along two main directions. The two points of view are to some extent complementary, each of them being suitable as a reference system. On one hand, one can represent the metal as a one component system in which the particles interact through an effective, short-range pair potential. The usual perturbation methods can be applied and a natural choice of the reference system is in this case the *Hard-sphere liquid* (HS). In the HS picture, the potential is separated into a harsh repulsion $v(r) = \infty$ appearing at short range ($r < d$, the hard sphere diameter) and a much smoother attractive potential $v(r) = 0$ acting at long range ($r > d$). An alternative approach is based on considering the ions as a *one component plasma* (OCP). In a OCP, the electrons are replaced by a uniform background, whose charge is identical but opposite in sign to that of the ions, modeled as identical point charges. To account for the effects of the ion-electrons interaction on the properties of the fluid, not included in the OCP, perturbation theories are then used.

In the calculations of S(k), used for the x-ray scattering simulations, we have followed the approach described in [86], where a system of charged hard spheres (CHS) in an uniform background of electrons was used as reference. In this context, the OCP model is used as reference system, but here the point ion charges are replaced by the effective hard core radius $R_c$, which can be greater than the actual ion-sphere diameter due to the Coulomb repulsion between the ion cores. This approach allows to account for their polarization, an important aspect in determining the short-range order. This approach has the great advantage that it can be solved analytically in the mean spherical approximation [86]. The CHS system is described in terms of the effective hard core diameter $R_c$, the packing fraction $\eta = \frac{\pi}{6} N_i R_c^3$ and the ion-ion coupling constant $\Gamma$, which involve the ion temperature and the ion density $N_i$ as the only parameters. The CHS model, hence, allows to calculate the OCP factor only as a function of these two plasma parameters. The resulting formula is explicit in [86] together with a complete description of this model. This approach has shows excellent agreement with experimental data from liquid metals as well as with Monte-Carlo simulations. Moreover it remains valid

at fairly high values of coupling parameters $\Gamma$ ($\lesssim 20$) so that thus allows to account for strong ion correlations.
The electron dynamic screening then needs to be considered. The electrons in the plasma do not form a rigid background as assumed by the OCP, but they are free to move and compensate any charge imbalance. In the model, the electron response to the ionic motion is thus taken into account through a linear-response approximation. A screened ion-ion structure factor is obtained [87] by considering the screening correction $f_v(k)$ on the bare ion-ion interactions. This requires the evaluation of the effective screening charge $q(k)$, which can be obtained in [83] and [85]. It is expressed in terms of the dielectric permittivity at frequency $\omega = 0$ and the electron-ion correlation function [75]. The screened ion-ion structure factor can then be expressed as, [87]:

$$S_{II}(k) = \frac{S_{II}^{OCP}(k)}{1 + f_v(k) S_{II}^{OCP}(k)} \tag{3.48}$$

where the OCP limit is reproduced if $f_v(k) = 0$, corresponding to a rigid background.
To complete the description of the first term in eq.3.47 we need to calculate the ion form factor $f_I(k)$. It can be deduced either from complicated calculations [88] or from the use of hydrogenoid wave functions, [89].

**The free electron feature** In most of WDM plasmas, the electrons are weakly coupled, while they exhibit strong degeneracy. The Random Phase Approximation (RPA), which can be seen as a mean field approximation, is the natural approach in the calculation of the electron structure factor. If strong coupling effects come into play, a local field correction (LFC) must be introduced. LCF calculations are anyway not an easy task and some approximations are required [82]. A detailed description of the electron structure factor determination is given in [80]. Here we will illustrate qualitatively the essential features in order to understand the experimental results.
As for the optical probe, the x-rays scattering in the collective or in the uncorrelated regime produces a different spectrum. Consequently, different are the parameters directly accessible in each regime. In order to account for coupling and degeneracy effects in the description of the scattered spectrum, a *generalized* scattering parameter $\alpha$ is introduced as $\alpha = 1/ks$, where s is the characteristic screening length of the electrostatic interactions. For an ideal plasma s is the Debye length and $\alpha \sim (T_e/N_e)^{1/2}$, the nature of the scattering (uncorrelated or collective) depending on both electron temperature and density. As degeneracy becomes important, the Debye length is no more representative of the screening. In the case of an ideal degenerate electron liquid, it must be replaced by the Thomas Fermi screening length $\lambda_{TF} = \sqrt{2\epsilon_0 E_F / 3N_e e^2}$, where $E_F$ is the Fermi energy ($E_F = \frac{\hbar^2}{2m}(3\pi^2 N_e)^{2/3}$ ). In this case $\alpha \sim (N_e)^{1/6}$ so that scattering weakly depends on the electron density while it is completely independent from the tempera-

ture. Finally in the strong coupled plasma case, the screening length is represented by the mean particle separation so $\alpha \sim N_e^{1/3}$.
For $\alpha \ll 1$ as mentioned before, the scattered spectrum is representative of the motion of single electrons. The scattered feature is shifted towards the low energies and it is broadened by the thermal motion of the electrons. Its evaluation thus gives a measurement of the electron temperature. In fig.3.18 we show the free electron feature for different temperatures. It is clear that the width of the free electron feature increases with temperature. Therefore the measurement of the broadening gives directly access to the electron temperature. In addition to the temperature, the scattered spectrum

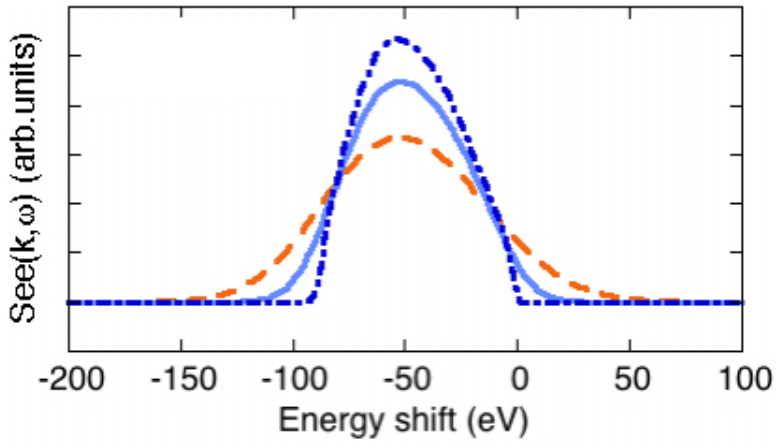


**Figure 3.18:** *Free electron dynamic structure in a degenerate plasma of* $Ne = 2.0 \cdot 10^{23} cm^{-3}$. *The incident radiation is at 4.5keV while the scattering angle is 90°.The scattering parameter is 0.5 for* $Te = 0.5$ *eV, dotted dark blue line,and* $Te = 5$ *eV solid light blue line while it is 0.4 for* $Te = 13$ *eV, orange dashed line.*

gives information on the ionization level. As the temperature is raised, the number of the electrons ionized or excited in the conduction band increases. As a consequence, the ratio between the inelastic and the elastic component is expected to get bigger. An estimation of ionization level is, therefore, directly accessible by comparing the inelastic to elastic scattering ratio in the cold material and in the dense plasma.
The feasibility of these measurements was demonstrated in [90]-[91], where non collective x-ray scattered spectra from a dense radiatively hated Be plasma were obtained. From these data, direct temperature and ionization measurements in a dense plasma via x-ray thomson scattered spectra were achieved.

When $\alpha \gtrsim 1$, the scattering reflects the collective behavior of the plasma and it shows frequency resonances (plasmon modes) which are directly related to excitations of fundamental modes of plasma oscillations, the electron plasma waves. As we will see,

the plasmon shift evaluation direct accesses the electron density. On the other hand, the dispersion yields information on the dispersion function $\epsilon(k,\omega)$. The knowledge of $\epsilon(k,\omega)$ in high density plasmas is of extreme interest as it determines reflectivity and transmission as well as thermal and electrical conductivities, thus being a critical parameter characterizing the state of WDM.
In an electron gas considering a linear response approximation, the dispersion relation for plasmons reads [24]:

$$\omega^2(k) = \omega_p^2 \left[1 + \frac{< p^2 >}{m_e^2}\frac{k^2}{\omega_p^2}\right] \tag{3.49}$$

where $\omega_p$ is the plasma frequency. For the classical ideal electron gas the specific mean kinetic energy is $\frac{< p^2 >}{m_e^2} = (3/2)k_B T$ and we get the usual Bohm-Gross relation. Introducing the thermal velocity, $v_T = \sqrt{k_B T/m_e}$ we get:

$$\omega^2(k) = \omega_p^2 \left[1 + 3v_T^2\frac{k^2}{\omega_p^2}\right] \tag{3.50}$$

If we then account for the Compton component, the dispersion relation fully reads:

$$\omega^2(k) = \omega_p^2 + 3v_T^2 k^2 + \frac{\hbar k^2}{2m_e}^2 \tag{3.51}$$

Here the first term depends on the electron density through the plasma frequency and it is the dominant contribution for large $\alpha$. The second term is associated to the thermal motion of the electrons, while the last one is the Compton contribution. For an ideal Fermi gas,the dispersion relation contains an additional term associated to the Fermi energy. It reads (S.Glenzer private communication):

$$\omega^2(k) = \omega_p^2 + 3v_T^2\left[1 + 0.0884 N_e \Lambda_e^3\right]k^2 + \frac{\hbar k^2}{2m_e}^2 \tag{3.52}$$

$\Lambda_e = h/\sqrt{2\pi m_e k_B T}$ being the de Broglie wavelength.
By spectrally resolving the scattered radiation in a collective regime, thus, we will be able to directly access the electron density through the observed shift of the satellite.

In fig.3.19 we show the electron-electron dynamic structure factor for different values of the density and of the parameter $\alpha$, while the electron temperature was kept at 5 eV. For a better understanding we have normalized the features at the same intensity. We remark, though, that, due to the $k_1/k_0$ dependence of the cross section, the intensity of the signal is weaker for higher values of $\alpha$, making the detection of the experimental signal in the collective regime much more difficult than in the incoherent case.
Fig.3.19 shows another fundamental feature characteristic of the x-ray regimes: a single

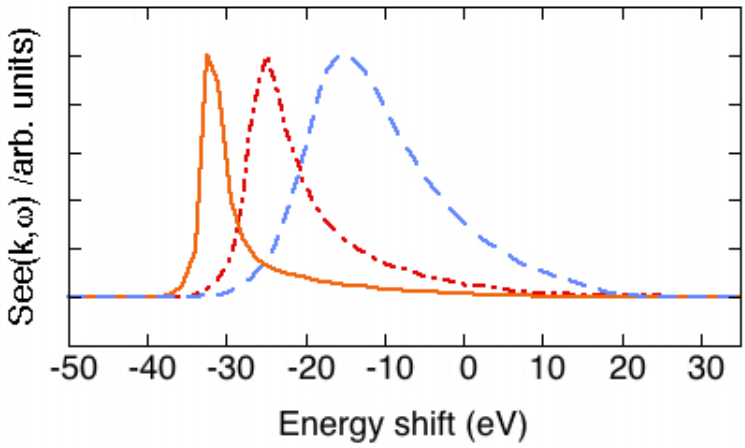


**Figure 3.19:** *Free electron dynamic structure for a plasma at different density with scattering parameters varying in the collective scattering regime. The incident radiation is 4.5 keV while the scattering angle is 30°, $Ne = 4.0 \cdot 10^{23} cm^{-3}$ for solid orange line, $Ne = 2.0 \cdot 10^{23} cm^{-3}$ for dotted red line, and $Ne = 0.5 \cdot 10^{23} cm^{-3}$ for dashed blue line corresponding to values of $\alpha$ of 1.6, 1.3 and 0.9 respectively. The three cases are normalized at the same intensity.*

plasmon appears, shifted towards the low energies. This is a consequence of the detailed balance principle[3] which requires that $S(\mathbf{k}, \omega)$ satisfies the following equation:

$$S(\mathbf{k}, -\omega) = exp(-\hbar\omega/k_B T) S(\mathbf{k}, \omega) \tag{3.53}$$

While in the optical regime $\hbar\omega/k_B T \ll 1$ and two satellites are visible, in the x-ray regime eq.3.53 translates in a strong asymmetry in the x-ray scattered spectrum, with the blue-shifted (or up-shifted) plasmon strongly damped. However, if the up-shifted plasmon is intense enough to be observable, a precise direct temperature measurement is possible from the evaluation of the ratio between the intensities of the up-shifted and down-shifted plasmon features. The detailed balance, in fact, implies that this ratio is $\sim exp[-\hbar\omega/k_B Te]$. A high temperature is necessary to observe both the plasmon features, as shown in 3.20. Again for a better understanding the three cases were normalized at the same intensity. In our experiments, though, the involved temperatures are considerably low, fraction to few eV, so that no up-shifted plasmon is observable.

**The bound-free electron feature** The last term in eq.3.47 corresponds to the density correlation of the tightly bound electrons within a single ion. Inner core electrons can be excited to continuum states by the probe radiation and the corresponding scattered radiation spectrum is of a Raman-type band. Clearly, transitions into the con-

[3]The detailed balance principle requires that the ratio of cross sections for scattering process $|\mathbf{k}_1, 1\rangle \rightarrow |\mathbf{k}_2, 2\rangle$ and $|\mathbf{k}_2, 2\rangle \rightarrow |\mathbf{k}_1, 1\rangle$ be equal to the ratio of the statistical weights $|1\rangle$ and $|2\rangle$

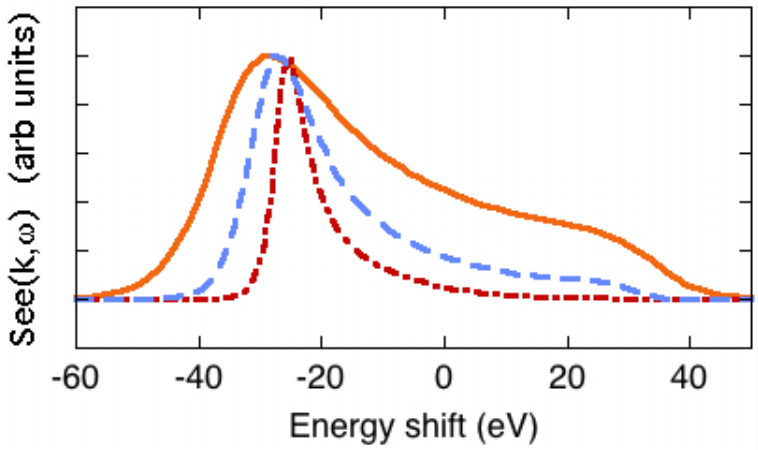


**Figure 3.20:** *Effect of the detailed balance on free electron dynamic structure for a plasma at different temperatures:* $Te = 20eV$ *solid orange line,* $Te = 10eV$ *dashed blue line and* $Te = 5eV$ *dotted red line. The three cases are normalized at the same intensity.*

tinuum occur only if the energy transferred from the photon to the electron is bigger than its ionization energy, $\hbar\omega > E_B$ and thus the dynamic structure factor has a cut off at the ionization energy for K- and L- electrons. In contrast to the usual Compton scattering, thus, the position of the Raman band is independent on k (and thus from the scattering angle) and it appears shifted from the free electron feature. As the threshold is determined only by the ionization threshold of the inner K shell or L-shell of the atom, the importance of this feature strongly depends on the material considered. For low Z metallic materials, the outermost electrons enter in the conduction band and they do not participate to bound-free transition. The contribution of the bound-free feature to the scattered signal is considerably low and can be neglected, as shown in [80] for the case of Be. For higher Z materials, though, the situation is quite different. In this case the contributions from bound-free transitions can be much more important than the free electron term. It must be then considered for a correct evaluation of the experimental profiles, if accurate measurements of the electron density, electron temperature and charge state must be performed.

In dense plasmas the importance of this feature is even heightened because of the continuum lowering effect. This phenomenon arises in dense plasmas as the potential distribution of a given ion is influenced not only by its own bound electrons but also by the neighboring ions. As a consequence, there is a ionization potential lowering, which strongly shifts the shell edges of the bound-free dynamic structure. A complete treatment of the bound-free feature can be found in [81].
In fig.3.21, we show the dynamic structure factor for both free (solid lines) and core (dotted lines) electrons for a carbon (blue lines) and a Be (red lines) plasma. For a better clarity the curves were normalized to the most intense feature for each material. For the

Be case the contribution of core electron is considerably low and can be neglected while it represents the major contribution for the carbon plasma. As a general consideration

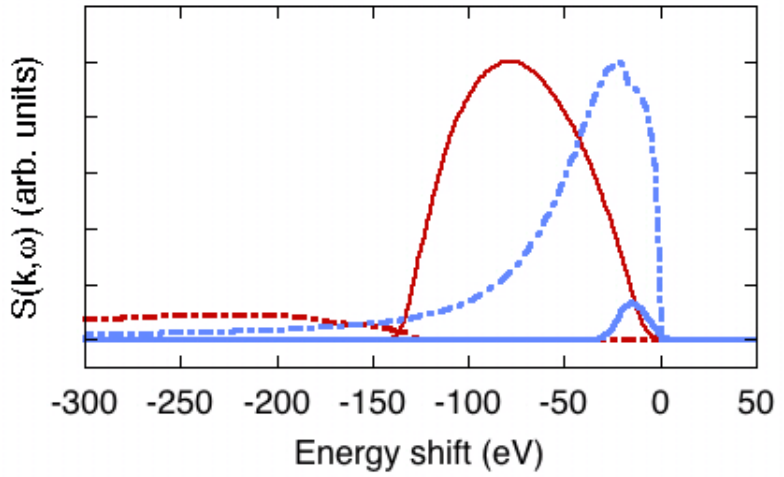


**Figure 3.21:** *Free (solid lines) and core (dotted lines) electron dynamic structure for a Be (red) and Carbon (blue) plasmas with* $\alpha \sim 0.4$. *The dynamic structure factors are normalized to the most intense feature.*

we can say that an extremely high contribution from bound-free transitions can obscure the free electron term, compromising the detection of the plasmon shift, and thus the density measurement. If this is the case, in order to be observed, the free electron feature must be shifted enough to appear in the low intensity wing of the bound-free signal. For instance, the free electron contribution for the carbon plasma in fig.3.21 must be shifted of $\sim 140$ eV in order to be distinguished from the bound free contribution. This fact is important as it imposes a minimum to the measurable density.

# Bibliography


[1] T. Löwer, R. Sigel, K. Eidmann, Phys. Rev. Lett, **72**, 20, 3186 (1994)

[2] M.Koenig, B. Faral, J.M. Boudenne, *et al.*, Phys. Rev. Lett., **74**, 12, 2260 (1995)

[3] A. Benuzzi-Mounaix, T. Löwer, M.K.B. Faral, *et al.*, Phys. Rev. E., **54**, 2, 2162 (1996)

[4] L. Da Silva,P. Celliers, G.Collins, *et al.*, Phys. Rev. Lett., **78**, 3, 486 (1997)

[5] M.D.Knudson, D.L.Hanson, *et al.*, Phys. Rev. Lett. **90**, 3,035505 (2003)

[6] W.J.Nellis *et al.*, J. Chem.Phys, **79**, 1480 (1983)

[7] M. D. Knudson *et al.*, Phys. Rev. Lett. **87**, 225501 (2001)

[8] S. I. Belov, G. V. Boriskov, A. I. Bykov, *et al.*, JETP Lett. **76**, 433 (2002)

[9] R. Cauble, T.S. Perry, D.R. Bach,*et al.*, Phys. Rev. Lett., **80**, 6, 1248 (1998)

[10] A.Benuzzi-Mounaix, M.Koenig, G.Huser,*et al.*, Phys. Plasmas, **9**, 6, 2466 (2002)

[11] N.Ozaki, *et al.*, "Absolute equation of state measurement for an important metal", poster section at EPS, Rome 2006

[12] D.G.Hicks, T.R.Boehly, P.M.Celliers *et al.*, Phys. Plasmas **12**, 082702 (2005).

[13] D. G. Hicks, T. R. Boehly, J. H. Eggert, *et al.*, Phys. Rev. Lett., **97**, 025502 (2006)

[14] D. Strickland and G. Mourou, Opt. Commun.**56**, 219 (1985)

[15] http://www.clf.rl.ac.uk

[16] August S.,*et al.* , Phys. Rev. Lett. **63**, 2212 (1989)

[17] Ilkov.,*et al.* , Journal of Physics B **25**, 4005 (1992)

[18] Lefebvre E. and Bonnaud G., Phys. Rev. Lett. **74**, 2002 (1995)

[19] Monot P., Auguste T., Gibbon P,*et al.*, Phys. Rev. Lett. **74**, 2953 (1995)

[20] Rozmus and V.T. Tikhonchuk, Phys. Rev. A **42**, 7401 (1990)

[21] A. Ng Phys. Rev. E **51**, 5208 (1995)

[22] W.L.Kruer "The physics of laser plasma interaction", Addison-Wesley, New York (1988)

[23] W.L.Eastbrook and K.G. Kruer, UCRL-50021-76 (1976)

[24] K.G. Kruer and W.L.Eastbrook, Phys. Fluids. **28**, 430 (1985)

[25] F.Brunel, Phys. Rev. Lett. **59**, 52 (1987)

[26] W.I.Linlor, Appl. Phys. Lett. **3**, 210 (1963)

[27] S.J. Gitometer, R.D. Jones, F.Begay, *et al.*, Phys. Fluids **29**,2679-2688, (1986)

[28] M.Roth, M.Allen, P.Audebert, *et al.* Plasma Physics and Controlled Fusion**44**, B99-B108 (2002)

[29] A.Pukhov, Phys. Rev. Lett. **86**, 3562 (2001)

[30] P. Mora, Phys. Rev. Lett. **90**, 185002 (2003)

[31] E.L. Clark, K.Krushelnick, J.R.Davis, M. Zepf,*et al.*, Phys.Rev.Lett. **84**,670 (2000)

[32] M.Zepf, E.L.Clark, F.N.Beg, *et al.*, Phys. Rev. Lett. **90**, 064801 (2003)

[33] R.A. Snavely, M.H.Key, S.P.Hatchett, T.E.Cowan,*et al.*, Phy.Rev.Lett. **85**, 2945 (2000)

[34] S.P.Hatchett, C.G.Brown, T.E.Cowan,*et al.*, Phys. Plasmas **7**, 2076 (2000)

[35] A.J.Mackinnon, M.Borghesi, S.Hatchett, *et al.*, Phys. Rev. Lett. **86**, 1769 (2001)

[36] A.J. Mackinnon, Y. Sentoku, P.K. Patel, D.W. Price, *et al.*, Phys. Rev. Lett. **88**, 22506 (2002)

[37] J.Fuchs, Y.Sentoku, S.Karsch, J.Cobble, *et al.*, Phys. Rev. Lett. **94**, 045004 (2005)

[38] H.A.Bethe, Ann. Phys., **5**, 325 (1930)

[39] B.A.Hammel, D.Griswold, O.Landen, *et al.* Phys.Fluids B **5**, 2259 (1993)

[40] F.J.Marshal, Q.Su, Rev. Sci. Intrum., **66**, 725 (1995)

[41] F.J. Marshal, J.A Oertel Rev: Sci. Intrum **68**, 735 (1997)

[42] J. H. Underwood, A. C. Thompson, J. B. Kortright, *et al.* Rev. Sci.Intrum., **67** 1 (1996)

[43] J.A.Koch, Y. Aglitskiy, C.Brown, *et al.* Rev. Sci. Instr. **74**, 2130 (2003)

[44] M. Dirksmöller, O. Rancu, I. Uschman, P. Renaudin, *et al.* Opt. Commun. **118**, 379 (1995)

[45] B.Remington, *et al.* Rev. Sci. Instr. **63**, 5080 (1992)

[46] D.G.Hicks, *et al.*, Bull. Am. Phys. Soc., **49** (8), 234 (2004)

[47] A.M. Koehler, Science, **160**, 303 (1968)

[48] D. West, A.C.Sherwood, Nature, **239**, 157 (1972)

[49] U. Schneider, E. Pedroni, Medical Phys., **22**, 353 (1994)

[50] P.Pemler *et al.*, Nucl. Instr. Methods Phys. Res. A, **432**, 483 (1999)

[51] C.W.Mendel and J.N.Olsen, Phys. Rev. Lett,**34**, 859 (1975)

[52] N.s.P. King *et al.*,Nucl. Instr. Methods Phys. Res. A, **424**, 84-91 (1999)

[53] M.Borghesi, A.Schiavi, D.H.Campbell *et al.*, Plasma Phys. Controlled Fusion, **43**, A267, (2001)

[54] M.Borghesi, D.H.Campbell, A.Schiavi, *et al.*, Phys. Plamsas, **9**, 2214 (2002)

[55] M.Borghesi *et al.* Rev. Sci. Instrum., **74**, 1688 (2003)

[56] M.Borghesi *et al.*, Phys. Rev. Lett., **82**, 1529 (2003)

[57] A.J.Mackinnon, P.K.Patel, R.P.Town, *et al.*, Rev. Sci. Instrum., **75**, 3531 (2004)

[58] M.Roth, Phys. Rev. Spec. Top. Accel. Beams, **5**, 061301 (2002)

[59] J.A.Cobble, R.P.Johnson, T.E.Cowan, *et al.*, J. Appl. Phys., **92**, 1775 (2002)

[60] M.Borghesi, A.J. Mackinnon, D.H.Campbell, *et al.* ,Phys. Rev. Lett. **92**, 5 (2004)

[61] A.J.Mackinnon, P.K.Patel, M.Borghesi, *et al.*, Phys. Rev. Lett. **97**, 045001 (2006)

[62] S.Kar, M.Borghesi, L.Romagnani, *et al.* RAL Annual report 2003-2004, 26

[63] S.Le Pape, M.Koenig, T.Vinci, *et al.*, Astrophys. Space. Sci, **298**, 313 (2005)

[64] J. Lindhard, Mat. Fys. Medd. K. Dan. Vidensk. Selsk. **28** (1954)

[65] H.H. Andersen and J.F. Ziegler, "Hydrogen Stopping powers and Ranges in all Elements", Pergamon, New York (1977)

[66] J.F. Ziegler, J. Appl. Phys., **85**, 1249-1272 (1999)

[67] R.C.Fernow "Introduction to experimental particle physics", Cambridge University Press (1986)

[68] L.Romagnani, M.Borghesi, O.Willi, *et al.*, CLF Annual Report 2001/2002, 26

[69] K.L.Bowles, Phys. Rev. Lett.,**1**, 454 (1958)

[70] E.E. Salpeter, Phys. Rev,**120**, 1528 (1960)

[71] M.Grewal, Phys. Rev. A, **134**, 86 (1961)

[72] M.N.Rosenbluth and N.Rostoker,Phys. Fluids, **5**, 776 (1962)

[73] S.Ichimaru, D.Pines, N.Rostocker, Phys. Rev. Lett.,**8**, 231 (1962)

[74] T.Hagfors, J.Geophys. Res., **66**, 1699 (1961)

[75] J.-P.Hansen and I.R. McDonald, *Theory of simple liquids", Elsevier Accademic Press*

[76] D.M.Villeneuve, H.A.Baldis, *et.al*, J. Opt. Soc. Am. B, **8**, 895 (1991)

[77] S.H.Glenzer, W.Rozmus, B.J.MacGowan, *et al.* Phys. Rev. Lett., **82**, 1 (1999)

[78] D.H.Froula,P.Davis,L.Divol, *et al.* Phys. Rev. Lett., **95**, 195005 (2005)

[79] O.L.Landen, S.H.Glenzer, M.J.Edwards, *et al.*, Journal of Quantitative Spectroscopy & Radiative Transfer **71** 465-478 (2001)

[80] G.Gregori,S.H.Glenzer,W.Rozmus, *et al.*, Phys. Rev. E, **67**, 026412 (2003)

[81] G.Gregori,S.H.Glenzer,F.J.Rogers, *et al.*, Phys. Plasmas, **11**, 5, 2754 (2004)

[82] G.Gregori, S.H. Glenzer, O.L.Landen, J.Phys.A, **36**, 5971 (2003)

[83] J.Chihara, J.Phys.F, **17**, 295-304 (1987)

[84] J.Chihara, J. Phys. Condens. Matter, **12**, 231-247 (2000)

[85] Y.V.Arkhipov and A.E. Davletov, Phys. Lett. A, **247**, 339 (1998)

[86] H.B.Singh and A.Holz, Phys. Rev. A, **28**, 1108(1983)

[87] G.Gregori, *et al.* J. High Energ. Dens. Phys. submitted (2006)

[88] R.W.James *The Optical Principles of the Diffraction of X-Rays*, Ox Bow, Woodbrige, CT (1962)

[89] L.Pauling and J.Sherman, Z.Kristallogr. **1**, 81 (1932)

[90] S.H.Glenzer, *et. al*, Phys. Rev. Lett., **90**, 175002 (2003).

[91] S.H.Glenzer, G.Gregori, F.J.Rogers, *et. al* Phys. Plasmas, **10**, 6, 2433 (2003)

[92] W.D. Kraeft, D.Kremp, W.Ebelin and G.Röpke, *Quantum Statistics of Charged Particles Systems* (Akademie-Verlag, Berlin, 1986)

# Chapter 4

# X-ray shock radiography

In this chapter, we will show how the concepts we have introduced in section 3.3.1.1 have been applied to our experiment. We will first describe the experimental set up, a common configuration for both x-ray and proton radiography. The attention will here be focused on the x-ray radiography of a shock compressed aluminum target. We will present the results, illustrating the procedure we have followed in the data analysis and demonstrating the validity of this novel diagnostic. We will also identify the principal problems we have encountered, key issues to be solved for future experiments.

## 4.1 Experimental Set Up

The experiment was performed at the Rutherford Appleton Laboratory, in the TAW experimental area. Three of the six ns beams of Vulcan laser were used to generate the shock in a first target (EOS target) while the interaction of Vulcan CPA beam with a second target (backlighter) produced the x-ray source. A time resolved self emission diagnostic was also implemented as a shock velocity diagnostic. A schematic view of the set-up is shown in fig.4.1.

**The 3 ns beams** The initial seed of the laser light is generated with a Nd:glass oscillator at 1054 nm. After going through successive amplifiers, each of the ns pulse beam can deliver up to 200 J at the principal wavelength. To limit preheating effects, shorter wavelengths are preferred so that frequency-doubled light was used. The doubling crystals have an efficiency near 40% so that at the entrance of the chamber each beam could deliver ∼80 J at 527 nm. The pulse had a super-gaussian temporal profile with a 2 ns FWHM. The three beams entered the vacuum chamber in the horizontal plane with an angle of $\sim 15^{\circ}$ between them. They were focused at the target chamber center (TCC) using a f/10 optics lying outside the chamber. Random Phase Plates (RPP)

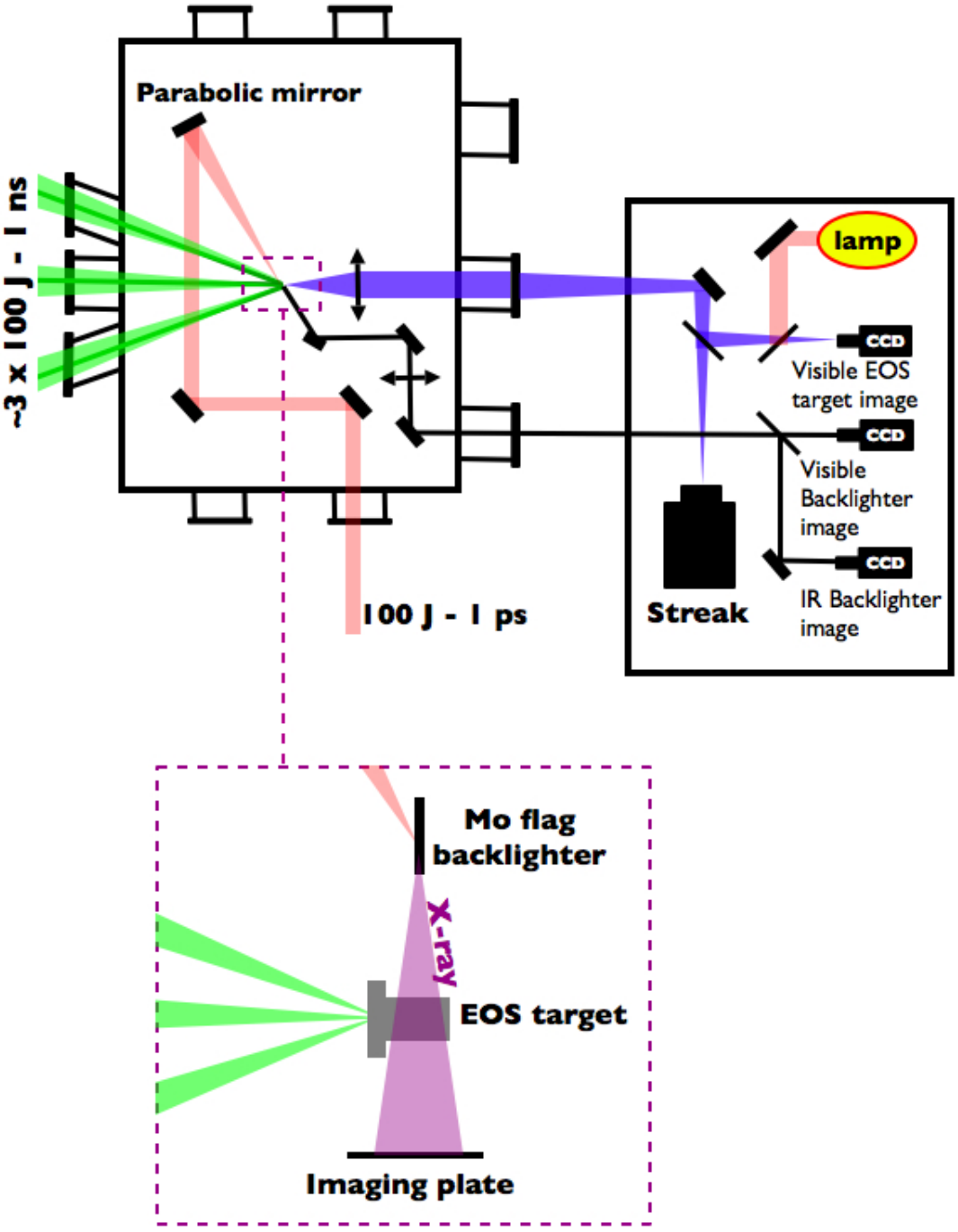


**Figure 4.1:** *Schematic representation of the experimental set up.*

were used as smoothing technique and they were placed in the beam right after the focusing lenses. The RPP is a transparent plate with a patchwork of square elements, obtained by a resin deposition. A typical RPP pattern is shown in fig.4.2, which also illustrates the working principle. The laser is diffracted by each square element which

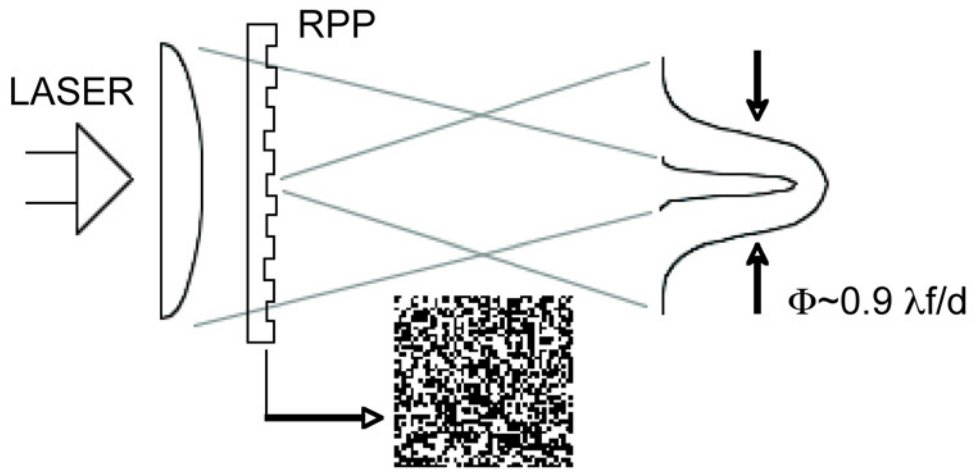


**Figure 4.2:** *Structure and working principle of a RPP.*

introduces a random phase-shift of 0 or $\pi$. The resultant intensity pattern is the typical one of the diffraction from a square aperture, a $sinc^2$ type. As the 0 diffraction order contains $\sim$ 82 % of the energy, the focal spot size $\Phi$ can be estimated as the FWHM of the 0 diffraction order:

$$\Phi = 0.9\lambda f/d$$

where $\lambda$ is the laser wavelength, f the lens focal length and d the dimension of the square element. In our case the focal spot was $\sim$ 300 $\mu m$ FWHM. The shock profile obtained with the RPP is quasi-gaussian which will facilitate the inversion for the density calculation.

**The CPA beam** The chirped pulse came perpendicular to the ns beams. It was used at the principal wavelength, 1064 nm and it had a gaussian temporal profile with a 1 ps duration. A f/3.5 off axis parabolic (OAP) mirror was used to focus the beam in a $\sim$12 $\mu m$ FWHM focal spot. The average power delivered by the laser was about 80 TW so we could obtain a peak intensity of the order of $10^{19} W/cm^2$ on the target. The control of the focal spot was done in two different ways, since it is a crucial element for

the proton generation in particular. A first imaging system looking from the back was set up to image the backlighter position both in the visible and in the infrared. The CCD camera looking in the infrared was used to check the focal spot before placing the target, while the visible one was disposed to verify the backlighter alignment, once the target was in place. Another imaging system was set up to cross check the alignment by using an internal CW laser, made precisely collinear with the main one. When the laser was focused on the target, the diffused light was reflected as a parallel beam in the path from the parabolic mirror, the target being at the right focal distance. The light losses from one mirror in the path was collected by another lens system, producing an image of the focal spot. In this way the focusing of the parabola on the target could have been directly checked just before each shot.
The short pulse could be delayed with respect to the three beams up to 11 ns, by modifying the path length. In this way, we could probe the compressed target at different times, and determine its time evolution.

**The alignment procedure** The target chamber center was pointed by two telemicroscopes mounted on the chamber and a third objective directly positioned inside the chamber. They were all made image a micro-balloon of 100 $\mu m$ diameter, determining the TCC.
The EOS and backlighter targets were mounted on a same kinematic plate. A scheme

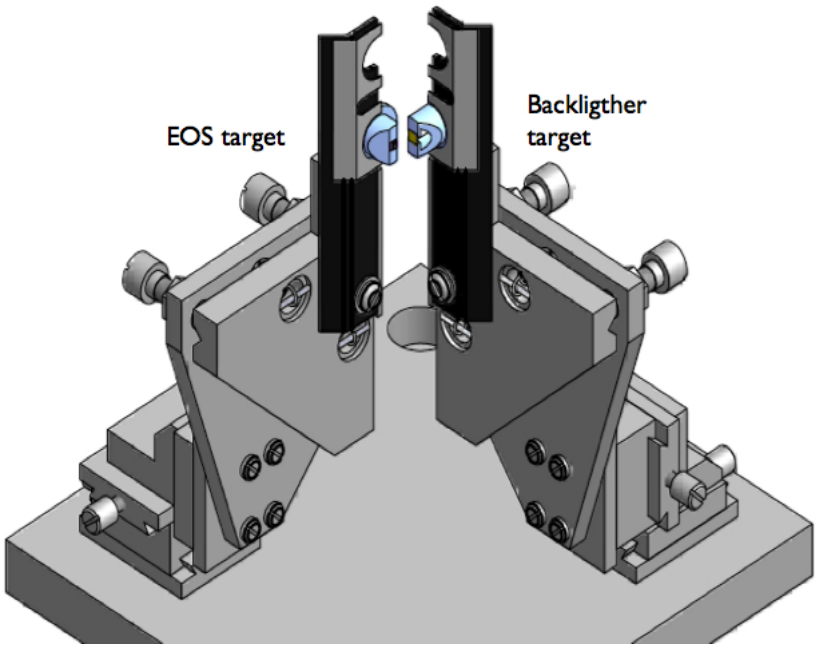


**Figure 4.3:** *The two targets were first pre-aligned one relative to each other.*

of the mount is shown in fig.4.3. At first, the backlighter was aligned with respect to the EOS target on a three axis external jig. The distance between the two targets was fixed at 3 mm on the radiographic direction. The whole plate was then placed in the chamber and by moving the common plate, the EOS target was aligned at TCC. The backlighter was then at the right position. The overall alignment precision was measured few (∼15) microns.

The objective in the chamber, looking at the rear side of the EOS target, was also used to collect the emission from the EOS target rear side. A flip-flop mirror allowed to send the light whether to the alignment CCD or to a streak camera's slit. The time resolved emission allow to determine the shock velocity.

## 4.2 The detectors

The x-ray radiation after propagation through the shocked target was recorded on imaging plates. A control of the radiation spectrum was obtained using a CCD camera operating in the single photon mode. We will here discuss the characteristics of these two detectors.

### 4.2.1 The imaging plates

The set-up configuration required the detector to be put close to the target. The use of a CCD was thus delicate since it could be easily damaged. Moreover, the small size of the CCD chip could have limited the magnification which was required rather high (∼ 40). For these reasons, a film like detector was preferred. We have employed the imaging plates (IP), a new phosphor technology widely used in the medical x-ray diagnostic field but only recently applied in laser-plasma diagnostics. Imaging plates are a film-like radiation image sensor which traps and store the radiation energy. "Photostimulated luminescence" (PSL) is the physical process involved in the imaging plate technology. This phenomenon involves a second radiation emission when stimulated by a light with a longer wavelength than the first stimulation one.
An imaging plate contains bunches of small crystals of photo-stimulable phosphors (barium fluorobromide). The ionizing radiation excites the electrons of the sensitive phosphor layer, which are trapped in metastable states, leaving temporary vacancies centers. In this way, we are able to record information about the amount and position of deposited energy. The data can then be extracted by optically stimulating the IP. A He-Ne laser at 633 nm provides enough energy to release the trapped charges and causes photostimulated luminescence in the blue (390 nm) at the trapped centers positions. The luminescence is then detected with a photomultiplier tube (PMT) and its output

is logarithmically amplified and converted into a digital image.

There are various advantages in using imaging plates comparing to other radiation image sensors. Among them, the most important are:

- Ultrahigh sensitivity
- Wider dynamic range
- superior linearity with incident fluxes

All these qualities, together with a high spatial resolution ($\lesssim$50 $\mu m$) makes these plates a suitable detector for our experiment.

In our experiment a FUJI BAS2500 scanner was used to scan the imaging plates. This system generates an image data as a logarithmic compression. Indeed, the pixel data stored after scanning consist in QL (Quantum Level) values, which are logarithmic data stored in the output file. Therefore, they must be transformed if quantitative information are required. The PSL value we need is a log to linear converted data from QL value and it represents the real physical quantity: the radiation dose stored on the Imaging Plate. The log to linear transformation can be done on the image by applying the following conversion formula:

$$PSL = \left(\frac{Res}{100}\right)^2 \frac{4000}{S} 10^{L\left(\frac{QL}{G}-\frac{1}{2}\right)}$$

where Res is the resolution in $\mu m$, G is Gradation i.e. the bit depth at one pixel, S is the sensitivity and L the latitude which can take the value 4 or 5. All these parameters values are typical of the scanning system and processing as well as on the imaging plate type. They are stored in a .inf file generated after the scanning. In our case the resolution is 50$\mu m$, Sensitivity $S = 4000$, $LatitudeL = 5$, $Gradation = 65535$ (16bit image) and QL are the image pixels values.

Since the imaging plates have just recently introduced in our scientific environment, their complete characterization is of extreme importance even because they are the best candidate proposed to replace CCD cameras in PW experiments, where the extremely intense fields prevent using any electronic device. In particular, while IP show a linear response with the incident flux, in the x-ray energy range their sensitivity greatly depends on the photon energy. Their response as a function of the incident energy has been investigated for both electrons [4],[5], and x-ray [6],[7].

### 4.2.2 Single photon counting CCD camera

The use of a CCD camera as a spectrometer is widely diffused in short pulse laser experiments, [8]-[11]. Single photon counting condition is reached by reducing the incident flux in such a way that the probability that two photons hit the same pixel is really small. If the x-ray energy is not too high, a significant fraction of the x ray energy is absorbed in one single pixel or in the few adjacent ones and the recorded intensity is proportional to the incoming X-ray photon energy. The histogram of the pixels intensity gives thus a good approximation of the incident x-ray spectrum. For a typical silicon chip, the pair creation energy is 3.65 eV at room temperature; a 1 keV x-ray photon, if absorbed completely in 1 pixel, will produce 274 photoelectrons (pe). It is then possible to detect multiple kilo-electron-volt x rays with ease (for scientific grade CCD cameras, a typical digitization level is $\sim$ 1 pe per digitization unit ADU).

## 4.3 The EOS targets

As already mentioned, the main objective of the experiment was to prove the possibility to produce and actually use hard x-rays ($>$ 10 keV and hence not available with standard long pulse irradiation) to probe high Z dense plasmas. In our experiment, we

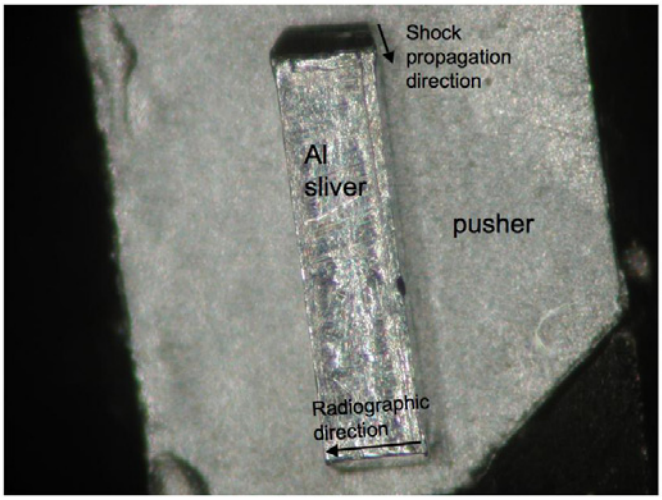


**Figure 4.4:** *Top view of a typical target used for the X-ray radiography. An Al sliver is glued on a CHAlCH pusher.*

have chosen to test this technique on aluminum, as it is often use as a reference material. Indeed, this is a good way to validate the results obtained with the new technique.

The EOS targets consisted mainly in two parts: the shock was generated in a multilayer pusher and then launched in an Al sliver glued on it. A typical top view of the target is shown in fig.4.4 The pusher was a CH-Al-CH sandwich, each layer being 10 $\mu m$ thick. The multilayer structure was designed to achieve high compressions and at the same time to prevent preheating of the target, which would modify its initial state. The different layers thicknesses were chosen on the basis of hydrodynamic simulations results, in order to optimize shock steadiness. The first CH layer allowed to reduce the x-ray radiation produced in the ablation process, source of preheating. This radiation is partially absorbed by the nearby Al layer, which is also used to block direct light from the laser, eventually transmitted trough the transparent CH. The last plastic layer was the effective pusher, the shock pressure being amplified when traversing the CH-Al sliver interface because of impedance mismatch.

The Al slivers were ∼400 $\mu m$ thick in the radiography direction and ∼250 $\mu m$ long

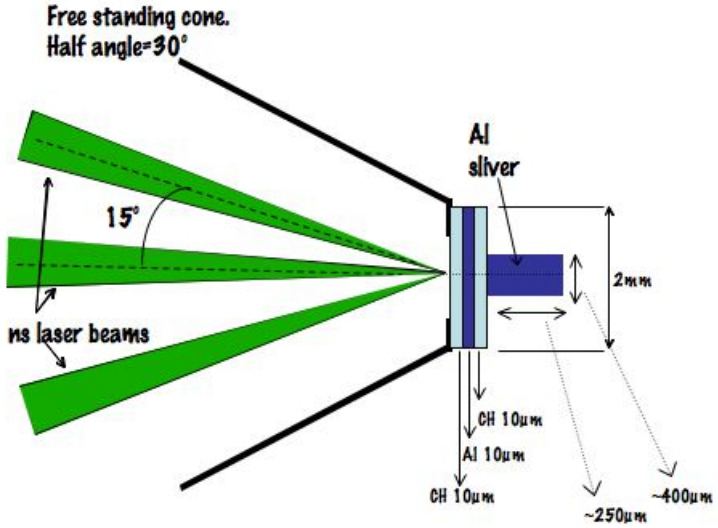


**Figure 4.5:** *Main target design. Sample with CH/Al/CH front layer is glued onto a cone, which will be then mounted on a stalk.*

in the shock propagation direction. For each target a precise characterization of the transverse thickness was done, as this is a fundamental information to infer the density from the radiography measurement.

The use of a sliver helped in the alignment procedure. If a simple planar target was used, a slight misalignment could have produced an obscuration of the shock in the radiography direction due to the target edge and its mount. The use of a sliver allows a less degree of precision in the alignment, providing that the shock has traveled far enough in the sliver. For the target geometry used (fig.4.5), an error greater than 1° was needed to obscure the shock after it has run more than 25 $\mu m$ in the sliver. The

whole CH-Al-CH sandwich was directly glued on a cone, which enabled the handling and positioning of the target in the chamber. The cone geometry was also suitable to protect the back-lighter foil from the long pulse plasma blow-off. In fig.4.5 the main target design is illustrated.

## 4.4 The backlighter target: a new geometry for high spatial resolution

The back-lighter geometry was designed in such a way to obtain a high resolution in the shock propagation direction. In order to probe $\sim \mu m$ size features, high magnification point projection requires source sizes smaller than 10 $\mu m$. The spatial extent of the $K\alpha$ emission is an important issue to be taken into account in the radiography resolution. One might think that, as the spatial distribution of the K$\alpha$ emission reflects the trajectories of the hot electrons, the K$\alpha$ source size is determined by the laser focal spot and by the lateral spreading of the hot electrons inside the target. This is true only for laser intensities $I < 5 \cdot 10^{17}\ W/cm^2$. In this case PIC codes are able to reproduce the K$\alpha$ spatial structure only using laser absorption and hot electrons scattering mechanisms. However, at higher laser intensities ($I > 5 \cdot 10^{17}\ W/cm^2$), $K\alpha$ radiation originates from an area much larger than the laser focal spot. In [1] it has been found that irradiating a Ti foil with an intensity of $I = 7 \cdot 10^{18}\ W/cm^2$ the half-width of the emitting area was about 70 $\mu m$ compared to the laser focus <10 $\mu m$. Moreover, it was observed that the peak intensity at the source center did not increase with increasing laser intensity. These observations evidenced the important role of electron recirculation over the target surface.
Therefore, the K$\alpha$ source size itself is too large to reach good resolution in radiography measurements. When low energy radiation is used in the point projection configuration, the source size is usually reduced by means of small pinholes. In the case of the CH radiography at ∼5 keV presented in fig.3.8, a 10 $\mu m$ pinhole on a 50 $\mu m$ thick Ta substrate was used to limit the emission size at the target. When dealing with more energetic sources, the choice of the pinhole substrate is much more limited. In addition, unsuitable x-ray radiation may be generated in the interaction of the material substrate with high energy electrons leaving the backlighter.
Recently, new techniques involving different targets geometries have been proposed [2] to reduced the natural source size of the K$\alpha$ radiation. The results are comparable with those obtained with pinholes. As K$\alpha$ yield is constant over a large range of foil thicknesses [2], high resolution can be achieved using 5-10 $\mu m$ thick foils, aligned in such a way that the edge is parallel to the feature to be radiographed, as shown in fig.4.6. In this direction, the spatial resolution is determined by the thickness of the radiating foil.

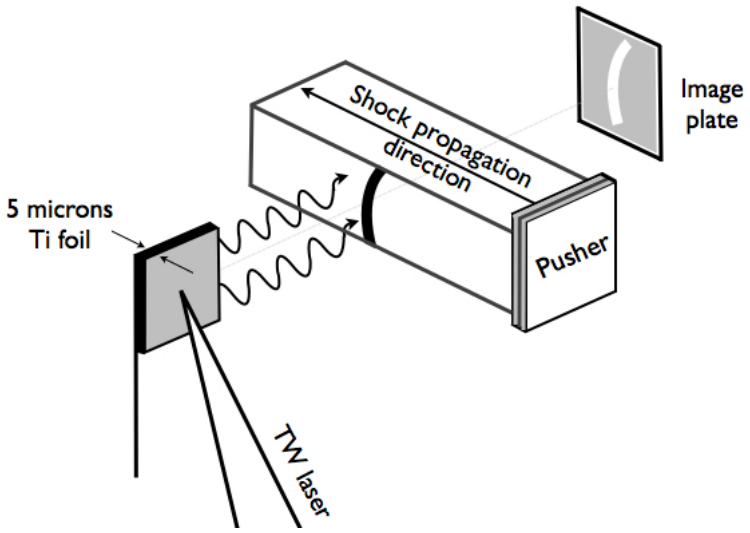


**Figure 4.6:** *Principle of the 1D high resolution scheme.*

In our experiment we used 5x250x250 $\mu m$ flag targets, aligned in such a way to reach the optimal resolution in the shock propagation direction. Indeed, the flag geometry

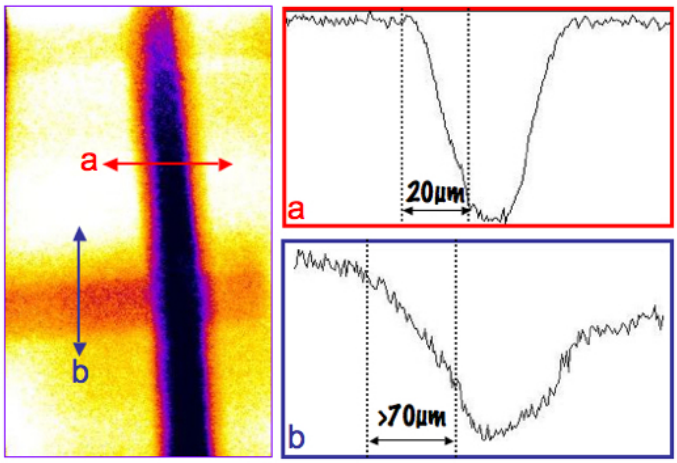


**Figure 4.7:** *Actual radiograph of a tungsten grid (left). Lineout in the horizontal direction which coincides with the shock propagation direction (a) and in the vertical direction (b). The difference in the resolutions values reflects the target geometry.*

allows high resolution only in one dimension, the other two sizes being too large to effectively limit electron recirculation. Fig.4.7 shows the resolution measurement results we obtained with a Tungsten grid radiograph. The grid was a 100 $mesh/inch$ with a 50 $\mu m$ wire diameter and 200 $\mu m$ open area. There is a clear difference in the resolution we obtained in the two directions. In the shock propagation direction, we have estimated a

$\sim 20\ \mu m$ resolution, while in the vertical direction, where the electrons can reflux on a larger surface, it is worse than 70 $\mu m$. However, the measured resolution is quite larger than the expected value of 5 $\mu m$. This fact might be attributed to a small tilt in the flag alignment, which increases the effective transverse area.

## 4.5 Shock Velocity measurement and simulations

In order to determine the sample plasma parameters independently from the radiography density measurements, we have measured at the same time the shock velocity. Since Al and CH EOS are well known up to 20 Mbar, [16] the compressed foil state can be deduced from the measurement of one parameter only. Here we use the experimental velocities to determine the input parameters for hydrodynamic simulations, from which we can deduce the plasma state. This approach allows to cross check the compression results obtained from the radiography diagnostic.

For a first estimation of the shock velocity, we can consider fig.4.10. There, as we will discuss later, we show two shock compressed Al radiographs taken at different times. Knowing the length of the slivers and the time delay between the two images, it is possible to have an estimation of the mean shock velocity. The distance the shock travelled through aluminum in fig.4.10(a) is $\sim$85 $\mu m$, while it is increased to $\sim$135 $\mu m$ in the case of fig.4.10(b). Since the time delay between the two shots was 3 ns, we can deduce a mean velocity of $\sim$16.7 $km/s$ in the Al sliver.
Sesame EOS gives a corresponding pressure of $\sim$ 4 Mbar and a compression of $\sim$ 2.

A time resolved self emission diagnostic was also set up for a more precise shock velocity measurement. The principle of the diagnostic was already mentioned in 3.1. The target shock compression is associated to a temperature increase which induces thermal radiation emission. The visible part of this emission is collected by an optical system and focused onto a streak camera slit. From the measurement of the time evolution of the self emission, it is possible to determine the shock transit time in the target. The mean shock velocity can then be easily calculated knowing the target thickness.
In our case, the opaque aluminum sliver prevented the collection of the visible emission before the shock breaks out from the target. Moreover, the shock break out in the vacuum was never clearly observable, due to the important length of the sliver: the shock was not steady and its strength decreased in time. We have hence followed a different approach.
We have considered various shots on simple pusher targets (CH/Al/CH) and on complete targets, where quartz slivers were glued on the pusher. In these cases, we could collect the emission from the last plastic layer of the pusher, either directly in the case

of simple pusher targets, or through the transparent quartz sliver. In fig.4.8 we show an example of the image recorded by the streak camera. Here the signal corresponds to the self emission through the rear side of a quartz sliver. Both the quartz and the plastic

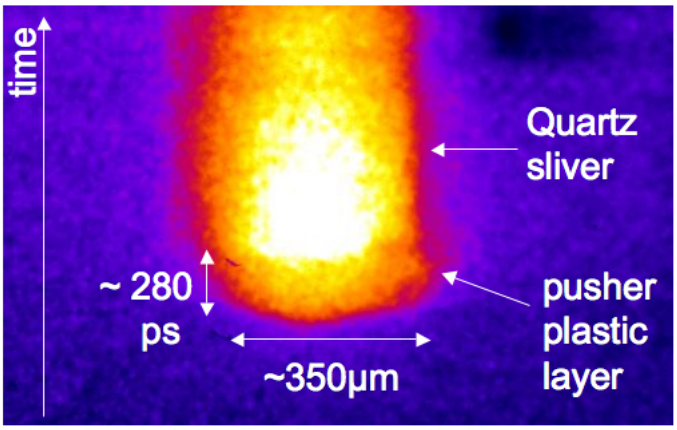


**Figure 4.8:** *Streak image of the temporal resolved optical self emission from the rear side of a pusher-Quartz sliver target.*

are transparent to the visible light and the emission from the plastic before and from the quartz later are clearly observable. The emission in the quartz is stronger than in plastic as a direct consequence of the impedance mismatch of the two materials. Time goes from bottom to top and the transit time in plastic is $\sim$ 280 ps, giving a mean shock velocity of $\sim$ 36 km/s in the last 10 $\mu m$ plastic.

These measurements were then used as input data in 2D simulations. Since it is difficult to well characterize the actual laser energy incident on the target, we have performed several simulations varying the laser intensity in order to match the velocities experimentally measured in the CH layer. The obtained intensities lie in the range of 5-8$\cdot 10^{13}$ $W/cm^2$, depending on the laser energy. Using this method, we can achieve a good confidence on the parameters to use in the simulation. We can then deduce the Al plasma state at the probe time.

In fig.4.9 we show the compression profile obtained from a 2D simulation run with an intensity of $5 \cdot 10^{13} W/cm^2$. The spatial shape was supposed gaussian with an initial 300 $\mu m$ FWHM, as given by our RPP characteristics. This figure represents the density profile 8 ns after the maximum laser intensity. The predicted compression is $\sim$ 2 and it will be compared to the results obtained with the x-ray radiography technique.
One last remark concerns the density sensitivity with the laser intensity used in the simulations. By varying the intensity parameter in the range of values deduced from the velocity measurements, we obtain a variation in density of 5%

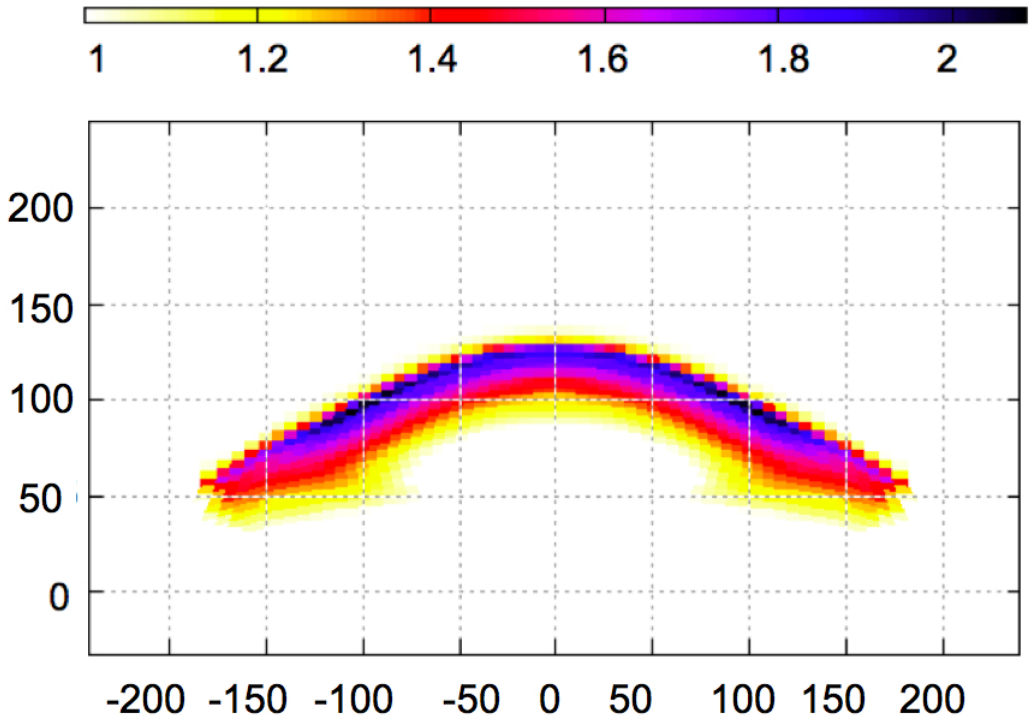


**Figure 4.9:** *Density profile obtained from a 2D simulation run with* $5 \cdot 10^{13} W/cm^2$.

## 4.6 Experimental Data and Results

In fig.4.10 we show two examples of the shocked compressed aluminum radiographs we have obtained during the experiment. For these snapshots, the time delay between the

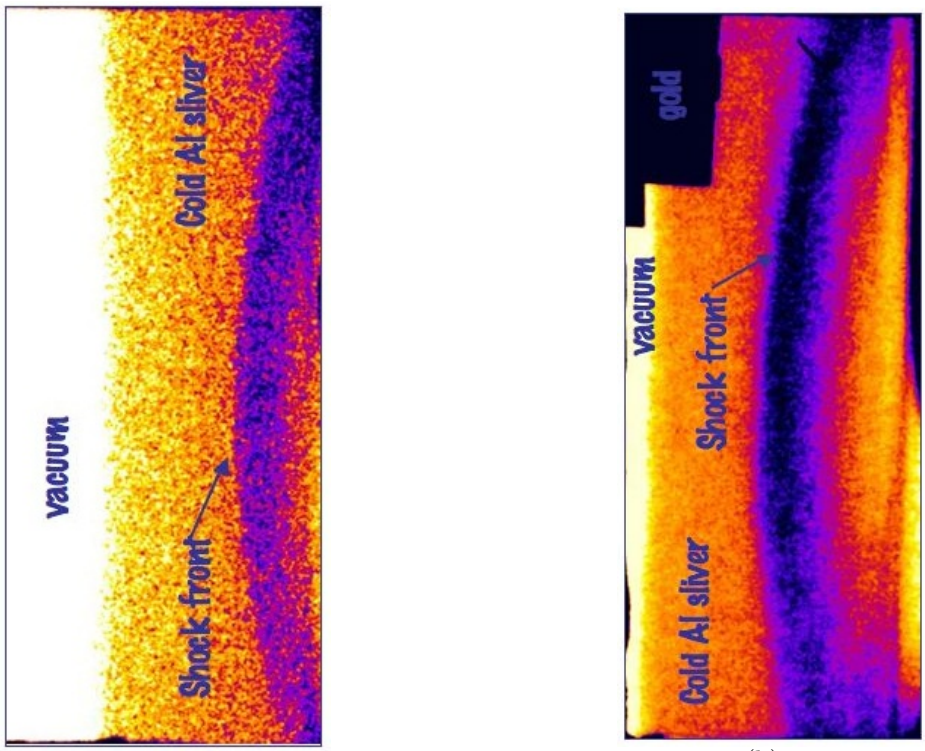


(a) (b)

**Figure 4.10:** *X ray radiograph of a shock propagating into an Al sliver. The time delay between the short pulse and the drive beams was 5 ns 4.10(a) and 8 ns 4.10(b).*

short pulse and the driver beams was 5 ns (4.10a) and 8 ns (4.10b). The 100% x-ray transmission is given from the x-rays passing through the vacuum only, next to the sliver edge. The cold and shocked part of the target are clearly distinguishable from the different transmissions, the compressed part appearing darker as more absorbing. The absorption profile taken along the shock propagation axis is shown in fig.4.11(a) together with a density profile given by hydrodynamic simulations. We first observe a qualitative agreement between the two profiles.

The shapes are typical of a decaying shock, most likely resulting from the end of the laser pulse. In this case, the source of pressure comes to an end and a relaxation wave propagates in the target, overtaking the shock. The density behind the shock (and the associated absorption) are therefore lowered (fig.4.11). However, we must remark that relaxation waves are also generated at the Al/CH interface in the pusher; being reflected at the other interfaces, they can travel in the Al sliver and reach the shock

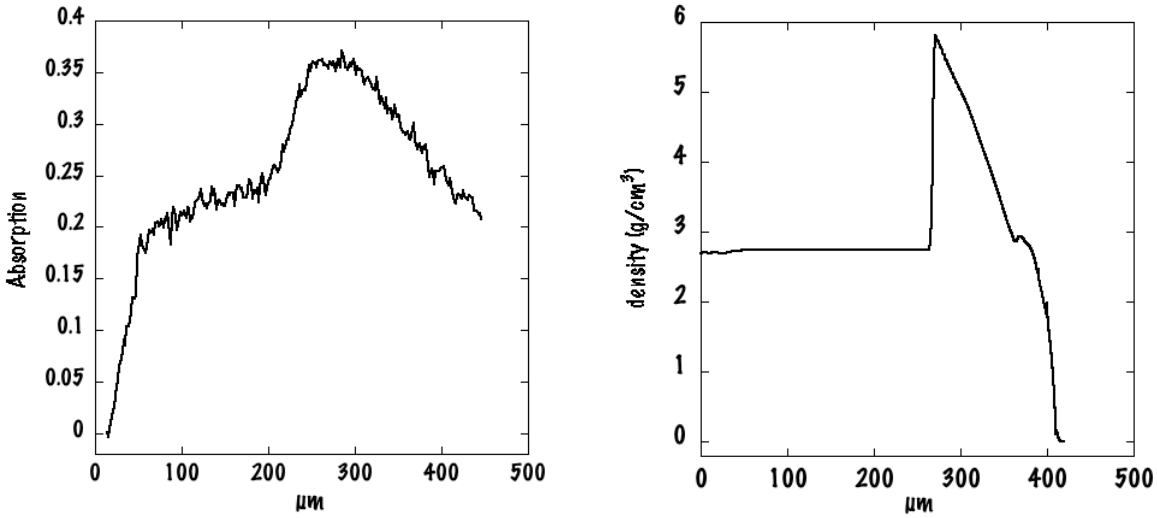


(a) (b)

**Figure 4.11:** *The experimental absorption profile taken along the shock propagation axis (a) and density profile extracted from hydrodynamic simulations (b).*

front.

The experimental profile in fig.4.11(a) also contains quantitative information on the absorption/transmission values of the cold and shocked parts of the target. In particular, the transmission recorded from the cold sliver is an useful information to get acquaintance with the incident x-ray spectrum. Indeed, a good knowledge of the source spectrum is extremely important for a proper evaluation of the absorption values and hence of the inferred density.

We can write the signal recorded on the imaging plate as:

$$Tr = \frac{\int_{\nu_{min}}^{\nu_{max}} I_0(\nu) e^{-\mu(\nu)\rho z} \mathcal{F}(\nu) R(\nu) d\nu'}{\int_{\nu_{min}}^{\nu_{max}} I_0(\nu) d\nu} \tag{4.1}$$

where $I_0(\nu)$ is the radiation spectrum, $\rho$ is the density of the material and z the target thickness, while $\mu(\nu)$ is the mass attenuation coefficient. $\mathcal{F}(\nu)$ corresponds to the filter transmission and $R(\nu)$ to the image plate response.

If we consider the cold material, the $\rho z$ value is well characterized and the most uncertain parameter in eq.4.1 is typically $I_0(\nu)$. Therefore, the experimental transmitted value Tr can be used to determine $I_0(\nu)$ with greater accuracy. This information will then be used in the case of the shocked sample in order to obtain the correct $\rho z$ value and hence the density.

We will now follow this procedure, characterizing each term in eq.4.1.

### 4.6.1 Filter transmission

A 50 $\mu m$ thick Mo foil was placed in front of the imaging-plates, which were also wrapped in 10 $\mu m$ Al. The global transmission is reported in fig.4.12.

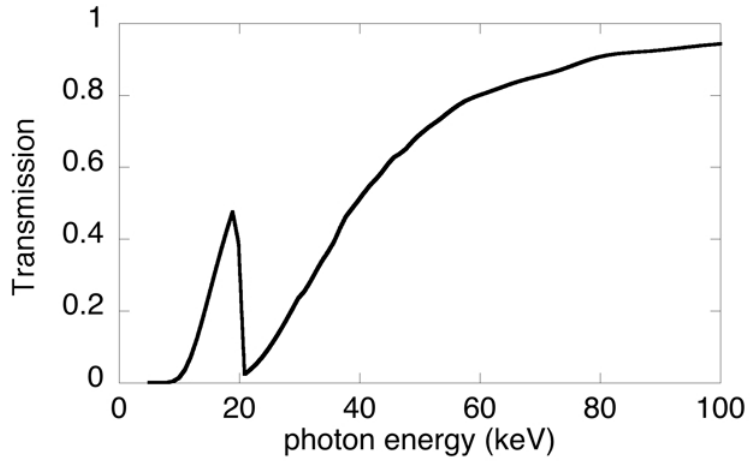


**Figure 4.12:** *Global transmission of the filter in front of the Imaging Plates. The Mo K-edge is responsible for the sharp decrease of transmission at 20KeV.*

The Mo foil acts as a K-edge filter. Its effect is to increase the role of the K$\alpha$ feature by lowering the high energy transmissions near the edge.

### 4.6.2 The image plates response

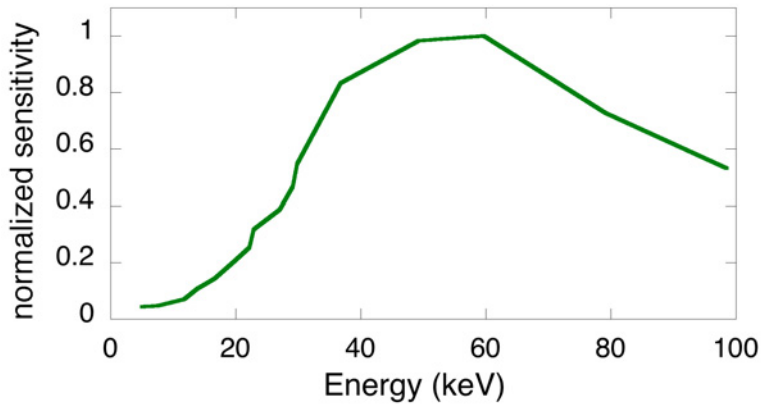


**Figure 4.13:** *Relative sensitivity of the imaging plate as a function of the incident photon energy.*

Another important aspect to be considered is the imaging plate response as a function of the incident x-ray energy. The relation between sensitivity and x-ray energy in the range of our experiment was investigated in [7]. The extrapolated values for the relative sensitivity are shown in fig.4.13.

### 4.6.3 The incident radiation spectrum

From fig.4.11(b), we deduce an absorption of 20-25 % (or equivalently a transmission of 75-80%) in the cold aluminum sliver.
If the Mo K$\alpha$ at 17.5 keV was the only component incident on the 394 $\mu m$ thick Al, we would expect a lower transmission of 61%. The same behavior is also observed for the transmissions values given by two other filters glued on the imaging plates as witnesses: 43 % for a 50 $\mu m$ thick Cu foil and 1.3% transmission for a 500 $\mu m$ thick Au. Again, these values are much higher than what expected from a monochromatic 17.5 keV spectrum, 11.7% and 0% for Cu and Au respectively. The higher transmission experimentally observed indicates the existence of a higher-energy photon component superimposed to the K$\alpha$ feature, which lowers the contrast between vacuum/shocked/unshocked regions.

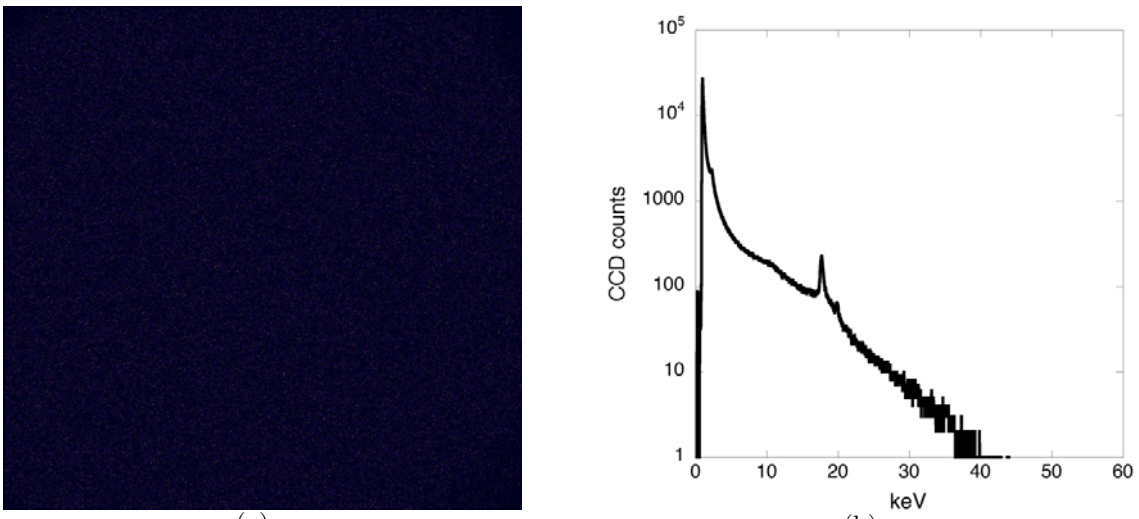


(a) (b)

**Figure 4.14:** *Single photon counting CCD image 4.14(a) and respective histogram 4.14(b).*

A first estimation of the spectrum generated in the Mo flag-laser interaction was obtained using a CCD camera operating in the single photon counting mode, which was implemented in the set up (par.4.2.2). The CCD camera was installed outside the chamber, about one and a half meter from the backlighter source. A 10 cm lead wall was used to shield the camera from x-rays scattered noise. A typical CCD image and

the related histogram are presented in fig.4.14. The Mo K$\alpha$ feature is clearly distinguishable at 17.5 keV, being more intense than the background. The Mo $K\beta$ is also visible at 19.6 keV. The histogram obtained, however, is not exactly representative of the incident spectrum. The reason lies in a loss of sensitivity of the CCD camera at high energies. Indeed, if the photon is too energetic, its energy may not be released in a single pixel, but might be spread into several neighbour pixels, causing low intensity pixel registration. In this case, in the final histogram, (which is, we underline, the histogram of the intensities on single pixels) a high energy photon would be counted as several low energy ones. To account for this effect, one should calibrate the single photon counting efficiency for the entire spectrum. Absolute calibration could be done using several radioactive sources. In [2], for example, Fe55 and Cd109 radioactive sources were used to calibrate the CCD camera at 5.9 keV and 22.1 keV respectively. Two values are, nevertheless, not sufficient to get a good extrapolation for the efficiency at higher energies and a different approach must be followed.
Nonetheless, we must underline that the use of this diagnostic was very useful to monitor the presence of the K$\alpha$ emission on a shot to shot basis, allowing to verify and optimize the flag alignment procedure.

In order to evaluate more precisely the source spectrum, we have performed Monte-Carlo simulations with the CALDER-MC [3]. The code gives the Bremsstrahlung and K$\alpha$ emission. The simulated radiation spectrum must indeed reproduce the transmission

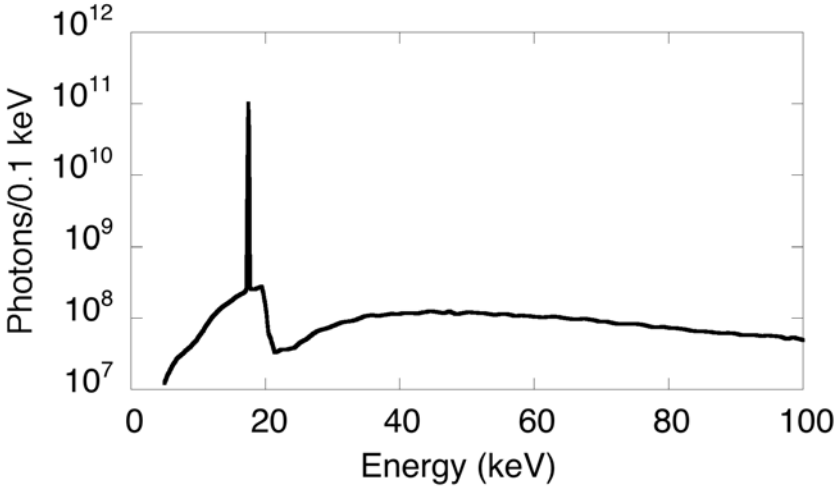


**Figure 4.15:** *X-ray spectrum calculated from Monte-Carlo simulations for an electron temperature of 100 keV.*

data experimentally observed from the three known filters, the 50 $\mu m$ Cu foil, 500 $\mu m$ Au foil and the 394 $\mu m$ cold Al sliver. The hot electron temperature $T_{hot}$ is the most

important parameter governing the emitted spectra. For laser intensities in the range of $10^{17} - 10^{19} W/cm^2$, it can be estimated by Beg's law [13]:

$$T_{hot}(keV) = 100(I/10^{17} W cm^{-2})^{1/3}$$

This law was obtained from experimental results and accounts for acceleration mechanisms other than the ponderomotive force. For typical intensities of $\sim 0.5 - 5 \cdot 10^{19} W/cm^2$, Beg's law predicts an electron temperature of 450 keV. However, in all our shots, the intensity was deliberately lowered by defocusing the parabola in order to decrease the Bremsstrahlung contribution. Moreover, in the flag geometry, the laser incidence was $\sim 75°$ with respect to the target normal. Typical intensities of $\sim 10^{18}$ $W/cm^2$ are then expected on the target, leading to $\sim 100 - 200$ keV electron temperature.
For a 100 keV electron temperature, the x-ray spectrum calculated from the Monte-Carlo code is shown is fig.4.15. We must remark that in our configuration, where the radiation is collected at 90° with respect to the flag thickness, the emission calculations (and the K$\alpha$ line in particular) show a strong dependence on the angle. As shown from the resolution results, the flag alignment presented some issues, which thus induce a uncertainty in the calculated spectra. The simulation results were hence slightly adjusted in order to well match the transmission values experimentally observed from the three known features: 75% for the cold Al sliver, 43% and 1.3% for the Cu and Au foils respectively.

### 4.6.4 Compression results

Having determined the incident radiation spectrum involved in the shock radiograph, we can proceed in the calculation of the target compression. We will consider image 4.10(b) which presents a good contrast, allowing a detailed analysis.
When dealing with a broad spectrum, the inversion procedure, involved in the density calculation from the transmission, is more delicate than the straightforward monochromatic case. If the spectrum is too wide, the problem arises from the fact that different attenuation coefficients cannot be easily combined into a single exponent. Thus, given a measured x-ray transmission, there is no direct way of extracting the optical depth like one can do with a monoenergetic spectrum, where it is simply given by the logarithm $\overline{\rho z} = -\frac{1}{\mu} ln\left(\frac{I}{I_0}\right)$.
To account for the broad spectrum, the mean areal density was found from numerical solutions of eq.4.1. Stated in a different way, we looked for the mean areal density $\rho z$ necessary to reproduce a given transmission value using the radiation spectrum given by the Monte-Carlo simulations. The mean areal density $\rho z$ was calculated as a function of the transmission, as shown in fig.4.16, where we show the curve $\rho z(Tr)$ obtained for

the spectrum we have found giving the correct transmission values for the cold sliver Al and Cu and Au filters. In these calculations the cold values for the mass attenuation

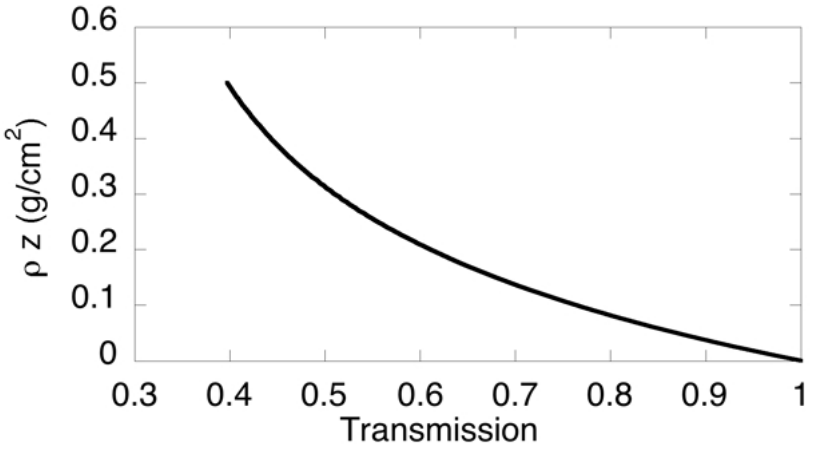


**Figure 4.16:** *Mean areal density values as a function of the transmission.*

coefficients were used. The reason of this approximation can be justified as follows. From hydrodynamic simulations we expect typical compression of $\sim 2$ and temperatures of few eV, ($< 3$ eV). For these plasma parameters, the Al ionization is $Z^* \sim 3$ and the 1s, 2s and 2p orbitals are the only ones to be bound and completely occupied. This structure is similar to the case of solid aluminum. The density effects begin to have weak influences on the 2s and 2p orbitals only. As the absorption is mainly due to photo-ionisation of the 1s orbital, it can be considered the same as in the cold solid sate [14].
The $\rho z(Tr)$ curve allows then to calculate the local optical depth associated to the transmission recorded on each pixel of the experimental image. These values were then inserted in eq.3.15 and the Abel inversion could be done on the quantity:

$$F(y) = \rho z/\rho_0 - L$$

To perform the Abel inversion, a simple routine was written. Since the inversion algorithm is highly sensitive to noise, we have followed an analytical approach. The profile of F(y) was taken along a direction perpendicular to the symmetry axis (fig.4.17) and fitted with an even function. The Abel inversion was then performed on the fitting function. In this way, we could reconstruct the compression along the whole shock front. For typical conditions (profile a in fig.4.17) a fourth order supergaussian function well matched the data as illustrated in fig.4.18a, where we show the experimental F(y) profile and its fit. In the same figure we show the compression profile obtained from Abel inversion (fig.4.18b). We can observe that the density is strongly peaked at the shock

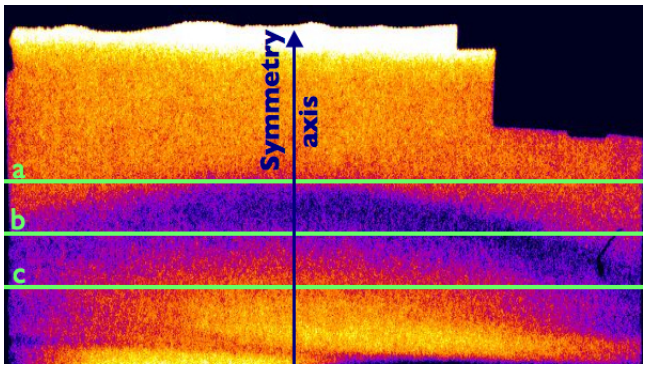


**Figure 4.17:** *Various profiles are taken at different positions along the axis perpendicular to the symmetry axis.*

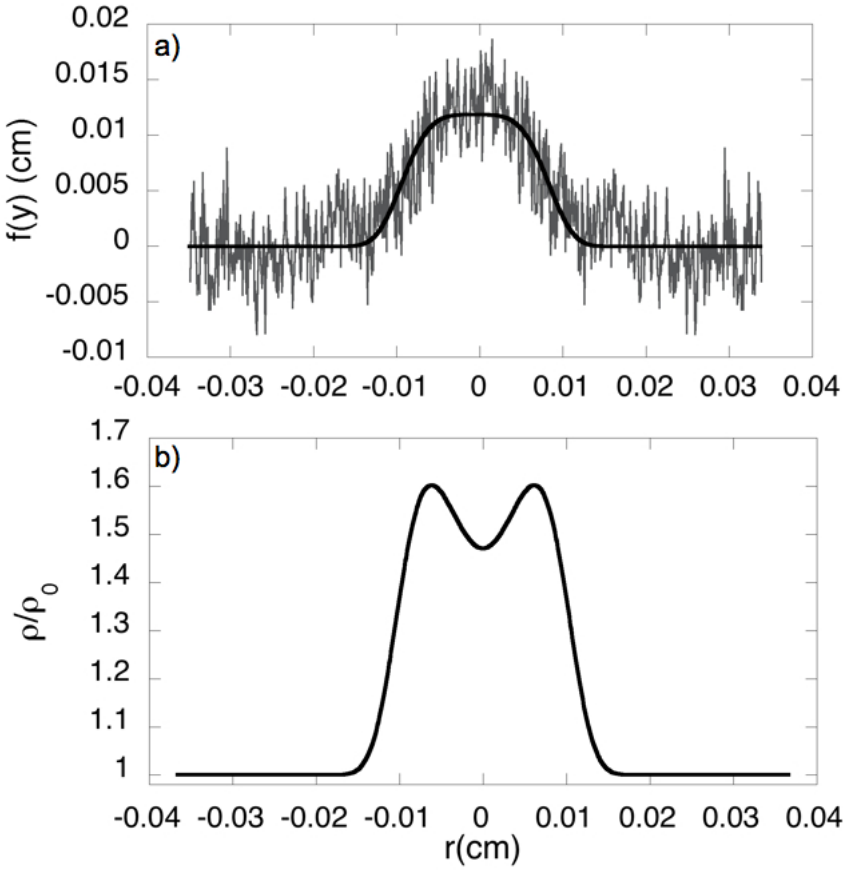


**Figure 4.18:** *F(y) profile with supergaussian fit a) and corresponding density profile from Abel inversion b).*

front and rapidly decreases towards the symmetry axis.

A profile different from the one obtained in fig.4.18a is found in portions of the image where the shock front is far away from the symmetry axis, (b or c in fig.4.17).

In this case, the data can be represented by a function of the form:

$$F(y) = \frac{a + by^2}{1 + exp(y - c)/d} \tag{4.2}$$

which reproduces the drop in the absorption observed when going towards the symmetry axis. The higher transmission is here associated to a density decrease caused by the relaxation wave most probably due to the laser shutdown. The compression value calculated with this function (fig.4.19a) are shown in fig.4.19b.

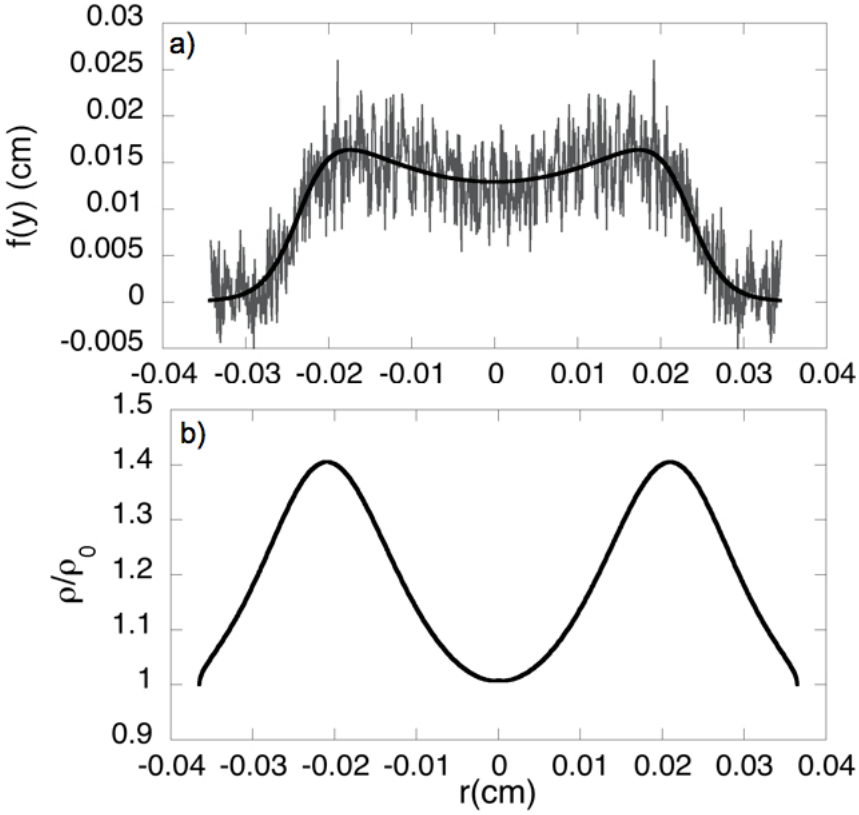


**Figure 4.19:** *a) F(y) profile taken in the lower part of the image 4.10(b) with the fitting function represented by eq.4.2; b) corresponding density profile from Abel inversion.*

The density profile along the whole shock was finally reconstructed considering severals profiles at different positions on the shock propagation axis (fig.4.17). The result is

shown in fig.4.20. Here a single profile corresponds to the density along the radiographic direction at a fixed point on the shock propagation axis, while the different profiles are associated to different positions on it.

On each profile, the peak density corresponds to the shock front. Therefore, consider-

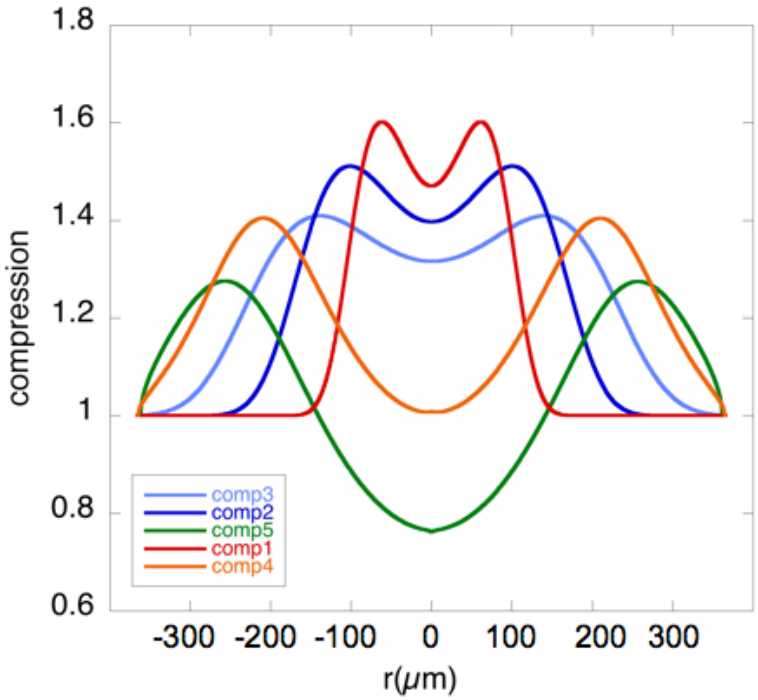


**Figure 4.20:** *Compression values obtained from different profiles along the shock front.*

ing the envelope of the peaks from all the curves, we can reconstruct the density along the whole shock front. We find a maximum compression of ∼1.6. In addition we note that a gaussian function fits the peaks distribution(fig.4.21). Indeed, this is the typical shape of a shock smoothed with RPP (section 4.1).

## 4.7 The error bars

Since in this experiment K$\alpha$ hard x-ray radiography of a shock compressed target was performed for the first time, some issues have been pointed out in the data analysis.

A first concern regards the incident spectrum, which, as already discussed, is not monochromatic as expected, but includes a continuum background affecting the transmission. In particular, given a transmission value, the contribution from a high energy component implies a higher compression.

We can therefore use the uncertainty on the experimental transmissions from cold Al and Cu to estimate the errors on the spectrum and thus on the inferred density. When considering the image in fig.4.10(b), a further difficulty is due to the limited region associated to the vacuum, which leaves an incertitude on the 100% transmission value. With the information available, we can deduce a ∼5% error on the transmissions of the three witness foils. Consequently, this induces an error on the incident radiation spectrum and on the corresponding $\rho z$(Tr) curves, which lead o different density values. Following this procedure, we find a total error of ±10% on the compression results, as shown in fig.4.21.

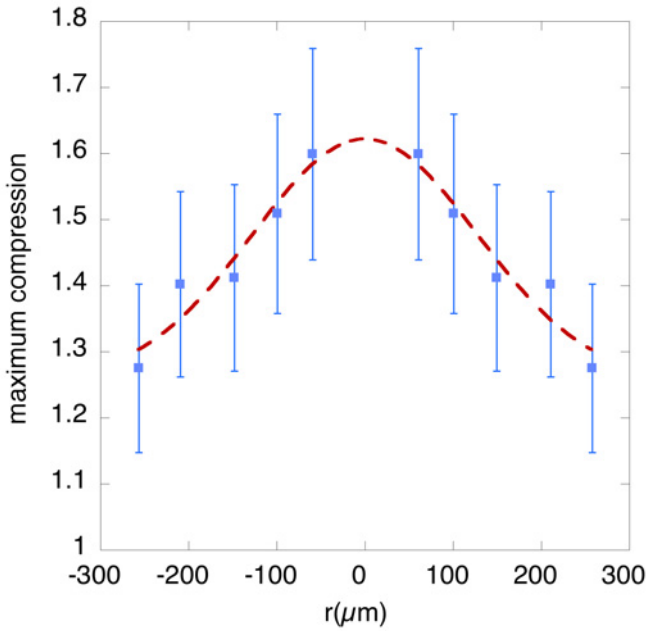


**Figure 4.21:** *Maximum compression for each profile of fig.4.20. The envelop of all the values gives the maximal compression along the shock front.*

The spatial calibration $cm/px$, also affects the results deduced from Abel inversion. In our case, this error is included in the higher uncertainty induced by the spectrum.

A further concern, that we have not considered in our treatment, is related to the source size. The intensity pattern at the detector is the convolution of the target transmission function and the source size. Therefore, the effect of a large source is to soften the density gradients at the shock front. This results in a lower estimation of the density. From the resolution results, we obtained a larger source extent than expected, $\sim 20\ \mu m$ in the shock propagation direction. Moreover, in the vertical direction, which is the one important for the Abel inversion, the source size is even larger. It was estimated

[15] that for a source size $\gtrsim 20\ \mu m$ the resulting compression can be underestimated by $\sim 20\%$.

### 4.7.1 Simulation vs experimental results

In section 4.5, we have discussed the velocity measurements and how they were used to infer the correct parameters for the hydrodynamic simulations. We can now compare the results given by these simulations with the compression values obtained from the radiograph analysis (fig.4.20).
In order to facilitate the comparison, we consider the simulated compression of fig.4.9 and we take lineouts along the radial direction r for different positions on the shock propagation axis z. In this way we obtain the simulated profile (fig.4.22) analogous to the experimental figure of 4.20.
We can first notice the qualitative agreement between the two data sets.

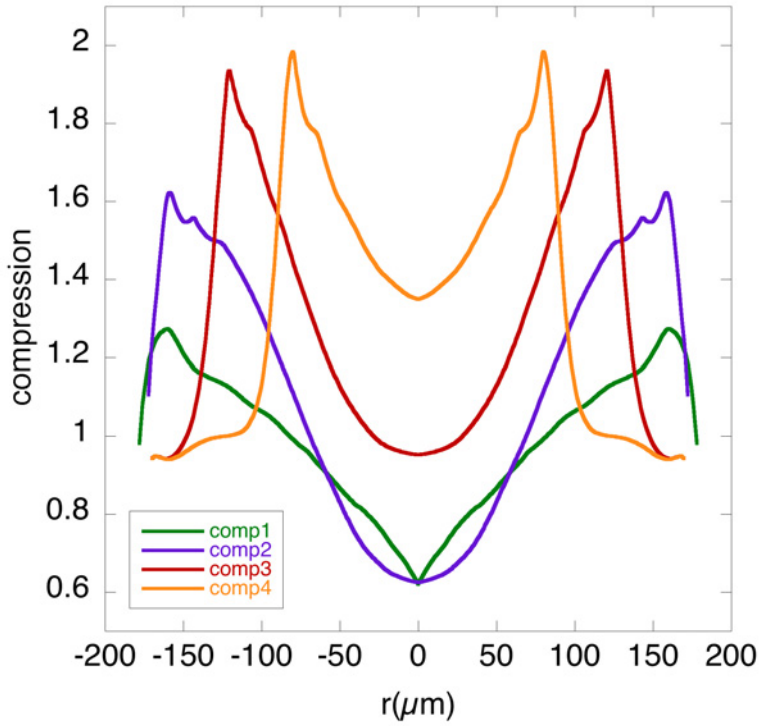


**Figure 4.22:** *Simulated compression profiles from fig.4.9. Each profile is taken along the radial direction r, while the different curves correspond to different positions on the shock propagation axis.*

As already observed in our experimental results, the simulated radial compression profiles show a peaked density at the shock front, rapidly decreasing towards the symmetry axis. Moreover, considering the peak density at different z positions, we can reconstruct the shock spatial profile. The same procedure on the experimental data evidenced a

gaussian shock (fig.4.21), consistent with the spatial imprint of the RPP. The simulations confirm this behavior, the peak density for the profiles far away from the symmetry axis being much lower.
We must, though, remark that the simulations predict a much higher compression, $\sim 2$, not fully consistent with our $\frac{\rho}{\rho_0} \sim 1.6$ result. The compression values we have found are $\sim$25% lower than the simulated ones. This disagreement is most probably associated to the effects of the source size, that we have not considered in the inversion process. As we have previously mentioned, the density measurements can be underestimated up to 20% neglecting a $\sim 20\ \mu m$ source. In our case, the vertical source size is even larger, leading to more important errors, in fair consistence with the observed discrepancy. This hypothesis is supported by the fact that the profiles showing a 2 fold compression are extremely narrow, the peak density dropping quickly within 10 $\mu m$ behind the shock front.

This discussion has evidenced the importance of a small x-ray source sizes for precise density measurements. In particular, 2D high resolutions, $\lesssim$10 $\mu m$, are necessary to well describe the density at the shock front.

## 4.8 Conclusions

For the first time, we have demonstrated the possibility to perform dense plasma density measurements using hard x-ray radiography. Energetic x-rays from K$\alpha$ radiation have been successfully used to probe high Z compressed materials. In addition, we have employed a new scheme, exploiting the target geometry to reach high 1D spatial resolution. The obtained results are promising and encourage the development of new 2D schemes to reach high resolution in two dimensions. This task will require new efforts in order to optimize the backlighter geometry, testing different configurations (embedded wires, small deposited dots, etc...)

The presented method we have used to directly extract the density from a single image, has also allowed to identify the major improvements for future experiments:

- Firstly, the evidenced importance of a highly monochromatic spectrum will imply specific experimental works for the K$\alpha$ emission optimization. A wide range spectroscopy diagnostic will also be necessary to monitor the continuum Bremsstrahlung radiation, which strongly affects the recorded transmission values. If single photon counting CCD cameras are used, an absolute calibration of the single photon efficiency for a wide range of energies is required. This diagnostic can be supported by using (gold) stepped foils of different thickness. Following an approach similar to the one we have here adopted, the transmission values associated to all the steps would impose several constraints on the incident radiation, allowing its correct determination. High-

energy x-ray spectrometers (HENEX) [17] can also be employed to have a more precise knowledge of the radiation spectrum for energies $> 60$ keV [18].

- Secondly, great efforts must be devoted to reduce the source size. This is of primary importance, as a large source highly compromises a precise density measurement. Its effect softens the gradients at the detector and leads to an underestimation of the compression values. A diagnostic for the emitting region imaging could be useful to monitor the source spatial extent at each shot.

- Finally, from the numerical point of view, more complex inversion algorithms, based on [19]-[20] for example, can be used. This would allow to take benefit of all the experimental image details and to reduce the role of the noise in the inversion process. The inversion can then directly be performed on the image, also removing the dependence on the fit precision.

In conclusion, the procedure we have followed has demonstrated the validity of this novel diagnostic. By overcoming the discussed issues, this technique will allow higher precision in the density measurements and will become an extremely powerful diagnostic tool for high Z dense plasmas.

# Bibliography


[1] Ch. Reich, I. Uschmann, F. Ewald, *et al.*, Phys. Rev. E, **68**,056408 (2003)

[2] H-S. Park, D.M.Chambers, H-K.Chung,*et al.*, Phys. Plasmas **13**, 056309 (2006)

[3] E. Lefebvre *et al.*, Nucl. Fusion **43**, 629 (2003)

[4] A.L. Gonzaleza, H. Li, M. Mitch, N. Tolk and D.M. Duggana, Applied Radiation and Isotopes **57** 875?882 (2002)

[5] K.A. Tanaka, T.Yabuuchi, T.Sato *et al.* Rev. Sci. Instr. **76**, 013507 (2005)

[6] M. Ito and Y. Amemiya, Nuclear Instr. Methods A, **310**, 369-372 (1991)

[7] H. Ohuchi, T. Satoh, Y. Eguchi and K. Mori, Radiation Protection Dosimetry, **117**, 4, pp. 432-439 (2005)

[8] F.N.Beg,*et al.*, Phys. Plasmas **4**, 447 (1997)

[9] K.Yasuike, *et al.*, Rev. Sci. Instrum. **72**, 1236 (2001)

[10] F.Ewald, H. Schwoerer, R.Sauerbrey, Europhys. Lett. **60**, 710 (2002)

[11] H.-S Park, N.Izumi,M.H.Key,*et al.*, Rev. Sci. Instrum. **75**, 10 (2004)

[12] http://www-cxro.lbl.gov/

[13] F. N. Beg, A. R. Bell, A. E. Dangor, *et al.*, Phys. Plasmas, **4**, 447 (1997).

[14] C. Blancard, private communication

[15] D.Hicks, private comunication.

[16] K. S. Holian, LANL Report No. LA-10160-MS UC-34, (1984)

[17] L. T. Hudson, A. Henins, R. D. Deslattes, *et al.*, Rev. Sci. Instr. **73**, 6 (2270)

[18] J.F. Seely, C.A. Back, C. Constantin, *et al.*, J. Quant. Spetrosc. Radiat. Transf. **99** 572?583 (2006)

[19] M. Kalal and K. A. Nugent, Appl. Optics **27**, 10 (1988)

[20] T. J. Asaki, R. Chartrand, K. R. Vixie and B. Wohlberg, Inverse Problems, **21**, 6, pp. 1895-1903 (2005)

# Chapter 5

# Proton radiography

In this chapter we will present the proton radiography results we have obtained during the experimental campaign performed on the VULCAN laser at the Rutherford Laboratory. A previous experiment, carried on at LULI in 2003 [1], has shown the major role played by small angle scattering in this technique. In that experiment the proton energies were not sufficiently high to overcome scattering blurring effects and the shock front could not be resolved. We will here discuss the approach we have followed to overcome this difficulty in our experiment, mainly by choosing adequate target characteristics. A description of the Monte-Carlo code developed to simulate the proton propagation and of the procedure adopted in the data interpretation will follow. The simulations results will be compared to the experimental data. Finally we will discuss the sensitivity of this technique as a density diagnostic.

## 5.1 The experimental set-up and backlighter target

The experiment was performed during the same x-ray radiography experimental campaign (chapter4). The set up was therefore the same one as described in the previous chapter, section 4.1, and is presented here in fig.5.1. The main differences concerned the backlighter foil, the sample material and the detector used.

Multi MeV protons were generated in the interaction of the CPA beam with a 12.5 $\mu m$ thick gold foil. The material foil as well as its thickness were chosen as a best compromise between spatial beam uniformity, proton and energy yield. On one hand, an uniform proton beam is necessary for the radiography technique and in particular, as we will see later, in its employment as density diagnostic. On the other hand, energetic protons are necessary to minimize the scattering blurring effects. Plastic targets usually produce a more intense signal with respect to metallic foils, but the induced spatial profile presents a significant non-uniformity across the beam. Similarly, maxi-

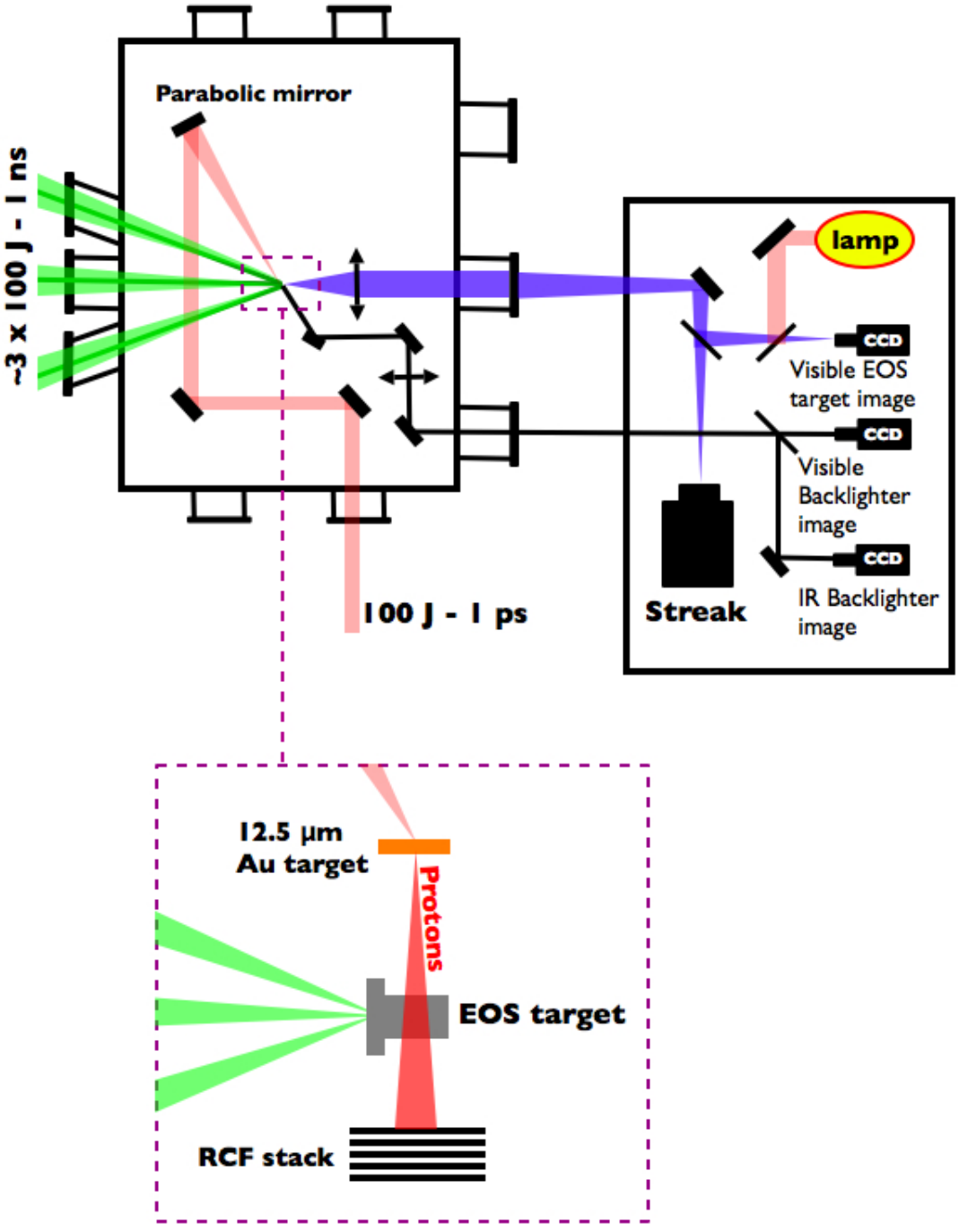


**Figure 5.1:** *Schematic representation of the experimental set up.*

mum proton energy and overall proton yield is increased when irradiating thinner foils, but the beam uniformity gets worse.

## 5.2 The target design

The choice of the sample material was done in order to overcome scattering blurring effects. The importance of small angle scattering depends on the proton energy and on the areal density of the material they propagate through. In order to have a good description of the shock front, a minimum resolution is necessary, typically 10 $\mu m$. A criteria to estimate the minimum distance that can be resolved at the target surface, is based on the evaluation of the scattering cones apertures. The principle is shown

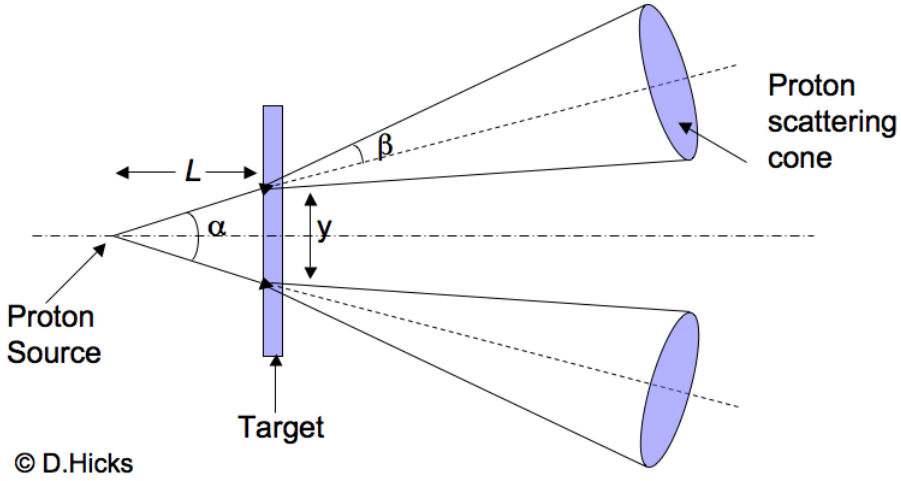


**Figure 5.2:** *To resolve the distance y at the target the scattering cones must not overlap.*

in fig.5.2, where the angle $\alpha$ is the divergence angle of the proton source; it depends on the distance between the target and the proton source (L) and on the protons energy. Assuming a maxwellian probability, we can consider the $1/e$ scattering angle, which represents a good estimation for the cone aperture $2\beta$ (63% of the particles are scattered within this angle). To resolve two distinguished features at a distance $y$ in the target plane, the scattering cones must not overlap. This imposes the condition $\alpha > 2\beta$, which, for small angles, translates into $y > 2\beta L$.
From Monte-Carlo codes simulating the proton propagation trough cold matter, we can estimate the $1/e$ scattering angle [6] and calculate the resolution limit for different materials and thicknesses. The results for 10 MeV protons are shown in fig.5.3, where we have considered a 3 mm proton source- target distance, as it was in our experiment. We can notice that the blurred images obtained in the previous LULI experiment are

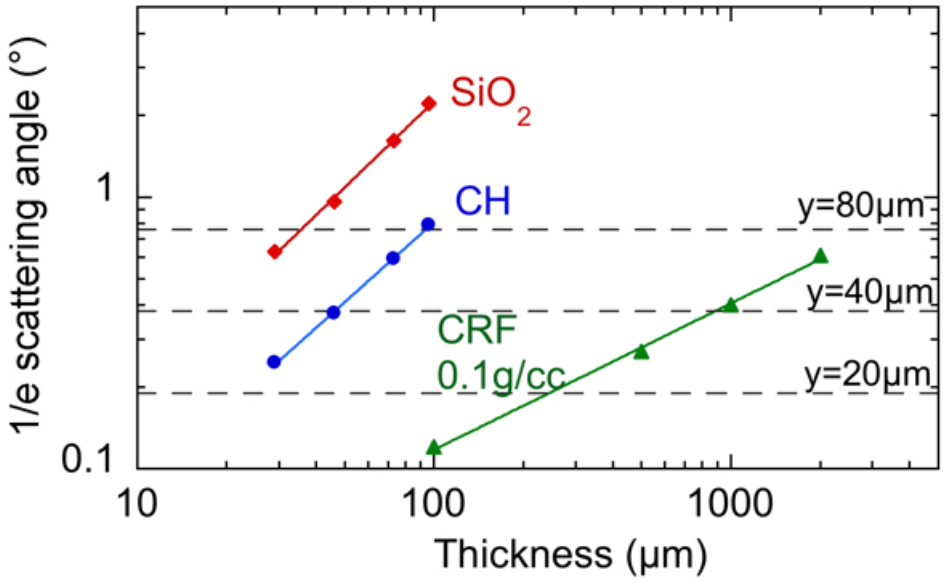


**Figure 5.3:** *1/e scattering angle as function of thickness for $SiO_2$ (red squares), plastic (blue dots) and 0.1g/cc carbon (CRF) foam (green triangles). The resolution limit of 20, 40, 80 $\mu m$ are also shown for a target-source distance $L = 3mm$*

consistent with a low resolution. In that experiment, protons with energies $\lesssim 10$ MeV were used to probe $\sim 150$ $\mu m$ thick quartz targets, giving a minimum spatial resolution $> 80$ $\mu m$. A much higher resolution can be achieved using lower density targets. For 0.1 g/cc carbon foams (CRF) we expected a $\sim$20 $\mu m$ resolution even with thick ($\sim 300$ $\mu m$) targets. This is the reason why we have chosen carbon foams as a test material in our experiment. Moreover, since proton energies exceeding 20 MeV were expected on VULCAN laser [3], CH and quartz targets were also considered. Nevertheless, due to the limitation of lasers performances, we could not obtain the expected proton energies and clear results were obtained only on low density carbon foams.
The main target structure was the same as for x-ray radiography, with the foam slivers glued on a CH/Al/CH pusher, as shown in fig.5.4

## 5.3 The detector: RCF

Multi-layer stacks of radiocromic films (RCF) were used to collect the proton beams, after their propagation through the shocked slivers. RCF are commonly employed in the detection of laser-produced protons thanks to their good spatial and spectral resolution and because they are of practical handling (no etching is required and they are not sensitive to the visible ambient light).

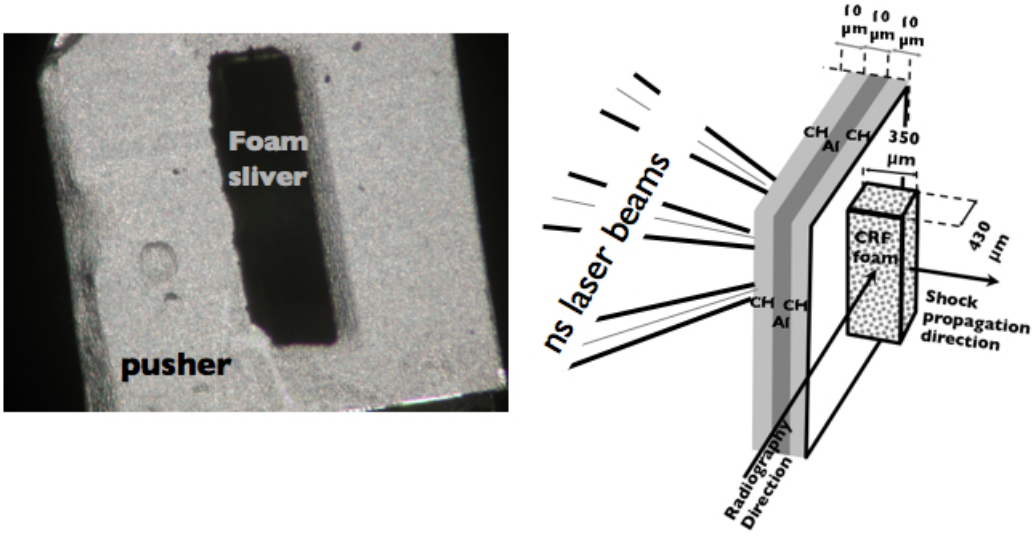


**Figure 5.4:** *Target used for the proton radiography. The pusher is the same as for the targets used for the X-ray radiography.*

High energy particles going through the RCF stack deposit their energy in the film. When exposed to ionising radiation, the RCF active layer, composed by crystalline diacetylene, undergoes to a solid state polymerisation reaction producing a dye polymer. The active crystals, which are transparent to visible light, change colour to cyan blue when the dye is produced. The amount of polymer produced, i.e. the depth of colour change and hence the optical density, is proportional to the absorbed radiation dose[1] or, equally, to the energy locally released by the incoming beam. Due to the sub-micro size of the crystals and to the fact that polymerisation does not spread between adjacent microcrystals, the RCF has an extremely high (sub $\mu m^2$) spatial resolution.
The multi-layer arrangement leads to a spectral capability of the detector. While the less energetic protons are stopped in the first layers of the stack, high energy protons can penetrate deeper, reaching the last films. As the energy is released mainly in correspondence to the Bragg peak at the end of the proton stopping curves, each layer acts as a filter for the following one and selects the protons whose Bragg peaks are localized within the active layer. Our RCF stack was composed by 6 films HD-810 type followed by MD-55 films, RCF labelled 1 being the first one the protons encounter during propagation. The whole stack was wrapped in a 13 $\mu m$ thick Aluminium foil, which acted as a shield for scattered laser light, debris of the target and heavy ions. The two types of film are characterized by different sensitivities. Their structures are shown in fig.5.5. MD 55 films have a double active layer which make them more sensitive and

[1]The dose is defined as the amount of energy given by ionizing particles to a unit mass of irradiated material at a place of interest. It is measured in Gray (Gy). 1 Gy= 1 J $kg^{-1}$

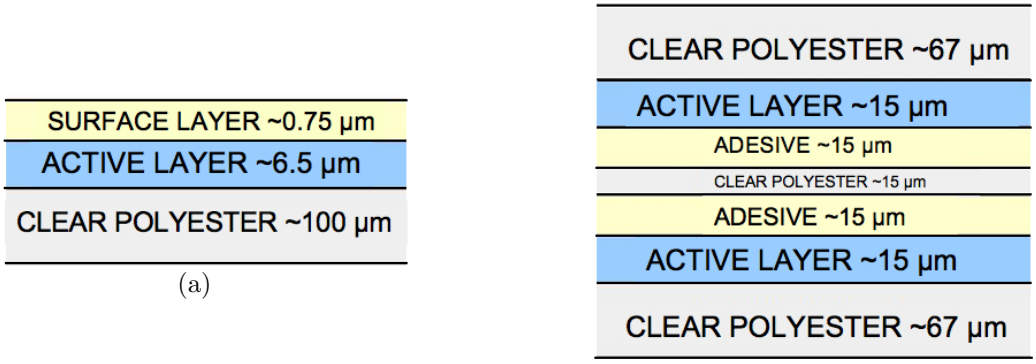


**Figure 5.5:** *Structure and composition of the RCF we used:5.5(a) HD-80 RCF and 5.5(b) MD-55 RCF*

are used to detect the higher energy protons, usually in a smaller number.
In order to infer the initial energy of the protons stopped in each layer, the energy deposition of the particle going through the detector was simulated by the Monte Carlo code TRIM [4]. TRIM calculates the final spatial and energy distribution of ions going through matter, taking into account energy losses, energy transfers to recoil atoms and other processes [5].

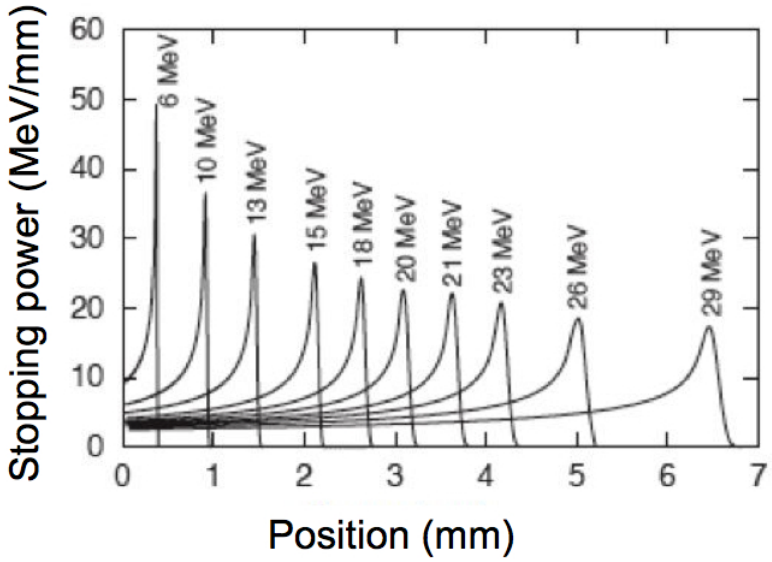


**Figure 5.6:** *Stopping power curves for protons of various energy propagating in Mylar evaluated using TRIM code.*

The active layer was modelled as a uniform block of polyester plastic with the same RCF density. Stopping curves in Mylar obtained with TRIM code for different proton energies are shown in 5.6. For higher proton energies, the Bragg peak is located deeper

in the detector and its value decreases. This is a consequence of the statistical spreading of the energy distribution, which is more important the longer the particle has travelled in the stopping medium. This is also the reason why the Bragg peak broadens significantly for high energies. The curves were interpolated in order to get a continuous stopping function $R(z, E)$ from which we were able to extract the stopping power for a proton at any depth $z$ in the detector and for any initial energy $E$. For any given active layer, the energy deposition as a function of the initial proton energy is obtained by integrating the stopping function over the spatial region spanned by the active layer. This is shown in fig.5.7 for all the RCFs in the stack. In the MD-55 the double layer

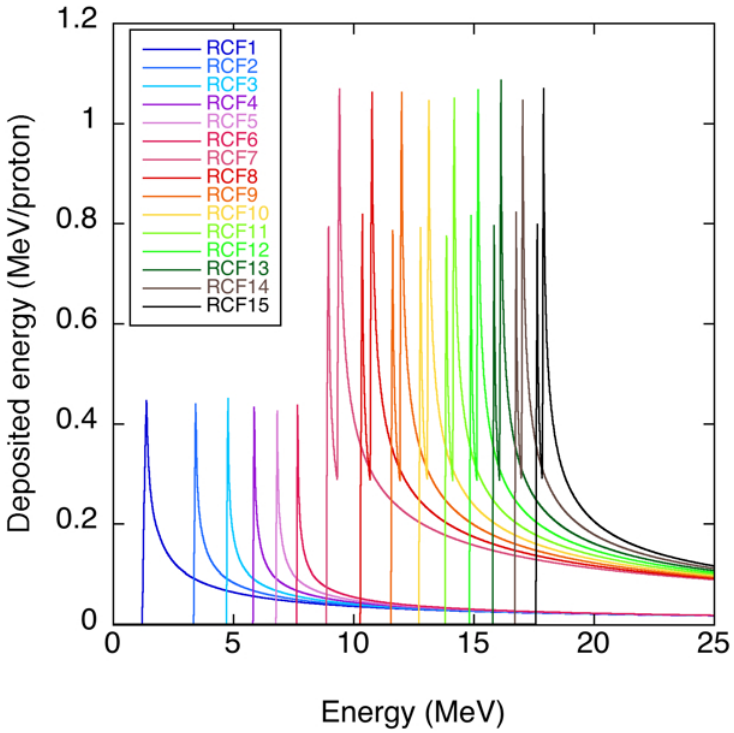


**Figure 5.7:** *Energy deposition in all radiocromic films in the detector stack. RCF labelled 1 is the first one the protons encounter. The first 6 films were HD-80, from the 7th being MD-55. The film structure shows a different sensitivity and response: the double peak, in particular, comes from the contributions of the two active layers in the MD-55.*

structure induces two peaks, whose contributions are summed up to give the entire film response. In our experiment, a clear signal was obtained up to the 12th-13th layer, corresponding to a maximum proton energy of $\sim$ 15-16 MeV.

In this calculation the evaluation of the energy distribution of protons is assumed to be uniform. In reality the contribution of each energy component must be rescaled according to the assumed spectral distribution. The typical spectrum of the laser produced protons is, indeed, a Boltzmann like function exp(-E/T ), where T represents the tem-

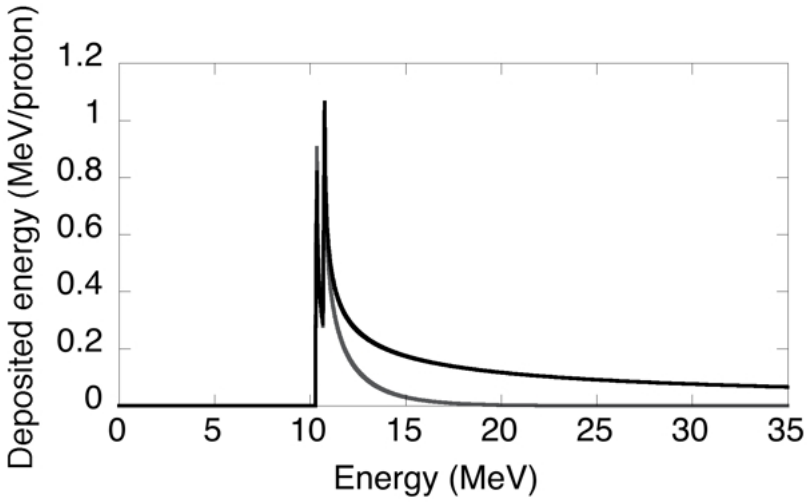


**Figure 5.8:** *Energy deposited in the 8th RCF layer without taking into account the proton spectral distribution (black line) and multiplied by an exponential spectrum of temperature 3 MeV (grey line).*

perature parameter of the beam. This parameter together with the maximum produced energy depends on the laser characteristics [18]. The temperature of proton beams produced on Vulcan laser is typically in the range 1.8 to 4.5 MeV [19]. These values are consistent with simple signal considerations on our whole RCF stalk: by considering the correspondence between the total signal and the proton energy associated to the same film, we can deduce a temperature of $\sim$ 3 MeV. When the RCF film response curve (fig.5.7) is multiplied by the proton spectral distribution, it is modified as shown in fig.5.8, which specifically refers to the 8th RCF layer. The film exhibits a narrow spectral response, nearly all the energy being deposited within the Bragg peak. The spectral resolution can be estimated to be equal to the width of this curve, typically of the order of 1-2 MeV.

## 5.4 Experimental results on CRF foams

In this section we will present a general overview of the data we have obtained, underlying the importance of the scattering in the proton radiography results. A more detailed analysis will follow in 5.7.

Fig.5.9 shows an example of a complete data set for a radiography taken 7ns after the shock main laser beams driving the shock. As a consequence of the energy resolution, a single data set comprehending a whole RCF stack has also a temporal multi-frame capability. This is due to the different times of flight from the source to the target for

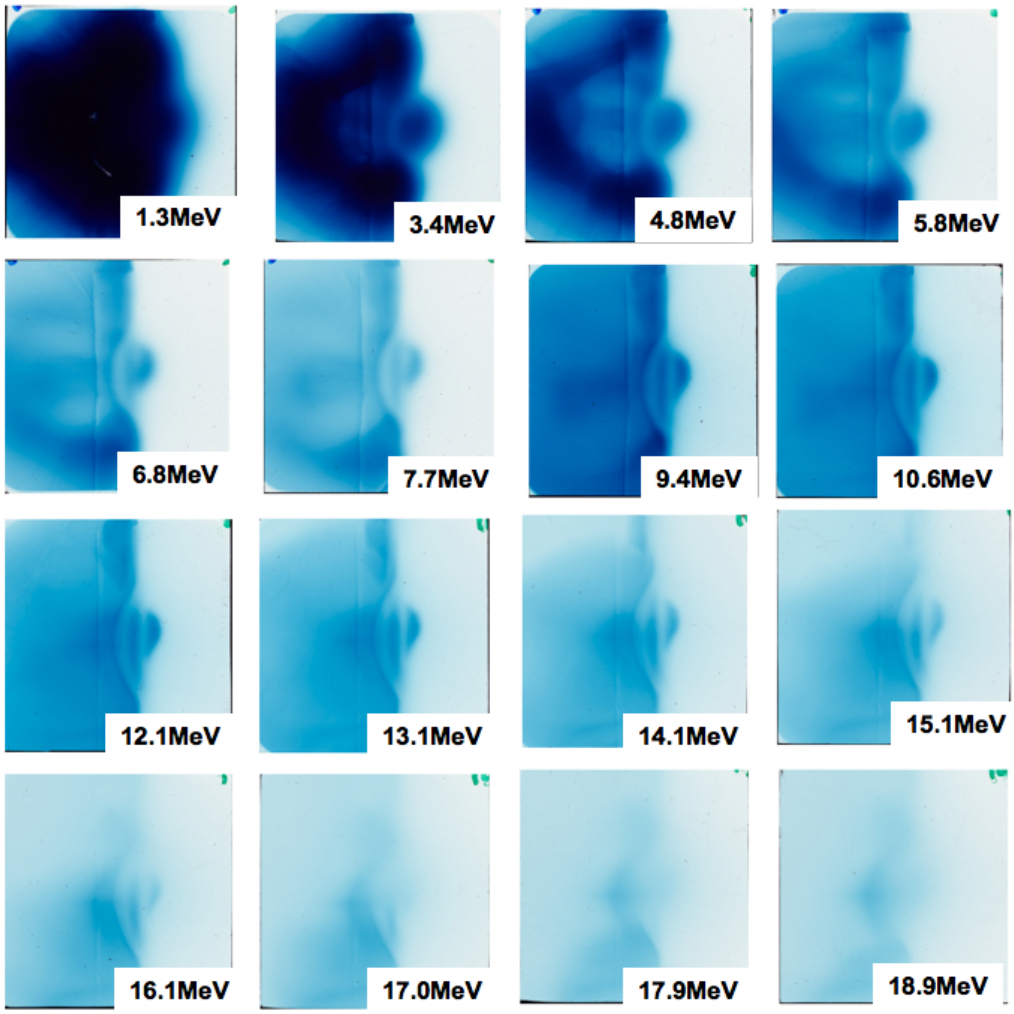


**Figure 5.9:** *Whole RCF set for a snapshot taken 7ns after the main ns pulse beams.*

protons with different energies, given by:

$$t_{flight} = l\sqrt{\frac{m_p}{2E}} \tag{5.1}$$

with $m_p$ the proton mass, $E$ its energy and $l$ the proton source to the target distance. For typical proton energies obtained in the experiment, the difference in the times of flight is of the order of a few picoseconds ($\sim$ 10 ps), much smaller than the typical hydrodynamic evolution time ($\sim$ 100 ps). We can thus assume that the whole set of RCF films gives an instantaneous snapshot of the plasma.
A first thing to be noticed is the sharpness of the cold sliver edge which can be observable on all the films. As the absorption in the cold foam is negligible even at modest energies (0.3 MeV for 5 MeV protons), the image is due to small angle scattering mechanism (as described in 3.3.2.4). Taking a lineout on the lower part of the image, we observe a sharp profile which is a signature of the perturbation produced in the proton beam, fig.5.10. The part of the beam propagating through the sliver is subjected to

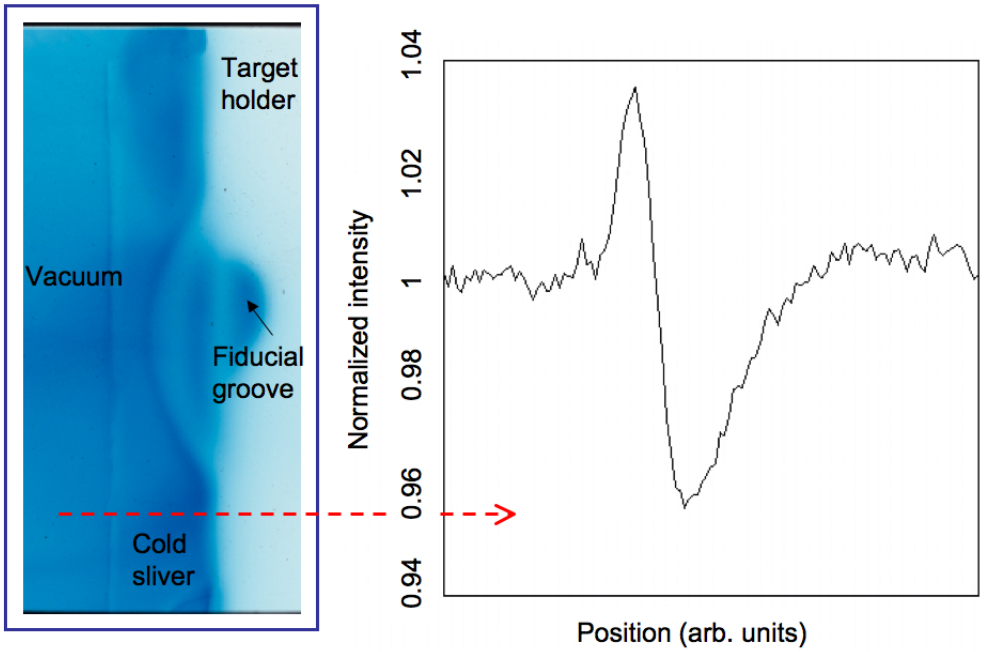


**Figure 5.10:** *~10MeV protons shock radiography. The cold edge/vacuum interface is imaged via small angle scattering: the accumulation region followed by the a deep minimum is clearly seen.*

a more important lateral spreading than the protons going through vacuum. In the region where the two beams interfere a modulation in the proton beam is observed (see section 3.3.2.4).
The shock front is also clearly visible on most of the RCF layers. It appears as a darker

zone, a sign of proton accumulation. Since the shock front is really sharp, it behaves almost like the foil edge, so that the modulation induced on the beam is due to small angle scattering. The mechanism is exactly the same: due to the density increase, the part of the proton beam going through the compressed foam undergoes a different transverse spread as compared to the beam going through the cold foam. The interference of the two parts of the beam induces a modulation in the proton signal. The specific shape of this modulation is then linked to the details of the density profile, such as, for example, the steepness of the shock front, its spatial extension as well as the density of the shocked layer. The resulting modulations can therefore be quite different from the simple case of the cold target edge-vacuum interface.

An additional comment needs to be done on the dark signal visible in the region near the target holder: this is simply associated to a groove in the target holder itself.

### 5.4.1 Resolution measurements

As we will see, a determination of the spatial resolution in the target plane is important to interpret the results. We have previously discussed how we can estimate the resolution limit due to the scattering process, as illustrated in fig.5.2. For 10 MeV protons propagating in a 300 $\mu m$ CRF foam at $0.1 g/cc$, the 1/e scattering angle $\sim 0.21°$ so that, in our configuration where $L = 3$ mm, we expect a resolution limit of $\sim 22$ $\mu m$. This was verified by performing a radiograph of a 1000 lpi Cu mesh glued on a foam

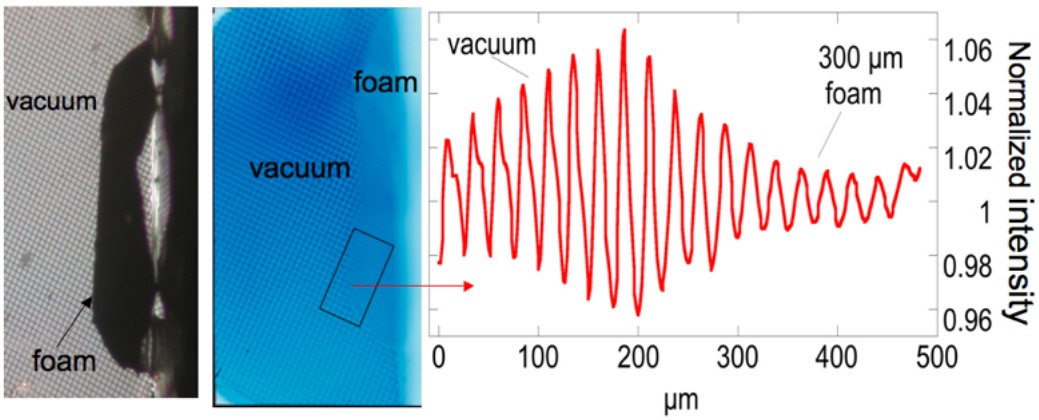


**Figure 5.11:** *Photo and 10MeV proton radiography of a 1000lpi Cu mesh. After propagation through the cold foam, 20$\mu m$ spatial features are still easily resolved, as shown in the lineout.*

sliver. The mesh spacing between two wires has been measured to be 20 $\mu m$, while

their thickness was $\sim 7\ \mu m$. The mesh image cannot be due to the stopping of the protons when crossing the mesh wires, the stopping range of 10 MeV protons in Cu being much larger than their thickness. It is due to small angle scattering only. Moreover, the mesh image is not destroyed by the additional scattering associated to the further propagation through the 300 $\mu m$ thick foam, as shown in 5.11. We can notice that we can still resolve a $20\mu m$ feature, in fair agreement with the resolution limit calculated above.
Resolution is reduced when lower energy protons are considered. The 3rd RCF, corresponding to 5 MeV protons, for the same mesh radiography is shown in fig.5.12. We can notice that in this case, the 20 $\mu m$ spacing is no more resolved.

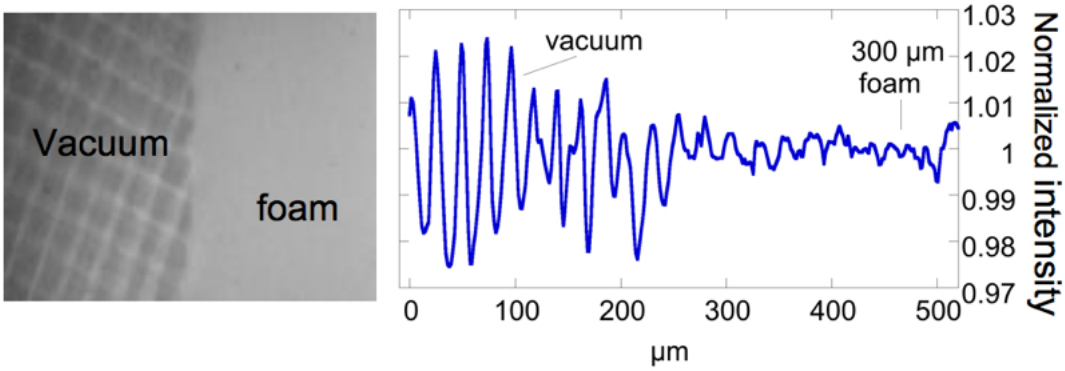


**Figure 5.12:** *5 MeV proton radiography of a 1000lpi Cu mesh. Propagation in foam strongly affect the resolution.*

### 5.4.2 Shock radiographs for different proton energies

As already discussed, the RCF layers allow us to select different proton energies. We can therefore investigate the effects of the propagation through the shocked target as function of the proton energy. We can notice that in fig.5.9 the shock front appears clearer on the RCF layer deeper in the stack, which correspond to higher energies.

In fig.5.13 we compare the $3^{rd}$ and $8^{th}$ RCF layers of a radiograph of the shocked foam. These two films correspond to $\sim$ 5 and $\sim$ 10 MeV protons respectively. We observe a clear image for the 10 MeV case, where the frontiers between vacuum-cold foam and cold-shocked foam interfaces are well defined. In the low energy case, the same features are smoother, due to the more important scattering. This is confirmed by a lineout in the shock propagation direction. More details of the density gradients can be observed at high energies, while at low energy the same features appear broadened and sometimes are not resolved. This is consistent with the small angle scattering process, which becomes much more important for low energies, increasing the blurring effects

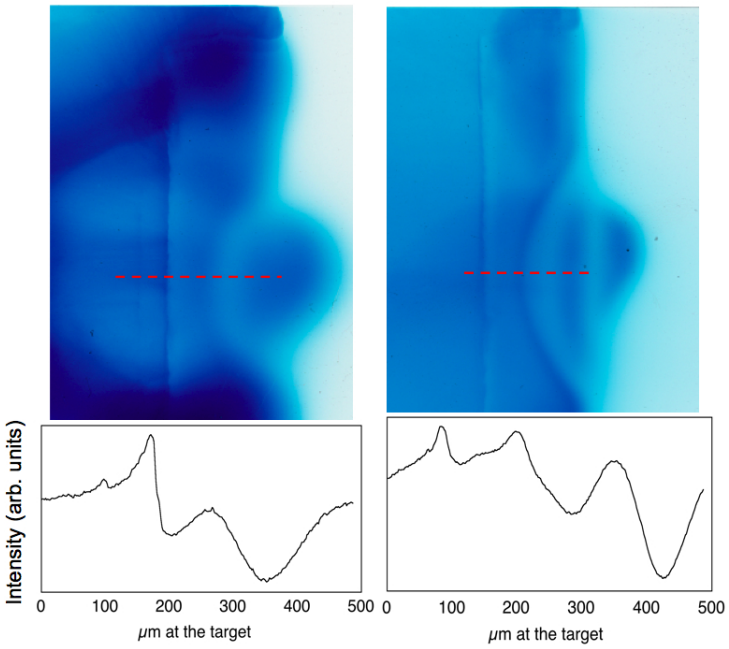


**Figure 5.13:** *$3^{rd}$ and $8^{th}$ layers of the same RCF stack, corresponding to $\sim$ 5 MeV and $\sim$ 10MeV respectively. At high energy, the image is clear and the details are well resolved, while the low energy image is much more blurred, as shown in the profiles taken along the dashed black lines.*

at the detector plane. Moreover, for 5 MeV protons, energy losses also begin to be important, up to 2 MeV if the whole 430 $\mu m$ thick sliver is compressed.

### 5.4.3 Shock radiographs at different times

By changing the delay between the shock drive beams and the CPA beam we could probe the shock propagation in the sliver at different times. This is particularly interesting in the temporal analysis of the compressed state.

Fig.5.15 shows the 8th RCF for a shot where the delay between the short and long pulse was 11 ns, together with the same RCF layer for the shot with a 7 ns delay, already presented in the previous section. The complete set of data at 11 ns is reported in fig5.14. At this later time we can observe a new feature which did not appear at the 7 ns, as underlined in the lineouts on fig.5.15. At 11 ns we can estimate that at 11 ns, the shock has almost broken out from the sliver. In order to better underline the differences in the two radiographs, in fig.5.15 we have taken the lineouts in a region where the shock is in both cases still in the sliver. This is possible because of the shock shape imprint by the gaussian intensity profile due to the RPP. In the lineouts, we observe the common peaks associated to the cold sliver/vacuum interface and the

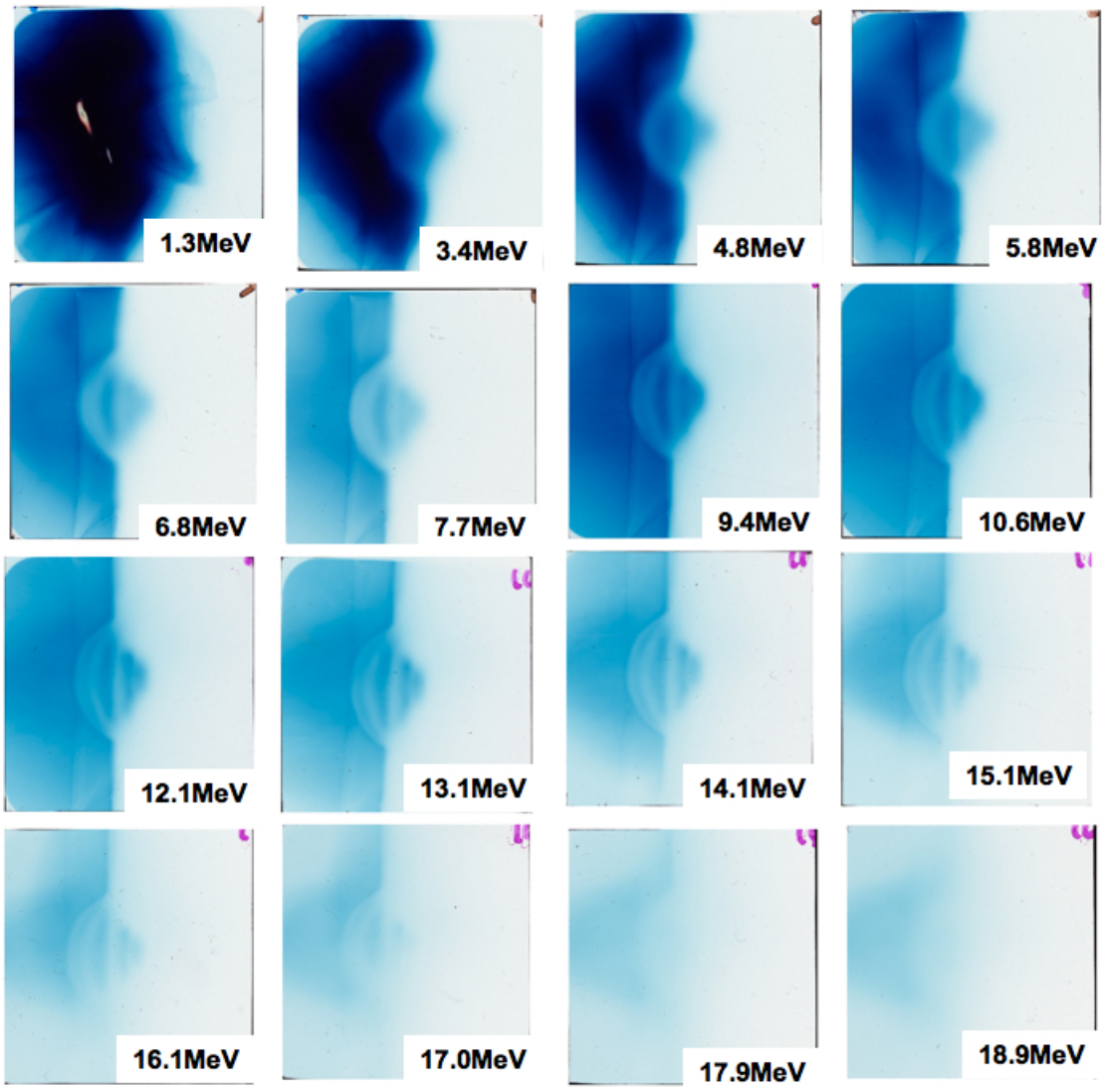


**Figure 5.14:** *whole RCF set for a shot taken 11ns after the ns beams.*

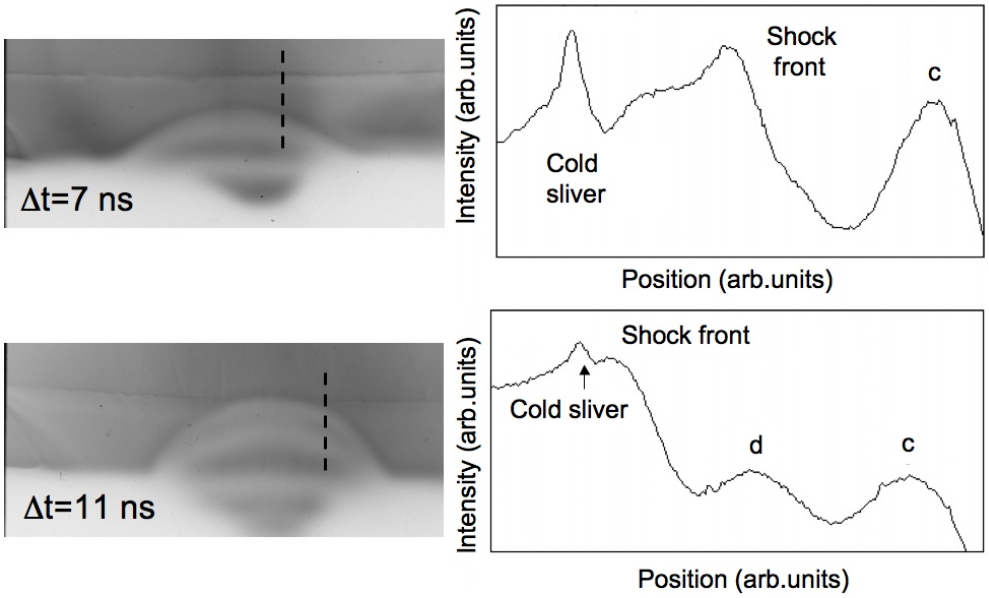


**Figure 5.15:** *8th RCF layer for shots where the delay between the backlighter and shock drive beams was 7 and 11 ns respectively. At later times a new feature ($d$) appears.*

modulations associated to the shock.

Moreover, at later times (fig.5.15b) we observe a further high intensity peak behind the shock front (labeled $d$ in fig.5.15). This peak is not clearly observable at 7 ns, probably just giving a change in the slope of the shock feature. As we will discuss later, when also the origin of the signal increase $c$ will be illustrated, this feature is associated to the pusher-foam interface behind the shock. Since the shock velocity is higher than the particle velocity, at later times the distance between the shock front and the pusher can be increased enough to produce two distinct modulations. This is illustrated in fig.5.16, which shows the temporal evolution of the density from a 1D hydrodynamic simulation. The parameters used in this simulation are the same ones inferred by the velocity measurements and discussed in 4.5. At earlier times, the shock front and the pusher are too close so the associated modulations are mixed together and cannot be resolved.

## 5.5 Results on CH targets

In order to check the possibility of imaging the shock front in dense targets, we have performed some shots on plastic targets, $\rho$ =1.044 $g/cc$. To reduce scattering effects as much as possible, the slivers were much thinner (116-170 $\mu m$ thick).

However in this case, due to the higher areal density, scattering is still too impor-

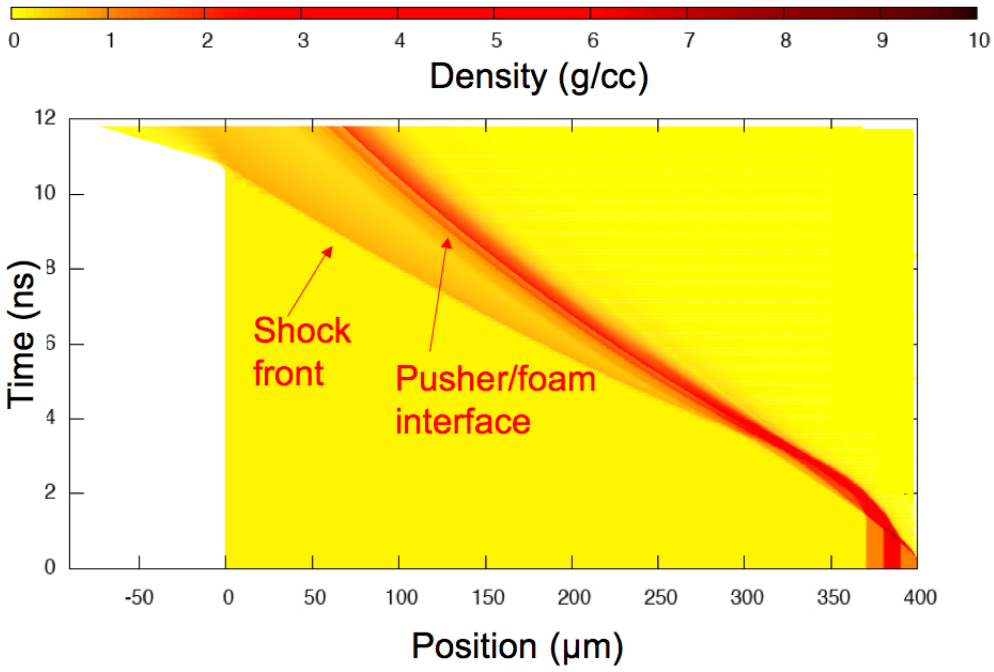


**Figure 5.16:** *Density time evolution from hydrodynamic simulation. The distance between the shock front and pusher interface increases with time.*

tant and the shock front image not clearly observable. This qualitative observation is confirmed by the Cu mesh radiograph, completely blurred, also at the highest energies. Different from the case of the low density foams, the modulations initially imprint by the Cu mesh are destroyed by the scattering associated to the further propagation in the plastic.
Once again, this result is in agreement with the resolution calculations discussed before, here giving a limit $> 35\mu m$. Fig.5.17 shows two images of the shock compressed plastic taken 7 ns after the main beams. These images correspond respectively to 5 and 14 MeV protons. We can notice that the shock is completely unresolved at low energy 5.17a. In this case the absorption is also important ($\sim$ 2 MeV for cold plastic) and the shocked part of the sliver is mainly characterized by a weaker signal. With higher energy protons, fig.5.17b, the shock front is better resolved, but its contrast is still much lower than in the foam case. In order to use the radiography technique in solid density materials much higher proton energies must be generated and used.

## 5.6 The Monte Carlo code

To better interpret the obtained data, we did some simulations of the proton propagation in the compressed sliver. A montecarlo code was developed as an evolution

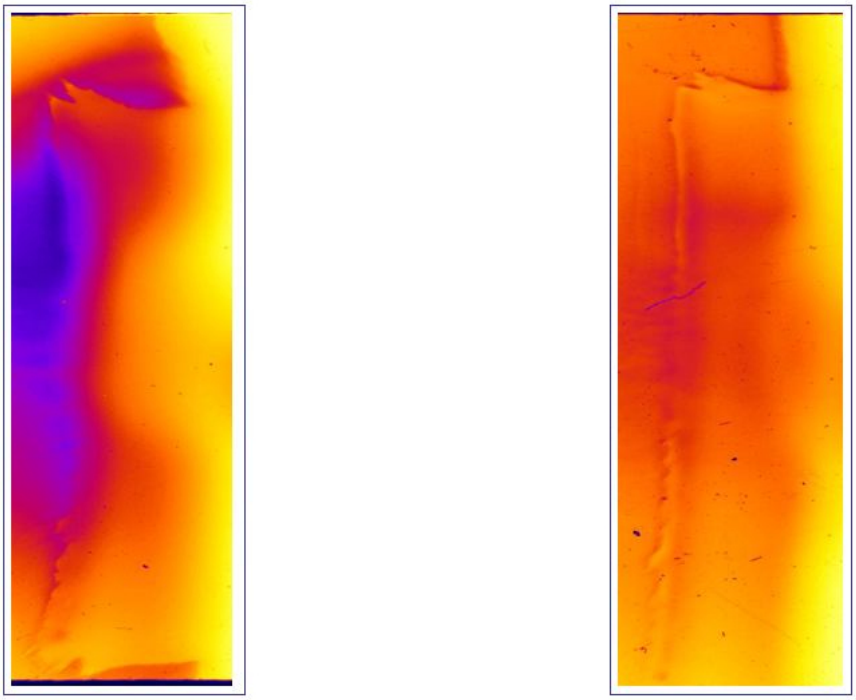

(a) (b)

**Figure 5.17:** *Images of a shock propagating into plastic obtained with ∼ 5 MeV (a) and* 14 *MeV (b) protons.*

of an existing code describing the interaction of relativistic electrons with a solid target, written by Laurent Gremillet [7]. The code reproduces the random character of collisions, simulating the probability functions which govern the particles trajectories starting from randomly generated numbers. The principal modifications done in the code are associated to the substitution of the electrons with the protons. They mainly concern the scattering cross sections and the stopping power calculations. The possibility to include a density gradient along the shock propagation direction, perpendicular to the proton beam, was also added. A particular treatment was then considered to correctly describe the proton propagation in low density materials.
The principal reason to write a new code was mainly related to the necessity to implement in a direct and efficient way the density profile along the shock propagation direction, which can be only partially considered in existing codes, such as TRIM (TRIM accepts complex targets made of compound materials with maximum eight layers).

The physics describing protons propagation in matter principally involves two processes: on one hand an angular deflection of the particle, which is induced by elastic collisions, and energy losses of the particle on the other, determined by inelastic excitation and ionization of atomic electrons.

In the description of the elastic collisions, we have followed the approach described in 3.3.2.3. The material in which the protons propagate is modeled as a layer with the proper thickness, density, atomic number, mass and number of atoms. Protons propagate along the Z axis. They are injected at the target surface at $Z = 0$, with X and Y positions randomly distributed on it. The initial position and the distance between the source and the target surface determine the initial direction vectors. The trajectories are then calculated in a 3D space as a succession of "broken" lines, each discontinuity representing a collision. Between two collisions, the particle goes on a straight line. At each step in the trajectory, the value of the areal density $\rho l$ that the particle can traverse before making a collision is calculated by giving a random variable $\xi$, uniformly distributed on $[0, 1]$, and the probability distribution function associated to the scattering cross section, according to usual Monte-Carlo techniques ([7]). We have decided to consider the areal density in addition to the mean free path (mfp) to be sure that the particle trajectory accounts for the steep density gradient induced by the shock wave. Using directly the mfp could have caused some issues when dealing with low density materials, as it is the case of our foams. While in dense material the mfp is considerably small ($\sim 10^{-2}\mu m$), in low density materials it can be significantly greater than the gradient length, hiding its effect on the particle trajectory.

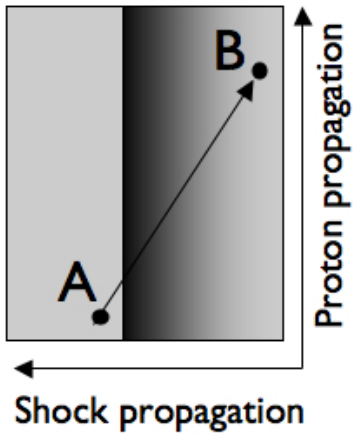


**Figure 5.18:** *The mean free path calculated from the density at the point A could bring the particle to the point B without accounting for the density gradient.*

This concept is illustrated in fig. 5.18: the mean free path calculated with the low density $\rho_A$ in the point $A$ brings the particle to the point $B$, without taking into account the density gradient, which would modify the probability of collision and hence the mean free path itself.
In the code we consider both the areal density and the mean free path. If the mean free

path is smaller than the density gradient length or than the hydrodynamic simulation cell dimension $l_c$ from which the density is extracted, then the particle can safely go through the whole distance. On the other hand, if the randomly calculated mean free path is larger than $l_c$, then the algorithm forces the particle to go through a series of steps of size $l_c$. At each step the density is checked and the value of the crossed areal density updated. The particle goes freely until it has passed through an areal density equivalent or larger[2] than the established value $\rho l$. It will then make a collision. The deviation angle is again randomly chosen, according to the cross section of eq.3.32.
The stopping power is also calculated at this point, giving the new particle energy. If the particle has lost all its energy it is stopped and the trajectory ends. If this is not the case, a check on the new coordinates reveals if the particle has gone out from the lateral edges of the target or if it has come to the end of the layer. If none of these situations is encountered we proceed in the calculation of the next step in the trajectory, otherwise a new trajectory starts. At the end of each trajectory, the final positions as well as the angles at the last step are given as output parameters. The energy left to the particles is also recorded.

Since in our experiments the proton energies lie in the range $1 - 20MeV$, we have used the Bethe-Bloch theory presented in 3.3.2.2 to describe the proton stopping power in matter. However, the theory correctly treats the case of cold materials only. Stopping power in hot matter is still an open question, particularly when dealing with low energy protons. So far, we can refer to the work done by Basko [8] and Melhorn [9]. Their works indicate that the stopping power for 10 MeV protons propagating in Al differs from the cold value by 13% (7% according to Melhorn) at 50 eV and by 2% at 10 eV. To evaluate the stopping power in our shocked targets, we have considered the plasma conditions predicted by hydrodynamic simulations and we have followed the approach suggested by Maynard [10]. He suggests to calculate the stopping power as the sum of the contributions from each free electron, considered as a single entity, and the contributions of each electron-shell. Therefore numerous parameters must be considered: the ionization degree of the atom, the number of electrons in each shell, their kinetic energy, the radius of the shell itself and the influence of the electrons in the inner shells on the incident particle (screening factor). From a first estimation [10], it results that for 10 MeV protons propagating in our targets, at typical temperatures of 10-20 eV and for a ionization level of $\sim 2$, the stopping power differs by $\sim$5% from the cold value. The effects of the temperature and ionization on the stopping power are thus neglected and in our case the Bethe-Bloch theory represents a good approximation.

[2] if larger, a normalisation to the correct distance is done by considering the ratio between the $\rho l$ and the larger value found.

Various tests were done to validate the code. In particular the absorbed energy and the scattering values were compared with the results given by TRIM code, commonly used in literature. We find a good agreement between our calculation and TRIM results. As an example, we discuss the propagation of 10 MeV protons through an uniform cold 500 $\mu m$ thick aluminum layer. With our code, the energy loss for each particle is $6.05 \pm 0.03$ MeV. Fig.5.19 shows, instead, the energy losses for a 10 MeV

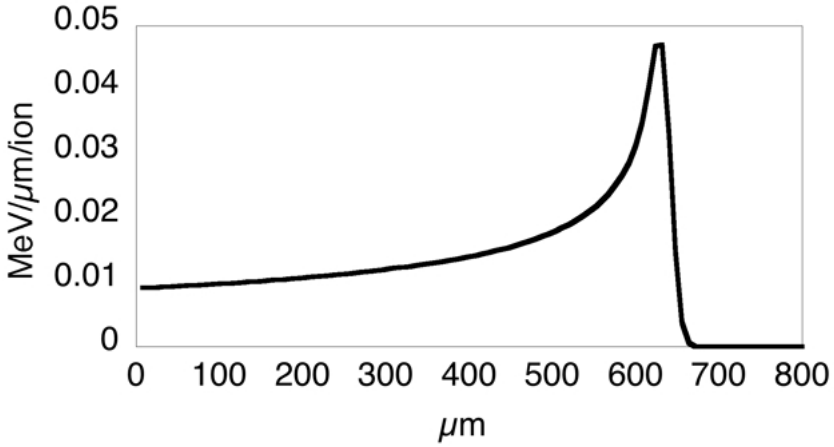


**Figure 5.19:** *Energy loss by 10 MeV protons in their propagation through an Aluminium slab from TRIM simulation.*

proton propagating through an Al slab calculated with TRIM. Integrating the curve up to $500\mu m$ we found that each proton has lost 6.02MeV, which is in good agreement with our result.

To verify the effects of elastic collisions, we compared the spread of the final positions at the slab surface. In TRIM, this information is given by the "Radial range" parameter $R_r = \sum_i (x_i^2 + y_i^2)^{1/2}/N$, which is the mean value of the distance from the propagation axis. The error is evaluated as the mean standard deviation: $\sigma = \sqrt{\frac{1}{N-1}\sum_i [(x_i^2 + y_i^2)^{1/2} - R_r]^2}$

For the same simulation as before, we show the scattering results in fig.5.20 obtained with our code and with TRIM. The figure shows the positions in the XY plane at the end of the of the slab ($z = 500\mu m$). If we calculate the same "lateral straggling" parameter for the two cases we find a value of $20.188 \pm 0.297$ $\mu m$ predicted by our code and $16.022 \pm 0.258$ $\mu m$ by TRIM. In this case our value is higher than the one given by TRIM, implying a more important role of collisions. The same tendency is found for simulations with different materials or different densities. The disagreement between the two values is of the order of $\sim 20\%$. However, we have to point out that a TRIM underestimation of the collisions has been previously put in evidence for example in [14] or, more recently, in [15].

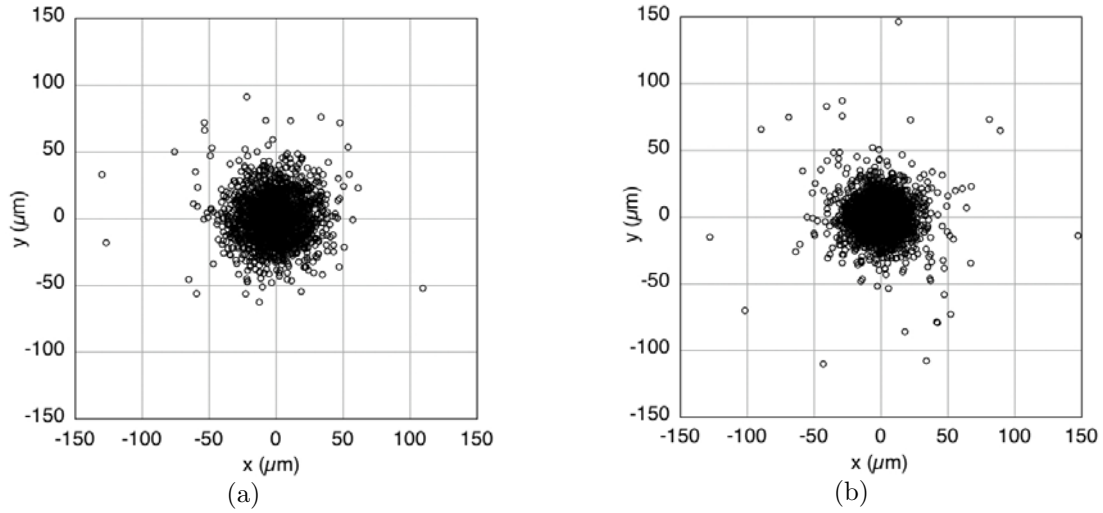


**Figure 5.20:** *Final positions in the xy plane of the 10MeV protons after propagation through* $500\mu m$ *thick Al slab obtained with (a) our code, (b) TRIM code.*

## 5.7 Data analysis

We can now analyze in deeper details some of the data previously presented.
The main objective of this analysis is to carry on an iterative process in which the effects of the density gradient on the proton propagation are simulated by the Monte-Carlo code. The input density profile is changed until the experimental results are well reproduced (see paragraph 3.3.2.1).

In this section, we will first describe the method we have used to compare the simulation data to the experimental ones. The density profile from hydrodynamic simulations will then be presented and finally the results will be discussed.

### 5.7.1 Data handling

In this work we have investigated a single RCF film. The analysis is focused on the $8^{th}$ RCF layer, which corresponds to ∼10 MeV protons. It represents the best compromise in terms of proton energy and proton number, which allows us to obtain a sharp image intense enough to be analyzed. High energy protons are too low in number to produce a clear signal, while strong blurring affects lower energy images.
Moreover, accounting for the density values expected (a ∼5 fold compression is predicted from hydrodynamical simulations, as we will see in section 5.7.2), the energy losses for 10 MeV protons (<1 MeV if the whole sliver thickness was compressed) are not high enough to be resolved by the RCF (whose spectral resolution is typically 1-2 MeV). Proton beam perturbation recorded on the 8th layer are hence induced mainly

by scattering and the analysis can evidence its effects.

In order to compare the Monte-Carlo results to the experimental data, we have normalized the modulation intensity induced on the proton beam to the signal value in the unperturbed region. This procedure is carried on both the experimental and simulation data.

**Modulations intensity on experimental images** In the experimental images, the modulations induced on the proton beam by the density gradient, result in corresponding modulations in the deposited energy. In particular, due to the linear response of the RCF, an accumulation of protons will make the film a darker blue color comparing to the unperturbed regions, as explain in 5.3. On the contrary lighter blue is characteristic of proton depletion regions.

To evaluate the importance of the beam modulations we normalize the deposited dose in the whole image to its value in the unperturbed region. The normalization procedure is hence a delicate point in the analysis.
In order to correctly perform it, we must first subtract the background level. As we have seen, when considering the spectral distribution, the RCF layer exhibits a narrow energy response. Therefore, in first approximation we can neglect the continuum energy deposition from higher energy protons.
There is another contribution corresponding to the energy uniformly deposited from relativistic electrons and from high energy radiation, to which the RCF are also sensitive. Its evaluation is quite straightforward as it can be done considering the signal on the last radiochromic films and subtract it from the image under investigation. The protons are not energetic enough to reach the last films. However, these are exposed to the electrons and radiation which loose nearly the same energy in all the RCF layers. This consideration is confirmed by the fact that the last films present rather the same signal, indication of an uniform energy deposition. In our experiment, the last layers containing a clear proton signal are the 12-13th while the background wass taken from the 21st layer, far enough to be sure that the corresponding signal is not due to proton deposition.

The proton beam spatial profile is another crucial parameter in the normalization process. A uniform beam is necessary to determine the modulation intensity on the whole image. Since the beam intercepts the target and its holder, we can only access a fractional part of the unperturbed proton beam which is used as reference. If the beam is not spatially uniform, the normalization process can induce an incertitude on the evaluation of the modulation intensity. Unfortunately, this is our case, where the

beam did not have a high spatial uniformity because of the laser instability during the campaign.
A general error estimation is obtained by considering the normalization results at different spatial positions. We find a 10% fluctuation in the intensity modulations associated to the cold sliver edge, the part of the image closer to the unperturbed beam. For regions deeper in the targets, including the shocked part, the error cannot be correctly estimated, as we do not have a precise reference for the normalization. For these regions, we can consider an error bar $\gtrsim 10\%$.

**Modulations intensity on Monte-Carlo simulations** When considering the results from Monte-Carlo simulations, the modulations intensity is calculated on the number of particles reaching the detector. This procedure is equivalent to dose estimations as soon as the assumption of proportionality between the absorbed radiation dose and the number of incident particles is valid, i.e. as soon as the film is not saturated.

The proton distribution at the detector is obtained from the simulation outputs. The Monte-Carlo code reproduces the proton propagation in the density profile until they have crossed the whole target thickness. The final positions and directions of each individual particle are then used to geometrically propagate it to the detector plane. This operation is considerably important as it has a great impact on the beam spreading. If the detector is too close to the target, the overlapping can be too small and no effects are recorded. This is equally the reason why scattering in the detector can be neglected. Moving away the detector from the target, the beam modulations can be observed. In our experiment the detector was put on a kinematic mount which allowed a precise and reproducible positioning. The distance from the target was $36 \pm 1$ mm.
The code is run with a number of particles sufficient to produce statistical fluctuations of the same order as the estimated experimental error ($\sim 10\%$). This number depends on the target transverse dimension (i.e. the sliver length) and on the proton spectral band considered in the calculations. In the analysis of the 8th RCF (as we have previously seen) we can neglect the effects associated to the energy losses. This allows to use a narrow proton spectrum, corresponding to the RCF spectral resolution, of the order of 1-2 MeV (section 5.3). Therefore, this is the spectral bandwidth considered in the code. In this case the simulations are run with 200000 particles, sufficient to satisfy our statistics requirements.
We remark that in a general case, absorption effects must be considered and the simulations must be run with the entire proton spectrum. The number of particles necessary to reach a high statistics, then, considerably increases.

### 5.7.2 The density profile

Hydrodynamic simulations are used to define the density profile associated to the shock propagation. We have described in section 4.5 the way we have derived the simulation parameters from the shock velocity measurements. The same parameters were used to run the hydrodynamic simulations on the foam targets, getting the density profiles to be inserted in the Monte-Carlo code.
The result is a non steady shock, whose velocity decreases from the initial value of $\sim 50$ $km/s$ to $\sim 35$ km/s during the 11 ns transit time. The pressure generated in the foam targets lie in the range $2.3 - 1.1$ Mbar, while a maximum $\sim 5$ fold is found in the foam.

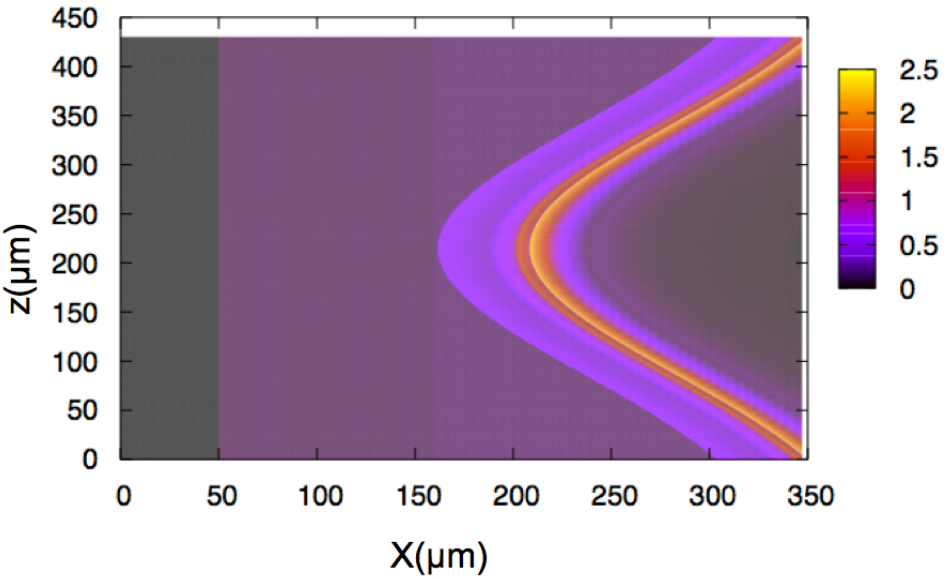


**Figure 5.21:** *Density profile at 7ns from hydrodynamic simulation.*

In order to model the proton propagation, the 2D density gradient structure is of primary importance since the sliver thickness, 430 $\mu m$, is larger than the shock curvature (initial FWHM of $\sim 300\mu m$). Non considering the density gradient in the proton propagation direction, hence, would cause an overestimation of the scattering, corresponding to the overestimation of the compressed thickness crossed by the particles. Because we are dealing with small angles scattering, the shock curvature in the third dimension, which also exists, has a weaker impact on our results and it will be neglected in this calculations. Its implementation in the code is almost quite straightforward and it can be achieved when needed.
Unfortunately at the time of the analysis, no useful 2D hydrodynamic simulations were available; we have therefore reconstructed 2D profiles from 1D simulations, taking the

shock front gaussian shape into account. The result at 7ns, is shown in fig.5.21.

### 5.7.3 Source size characterization

The proton source size can affect the intensity of the proton beam modulations. Its characterization is therefore very important for a correct interpretation of the experimental results.

The details of the proton emission are in agreement with a picture of a small virtual source size located at a distance $z$ ($\sim 300 - 400 \mu m$) in front of the target (fig.5.22). At

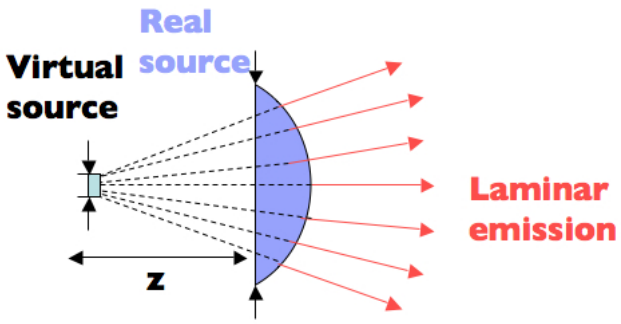


**Figure 5.22:** *Proton emission mechanism. The details of the proton emission are in agreement with a picture of a small virtual source located in front of the target. At the target surface, the emitting region is much larger.*

the target surface, the emitting region is much larger. The radius $r$ of the real source depends strongly on the energy of the protons considered; typically it is 80 $\mu m$ for 12 MeV protons but it can be increased up to 250 $\mu m$ for 6.5 MeV. The protons are emitted in a quasi-laminar fashion, within an angle $\theta \pm \Delta\theta$, with $\theta \sim r/z$ and $\Delta\theta \sim a/2z$, where $a$ is the virtual source radius.
However, the properties of the proton source size are strictly connected to the laser characteristics and in particular strongly depend on the quality of the laser focal spot. Its characterization is thus necessary in each experiment to correctly describe the modulations intensity and, consequently, the density gradient that can be deduced.
In order to characterize the proton source size, we focus the attention on the modulation observed at the cold foam edge-vacuum interface. In this case, both the density values and its spatial profile are well known. Eventual disagreements between the experimental and simulated results can thus be attributed to the proton beam properties only.
We can describe the vacuum-foam interface as a density discontinuity between 0 and 0.1 g/cc. The Monte-Carlo simulation results obtained with a point source do not reproduce the experimental modulations. To find consistency with the experiment we

need to insert a 20 $\mu m$ source size. A similar result was found in [13], where a source size of 10 $\mu m$ was necessary to reproduce the correct modulation intensity for a proton beam scattered by an Al grid. It is important to notice that this result was obtained on our same laser system (the VULCAN laser at RAL). Different experiments performed on different laser facilities, [16],[17], are consistent with smaller source sizes. On the LULI100TW laser system, the source size was measured $\lesssim 4\mu m$ [17]. In that case, the proton beam appears highly uniform on the RCF. On the contrary, the inhomogeneities in the proton spot observed in our shots are a signature of a lower collimated beam, consistent with bigger source sizes.
The results given by the code with a point (light gray curve) and a 20 source $\mu m$ (dark graycurve) are compared with the experimental results (blackcurve) in fig.5.23. Both

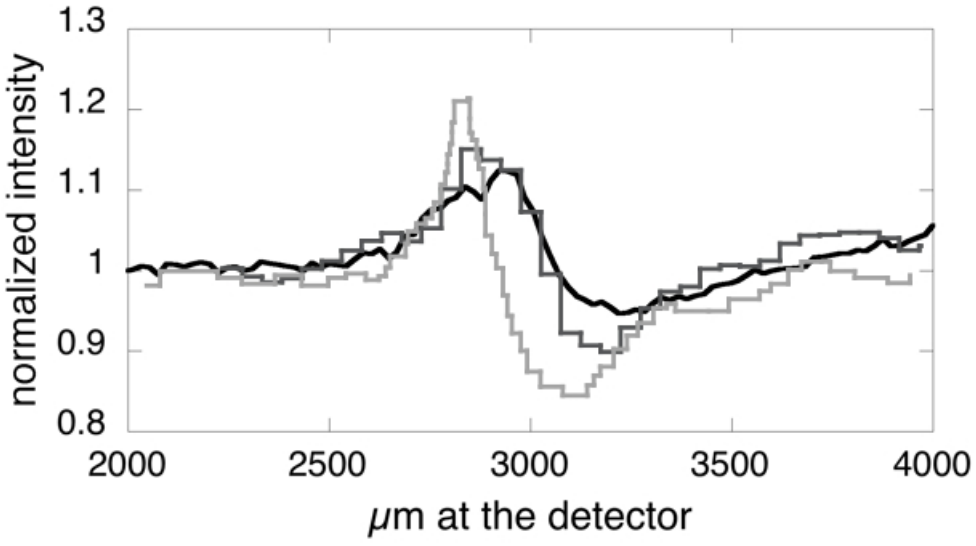


**Figure 5.23:** *Normalized modulations induced by the cold foam edge experimental data (black line) and MC code with a point source size (light gray line) and with a 20 $\mu m$ source size (dark gray line).*

the perturbations spatial extent and intensity are in agreement with a 20 $\mu m$ source size, the profile obtained with a point source being too narrow and too intense.
Having determined the source characteristics, we can now investigate the net effects of the density profile on the modulations. In particular, we will consider the effects of the density gradient at two different times 7 and 11 ns.

### 5.7.4 Experiment and code results at 7 ns

When we insert the density profile at 7ns, shown in fig.5.21, and considering a 20 $\mu m$ source size, the code results are shown in fig.5.24. In the same figure, they are compared

to the experimental profile taken along the symmetry axis, where the laser intensity is maximum.

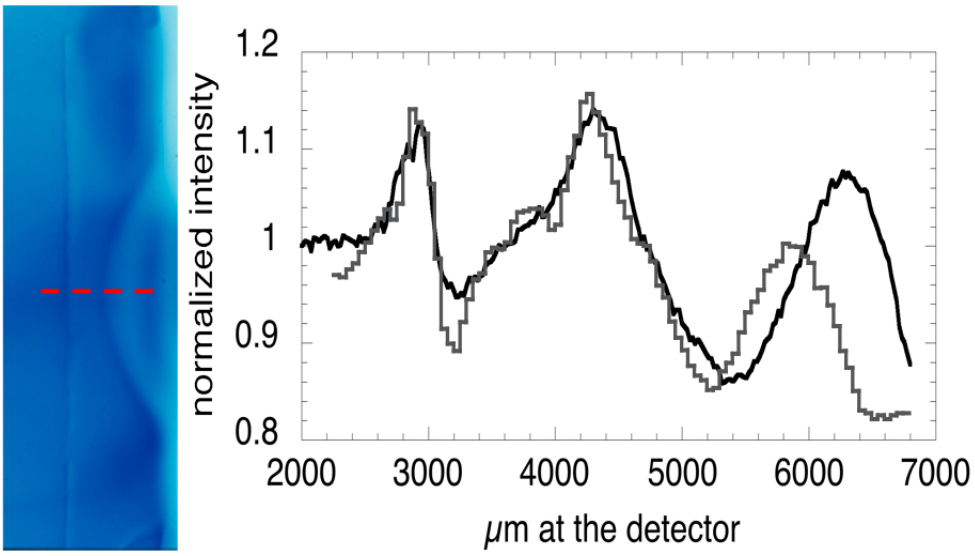


**Figure 5.24:** *Contrast profile results from the experimental data (black line) and from the montecarlo simulation (gray line). The contrast at the cold foam edge is well reproduced as well as the general structure.*

We can notice that the experimental profile and the contrast values are well reproduced. In order to better understand the origin of each intensity modulation, we shall consider the 1D density profile as given in fig.5.25 (a). We can attribute the main intensity modulations to the scattering from three principal density changes in the sample:

- the cold foam edge
- the shock front
- the compressed pusher

The intensity modulation induced by each density variation are sketched in fig.5.25 (b).

Scattering from the cold foam edge causes the typical accumulation zone and the associated depletion region.

Because of the narrow spatial extent of the shock front and of the pusher, their effects are similar to those induced by a thin wire (section 3.3.2.4). Two accumulation regions at each side of the narrow feature are observed separately while the depletion regions are superimposed in a unique deep minimum. The width and intensity of

the accumulation and depletion zones can be different according to the density profile details. In particular, the beam perturbation inferred by the shock front is affected by the gradient behind it.

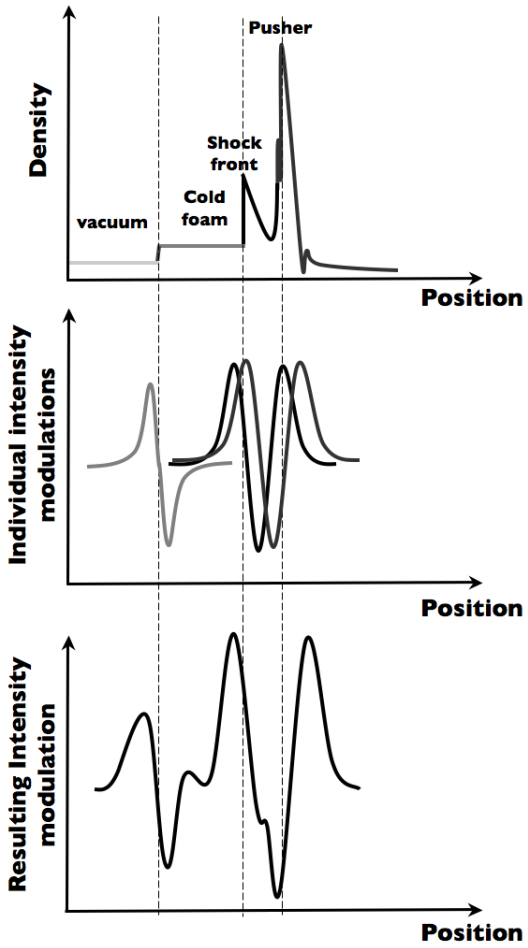


**Figure 5.25:** *Schematic representation of the intensity perturbation induced on the proton beam by the density profile. The effects of each single feature are mixed together producing a profile similar to the observed at earlier times (7ns).*

If the pusher and the shock front are not separated enough, their effects are mixed in a single modulation. The resultant intensity profile is sketched in fig.5.25 (c), in which we recognize the characteristics of the experimental and simulated profiles of fig.5.24.

We can verify that, at this delay, the pusher and shock front cannot effectively be resolved. First, from hydrodynamic simulations, we estimate the distance between these two interfaces, $\sim$40 $\mu m$ at 7 ns (fig.5.16). We can then use the criterion discussed in 5.4 to determine the condition for the two features to be resolved. In 5.4, the resolution limit accounted for the scattering in a single material. Here, on the contrary,

the scattering effects are different for protons going trough the pusher or through the shocked foam. This fact implies that the scattering cones associated to the foam and to the pusher have different apertures, $2\beta_1$ and $2\beta_2$ respectively. As before, in order to resolve the two features, we require that these two cones do not overlap. Therefore, the condition of section 5.4 can now be rewritten as: $y > (\beta_1 + \beta_2)L$. Considering the compressed material thickness crossed by the protons, we find $(\beta_1 + \beta_2) \sim 1.2°$, leading to a resolution of $\sim$60 $\mu m$ for our 3 mm proton source/shocked target distance. This value is bigger than the $\sim$40 $\mu m$ deduced from the simulations, confirming that the modulations induced by the shock front and the pusher can not be resolved. Their effects are mixed together, in accordance with the experimental result.

Since it is not possible to isolate the effect of the shock alone, the shocked target density cannot be determined with good accuracy for this shot.

### 5.7.5 Experiment and code results at 11 ns

At 11 ns the shock has just broken out from the sliver. As before, we have inserted the density profile from the hydrodynamic simulations (now calculated at 11 ns) in the code. The source size is also maintained at 20 $\mu m$, while the shock FWHM is slightly increased because of its expansion.

The comparison between the experimental results and the simulations still shows good

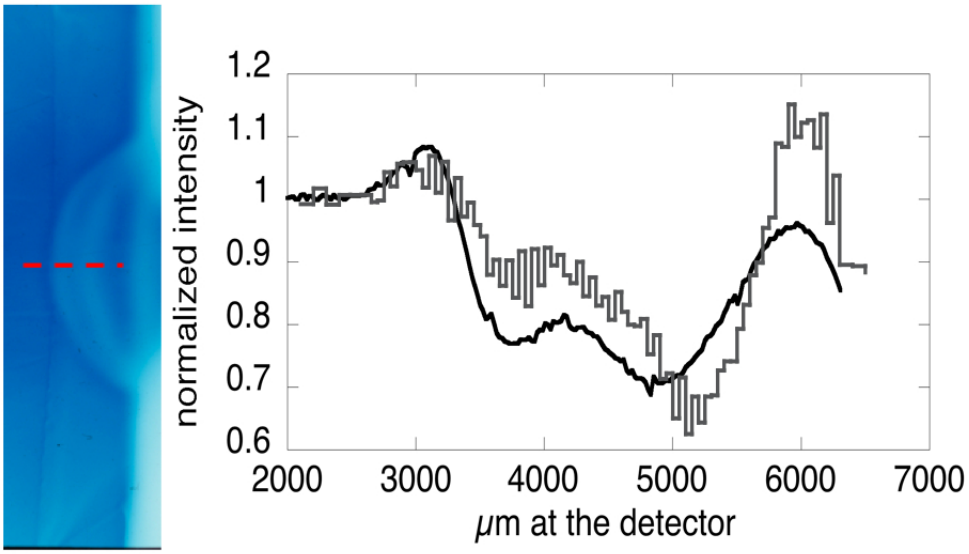


**Figure 5.26:** *Contrast profiles at 11ns. The experimental data (black curve) is compared with the MC simulations (gray curve).*

agreement, as shown fig.5.26. In this case, the profiles are quite different from the one

obtained at 7 ns. The cold foam edge effects are no more observable, because the shock has broken out into vacuum. Here, the modulations observed are caused by the shock front unloading in the vacuum and by the pusher only, which now becomes distinguishable.
We illustrate this situation in fig.5.27. As before, we show the 1D density profile together with the scattering effects on the proton beam. Fig.5.27 (c) shows the resulting modulations. We can observe the same structure as in fig.5.26, but as opposed to the profiles at 7 ns, the accumulation and depletion zones do not completely overlap. Therefore, we observed an additional modulation, not perceived at 7 ns (section 5.4.3).

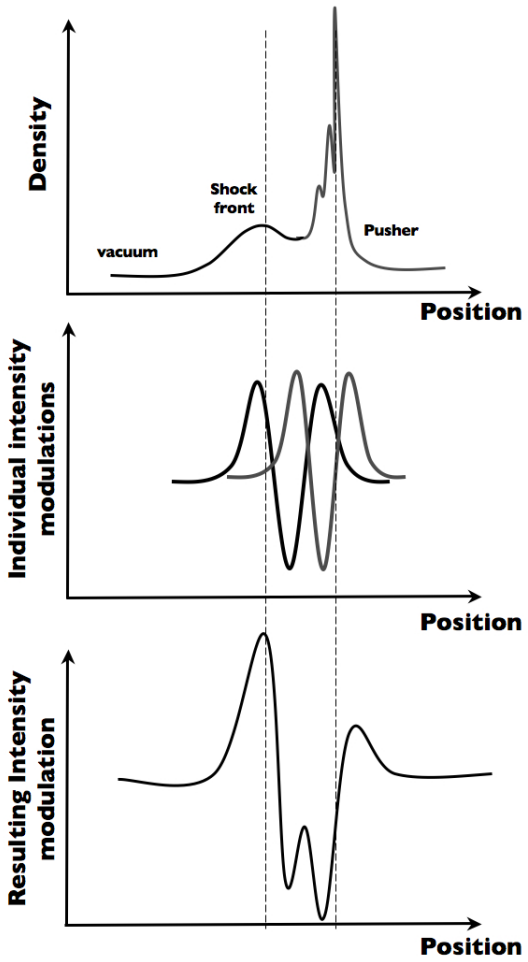


**Figure 5.27:** *Schematic representation of the intensity perturbation induced on the proton beam by the density profile at later times. The shock-front pusher distance is increased enough so that the associated effects can become distinguishable.*

At this delay, we can verify that we can effectively spatially resolve the pusher and the shock front unloading into the vacuum, by calculating the resolution limit. Using

the same procedure as before, we find a resolution limit of ∼60- 70 $\mu m$, while at $t = 11$ ns, the distance between the shock front and the pusher is increased up to 80 $\mu m$, fig.5.16. Indeed at 11 ns the scattering effects associated to the shock front and to the pusher start to become distinguishable.

Having verified that we can to isolate the shock effects, we can deduce the foam density from the Monte-Carlo simulations. Fig.5.26 indicates that the 4 fold compression, predicted by the hydrodynamic simulations at this delay, is sufficient to reproduce with good accuracy the intensity contrast associated to the shock break out. The width and the positions of all the other features is also quite well matched, even if their contrast is not optimal. In this case, probably, the reconstructed density profile from the 1D simulation does not allow us to reproduce with good accuracy the released part and to catch all the details of the released and of the still highly compressed parts of the target. A complete 2D simulation is then necessary for a deeper analysis.

## 5.8 Sensitivity as density diagnostic

A general estimation of the sensitivity of this diagnostic to the density is not easy to do in this regime, where only scattering comes into play. It strongly depends on the material under consideration, since the modulations are induced by the different lateral spread due to the cold and shocked material. Therefore, same compressions in different materials would cause a different effect. Moreover, the density spatial profile, is a crucial parameter in determining the modulations on the beam. The shock spatial characteristics, among which its curvature in particular, will then determine the observed effects. For the specific case of the low density foam, we can estimate the sensitivity to the density by comparing the profiles obtained from the proton propagation through a step-like density profile and varying the amplitude of the step. The most simplified scheme for the density on the shock propagation axis, can be given as a first vacuum region followed by a first step at 0.1 g/cc representing the uncompressed foam and a further step for the shocked part. We have run MC simulations considering different values for the compressed foam layer. We show in fig.5.28 the result obtained for a 0.4 g/cc and 0.6 g/cc step. In both cases, the energy losses are neglected since $\lesssim 1MeV$, i.e. not experimentally resolved by the RCF stalk. In order to estimate the real potentiality of the technique, in the profiles shown in fig.5.28, we have considerer a 10 $\mu m$ source size, which can be achieved in typical experiments, where the beam quality is good, but still not optimal! We can notice that the two profiles are considerably similar. The differences can not be observable in conditions similar to ours, where the experimental fluctuation is ∼10%.

Another interesting analysis can be done by varying the steepness of the density jump.

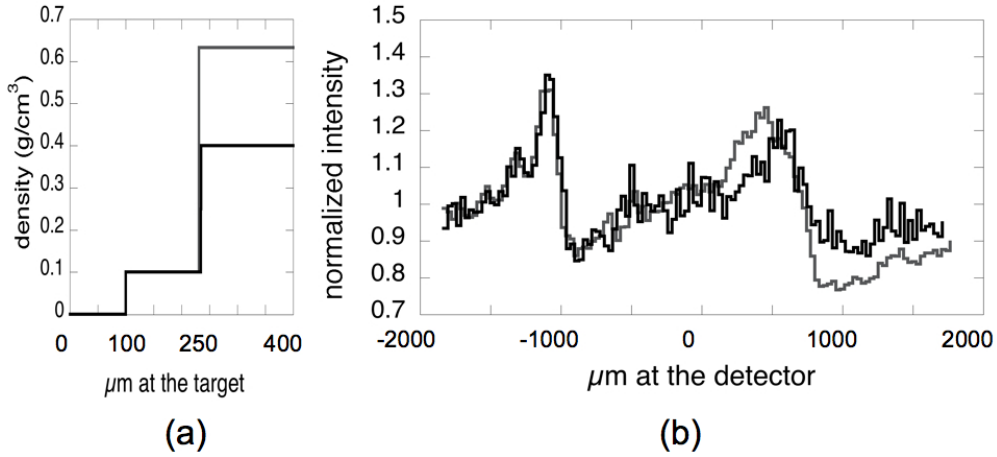


**Figure 5.28:** *Contrast profile results for a double stepped density profile (a). In both curves the first step is at 0.1g/cc and represents the cold foam edge. The shock compression is modeled with a second step of 0.4 g/cc (black line) and of 0.6 g/cc (gray line).*

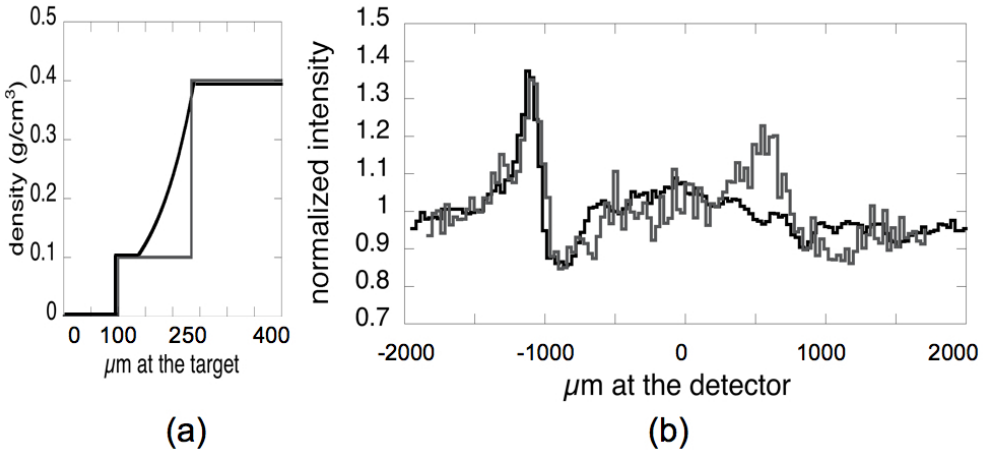


**Figure 5.29:** *Contrast profile results from different density gradients (a). In both curves the first step is at 0.1g/cc and represents the cold foam edge. The shock compression is modeled with a second step of 0.4 g/cc (gray line) and with a exponential function of* $1/e \sim 75\mu m$ *(black line).*

In fig.5.29 the maximum compressed density is kept at 0.4 g/cc, but the density increase is smoothed (exponential, with $1/e$ increase in $\sim$75 $\mu m$). In this case, a substantial difference is observable in the two profiles. In particular, the effects associated with the smooth gradient are far less marked. Therefore, completely blurred images could result from too gentle gradients radiographs.

## 5.9 Conclusions

For the first time we have demonstrated the possibility to use proton radiography as a WDM diagnostic. High quality radiography of shock compressed targets have been obtained with laser produced protons. Thanks to the short temporal duration of these proton beams, this technique can probe a precise state of plasma and therefore the shock propagation history. In particular, we have been able to resolve the pusher-shock interface at late delays. In this case, we were able to isolate the effects of the shock discontinuity on the proton propagation, allowing its direct characterization.

We have carried on a first study to investigate the potentiality of this diagnostic as a direct density measurement. In particular we have focused the analysis on films corresponding to high proton energies, where the energy losses are negligible and the image is mainly due to small angle scattering. Using a Montecarlo code, we have proved that the perturbations induced on the proton beam can be reproduced by introducing a correct density profile, which was obtained from 1D hydrodynamical simulations. In this regime, where only scattering is involved, the analysis is not highly sensitive to the compression value. Nevertheless, it shows a good sensitivity to the density gradient spatial details. This quality makes it particularly suitable in experiments requiring both spatial characterization and compression information within a discrete precision (symmetry implosion control, instabilities detection,...).

The used method has very promising perspectives and can be strongly improved.

- The real potentialities of the diagnostic can be understood by performing a deeper and complete analysis on the whole RCF stalk. For example, a parallel analysis on each film could restrict the density characteristic requirements, hence reducing the uncertainty. In this procedure, when considering the first films, corresponding to less energetic protons, absorption must also be accounted for. Therefore, in this case, a well characterization of the proton spectrum is necessary for a correct evaluation of the absorption and, hence, of the density.

- Additional improvements of the Monte-Carlo code can also be considered. In particular its routines must be optimized to use a larger number of particles, necessary for better statistics.

- If a spherical shock is created, 2D hydrodynamical simulations can be used to achieve a more accurate description of the density profile, for late delays in particular. In these cases, compression details can be considerably different along the spatial shock profile. A 3D approach can also easily be implemented in order to give a more realistic description of the propagation process.

- From the experimental point of view, improvements of the proton beam quality is of fundamental importance in this measurement. Its spatial properties are crucial parameters for the correct evaluation of the modulation intensities.

As a conclusion, this technique is worth to be pursued in future, the first results being highly encouraging. In particular, access to large scale facilities (PICO2000, OMEGA EP, ...) will provide higher proton energies, which will extent this diagnostic to high density materials.

# Bibliography


[1] S.Le Pape, M.Koenig, T.Vinci, *et al.*, Astrophys. Space. Sci, **298**, 313 (2005)

[2] A. J. Mackinnon, P. K. Patel, M. Borghesi, *et al.*, Phys. Rev. Lett. **97**, 045001 (2006)

[3] M.Borghesi, A.Schiavi, D.H.Campbell *et al.*, Plasma Phys. Controlled Fusion, **43**, A267, (2001)

[4] www.srim.org

[5] J. F. Ziegler, *The Stopping and Range of Ions in Matter*, Vol. 1, Pergamon Press, New York (1985).

[6] D.Hicks, private communication

[7] L. Gremillet,Étude théorique et sperimentale du transport des électrons rapides dans l'interaction laser-solid à très haut flux, Thèse de docteurat de l'École Polytechnique

[8] M.M.Basko, Sov. J. Plasma Phys., **10**, 6 (1984)

[9] T.A.Melhorn, J. Appl. Phys. **52**, 11 (1981)

[10] G.Maynard, private communication.

[11] R.C.Fernov, Introduction to experimental particle physics, Cambridge University Press (1986)

[12] J.D.Jackson, Classical Electrodynamics

[13] M.Borghesi, A.J. Mackinnon, D.H.Campbell, *et al.* ,Phys. Rev. Lett. **92**, 5 (2004)

[14] C. Michelet, Ph. Moretto, G. Laurent, *et.al*, Nucl. Instr. and Meth. B **181** 157 (2001)

[15] P.Reichart, D.Spemann, A.Hauptner, *et.al*, Nucl. Instr. and Meth. B **249** 286 (2006)

[16] T.E.Cowan, J.Fuchs, H.Ruhl, *et al.* ,Phys. Rev. Lett. 92,**20**, 2004

[17] J.Fuchs, submitted to Phys. Plasmas

[18] J.Shreiber, F.Bell, F.Grüner, *et al.*, Phys. Rev. Lett. **97**, 045005 (2006)

[19] M. Zepf *et al.*, Phys. Plasmas, **8**, 2323 (2001)

# Chapter 6

# X-ray Thomson Scattering

In this chapter we will describe the experiments we have performed on x-ray Thomson scattering. The main objective was to probe collective regimes, where the scattered spectrum is representative of the collective response of the medium. Two experimental campaigns were conducted on different laser facilities. The first one was performed on the LULI2000 laser at the Ecole Polytechnique, while the second was lead on Janus facility at Livermore National Laboratory, California. We will begin introducing the LULI experiment. The set up will include both x-ray and optical diagnostics. We will describe each diagnostic system and present the experimental results obtained. In particular, the discussion of the x-ray scattered data, will require the support of simulations. We will be able to evidence interesting effects of strong ion correlations on our scattered spectra.
Janus experiment will then be discussed. Here, only x-ray diagnostics were included in the set up. The main results obtained at LULI will thus be used to analyse the data.

## 6.1 Experiment at LULI

The LULI experiment presents two main aspects of relevant interest. First of all, for the first time, scattering results have been obtained in the collective regime. The simultaneous use of optical rear side diagnostics, routinely used in shock wave experiments, then allowed a cross check of this novel technique.

In this section, after a description of the experimental set-up, we will first determine the plasma parameters from the analysis of the optical diagnostics data. We will then report the x-ray scattered spectra obtained at different times in the evolution of the plasma. In this way, different plasma states will be probed. A x-ray scattering code will be used for the interpretation of the results. Agreement between simulations and experimental data will be found only when strong coupling and degeneracy effects are

considered in the code. A quick discussion on the theoretical basis of these aspects will also be given. Finally, we will illustrate the main results, comparing the simulated spectra with the experimental data.

### 6.1.1 Experimental set up

The experiment was performed on the LULI2000 facility. The laser has two beams delivering up to 1kJ each at the principal wavelength 1053nm in a squared pulse, whose length can be varied in the range 0.8-5 ns. Both beams were converted into $2\omega$ light by means of KDP crystals. The conversion efficiency was about 40% so that each beam could furnish up to 400 J of green light. On fig.6.1 we show the experimental set up. One beam was used to produce the x-ray source while the second was employed to generate a high density plasma through shock compression.

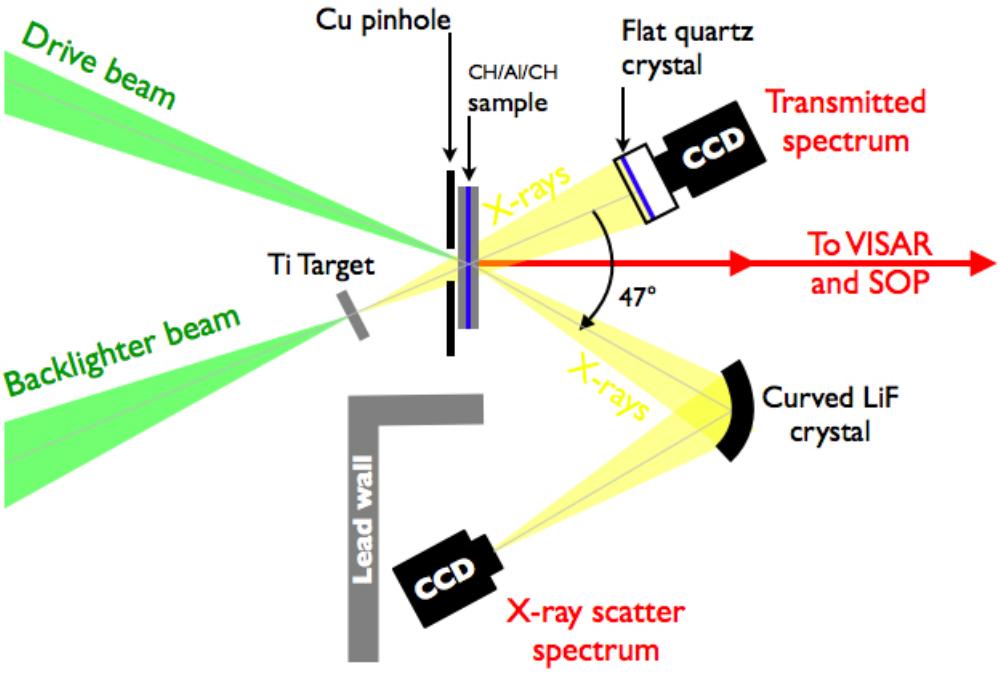


**Figure 6.1:** *Schematic representation of the experimental set-up at LULI.*

The "north" beam (backlighter) was used to produce an intense x-ray source using a 5 $\mu m$ thick titanium foil. The generated radiation is the typical x-ray spectrum emitted from thermal plasmas produced with long pulse lasers. In our conditions, the Ti He-$\alpha$ line, centred at 0.26 nm, was the most intense feature. Following previous work, [1], maximum conversion efficiency is obtained with an intensity of the order of $10^{15} W/cm^2$. We were able to reach this intensity by focusing the 400 J beam in a 100 $\mu m$ FWHM spot. According to [1], a ns pulse can produce up to $\sim 4 \cdot 10^{12}$ $photons/(J \cdot sr)$ in the

He-$\alpha$ line and its satellites. With 400 J available, we could achieve up to $\sim 1.6 \cdot 10^{15}$ photons/sr, which was sufficient to have a detectable scattered signal from our plasma.

A short temporal duration of the x-ray source is highly suitable as it allows probing a unique plasma state. Since the x-ray thermal emission (He$\alpha$ line) lasts for the entire laser duration (at least), it is desirable to use short pulse beams. In our case, the choice of the laser temporal length was an important issue. First, at the time of the experiment, short pulse was not available yet on the LULI2000 facility and only ns beams were accessible. In addition, the two beams were generated by the same oscillator, which represented a further limitation on the shortest useful pulse duration. Indeed, a long enough pulse is required to generate a steady shock, necessary to create uniform plasma conditions. To satisfy both requirements, we have chosen a 1 ns squared pulse as the best compromise.

Dense plasma conditions were created using the "south" beam (drive beam). A phase zone plate (PZP) [2] was employed to eliminate large scale spatial intensity modulations and to obtain a flat intensity profile in the focal spot. A PZP is made of a Fresnel lenses array, each with a long focal length $f_z$. The Fresnel lenses are randomly dephased by 0 or $\pi$ so that the laser coherence is broken and smoothing effects are obtained. The PZP are placed in the vacuum chamber just after the focusing optics, of focal length f. The laser beam is thus divided into many small beams which are focused at a different position on a plane at distance $f_{tot}$, with $1/f_{tot} = 1/f + 1/f_z$. Because $f_z \gg f$, $f_{tot} \sim f$, all the small beams are superimposed on the plane which is close to main lens focusing plane. The zero diffraction order of each Fresnel lens is then superimposed giving a profile characterized by a central peak. By defocusing by a few hundred microns, we can find an optimal position where the focal spot profile is determined by the higher diffraction orders. It results in a supergaussian spatial profile, with a FWHM depending on the plate characteristics. The best position was experimentally found by directly looking at the focal spot by means of a microscope objective placed at the chamber center. In our experiment we have used a large flat top region, of the order of $900\mu m$ FWHM, large enough to be sure that the scattering radiation came from the shocked part of the sample.
The sample was an aluminum plasma created by shock compression of a multilayer CH/Al/CH sandwich target. The CH layers were 4.5 $\mu m$ thick, while the Al thickness was 6 $\mu m$. The aluminum layer was compressed by the shock and its expansion was constrained by the last plastic layer. A 1 mm pinhole on a thick copper substrate was glued on the target to limit the collection of the radiation scattered by the shocked region only. The sample target was placed at the chamber center, 7mm away from the backlighter. Such a large distance allowed to reach a more uniform illumination on the

target and prevent it from being perturbed by the source radiation.

A high magnification microscope was used to monitor the target chamber center. The rear side diagnostics could then be used to cross check the alignment, so that we can estimate a precision of $\sim 30 - 40\mu m$ in the determination of the target center. The two targets were mounted on a common stage, which had 6 motorised motions. In a first step, the principal target was aligned at the chamber center. Successively, the whole stage was moved by a known vector, representing the correct backlighter distance from the principal target. A small motor on the backlighter mount, then, allowed to adjust its positioning. Finally, moving back the whole stage in the original position, each target was at the correct position. A further lens system imaging the backlighter position allowed to verify the final alignment.

The main diagnostic consisted in a crystal spectrometer collecting the scattered radiation and focusing it on a X-ray CCD camera in the Von Hamos configuration. Another spectrometer was used to monitor the source by looking at the transmitted radiation. A system of rear side diagnostics (VISAR+SOP) was also implemented in the set up to infer generated plasma state. By measuring the shock velocity in CH or in Al, from these diagnostics we could deduce important plasma parameters such as temperature and density, the EOS of the aluminum being well known, [3]. A precise knowledge of the plasma parameters allows to test the results obtained with the x-ray scattering technique, as well as scattering calculations to which they are compared.

#### 6.1.1.1 X-ray diagnostics

The x-ray source was spectrally resolved with crystal spectrometers coupled to CCD camera detectors. We used two different crystals to collect the transmitted and scattered radiation, accomplishing different requirements.

The source emission was directly monitored by collecting the transmitted radiation. In this case no particular requirements were imposed nor on efficiency neither on dispersion properties. A simple flat Si crystal was thus suitable to obtain high quality spectra. The spectrometer was placed directly on the backlighter beam axis, collecting the radiation transmitted through the plasma. For Si(111) crystals the distance between the crystal planes is $d = 3.13$ Å and first order Bragg condition for 2.6 Å radiation is satisfied for an angle $\theta = 24.6°$. Recording the source emission at each shot helped in the analysis of the scattered data, first giving a good control of the incident radiation spectrum and then allowing to characterise new features and their respective intensity in the scattered spectra.

When dealing with x-ray Thomson scattered radiation, one of the main experimental difficulties is due to the low intensity signal produced. A high efficiency spectrometer is thus necessary to enhance the intensity of the collected signal and make it observable with standard detectors. Bent crystals are much more efficient than flat crystals because

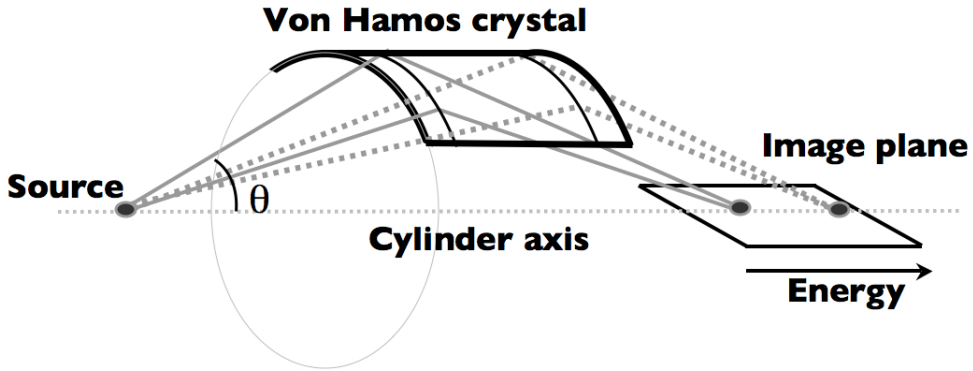


**Figure 6.2:** *Schematic diagram of a Von Hamos spectrometer. The radiation is focused on the spectrometer axis.*

of their focusing properties and are hence more suitable for low intensity signal detection. In a Von Hamos scheme, represented in fig.6.2, a crystal is bent into a cylindrical surface and both the source and the spectrum lie on the cylinder axis. A bent crystal in a Von Hamos configuration can be $10^2 - 10^3$ times more efficient than a flat one, when considering small source sizes. In a plane perpendicular to the spectrometer axis, the Von Hamos scheme has a large collection solid angle and focuses the collected radiation on the axis itself. Besides a higher luminosity, cylindrically bent crystals also present good dispersion properties. The diffraction planes are parallel to the spectrometer axis which means that from the dispersion point of view a curved crystal in a Von Hamos scheme behaves like a flat one. Different wavelengths are diffracted according to the Bragg's law on the cylinder axis.

In the experiment we used a LiF(200) crystal. It was positioned in a forward scattering configuration, which allowed us to reach a collective scattering regime. The smallest the scattering angle is, the easier the achievement of collective regimes. In our experiment though, the smallest observable angle was imposed by the actual dimensions of the crystal and the detector mount. Indeed, they were required not to obscure the rear side diagnostic field of view. The smallest angle we could probe was therefore 47°.

The distance of LiF(200) reticular planes is $d = 2.014$ Å so that He-$\alpha$ radiation at 2.61Å is reflected in the first order at a Bragg angle of $\theta = 40°$. The Bragg angle together with the crystal focusing properties, which are directly related to the curvature

radius, fixed the geometry of the target-crystal-detector system.

The spectrometer axis was aligned along the target surface, as shown in fig.6.3. The

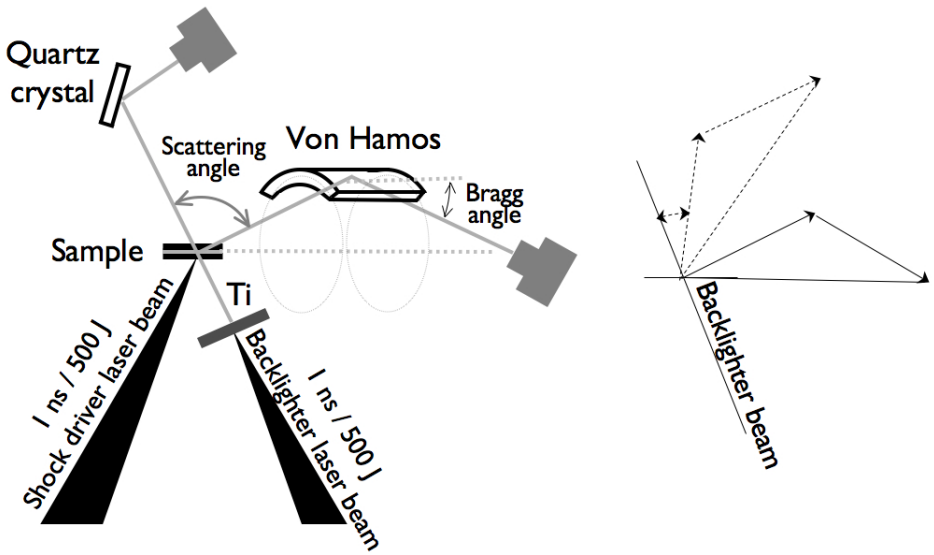


**Figure 6.3:** *In the Von Hamos configuration the detector is aligned along the target surface and they both lie on the spectrometer axis. The collecting scattering angle can be changed by rotating the whole "triangle" target-crystal-ccd around the target center chamber.*

whole target-crystal-detector ensemble could then be moved around the target chamber center (TCC), according to the scattering angle to be probed. After having set the crystal and the CCD at the positions imposed by the Von Hamos geometry, a first adjustment of the crystal focusing was done by placing at TCC a small optical fiber, in which a He-Ne laser was injected. The reciprocal distances could be set by optimizing the He-Ne focal spot, directly looking on the CCD camera. A final alignment was then performed by shooting on a Ti foil at the TCC and optimizing the acquired x-ray spectra.

The LiF crystal was also chosen because of its high reflectivity, which made the weak scattered signal detection possible. LiF reflectivity is one of the highest among the low mosaic crystals; for the LiF(200) the integrated reflectivity at first order is 1.57 mrad, $\sim$ 2.5 higher than the efficient Ge(111) or even $\sim$4.5 times higher than Si(111), whose reflectivity is $\sim$ 0.346 mrad, [4].

Being able to resolve the plasmon feature was the main condition that imposed the resolution requirements. For our experiment, plasmon energy was of the order of $\sim 20eV$ so that a spectral resolution of this order was all we needed. In our conditions, a modest resolution $\lambda/\Delta\lambda \sim 10^3$ corresponding to $\sim$5 eV, was sufficient to resolve the plasmon feature, so that dispersion requirements did not put a real constraint on the choice of the LiF crystal.

#### 6.1.1.2 Plasma diagnostics

As previously mentioned, if we consider the Al EOS known, the state of the aluminium plasma can be inferred by measuring a single parameter, the shock velocity in our case. As for the x-ray radiography, the inferred state can be compared to the measurement obtained with the new diagnostic, allowing a cross calibration of the technique. Furthermore, an accurate characterization of the plasma was of particular importance for a correct interpretation of the scattering results, as they revealed a high sensitivity to degeneration and coupling effects.

Two rear side diagnostics were implemented in the set up for the shock velocity measurement: time resolved self emission (SOP) and VISARs interferometers. A detailed scheme of this specific part of the set up is shown in fig.6.4. The sample targets were $CH(4.5\mu m)/Al(6\mu m)/CH(4.5\mu m)$ sandwiches so that the velocity in the last transparent plastic layer could be measured [5].

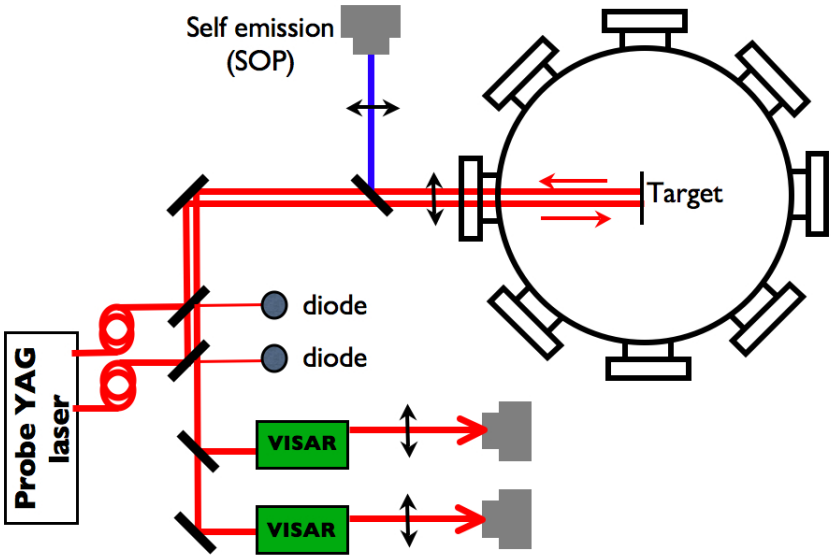


**Figure 6.4:** *Part of the set up relative to the rear side diagnostics for the plasma conditions measurements.*

Both the diagnostics, imaged the target rear side on the detectors (streak cameras). For the VISARs, a probe YAG laser at 1064 nm with a 8 ns gaussian pulse was injected into two optical fibers. Being reflected by the target rear side, it is injected in two VISARs interferometers with different sensibilities. The interference pattern on the last beam splitter of each interferometer was then imaged onto two streak camera slits, one for each VISAR.

**Self emission diagnostic** The sudden temperature increase associated to the compression induces the shocked plastic to emit thermal radiation (self-emission) which is transmitted through the transparent, unshocked, cold CH. By simply imaging the target rear side, we can collect the emitted radiation and measure the shock transit time in the last CH layer. It is then straightforward to determine the velocity of the shock knowing the thickness of the layer.

The shock transit time is measured as the time interval during which radiation is emitted, which corresponds to the time delay between the shock breakout at the Al-CH and CH-vacuum interfaces. At earlier times the emission is blocked by the opaque aluminum, while, after the break out in vacuum, the plasma cools down because of the expansion and, consequently, emission ceases rapidly.

**The VISAR interferometer** Instantaneous shock velocity were inferred from the VISARs. For a transparent material which becomes reflective under shock compression, the VISARs give access to both mean and instantaneous shock velocity, allowing a higher precision in the velocity measurement. A detailed description of the VISAR can be found in [6]. Here we just present the main principles, in order to be able to understand the experimental data.

The VISAR (Velocity Interferometer System for Any Reflector) was proposed in 1972 by Barker and Hollenbach [7]. It is a velocity interferometer which allows a high precision measurement of the velocity of any moving reflective surface and it is widely used in shock wave experiments. The velocity measurement is obtained from the interferometry pattern, considering in particular the fringe shifts, which are directly linked to the Doppler effect.

Among the various possibilities for the interferometer configurations we have chosen to use the Mach-Zendher geometry proposed by Celliers *et al.* in [8], where the two arms are recombined at a small angle. Its design is shown in fig.6.5

A probe beam is made reflect on a moving surface and it is then injected in the VISAR. The first beamsplitter BS1 separates the beam into two parts. One part is transmitted to a mirror M1, while the other part is reflected to a second mirror M2, in front of which the etalon is placed. The two beams are then recombined at the beamsplitter BS2, where they interfere. The etalon introduces a few ps time delay $\tau$, so that the fringe pattern is representative of the interference between light reflected at a given time $t_0$ and light reflected at time $t_0 + \tau$. In a usual interferometer the time delay is obtained by changing the length in one of the two arms. To produce a path length difference able to evidence the Doppler effect for $\sim$ 10km/s (typical of our shocks), the difference in length should be of $\sim mm$. Such an important length

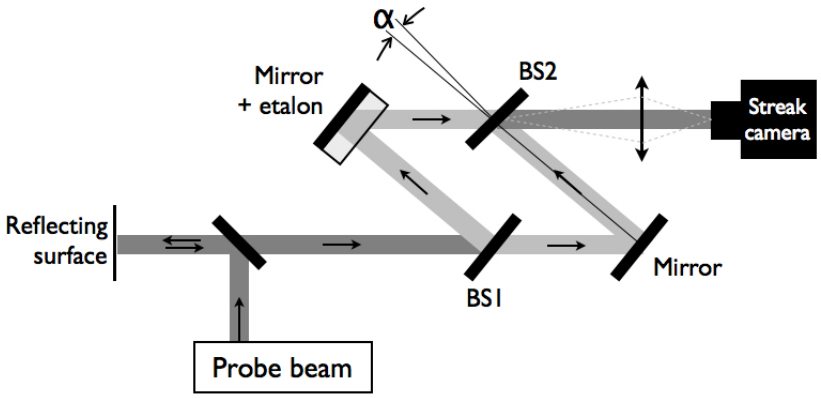


**Figure 6.5:** *Mach Zender configuration of the VISAR.*

difference, though, would make the light loosing coherence. The use of the etalon in the VISAR allows, instead, to introduce a time delay, while keeping the coherence. To satisfy this condition, the VISAR is aligned in such a way that the two arms have the same apparent length. In a first step, a "null position" is determined, by removing the etalon and setting a perfectly equal path for the two arms. The etalon is then placed in front of the mirror M2. The whole ensemble etalon+mirror is moved by a distance d, calculated to place the image of the mirror plane, as viewed through the etalon, coincident with the null position. The distance d is calculated as:

$$d = e(1 - \frac{1}{n})$$

where e is the etalon length and n its refractive index. The resultant optical time delay $\tau$ is then:

$$\tau = \frac{2e}{c}(n - \frac{1}{n})$$

The velocity v(t) of the reflecting surface affects the interference pattern because of the wavelength change $\Delta\lambda$ associated to the Doppler effect:

$$\Delta\lambda = \lambda_0 \left[1 + 2\frac{v(t)}{c}\right] \tag{6.1}$$

In particular the Doppler shift is manifested as a fringe shift F at the output of the interferometer:

$$F = (1 + \delta)\frac{c\tau}{\lambda_0}\frac{\Delta\lambda}{\lambda_0} \tag{6.2}$$

where the factor $1+\delta$ accounts for the dispersion of the etalon. This fringe shift can then be related to the reflecting surface velocity U by the velocity interferometer equation [7]:

$$U = \frac{\lambda_0}{2\tau(1 + \delta)}F \tag{6.3}$$

In our targets, the probe beam is reflected at the interface between the cold and hot CH, which metallizes under the shock compression, at relatively low pressures ($\sim 1$ Mbar [9]). Because the probe beam propagates through a medium (CH), the refractive index $n_{CH} \neq 1$ affects the optical path length, modifying the final equation:

$$U_s = \frac{\lambda_0}{2\tau(1+\delta)n_{CH}}F \tag{6.4}$$

From the fringe shift we can thus access to the instantaneous shock velocity in the plastic. By imaging the output beamsplitter (BS2 in fig.6.5) on the streak camera slit, we can then record the fringe shift as a function of time, accessing the shock velocity temporal evolution.
It should be underlined that from the fringe pattern, it is possible to measure only the fractional part of the fringe shift and an ambiguity on the integer part arises when the phase shift is greater than $2\pi$. Physical considerations or other independent velocity data must be used to resolve this ambiguity. Another method consists in recording the data simultaneously with two VISARs of different sensitivities. The so called standard sensitivity of the VISAR is often quoted as the velocity-per-fringe, VPF.

$$VPF = \frac{\lambda_0}{2\tau(1+\delta)} \tag{6.5}$$

In our targets, we need to account for the CH layer and the real sensitivity becomes: $VPF = \frac{\lambda_0}{2\tau(1+\delta)n_{CH}}$.
With a dual interferometer set-up, the comparison of the two independent data sets lead to a unique determination of the Doppler shift and of the resulting velocity.
The velocity values inferred by the VISARs can be accurate up to few %, the precision depending only on fringes quality and on the accuracy in determining the phase shift.

### 6.1.2 Plasma state

We will present here the shock velocity measurements from the self emission and VISARs diagnostics in our experiment. The inferred values will allow to perform hydrodynamic simulations from which we will access to all the other plasma parameters.

#### 6.1.2.1 Self emission measurement

Fig.6.6 shows a typical image obtained with the self emission diagnostic. An interferential filter at nominal wavelength $450 \pm 30$ nm was placed in front of the slit, so the recorded radiation lies in the blue part of the visible spectrum.

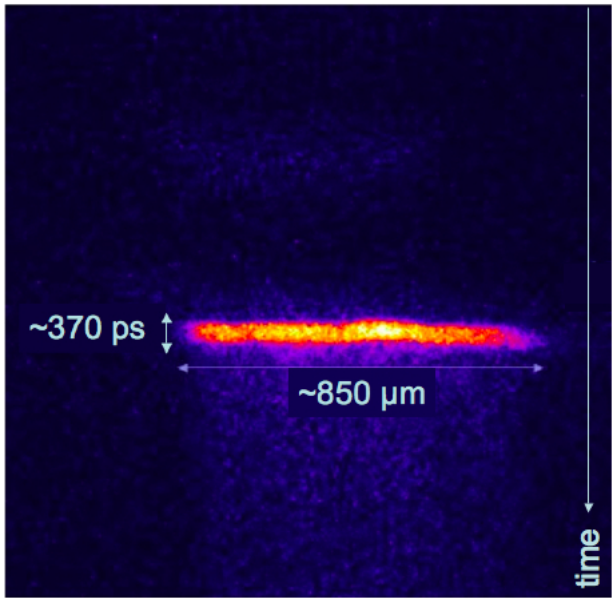


**Figure 6.6:** *Self emission data.*

In fig.6.6 emission from the rear side CH layer, corresponding to the shock transit time, lasts 365±20 ps. Considering the CH thickness, 4.5 $\mu m$, we deduce a mean velocity of $\sim 12.33 \pm 0.65\ km/s$. A 10 magnification factor in the optical system allowed to record the emission from the whole shocked part of the target. It is interesting to note the spatial shape of the emission, which reflects the spatial structure of the shock. The flat spatial profile is typical of a PZP smoothed beam with a flat region of $\sim 850\mu m$. This spatial shape differs from the gaussian profile arising from the RPP we had used in the radiography experiment.

#### 6.1.2.2 Visar measurement

From the VISAR data, it is possible to determine both mean and instantaneous shock velocity. The image corresponding to the same shot shown in fig.6.6 is presented in fig.6.7 for one of the two VISARs. Time goes from the bottom to the top, while the right-left axis is the spatial dimension. Each line corresponds to a horizontal cut in the interference pattern taken on a time interval corresponding to one pixel. The temporal resolution is determined by the streak camera sweep speed, 10.4 ps/px in fig.6.7. In the first part of the image, the interference pattern does not change. This situation corresponds to the reflection of the probe beam from the unperturbed CH/Al interface. When the shock wave breaks into the last CH layer, at time $t_1$, it induces a rapid ionisation of the plastic which starts reflecting the probe laser beam. From this instant, the reflective surface (the shock front) moves at the shock velocity resulting in a sudden

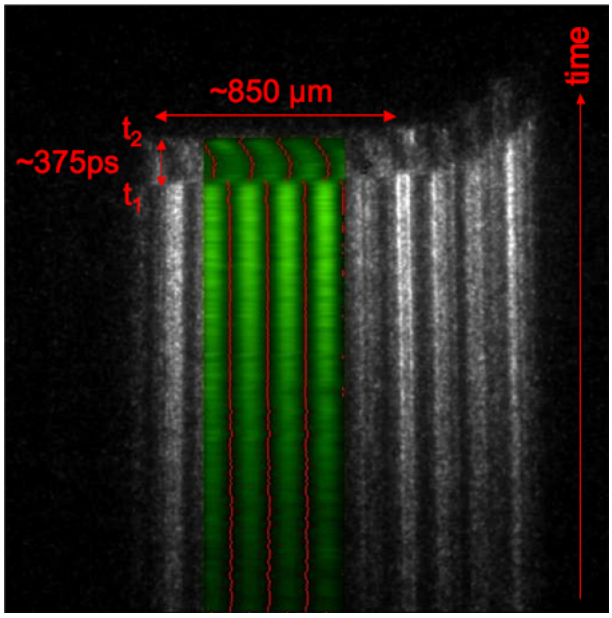


**Figure 6.7:** *VISAR data for the same shot as fig.6.6. The red curve corresponds to the numerical fit done to extract the phase as a function of time.*

shift in the fringes. If the shock velocity is constant in time, the fringes remain unshifted afterwards. A decaying shock wave is instead characterized by a continuous movement in the interference pattern. When the shock wave breaks out into vacuum, at time $t_2$, the expanding plasma absorbs the probe beam and the fringes disappear. We can thus first estimate the mean velocity by measuring the time delay between $t_1$ and $t_2$, corresponding to the shock transit time in the plastic layer. For fig.6.7 we obtain 375±31 ps, i.e. we deduce a mean shock velocity in the plastic of $12.00 \pm 1.08\ km/s$, in good agreement with the self emission diagnostic.

To determine the instantaneous velocity as a function of time we need to infer the fringe shift at each time with respect to the initial stationary pattern. A numerical fit was used to calculate the phase at each pixel and the results are represented as a red curve in fig.6.7. The corresponding velocities are found by using the eq.6.4. In the experiment we used etalons of thickness 8.13 mm and 15.18 mm corresponding to standard VISARs sensitivities of $12.7\frac{km}{s \cdot fringe}$ and $6.8\frac{km}{s \cdot fringe}$ respectively. Taking into account the cold CH refractive index, $n_{CH} = 1.57$, the real sensitivities were 8.1 $\frac{km}{s \cdot fringe}$ and $4.3\frac{km}{s \cdot fringe}$ The uncertainty in the integer part of the fringe shift was completely resolved by the combined use of two VISARs and from the self emission. The velocity profile for the interferometer pattern is shown in fig.6.8 for the VISAR with a 8.1 $\frac{km}{s \cdot fringe}$ sensitivity.

As shown in fig.6.8, the shock is decaying from $12.8 \pm 0.4\ km/s$ at $t_1$ down to $\sim$ 10 km/s when it breaks into vacuum ($t_2$).

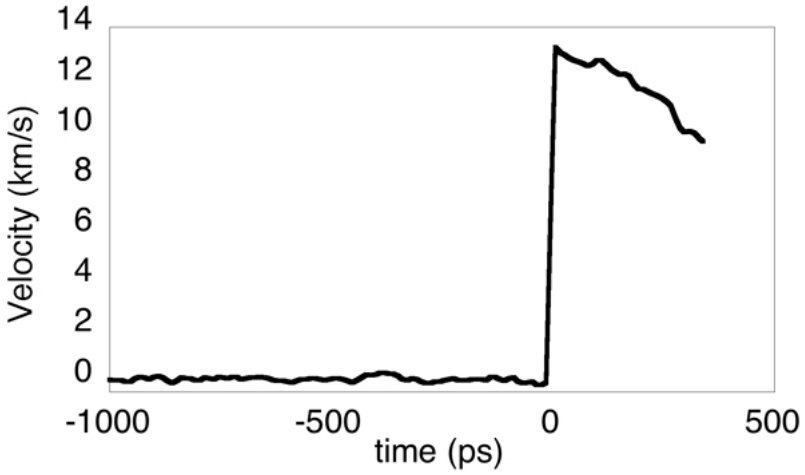


**Figure 6.8:** *Velocity vs time deduced from fig.6.7. The time 0 corresponds to the shock breakout into the plastic layer.*

#### 6.1.2.3 Hydrodynamic simulations

In order to deduce the plasma parameters we have run hydrodynamic simulations with the code MULTI [10]. This code is currently used in the analysis of shock wave experiments and it has already been widely validated. As we did not have a reliable measurement of the energy on the target, we have used the laser intensity as a free parameter in the simulations. By varying the laser intensity in the code, we can simulate different shock velocities in the plastic. We could reproduce the experimental ∼12 km/s mean shock velocity in the last CH layer using an intensity of $I = 0.5 \cdot 10^{13} W/cm^2$. In fig.6.9 we show the pressure as given by the simulation for such a laser intensity. Here the 0 position represents the target rear side, while the drive laser beam comes from the right. The shock wave propagation induces a high pressure increase. The shock transition at the CH-Al and Al-CH interface is characterized by the appearance of the reflected waves. At the first interface, situated at 10.5 $\mu m$ in this representation of the target, the shock goes from the CH to the Al layer. A shock is transmitted in the Al layer and the reflected shock propagates in the CH (see 2.3.1). The pressure of the reflected shock is ∼2.5 Mbar. At the other interface, at 4.5 $\mu m$ the situation is reversed and a relaxation wave travels back in the Aluminium lowering the pressure down to 1.1 Mbar while a shock of the same pressure is transmitted in the last CH layer. According to SESAME EOS, this pressure corresponds to an instantaneous shock velocity of $\sim$ 13.2 km/s. Nevertheless, since the shock is not steady, during its propagation the pressure is decreased down to $\sim$ 0.6 Mbar, corresponding to a shock velocity of $\sim$ 10 km/s, in good agreement with the experimental results.

With a good confidence on the laser intensity used in this simulation and consider-

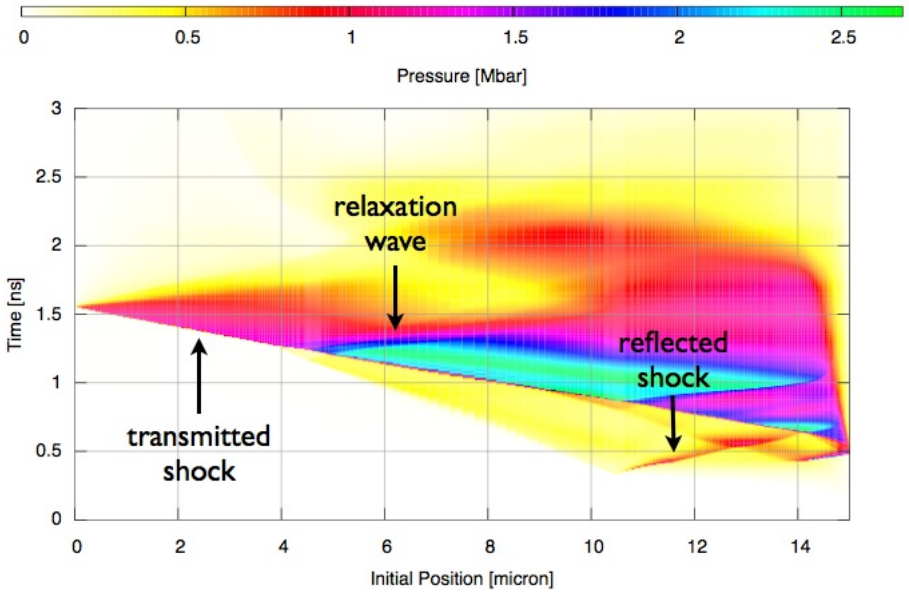


**Figure 6.9:** *Pressure in the* $(x,t)$ *plane from hydrodynamic simulation for a laser intensity of* $0.5 \cdot 10^{13} W/cm^2$. *The maximum laser intensity is at 0.6 ns.*

ing that the aluminum equation of state is well known in this pressure regime, we can deduce all the plasma parameters. In particular we have access to the electron density, temperature and ionization level which are the main parameters in the physics of the scattering process.

The VISARs and self-emission were run at each shot allowing to monitor any change in the plasma conditions. In particular, we wanted to investigate different plasma states by changing the shock driver beam /x-ray source delay. In the experiment, the backlighter beam was either 0.5 or 5 ns later than the shock driver beam. Unfortunately, as mentioned previously, we could not probe a unique plasma state using a ns laser to generate the x-ray source. Indeed, the He-$\alpha$ radiation is emitted during a long enough time for the plasma to significantly evolve. In fig.6.10, we show the pressure 500 ps after the laser has reached its maximum intensity and its time evolution during 1ns.

The plasma considerably changes during the probing time, so that we can only determine the mean conditions. In fig.6.11 we present the mean values encountered during the acquisition time as given by the simulations for the electronic density, ionization and electronic temperature in the two cases: 0.5 and 5 ns after the laser maximum (set at 0.6 ns in the simulation).

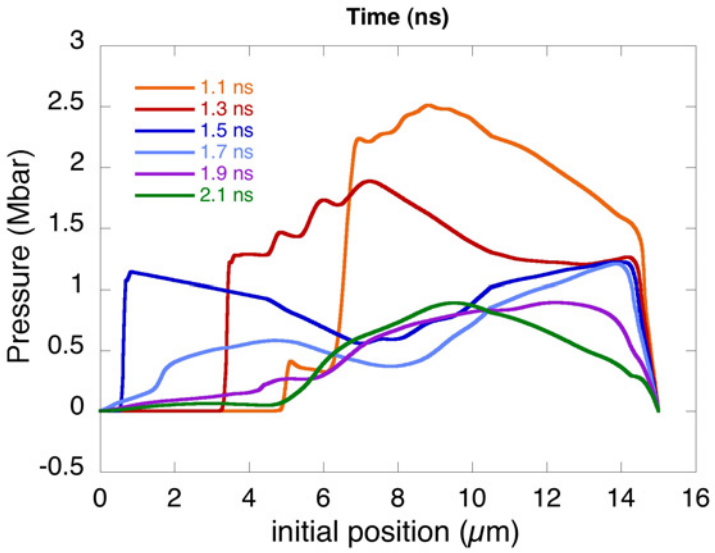


**Figure 6.10:** *Pressure 500 ps after the laser has reached its maximum intensity and its temporal evolution during 1ns.*

### 6.1.3 Spectrum calibration shots

In the analysis of the scattered spectra, most of the information is contained in the energy shifted component from the incident radiation. If the incident spectrum is composed by a single line, the identification of the scattered feature is quite straightforward. Nevertheless, in our spectra the incident radiation has a line structure which complicates the identification of the different scattered features. A good knowledge of the incident radiation spectrum associated to a precise characterisation of the crystal dispersion properties is necessary for a correct interpretation of the data. We have therefore performed an absolute calibration of the source spectrum.
The calibration is done by shooting on a Titanium foil at the target center chamber, in the exact position where the scattering sample lies in a "scattered" shot. The recorded spectra then give the absolute position of the radiation source that can be used as a reference in the scattered shots.

The x-ray source spectrum in our experiment is typical of the plasma emission generated by a ns pulse laser. At laser intensity of $10^{15-16} W/cm^2$, the generated plasma is very hot and the K-shell emission is the most intense. A typical spectrum obtained is shown in fig.6.12. The adequate signal level was obtained with an appropriate choice of filters: a $75\mu m$ thick Al together with 125 $\mu m$ Be for the calibration shots, the total transmission being $10^{-2}$. We can clearly see that the most intense line is the resonance of the He-like ion, corresponding to the transition $1s2p - 1s^2$, often called He-$\alpha$. The

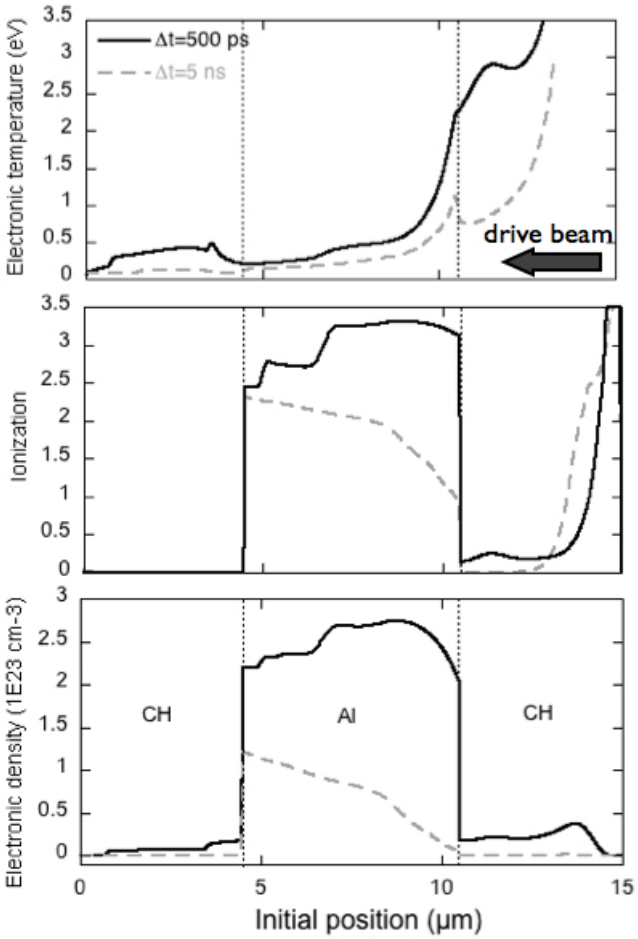


**Figure 6.11:** *Electron temperature (a), ionization (b) and electronic density (c) from hydrodynamic simulations at 500 ps (solid black line) and 5ns (dotted gray line) after the laser maximum.*

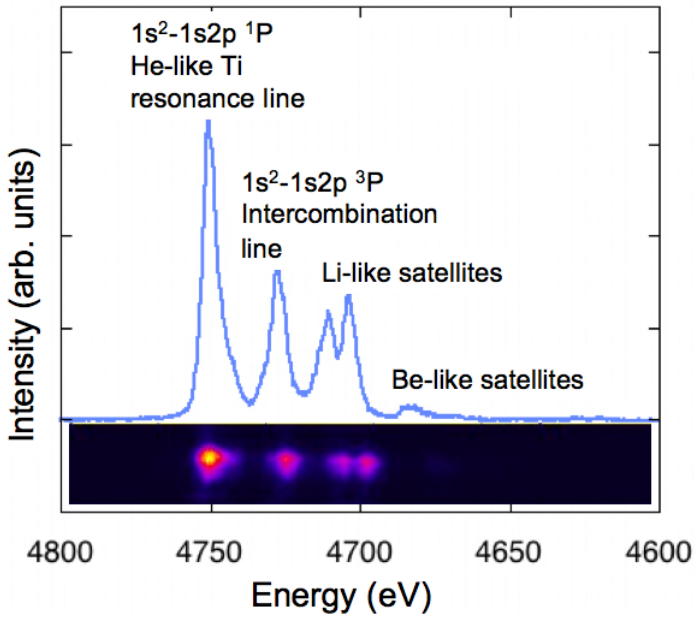


**Figure 6.12:** *Spectrum emitted from a Ti plasma created by a ns pulse laser. The most intense line is the $He\alpha$ resonance line with the intercombination line. Li-like and Be-like satellites are also present.*

ions interested in this process have 2 electrons and thus come from the 20 times ionized Ti atoms. Transitions of the same type (1s-2p) can anyway occur in weaker charged ions, where one or more electrons lay in the upper levels. For example Li-like ions, with 3 electrons, can give transitions of the type $1s2p2l - 1s^22l$. The corresponding emitted lines are close to the resonance He$\alpha$, but they are shifted towards the weaker energies due to the screening effect of the third electron. These transitions are called resonant line satellites. In our conditions, Li-like and Be-like satellites are observed. Between the Li-like satellites and the resonance there is another intense line: it is a "forbidden" transition, corresponding to the triplet ($S = 1$) $1s2p^3P$ which in principle cannot relax to the fundamental singlet level ($S = 0$) ($\Delta S \neq 0$).
This spectrum was used to determine the dispersion on the detector. The energies of the resonance and of the satellites are tabulated (see for example [11]. In the case of the Ti spectrum we can associate the principal lines observed to their tabulated energies:

- $1s^2\ ^0S$ -$1s2p\ ^1P$ He-like Resonance @ 2610 mÅ (4750 eV)
- $1s^2\ ^0S$-$1s2p\ ^3P$ He-like intercombination @ 2623mÅ (4727 eV)
- Li-like satellites @2632-2636mÅ (4710-4703 eV)
- Be-like satelites @2648mÅ (4680 eV)

By measuring the distances between the different lines on the CCD, we find the dispersion: $0.31 \pm 0.05$ eV/px. The calibration allows to determine the energy of new features eventually appearing during the scattering process. This process, as already underlined, need that the target/crystal/detector configuration remains unchanged in all the shots. To verify this condition, a calibration shot was regularly taken before the scattering shots. The agreement of all these "calibration shots" evidences a good confidence in the alignment procedure, enabling us to consider the absolute position of the He-$\alpha$ line as a reference.

The precision in the alignment is here a big issue, as any difference in the positioning between the Ti foil and the sample target would have been recorded as an energy shift in the spectra. For this reason, as previously mentioned, we have set up an alignment diagnostic system that allowed a $30 - 40$ $\mu m$ accuracy in the target positioning. This error is totally negligible in the analysis of the scattered data as it leads to a shift $< 0.4$ eV.

### 6.1.4 Scattering results

Before presenting the scattered spectra, we will discuss some general considerations on the obtained signal, showing that it comes from the shocked target only and that its intensity is consistent with what expected for Thomson scattering.

**General considerations** In order to get information on the plasma parameters from the x-ray scattered spectra, the crucial condition is that the observed signal comes from the shocked plasma. In order to avoid collection of the signal from the unshocked part of the target, a 100 $\mu m$ thick Cu pinhole of 1mm diameter was glued on the sandwich target. In this way, the incident x-ray radiation only interacted with the compressed part of the target, the spatial extent of the shock being ∼850-900 $\mu m$, see fig.6.6.

A test shot was then taken to verify that the recorded signal came uniquely from the sample target. In the test shot the x-ray beam is incident on the Cu pinhole positioned at the center of the chamber but no sample is put behind it. In this case no signal was detected, demonstrating that nothing except the sample is responsible for the observed scattered spectra.

Another important consideration must be done on the scattered signal intensity. In all the scattered shots, we reduced the number of filters, only leaving 125 $\mu m$ thick Be, which corresponds to a ∼0.9 transmission. Considering the ratio of CCD counts in the calibration and in the scattered shots, taking the filters transmission into account, we can estimate that $\sim 10^{-5}$ of the incident light is contained in the scattered spectrum.

This result can be compared with the expected value, which we can simply estimate as following. The number of incident photons is $N_{IncPh} = E_i \eta \Omega_2 A$, where $E_i$ is the laser energy for the calibration shot, $\eta$ the conversion efficiency of the Ti He$\alpha$, $\Omega_2$ the solid angle collected by the crystal and $A$ a constant accounting for the crystal (reflectivity, etc..) and CCD (quantum efficiency, collection angle,...) properties. In the same way, we can estimate the number of scattered photons as $N_{ScattPh} = N_{IncPh}\Omega_1 N \sigma_T A \Omega_2 = E_s \eta \Omega_1 N \sigma_T A \Omega_2$. Here, $E_s$ is the laser energy of the scattering shot, $\Omega_1$ the incident radiation solid angle, determined by the pinhole dimensions and the backlighter-sample distance, $\sigma_T$ the Thomson scattering cross section for a single electron and N the number of electrons per unit area. This last parameter can be estimated as $N = N_e x$, $N_e$ being the electron density and $x$ the thickness of the target. We can thus estimate:

$$\frac{N_{ScattPh}}{N_{IncPh}} = \frac{E_s}{E_i} N_e \sigma_T x \Omega_1 \tag{6.6}$$

Assuming the aluminum target at solid density and a solid angle of $5 \cdot 10^{-3} - 10^{-2}$ rad from the experimental configuration, we find a fraction of $5 \cdot 10^{-6} - 1 \cdot 10^{-5}$, scattered photons, in agreement with our experimental data.
We will now present the main features observable in the scattering results obtained at the two probed times, 500ps and 5ns after the maximum of the shock drive beam. For all the shots presented here, the scattering angle was 47°±0.8. For this configuration the expected Compton shift is 14±0.4 eV, with a **k** vector of 1.92 Å. The scattering regimes as well as other important parameters, such as coupling constants, depend on the plasma conditions.

**Scattering results in highly correlated regime** When probed the sample 500 ps after the laser maximum, the plasma is extremely dense ($N_e \sim 10^{23}\ cm^{-3}$), while its temperature is quite low (T$\lesssim$1 eV). The values for the electron density, temperature and ionization obtained from the hydrodynamic simulations are shown in 6.11, as the solid black lines. As we have already mentioned, these are not instantaneous values, but the mean conditions encountered during the whole acquisition time interval, longer than 1ns. We deduce a mean electronic density of $2.5 \cdot 10^{23} cm^{-3}$, a mean temperature of 0.35 eV and an average ionization of 2.9. Under these conditions the electrons exhibit high degeneracy level, $T_e/T_F$ ∼0.03 and a low degree of coupling. On the contrary, the ions are extremely highly coupled, with a coupling parameter $\Gamma \sim 240$, while they remain classical. In multi-component plasmas the effect of screening tends to attenuate the electrostatic interactions and it has been suggested [12] that a more appropriate coupling parameter is $\Gamma_s = \Gamma \exp(-k_s a) \sim 19$ , where $1/k_s$ is the short-range screening length. The scattering regime is quasi collective, with $\alpha \sim 1$ .

The scattered signal obtained is shown in fig.6.13, solid red line, together with the transmitted spectrum recorded (dotted blue line). We can notice that the transmitted

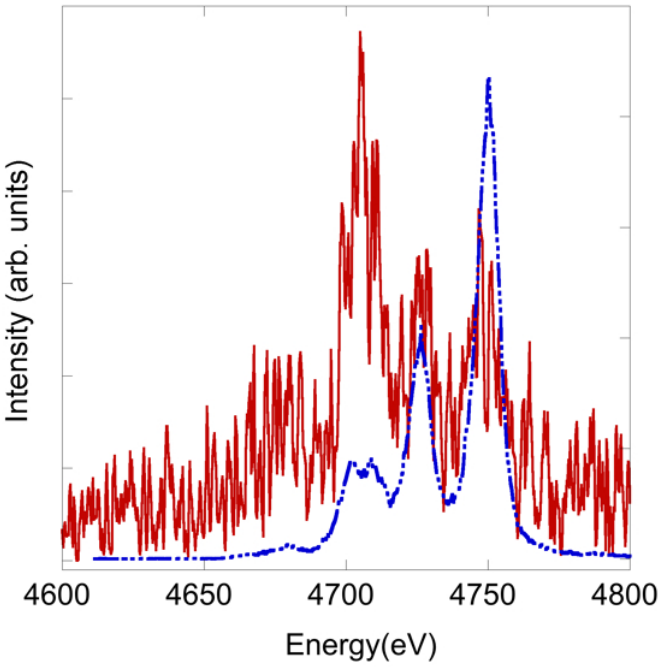


**Figure 6.13:** *Scattered spectra, solid red line, and transmitted spectra, dotted blue line, for a shot taken with a temporal delay of 500ps between the backlighter and the shock drive beams.*

spectrum is the typical Ti emission (fig.6.12), the He-$\alpha$ being the most intense line. In the scattered spectrum, on the contrary, the strongest signal appears at the satellites energy position. Indeed, this remark reveals the most interesting result evidenced in our data: the inelastic scattered component appears stronger than the elastic one. This observation is in contrast with previous results, [13], which (we must underline) were obtained in a different regime, i.e. on weakly coupled plasmas.
Several considerations lead us to the stated conclusion. First, the intense feature cannot be the elastic component from the satellites lines only, as it would be considerably weaker than the elastic scattering from the He$\alpha$ line. The difference in energy is in fact too small to cause significant change in the structure factor and the contribution to the elastic scattering is simply proportional to the intensity of each incident line of the source (see eq.3.46). An absorption effect is then also excluded, since the same effect would be recorded by the straight through spectrometer. Indeed, the plasma thickness crossed by the x-ray radiation was similar for both spectrometers due to the set-up geometry. The observed signal is rather a combination of the negligible satellites elastic scattering and a more intense inelastic scattering from free and weakly bound electrons. Moreover bound free transitions from carbon ions in plastic need to be included.

**Scattering results in moderate correlated regime** At later times, 5ns after the laser maximum, the shock has broken out from the target rear side and a relaxation wave travels back in the target. The plasma parameters are now quite different and are

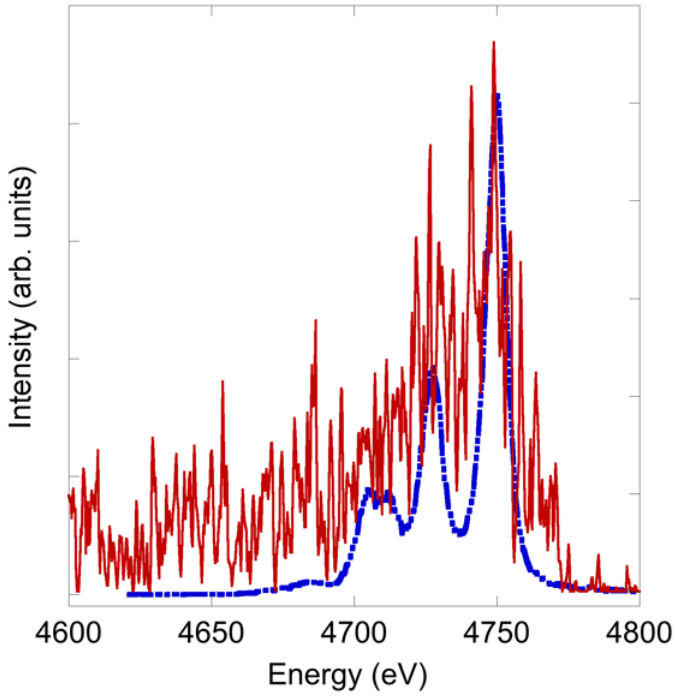


**Figure 6.14:** *Scattered spectra, solid red line, and transmitted spectra, dotted blue line, for a shot taken with a 5ns time delay between the backlighter and the shock driver beam.*

shown in fig.6.11 as dotted gray line. The electron density is lower, $N_e \sim 8.5 \cdot 10^{22} cm^{-3}$, while the temperature is now $T_e$ ∼0.25 eV and the ionization $Z^* \sim 2.1$. Under these conditions, the ion coupling parameter is lower, $\Gamma_s \sim 5$, while $\alpha \sim 0.75$.
The scattered spectrum for this delay is now shown in fig.6.14. This result is significantly different from the one obtained at earlier times. In this case, only the elastic component is observable, while the inelastic feature cannot be clearly distinguished.

### 6.1.5 Data Analysis

In order to understand the importance of the various scattering processes, our experimental data have been compared with x-ray scattering simulations. The code calculates the scattering cross section given by eq.3.46. The partial dynamic structure factors are calculated according to the general analysis done in 3.3.3.5 and in more details in [15]-[16]. This code was already used to interpret scattering data from weakly coupled plasmas in non-collective regimes, [13]-[14], where the temperature and the mean ion-

ization were deduced from the best fit to experimental data.
The most remarkable result evidenced in our data is the low intensity of the elastic Rayleigh scattering, which, at earlier times, appears weaker than the inelastic Compton contribution. This behavior was not observed for weakly coupled plasma and can not be reproduced by the same code if corrections for strong coupling are not included. A correct description of the elastic scattering from our dense plasmas must include a full treatment of ion correlations and self energy correction for the ion mass [25]. We must here underline that two temperatures effects, which can as well lead to a reduction of the elastic component [17], must be excluded in our case. At these densities, energy relaxation time is much shorter than the characteristic hydrodynamic timescale [18]. Thermodynamic equilibrium (with $T_e = T_i$) is reached over the whole plasma except for a small region across the shock front which weakly contributes to the scattered signal.

#### 6.1.5.1 Strong coupling effects

**Debye-Waller factor** In a crystal lattice, scattering does not comes from thermal fluctuations as in the case of the plasma, but it is due to the coherent superposition of diffusing waves from the ion lattice sites. This modifies the scattered spectrum and in particular leads to the appearance of a Bragg peak. In strongly correlated plasmas, an incipient long-range order appears and, even if it does not persist forever, it can be preserved during typical scattering time, [19]. In fact, as a consequence of the long-range of the Coulomb potential, each ion interacts not just with a limited number of neighbours but with all the other particles. Lattice-like effects arises, as "caging" effects [20], for instance, which can appear under extremely strong coupling: each ion finds itself trapped for some period of time in the cage formed by its immediate neighbours, rebounding against it and thus slowing down the fluid diffusion motion. In [21] the macroscopic dynamics of a one component plasma (OCP) in strongly coupled regimes was investigated. It was shown that for $\Gamma \gg 50$ the OCP exhibits a highly correlated fluid-like behaviour undergoing to Wigner-Seitz crystallization at $\Gamma \sim 175$. For our conditions, strong correlations between ions induce collective lattice-like vibrations. In this picture the ions motion can be described as a composition of two different terms: an oscillation (vibration) around the instantaneous center of mass and a global translation (diffusion) of the center of mass, typical of the fluid behavior. The two mechanisms contribute to the shape of the ion-ion structure factor $S_{II}(k)$.
In its most general definition, the ion-ion structure factor for a system of N ions can be written as, [23]:

$$SII(k,\omega) = \frac{1}{2\pi N} \int \sum_r < e^{i\mathbf{k}\cdot[\mathbf{R}_r(t) - \mathbf{R}_0(0)]} > e^{i\omega t} dt \tag{6.7}$$

where $\mathbf{R}_r(t)$ is the position vector of the r-th ion at time $t$ and $\mathbf{R}_0(0)$ is its initial position. Following the approach developed in [17], we can account for the ion oscillation motion $\mathbf{u}_r(t)$ and for the global diffusion motion $\mathbf{x}_r(t)$. The position vector $\mathbf{R}_r(t) = \mathbf{U}_r + \mathbf{u}_r(t) + \mathbf{x}_r(t)$, where $\mathbf{U}_r$ is the atom position in the initial cold solid state. Inserting this expression in eq.6.7 and considering the vibration and the translation motion statistically independent, eq.6.7 can be written as:

$$SII(k,\omega) = Sii(k,\omega)[(1 - e^{-2W}) + e^{-2W} b(k)] \tag{6.8}$$

In this equation $b(k) = \dfrac{1}{N} \sum_{r,s} e^{i\mathbf{k}(U_r - U_s)}$ represents the Bragg peak while

$$Sii(k,\omega) = \frac{1}{2\pi N} \int \sum_r \left\langle e^{ik\cdot[x_r(t) - x_0]} \right\rangle e^{i\omega t} dt \tag{6.9}$$

is associated to the diffusion motion. W is called the *Debye-Waller factor* [22]. It is usually associated to a lattice structure. We would like to underline, though, that its appearance does not require a strict crystalline structure but naturally arises as a direct consequence of the ion vibrations. It represents the degree of thermal fluctuations $\mathbf{u}$ of the ions around their positions $2W = k^2 < \mathbf{u}^2(t) > /2$. It is associated to the ion temperature $T_i$ and can be written as [22]:

$$W = \frac{3\hbar^2 k^2}{2M k_B T_D} \left(\frac{T_i}{T_D}\right)^2 \int_0^{T_D/T_i} \frac{u du}{e^u - 1} \tag{6.10}$$

where $T_D$ is the Debye temperature. In a plasma, it can be expressed as $T_D = \dfrac{\hbar}{k_B} \left(\dfrac{Ze^2 N_e}{4\pi\epsilon_0 M}\right)^{1/2}$ where $M$ is the ion mass. In diffraction from solid lattices, a temperature increase makes the Debye-Waller factor larger and, consequently, reduces the Bragg peak. This is a well known effect and often referred as *thermal diffuse scattering*. In high temperature plasmas, $e^{-2W} \sim 0$ and the Bragg peak is suppressed.

**Effective mass** The effects of strong coupling and screening on the density fluctuations can be treated in terms of an *effective mass* [25]. At high couplings, the ions tend to react together and a long range order is set. At the same time short range screening becomes important. In the effective mass picture, the ion plus its screening charge is seen as an individual *quasi particle*, with an effective mass $M^*$ different from the bare ionic value $M$.
While accurate estimations of the effective mass based on self energy calculations, [24], are well adapted to weakly coupled plasmas, they fail when coupling increases. The screened OCP model can be used to get more accurate evaluation on the effective mass of a particle moving in the strongly coupled regime, as illustrated in [25]. Here we shall not give a deep description of the model, but we will expose the main concepts.

The effects of screening on the bare ionic mass are treated in terms of the charge-charge correlation function $S_{ZZ}(k\omega)$. We consider the simple case where the ions oscillate at normal frequency $\pm\omega_k$, such that the spectral density fluctuation can be written as:

$$S_{II}(k,\omega) = \frac{1}{2} S_{II}(k) \left[\delta(\omega - \omega_k) + \delta(\omega + \omega_k)\right] \tag{6.11}$$

by using conservation rules, it can be demonstrated that:

$$\omega_k^2 = \frac{k^2 k_B T_i}{M S_{ii}^{ZZ}(k)} \tag{6.12}$$

where $\omega_k^2$ is related to the single particle energy of an ion moving in the plasma and $S_{ii}^{ZZ}(k)$ is the low frequency ionic part of the charge fluctuations. It is directly related to the ionic static structure factor $S_{II}(k)$ as well as to the screening charge q(k) (i.e. the fraction of the electrons that kinematically follows the ion, introduced in section 3.3.3.5):

$$S_{ii}^{ZZ}(k) = S_{II}(k) \left[1 - \frac{q(k)}{Z^*}\right]^2 \tag{6.13}$$

As for the solid state approach, we can define the effective ionic mass by taking the second derivative of eq.6.12 and setting $M^* = M$ in the free particle limit, where $S_{ii}^{ZZ}(k) = 1$:

$$\frac{1}{M^*} = \frac{1}{2k_B T_i} \frac{\partial^2 \omega_k^2}{\partial k^2}, \tag{6.14}$$

The next step is considering that this expression is valid even for interacting particles, where $S_{ii}^{ZZ}(k) \neq 1$. We can then substitute eq.6.12 in 6.14, obtaining:

$$\frac{1}{M^*(k)} = \frac{1}{2M} \frac{\partial^2 k^2 / S_{ii}^{ZZ}(k)}{\partial k^2}, \tag{6.15}$$

which we consider as a definition of the ion effective mass in the dense plasma.
The k dependence of the effective mass accounts for the different screening charges at different probing wavelength.

The screened OCP model presented in 3.3.3.5 is used to calculate the static ion-ion structure factor and then $S_{ii}^{ZZ}(k)$ trough eq.6.13. The effective ion mass can then directly determined from eq.6.15. In fig.6.15 we present the effective mass variation for an Al plasma at density $2.5 \cdot 10^{23} cm^{-3}$ and $Z^* = 2$ as a function of coupling. The two curves represent calculations for $k = k_F$ (solid black line) and $k = 1.5k_F$ (dashed red line), where $k_F = (3\pi^2 N_e)^{1/3}$ is the Fermi wavenumber. We observe that the effective ion mass strongly decreases with increasing coupling.

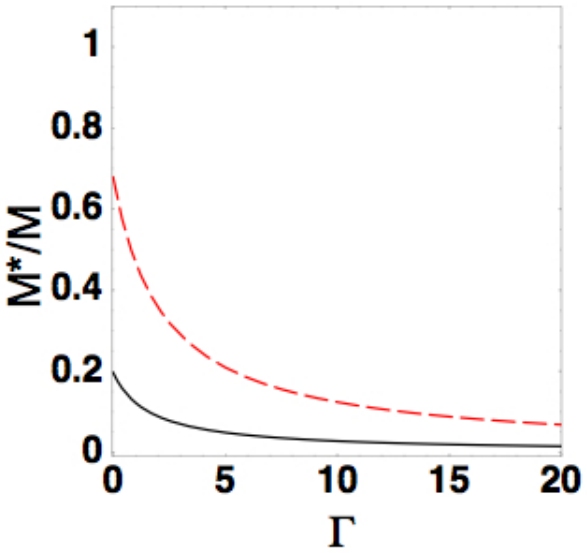


**Figure 6.15:** *Effective ion mass as a function of* $\Gamma$ *for a plasma with density of* $2.5 \cdot 10^{23} cm^{-3}$ *and* $Z = 2$ *and calculated for* $k/k_F = 1$ *(solid black curve) and* $k/k_F = 1.5$ *(dashed red curve).*

#### 6.1.5.2 X-ray scattering simulations

In order to take into account the screening effects in our model, we need to include the ion effective mass in the expression of the Debye-Waller factor, eq.6.10. As a result, W also decreases with increasing coupling and the correction associated to the term $1 - exp(-2W)$ in eq. 6.8 for the cross section becomes more important. Therefore, the effect of strong correlations reduces the ion structure factor and consequently the elastic scattering cross section (see eq.3.47).
As already mentioned, by probing the plasma at different times we could reach different coupling regimes. This is of particular interest in the present case as it provides a way to experimentally evidence the effects of strong correlations predicted by the theory described above. In fig.6.16, we show how $1-exp(-2W)$ changes in time as a consequence of the plasma parameter evolutions. The change in the plasma parameters, deduced from the hydrodynamic simulations, modifies the strength of the correlations and different ion coupling regimes are encountered. We can notice that the $(1 - e^{-2W})$ value is much smaller at early times, when the shock strongly compress the target, inducing a strong ionic coupling. At later times, the shock has broken out in the vacuum and releases, inducing a relaxation wave which travels back in the sample. Both the plasma temperature and density decay, lowering the strength of the ionic correlations. In this case, the $(1 - e^{-2W})$ correction is far less important, a factor of $\sim 10$.
This effect was directly evidenced in our data as a different attenuation of the elastic scattering component at the two probed times. In agreement with what discussed

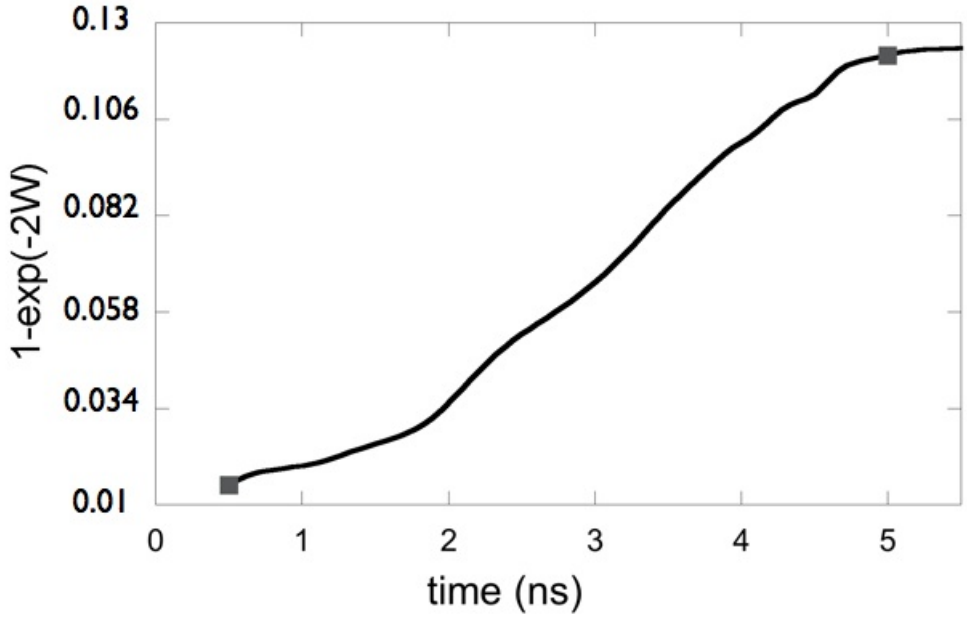


**Figure 6.16:** *Calculated* $(1 - e^{-2W})$ *as a function of the time evolution of our plasma.*

above, the damping effect is much more important at early times, where the elastic scattering signal is weaker than inelastic scattering one. At later times, on the contrary, the elastic component is only slightly reduced and it represents the most intense feature in the scattered spectrum. Again, this is consistent with what predicted by the presented theory.

We have then introduced in the code the full treatment discussed above. Eq.6.8 was used for the ion structure factor, where in the zero phonon approximation, Bragg scattering is neglected for angles which do not satisfy Bragg conditions, as it is in the case for this experiment (for polycrystalline Al 200 Bragg condition is satisfied at 40°). The input spectrum in the code was the experimental Ti spectrum obtained from the calibration shot convoluted with the scattering source size and corrected for the appropriate resonance-satellites intensity ratio[1]. The results are shown in fig.6.17 and fig.6.20, for the shot taken at 500 ps and 5ns respectively.

**$\Delta$t=500 ps** Fig.6.17 shows the experimental results (solid orange line) with the simulated spectrum (solid blue line) for early times (500 ps between the two laser beams), where ion coupling effects are expected to be important. In the calculation of the scat-

[1]We remind that for the calibration shots, the backlighter beam energy was weaker than for the "scattering" shots. The satellites, thus, can appear more intense as a consequence of a lower ionization state.

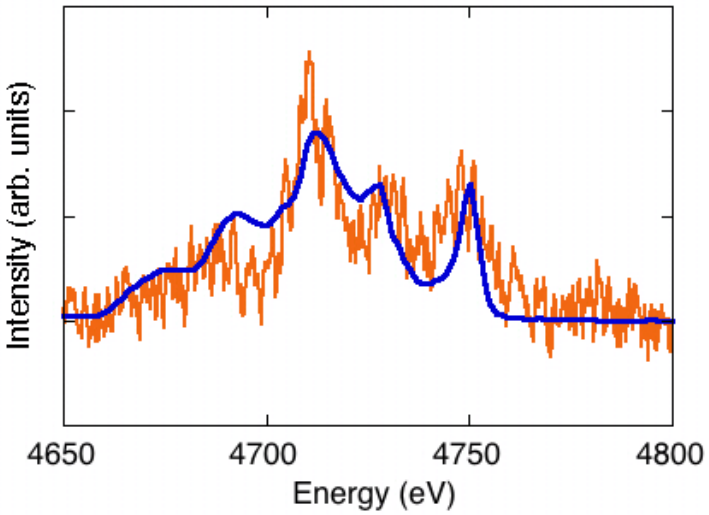


**Figure 6.17:** *Experimental and simulated profile of the x-ray scattered spectrum at early times. The simulated spectrum, solid blue curve, was calculated using the plasma parameters inferred from the hydrodynamical simulations reproducing the VISAR and SOP measurements (Te=* $0.35$ *eV, Ne=* $2.5 \cdot 10^{23}$ $cm^{-3}$ *and* $Z^* = 2.9$*).*

tered spectrum we have used the plasma parameters deduced from the hydrodynamic simulations associated to the VISAR and SOP velocity measurements. To account for the plasma evolution during the probing time, individual scattered spectra at different times were added together. Moreover, the contribution of the CH layer is considered. The calculated spectrum shows very good agreement with the experimental data. In particular, the low intensity elastic component is well reproduced, as evidenced at the resonant He-$\alpha$ line. Here the signal is entirely due to elastic scattering, since, on one hand, there is no high energy line producing a down shifted component and, on the other, the temperature is not sufficiently high to generate an upper-shifted plasmon (paragraph 3.3.3.5).

The free electron feature (which must be convoluted with the input spectrum), then, well describes the high intensity signal at the intercombination line and satellites energy. Moreover, the bound-free transitions from CH carbon atoms are accounted at the low energies (L-shell carbon edges are at ∼15 eV for our ionization state).
Since temperature is one of the most delicate parameter to measure, the sensitivity of the simulated spectra to its variation was also tested. By changing the temperature, the main effect is to change the coupling conditions and, hence, the correction associated to the $(1 - e^{-2W})$ term. In fig.6.18 we have varied the temperature, both increasing it at 0.55 eV (dotted red curve) and decreasing it at 0.15 eV, (dashed light blue line). We can notice that for the lowest temperature, which implies stronger coupling conditions, the Rayleigh component is too strongly damped and it does not agree with our data

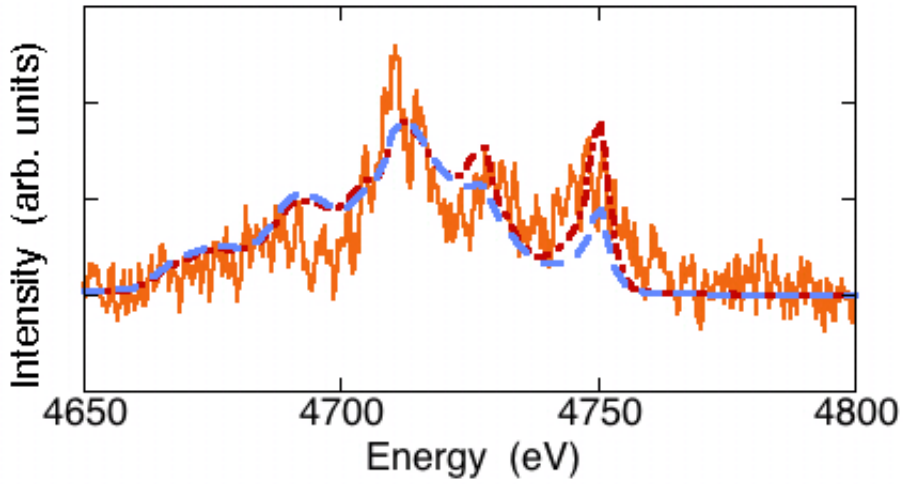


**Figure 6.18:** *Calculated scattered spectra obtained with the same plasma parameters as fig.6.17 but with a different temperature of 0.15 eV (dashed light blue line) and 0.55 eV (dotted red line).*

anymore. Similarly, when the temperature is too high the coupling effects are less important so that the resulting Rayleigh component becomes too intense.

The same trend is evidenced if we vary the electron density, as shown in fig.6.19, where stronger coupling conditions are associated to higher densities. In addition, we can observe that the calculations best match the experimental spectral position of the inelastic component for an electron density of Ne= $2.5 \cdot 10^{23}$ $cm^{-3}$, already considered in fig.6.17 (solid blue line). For higher densities, the plasmon is more shifted than experimentally observed (red dotted curve in fig.6.19). Similarly, if we consider a lower density the spectral shift is smaller than experimentally obtained (light blue dashed curve). This behavior is in agreement with what expected from eq.3.51 or eq.3.52 and gives us an error estimation on the plasma electron density deduced from the scattered spectrum.

**$\Delta$t=5 ns** At later times, the probed plasma is less dense and colder (Ne $\sim 8.5 \cdot 10^{22} cm^{-3}$ Te= 0.25 eV, see section 6.1.4). Under these conditions the effects of the correlations are softer and the coupling parameter is decreased down to $\Gamma_s \sim 5$. Again, the calculated spectrum (fig.6.20) shows very good agreement with the experimental data using the plasma parameters inferred from the simulations. There, the elastic component is the dominant feature, while the inelastic scattering is not clearly distinguishable. Due to a weaker coupling, the Debye-Waller correction is decreased. The elastic contribution to the scattering cross section increases and become larger than the inelastic one.

Under thee conditions, the simulated scattered spectra are not sensitive to temperature

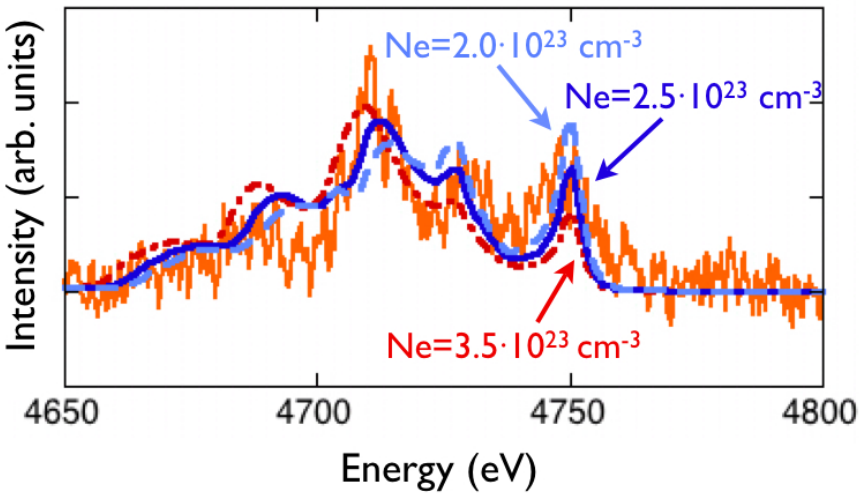


**Figure 6.19:** *Calculated scattered spectra obtained with the same plasma parameters as fig.6.17 but with a different electron density, of 3.5·$10^{23}$ $cm^{-3}$ (dotted red line) and 2·$10^{23}$ $cm^{-3}$ (dashed light blue line)).*

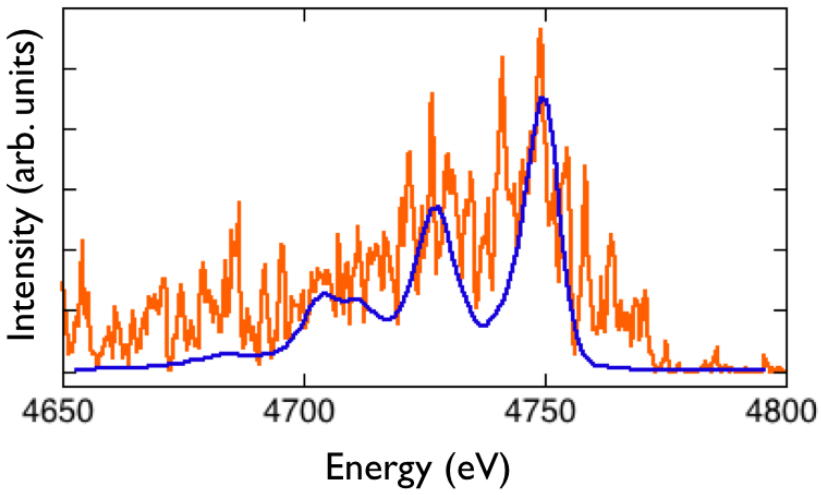


**Figure 6.20:** *Experimental (solid orange line) and simulated (solid blue line) x-ray scattered spectra at later times. In this case the coupling is decreased and effects associated to correlation effects are soften. The calculated spectrum is obtain using the plasma parameters deduced from the simulations, Ne= $8.5 \cdot 10^{22}$, Te= 0.25 eV and $Z = 2.1$.*

variations. The Rayleigh component remains the most intense feature over a wide range of temperatures, so that an absolute calibration of the experimental Rayleigh cross section is here necessary to lead a deeper analysis.

## 6.2 Experiment on Janus

So far, successful experiments were only performed on large scale laser facilities (the LULI2000 laser at LULI and on the Omega laser at the Laboratory for Laser Energetics (LLE) in Rochester, NY); the reason lies in the necessity of using kJ laser beams in order to generate intense backlighter sources, necessary to obtain useful signal to noise ratios.
We performed another collective x-ray Thomson scattering experiment on the Janus laser at LLNL. The experiment aimed at demonstrating the possibility to perform collective x-ray scattering using less than 200 J laser pulse. Scattering measurements from low incident flux ($\sim 10^{12}$ photons incident on the target) can be obtained by using high efficiency curved crystals together with effective x-ray detectors, allowing the extension of the technique to smaller facilities.
In addition, we wanted to investigate the scattered signal from both shocked and radiatively heated plasmas, in order to gain information on the different conditions attained and on the consequent different coupling regimes.
No plasma diagnostics were implemented in the set up and the created plasmas are far less characterized than in the experiment performed at LULI. Nevertheless, using the x-ray scattering code already validated at LULI we have been able to estimate the plasma parameters from the obtained x-ray scattered spectra.

### 6.2.1 Experimental set-up

The experiment was carried on the Janus laser at the Jupiter Laser Facility (JLF) of Lawrence Livermore National Laboratory (LLNL). The system delivers two synchronized laser pulses with energies up to 200 J per beam at the second harmonic $2\omega$ (at 527 nm). The main difference with the LULI configuration lies in the target design. Here, the backlighter and the sample targets were implemented on the same structure (fig.6.21) which was aligned at the chamber center. In this way the position of the backlighter target relative to the sample was fixed and no fictitious shift coming from a misalignment could occur. We used one of the 2 laser beams focused on a 12.5 $\mu m$ thick Saran (polydenchloride $(C_2H_2Cl_2)_n$) backlighter target to generate chlorine Ly-$\alpha$ emission at 2.96 keV. The pulse shape of the backlighter beam was a quasi squared profile with 200 ps or 1 ns duration. The x-rays entered a big 50 $\mu m$ thick gold housing through

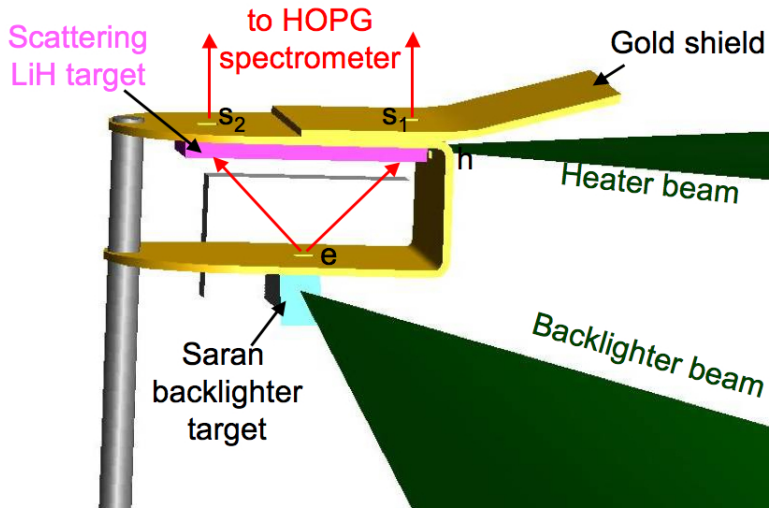


**Figure 6.21:** *Schematic view of the experimental set up and target structure used for the experiment on Janus laser facility.*

a small laser cut hole positioned at 90° (indicated with $e$ in fig.6.21) being absorbed in all the other directions. The sample target was enclosed in the gold housing and it was made by pressed lithium hydride powder. Two diagnostic holes ($s_1$ and $s_2$) in the gold housing allowed the detection of the scattered signal with a crystal spectrometer. The dimensions of the 2 holes, 300 x 500 $\mu m^2$ were optimized to maximize the solid angle for high efficiency still limiting the range of the possible scattering angles as seen by the spectrometer. The two holes were separated by 2.5 mm and their distance from the source could be chosen between 1, 2, 3 mm, allowing to probe different scattering angles.
The scattered radiation was spectrally resolved by means of a highly oriented pyrolytic graphite (HOPG) crystal in the focusing mode (see next section) and detected by BAS-TR imaging plates or x-ray CCD camera. In time resolved measurements, the two holes allow the collection of the scattered light from two distinguished spatial positions on the sample target, giving the possibility to record the scattered signal from the cold sample and from the heated material on a single shot.
The heating, was obtained with a second laser beam going through an additional hole (400 x 400 $\mu m^2$) on the side of the gold structure, ($h$ in fig.6.21) and irradiating the target. In this way, a shock wave propagating in the target was generated. Alternatively, a side on aluminum coating served as x-ray converter for radiative heating of the sample. When a correct temporal delay between the backlighter and the laser heater beams was chosen, the scattered signal from $s_1$ would have come from a heated part of the target, while the radiation through $s_2$ would be scattered by the further portion of

the target still maintained cold. An additional gold shield was also added in order to block the blow off from the plasma, preventing it from reaching the spectrometer.

#### 6.2.1.1 HOPG crystal spectrometer

The use of a high efficiency crystal is of extreme importance in the detection of the scattering signal from low photon fluxes incident on the sample. Highly Oriented Pyrolytic Graphite (HOPG) is a mosaic crystal which consists of a large number of small nearly perfect crystals. Their high reflectivity makes this kind of crystal extremely interesting for scattering experiments. The mosaicity is responsible for the reflectivity enhancement: for a divergent monochromatic x-ray beam, the random distribution of the crystals planes increases the possibilities to satisfy Bragg condition. In a 1:1 geometry mosaic focusing is then achieved and all the x-rays are refocused on a single point at the image plane. The mosaic spread $\gamma$ is defined as the FWHM of the gaussian distribution of crystals planes orientations off the normal axis to the surface. Two different types of HOPG are usually used, Advanced Ceramics ZYH crystals with $\gamma = 0.4$ and ZYH crystals with $\gamma = 3.5$

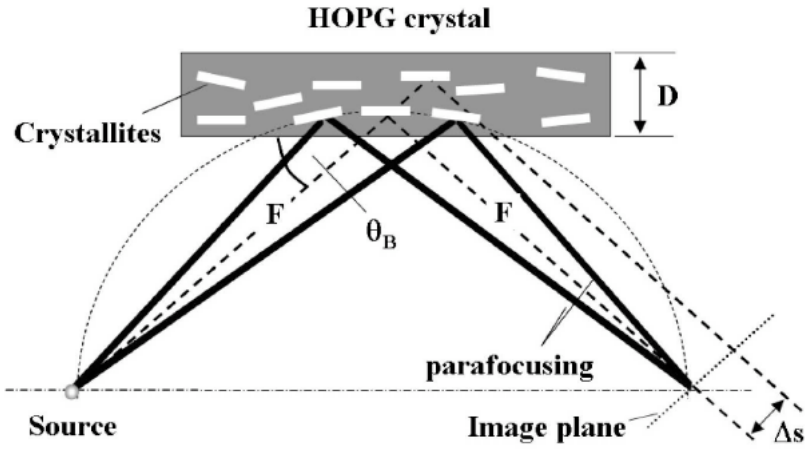


**Figure 6.22:** *Schematic representation of focusing properties of a HOPG crystal as well as of mosaic broadening mechanism.*

Fig.6.22 shows the HOPG working principle. It can be noticed that if the angular spread is sufficiently wide the mosaicity highly enhances the overall reflectivity. In the opposite case, i.e. if the angular spread is not sufficient to cover all the possible range of plane orientations, the reflectivity can be reduced.
As a counterpart to the high efficiency, the resolution of a HOPG crystal is generally worse than that one of a flat crystal. This is due to the mosaicity and to the fact that the photon has to penetrate deeper into the crystal before being reflected [30]. Another

interesting property of the HOPG is its facility to be bent, increasing the effective collection solid angle and, thus, the efficiency. In our experiment a cylindrically curved (radius of curvature of 115 mm) HOPG crystal was used in the van Hamos geometry.

### 6.2.2 Janus experimental results

In this section we will present the results obtained from this experimental campaign. We will firstly introduce the Cl x-ray source spectrum, focusing the attention on the optimization of the Ly$\alpha$ line. We will then illustrate the scattered data obtained from cold targets, underlining the relevant characteristics for a comparison with the data from the hot samples. The scattering analysis from socked and radiatively heated targets will then follow.

#### 6.2.2.1 Cl x-ray source

In [31], Cl Ly-$\alpha$ radiation was suggested as a good candidate for collective Thomson scattering experiments because of conversion efficiency and spectral bandwidth. The choice of Cl Ly-$\alpha$ was motivated by the work done in [32], where temporally resolved emission spectra showed a narrow band emission.

In fig.6.23 we show a typical spectrum obtained by directly irradiating the Saran. The

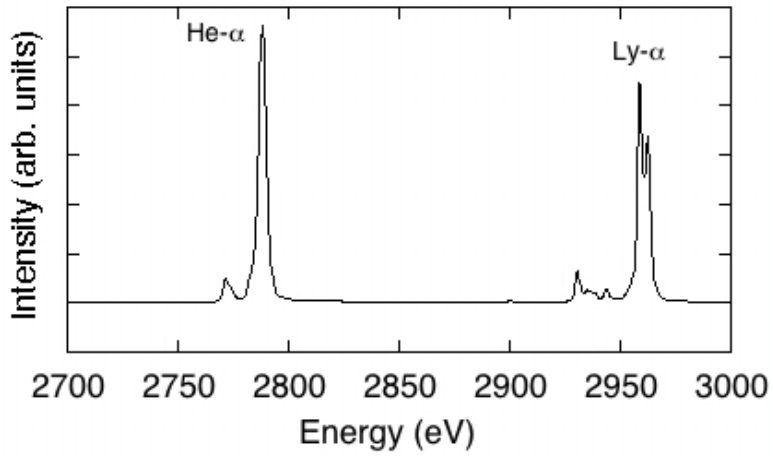


**Figure 6.23:** *Typical emission spectrum from the Saran backlighter featuring the Ly-$\alpha$ feature at 2.96 keV with electronic satellites on lower energies. He-$\alpha$ emission is also visible at 2.79 keV with the intercombination line.*

Ly$\alpha$ resonance is at 2.96 keV and satellites lines are on the low energy side. The spatial extent of the source at the detector is of the order of 2.5 mm and it is dominated by the mosaic broadening of the ZYB HOPG crystal used. Spectral broadening is of the

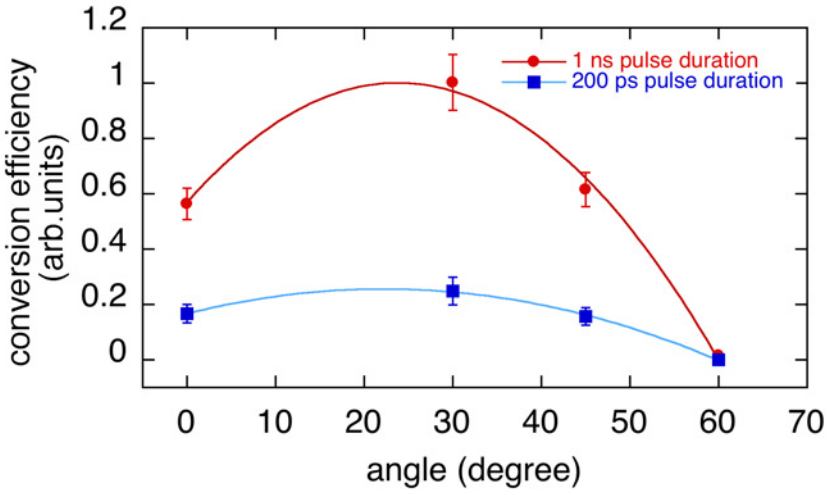


**Figure 6.24:** *Conversion efficiency for Ly$\alpha$ line for different angles between the laser propagation direction and the normal to the target.*

order of ∼7eV mainly due to spatial aberrations from the curved crystal. Cl emission as a function of the laser incident angle was studied in order to maximize the source signal. The results are shown in fig.6.24 where we show the intensity of the Ly-$\alpha$ line, normalized to the incident laser energy, for different incident angles and both 200 ps and 1 ns pulse. The angle here considered is referred as the one between the laser propagation direction and the normal to the target. The optimal configuration was found at 30°, where, after detector calibration, a conversion efficiency of $\sim 10^{-3}$ from laser energy into Cl $Ly\alpha$ photons was measured, [33]. It was then estimated that $\sim 10^{12}$ x-ray photons were incident on the target.

#### 6.2.2.2 Scattered results from cold targets

In this case the x-ray source was produced with a 200 ps and less than 200 J laser beam. A short pulse length is desired in order to reduce the plasma blow-off extension, preventing its self-emission from reaching the spectrometer. This can be an issue in time integrated measurements since the emission could mask or disturb the data. A CCD camera was used as detector. The spectral range acquired on the CCD was centered on the Ly$\alpha$ line. A typical result is shown in fig.6.25

We observe an intense elastic scattering signal at the resonance position and a broad down-shifted plasmon feature. Accounting for the signal recorded in the source and scattered spectra, we can estimate that a fraction of $10^{-5}$ of the incident light lies in the scattered feature. This is in good agreement with what expected from simple calculations (as explained in section 6.1.4), considering the LiH density at $\sim 0.8\ g/cm^{-3}$ and the target thickness of 300 $\mu m$.

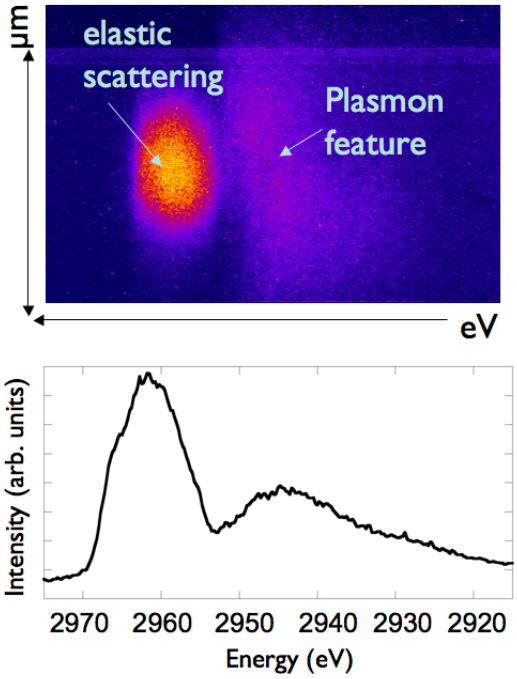


**Figure 6.25:** *Scattered spectrum from cold LiH on the CCD camera chip. The observed signal comes from scattering from the Cl Ly$\alpha$. Unshifted Rayleigh peak is visible together with the downshifted plasmon resonance.*

Some general observations on the scattered spectrum can then be done. First of all, the ratio between the intercombination and the satellites lines is much higher than observed on the source spectrum, fig.6.23. This suggests that at the satellites energy the elastic scattering from the satellites themselves blends with Compton scattering from the Ly$\alpha$ feature. Moreover, the inelastic component is less intense than the elastic scattering one, an interesting remark to be reminded in the following.
The acquired data are of great interest since for the first time they demonstrate the possibility to perform scattering experiments using shorter pulse length few hundred joules class laser systems.

#### 6.2.2.3 Scattered results from shocked and radiatively heated targets

When using the heater beam an issue on the CCD camera obliged us to change the detector. Imaging plates were then used and, in this case, a useful scattered signal was only obtained on shots where the 1ns laser pulse was employed. Moreover, the appearing of strong features in the Ly$\alpha$ spectral region masked the weaker scattered spectrum, obliging us to focus the analysis on the He$\alpha$ line. The origin of this disturbing radiation is not completely clear yet. One possibility is that this is direct emission from gold, observed in forth order diffraction from the HOPG crystal.
The signal from the cold sample can then be compared to the one obtained from shock and radiatively heated targets. Different plasma conditions are expected using the two heating processes. On one hand, by means of a shock wave, we expect inducing a few fold compression and temperatures typically of some eV with a high ion coupling degree; the plasma created by radiative heating, instead, is presumably almost at the solid density, with a higher temperature (of some tens of eV [13]), exhibiting weaker ion-ion correlations.

**Shocked compressed targets** The scattered spectra from the shocked target is shown in fig.6.26. We notice a behavior similar to the one observed in the LULI data. While in the source spectrum (as shown in fig.6.23) the He$\alpha$ resonance line is much more intense than the intercombination, the scattered spectrum shows a weak elastic component at the resonance and a more intense inelastic component lying at the intercombination energy. Inelastic scattering from the intercombination line is also visible, at lower energies.

In the analysis of the LULI data previously presented, cross measurements have demonstrated the validity of the x-ray scattering simulations as a tool to infer plasma parameters. In that case, the experimental spectrum could be reproduced only using plasma parameters in good agreement with those measured from independent rear side diagnostics. We have thus used the same x-ray scattering code to deduce the plasma parameters for the shots obtained in this experiment. The best fit, presented in fig.6.26

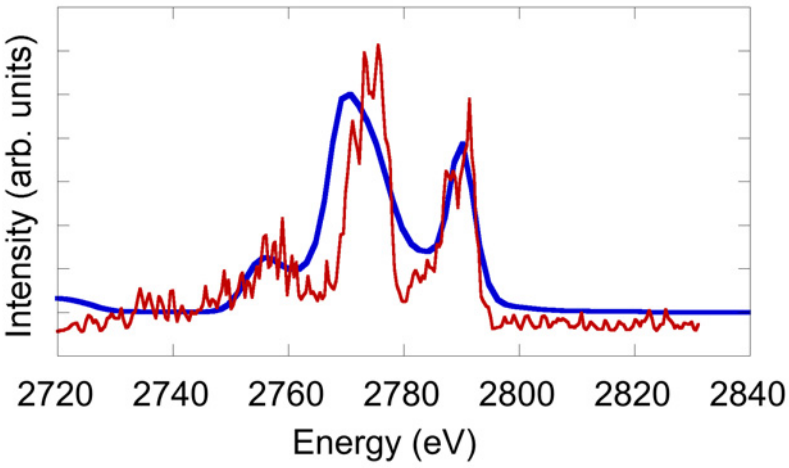


**Figure 6.26:** *Experimental (red) and simulated (blue) scattered spectra from a shocked LiH target.*

as a solid blue line, indicates a temperature of 1.2 eV, a ionization of $Z^* = 1$ and an electron density of $\sim 2.0 \cdot 10^{23} cm^{-3}$. Considering that the LiH samples are made of compressed powder, for cold targets we can estimate a density of 10%-20% less than the nominal solid density, i.e. $\sim 0.75 - 0.65$ g/cc. The Ne and $Z^*$ values found from the scattered data, therefore, correspond to a compression of $\sim 1.7 - 2.0$, in fair agreement with hydrodynamic simulations predicting a compression of $2 - 2.5$.

**Radiatively heated targets** When a thin Al foil was glued on the LiH target, in correspondence to the heating hole $h$ (fig.6.21), the sample is mainly heated by the x-rays produced in its interaction with the laser beam. A typical scattered spectrum obtained in this case is shown in fig.6.27. This spectrum appears considerably different from the one obtained from shock heated targets. In this case the elastic scattering feature appears stronger than the Compton component, in contrast with what observed from the shock compressed targets. With the same code we can reproduce the experimental results setting an electronic density of $1 \cdot 10^{23} cm^{-3}$, a ionization of 2 and a temperature of 5 eV, (see fig.6.27). These conditions imply a lower degree of ion coupling ($\Gamma \sim 7$), which could be the reason of the differences observed in the scattered results. The analysis is anyway limited by the little control on the efficiency of the heating mechanism. Additional data with a precise control of the created plasma are anyway absolutely necessary to confirm the obtained results and to conduct a deeper analysis.

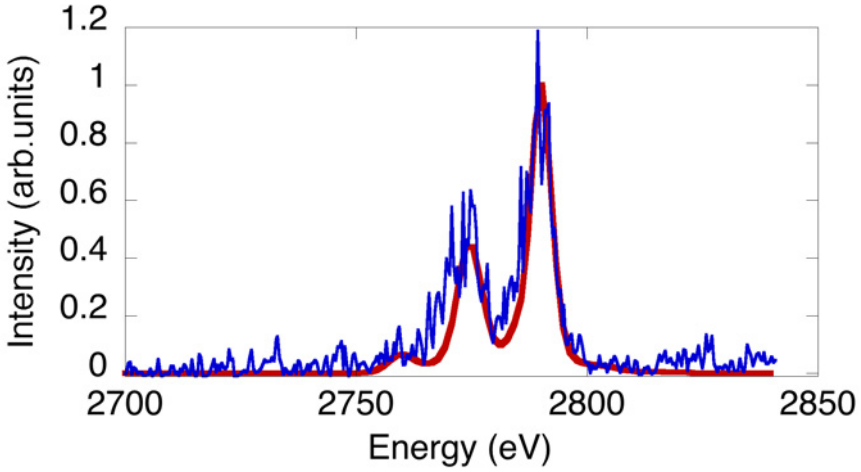


**Figure 6.27:** *Scattered spectrum from a radiatively heated LiH plasma.*

## 6.3 Conclusions

For the first time, quasi collective x-ray Thomson scattering data have been obtained from a shock created plasma. These results confirm that spectrally resolved x-ray Thomson scattering is a powerful diagnostic for warm dense plasmas. Indeed, dense plasma parameters (electron density, temperature and ionization state) can be obtained by spectrally resolving the scattered radiation. In addition, our experiment has revealed the further capability of collective XRTS to directly access strong ion coupling dynamics. Our results have shown strong correlation effects in a dense plasma, observed as a reduction of the elastic scattering component. This effect was recently predicted by theoretical works [25], but never experimentally evidenced. In addition, we have performed scattering simulations, in which electron degeneracy, strong coupling and self energy corrections have been implemented. The simulated spectra are consistent with the experimental data, both in highly coupled plasma, where the inelastic scattering dominates the elastic component, and in the moderate coupling regime, where the elastic component represents the most intense feature. Moreover, the plasma parameters deduced from these scattering simulations were cross checked with currently used optical rear side measurements, validating this technique as a dense plasma diagnostic tool.

Further experiments are nontheless necessary to improve the obtained data and use x-ray Thomson scattering as a routine diagnostic. In particular, the x-ray source must be improved, mainly using short backlighter emission required to probe a well defined plasma state. K$\alpha$ radiation produced by ultra-intense laser could be a good candidate. Its temporal emission, of the order of the laser pulse length (typically few ps), is much shorter than typical hydrodynamic evolution time ($\sim 100ps$). Moreover, it presents a

narrow spectral band, with no red wing satellites, which is a characteristic that would strongly improve the measurement quality and facilitate the spectra analysis. However, its efficiency (of the order of $\sim 10^{-5}$) is still an issue, being not sufficient for single shot measurements. This difficulty can be overcome in future facilities (the new PICO2000, TITAN etc...) where a high intensity (PW) CPA beam and high energy ns beams will be simultaneously available.

# Bibliography


[1] D. Riley, N.C. Woolsey, D. McSherry, F.Y. Khattak and I. Weaver, Plasma. Sources. Sci. Technol. **11**, 484-491 (2002)

[2] T. H. Bett, C. N. Danson, P. Jinks *et al.*, Appl. Opt. **34**, 4025 (1995).

[3] K. S. Holian, LANL Report No. LA-10160-MS UC-34 (1984)

[4] J.D.Dlouhy and K.N Stoev, JCPDS-International Centre for Diffraction Data (1997)

[5] M.Koenig, A.Benuzzi-Mounaix, D.Batani *et al.*, Phys. Plasmas. **12** 012706 (2005)

[6] P.M.Celliers, D.K.Bradley, G.W.Collins, *et al.*, Rev. Sci. Instr. **75**, 11, 4916 (2004)

[7] L.M.Barker and R.E.Hollenbach, J.Appl.Phys. **43**, 4669 (1972)

[8] P.M.Celliers, G.W.Collins, L.B. da Silva, *et al.*, Applied Phys. Lett. **73**, 1320-1322 (1998)

[9] M.Koenig, F.Philippe, A.Benuzzi-Mounaix, *et al.*, Phys. Plasmas **10**, 7, 3023 (2003)

[10] R. Ramis, R. Schmalz, and J. Meyer-tervehn, Comput. Phys. Commun. **49**, 475 (1988).

[11] http://cfa-www.harvard.edu/amdata/ampdata/kelly/kelly.html

[12] S. Ichimaru, *Statistical Plasma Physics*, Addison-Wesley, Reading (MA), 1991

[13] G.Glenzer, *et. al*, Phys. Rev. Lett. **90** 175002 (2003)

[14] S.H.Glenzer, G.Gregori, F.J.Rogers, *et. al* Phys. Plasmas **10**, 6, 2433 (2003)

[15] G.Gregori,S.H.Glenzer,W.Rozmus, *et al.*, Phys. Rev. E **67**, 026412 (2003)

[16] G.Gregori,S.H.Glenzer,F.J.Rogers, *et al.*, Phys. Plasmas **11**, 5, 2754 (2004)

[17] G.Gregori, G.H.Glenzer, O.L.Landen Phys. Rev. E **74**, 026402 (2006)

[18] A.Ng and T.Ao, Phys. Rev. Lett. **91**, 035002 (2003)

[19] D.A.Baiko, A.D.Kaminker, A. Y. Potekhin and D.G.Yakovlev, Phys. Rev. Lett. **25**, 5556 (1998).

[20] Z.Donkó, G.J.Kalman, K.I.Golden, Phys. Rev. Lett. **88**, 225001 (2002)

[21] J. Daligault, Phys. Rev. Lett. **96**, 065003 (2006)

[22] B.E.Warren, *X ray Diffraction* (Dover, New York, 1976)

[23] J.Chihara, J. Phys.: Condens. Matter **12**, 231 (2000)

[24] W.D. Kraeft, D.Kremp, W.Ebelin and G.Röpke, *Quantum Statistics of Charged Particles Systems* (Akademie-Verlag, Berlin, 1986)

[25] G.Gregori, *et al.* J. High Energ. Dens. Phys. submitted (2006)

[26] J.-P.Hansen and I.R. McDonald, "Theory of simple liquids", Elsevier Accademoc Press

[27] H.B.Singh and A.Holz, Phys. Rev. A **28**, 1108(1983)

[28] H.Totsuji, Phys. Rev. A **38**, 5440 (1988)

[29] G. Chabrier, J. Phys. C: Solid State Phys. **20**, 357 (1987).

[30] A.Pak, G.Gregori, J.Knight, *et al.*, Rev. Sci. Instr. **75** 3747 (2004)

[31] M.K.Urry, G.Gregori, O.L.Landen, A.Pak, S.H.Glenzer, J. Quant. Spetrosc. Radiat. Transf. **99**, 636 (2006)

[32] S.H Glenzer, C.A.Back, K.G.Estabrook, *et al.*, Phys. Rev. E **55**, 927 (1997).

[33] P.Neumayer, G.Gregori, A.Ravasio, *at al.*, Rev. Sci. Instr. **77**, 10F317 (2006)

# Chapter 7

# Conclusion and perspectives

## Conclusion

Despite its great importance, a satisfactory characterization of Warm Dense Matter is still missing from both theoretical and experimental point of view. In particular, one of the main issues associated to the experimental results is their precision, often not sufficient to discriminate between models. In this context we have developed new diagnostics for direct density and temperature measurements. We have studied three techniques, hard x-rays and proton radiography and x-ray Thomson scattering, focusing the attention to their applicability to shock compressed targets.

For the first time, a high Z plasma has been characterized by means of high energy x-ray radiography. Direct density measurement of shock compressed Al has been obtained from a single side-on radiograph at 17.5 keV. We have proved that K$\alpha$ radiation is a suitable source for this technique, providing that its intensity is increased over the Bremsstrahlung background. A new backlighter geometry for high resolution of 1D features was then tested. We have demonstrated the validity of this approach, encouraging further developments. The importance of the x-ray source size was also evidenced, underlining its effects on the density measurements.
The results obtained have shown that this technique is almost able to be routinely applied to high/mean Z shocked materials.
Nonetheless, we have underlined that a precise knowledge of the radiation spectrum is necessary to achieve the precision required to distinguish between the different EOS models. Therefore, improvements in the technique must include precise diagnostics to check the source spectrum, including high energy spectrometers (HENEX) or stepped (gold) foils to access fiducial transmission values. Strong efforts must also be devoted to optimize the K$\alpha$ intensity over the Bremsstrahlung background to produce a quasi monochromatic spectrum.

A correct density measurement also requires a high spatial resolution ($< 10\ \mu m$). New backlighter geometries can be used in order to reach the required resolution. This allows to overcome several issues associated to the use of pinholes an improvement of the flag alignment will results in a reduction if the source size, and hence, in a higher resolution. In this context, an ultimate improvement is related to the development of backlighter geometries for high 2D resolution. Through a systematic study of different geometries, mainly involving fine wires, we will be able to identify the optimal configuration.

High energy proton beams produced in laser matter interaction were successfully employed in the radiography of a shock compressed sample. The results obtained in this thesis have for the first time demonstrated the feasibility of the technique in shock wave experiments, in particular as a density diagnostic. We have probed low density carbon foams (CRF) in order to reduce scattering blurring effects. The sample density was deduced through a self consistent method combining hydrodynamic and Monte-Carlo simulations. We have lead the analysis in the regime where energy losses are negligible and small angle scattering is the main imaging mechanism. In this case, the analysis of a single RCF film, corresponding to a narrow band of proton energies, did provide a good characterization of the density gradient but we could not infer the absolute density values with the required precision. However, a higher precision can probably be obtained from the analysis of the whole RCF stalk. In this case the density must account for the effects on all the films, i.e. at different energies, and the uncertainty could be lowered.
Even if our results are highly promising, further developments are necessary. In particular, in order to investigate higher density materials, the proton energies must be increased so to overcome scattering blurring effects.

We have finally developed x-ray Thomson scattering as a dense plasma diagnostic. Here we have investigated highly coupled matter, generated by shock compression. In this case, scattering is representative of the collective behavior of the plasma. The spectrally resolved scattered light provides information on electron density, temperature and ionization state. The results inferred from the scattered spectra have been compared to optical rear side measurements (VISAR and SOP), routinely used in shock wave experiments. The good agreement between the two independent measurements gives a first cross check on this new techniques. One of the most relevant result in our data, is represented by the low intensity signal of the elastic Rayleigh scattering component, observed for high ion coupling parameters ($\Gamma_{ii} \sim 140$). Here, the inelastic component is the most intense feature in the scattered spectrum. This behavior is attributed to strong ion correlations effects, in agreement with what predicted by recent theories, which account for strong coupling, electron degeneracy and self energy corrections. At

lower coupling parameter values, the importance of these corrections decreases and the elastic component dominates the scattered spectrum.
More results from new experiments are necessary to confirm these data and to provide better understanding of this technique in the investigation of strongly correlated plasmas.

As a conclusion, the new diagnostics presented in this thesis have shown remarkable results, encouraging further developments.

# Perspectives

The urgent necessity to have new diagnostics available for a real breakthrough in warm dense matter, is attested by the rapid development that the presented techniques are subjected to. While in the next few months further XRTS experiments are planned at Rutherford laboratory and LLNL in order to confirm the results we have obtained, the great potentiality of the x-ray radiography has recently been validated in a new experiment performed on TITAN laser at LLNL. Ensuing the improvements suggested by our experimental results, they have focused the attention on the source spectrum and source size optimization. A quasi monochromatic spectrum was obtained increasing the K$\alpha$ component intensity by using a 200 J 40 ps laser beam. Moreover, a 5 $\mu m$ resolution was achieved by fully exploiting the flag target geometry. The acquired data are of extremely high quality and accurate density measurements (few % error bars) are expected. These data are actually under analysis.

In the near future, important perspectives are related to the upgrade of laser facility, such as LULI2000 and OMEGA EP, where intense petawatt lasers will be coupled to the existing high energy long pulse beams. New experiments on these facilities will allow us to test the techniques presented in this thesis for long term ICF projects. New important scientific results are also expected.

On the new LULI2000 facility, a new experiment is planned in order to test the real potentiality of the hard x-ray radiography by applying this technique to quartz targets. Particular attention will be devoted to the investigation at the melting point (around 4 Mbar), where almost 10% difference in density is expected by theoretical models. The goal is to reach sufficient precision to discriminate between the different models. Once ultimate, the extension of this technique to higher x-ray energy source will allow us to study iron samples. A deeper investigation of dense iron plasma is fundamental to resolve open debates, like the melting temperature at the IOB, already discussed.

The use of petawatt beams will also open the perspective of a wider application of proton radiography. This opportunity will allow us to generate higher proton energies, able to probe higher density materials. Indeed, proton radiography will be implemented in the investigation of quartz targets in the already discussed LULI2000 experiment. Moreover, direct probing of ICF capsule core can be obtained using >50 MeV proton beams, easily accessible with PW lasers. In addition to shock compressed states, this technique could be applied to probe shocked released states. Few experimental data are available in these regimes and their theoretical description is extremely difficult.
Finally, the remarkable sensibility to the density gradient observed in our experiment, suggests to consider this technique in the study of hydrodynamic instabilities growth.

The use of petawatt beams will also significantly improve the x-ray source for XRTS technique. First of all, the short pulse duration will allow us to generate shorter x-ray beams, able to probe a unique uniform plasma state. Moreover, the high energy available in this beam will allow to obtain higher x-ray fluxes, improving the quality of the scattered signal. The important amount of energy will also increase the K$\alpha$ flux, probably sufficiently to produce an observable scattered signal. The use of K$\alpha$ radiation in the scattering measurement would be a great advantage for the interpretation of the results, due to the lack of red wings satellites.
Once developed in this direction, XRTS will represent one of the most promising technique to infer density and temperature measurements in imploding ICF capsule. XRTS technique also opens an exciting scenario in the investigation of highly compressed iron. In the IOB context, the combined use of XRTS and x-ray diffraction can provide simultaneous insight on both temperature and crystal structure. This dual information will allow to verify the recently proposed "metastable superheating" theory, predicting the possibility to obtain iron solid states at temperatures higher than the melting curve.
Concerning EOS measurement in general, the simultaneous use of x-ray Thomson scattering, x-ray radiography and VISAR diagnostics can access to a complete set of information, allowing a precise characterisation of the EOS. The feasibility of this approach will be tested in a further experiment on the LULI2000 facility. In this case shock compressed CH target will be probed with these techniques, allowing a cross check of the EOS through the three independent measurement. The high intensity x-ray flux provided by the PW laser beam will also allow time resolved XRTS. By focusing the scattered radiation on a x-ray streak camera, the plasma dynamics can be followed in a single shock. Associated to the VISAR, this technique will highly improve the precision in determining the material EOS. The ion dynamics will be also accessed, by considering the evolution of the elastic scattering component.
Simultaneous measurement of forward (collective) and backward (non-collective) scattering are also useful in the theoretical framework, allowing to test dense matter theory.

The importance of the developed diagnostics is also confirmed by the role they invest as main diagnostics on future larger facilities devoted to fusion research, as NIF, LMJ or HIPER (High Power laser Energy Research). Indeed, the three techniques presented in this thesis will be the best candidate to probe ICF capsule cores.
Moreover, in a long range view, exciting perspectives are opened by the development of extremely energetic sources. Particular interests are represented by the Linac Coherent Light Source (LCLS) at SSRL (Stanford) and the X Free Electron Laser (XFEL) at DESY (in Hamburg), planned to be operational in 2009 and 2012 respectively. These sources will present real advanced properties that none of the existing facility owns. The key is the tunable, narrow band ($\sim 0.1\%$) x-ray source with very short pulse duration ($\sim$100 fs), which will allow to measure dynamics of the microstates with sub picosecond resolution. The XFEL will combine unique capabilities to both create, via isochoric heating for example, and probe WDM, using both imaging techniques (to directly access the density) and diffraction and scattering techniques (allowing the study of high pressure transitions, lattice and liquid structures as well as electron structure). These characteristics will make the XFEL the most promising source for plasma based research.

In the high energy particles context, the biggest project is represented by the SIS100 upgrade proposed at GSI, Darmstadt, able to generate high energy ion beams. Besides improvements of the diagnostic techniques already discussed mainly associated to the high particles energies, heavy ions can be successfully used to create WDM conditions in an alternative manner in respect to standard approaches. This approach will enable leading new investigation of WDM regimes. Moreover, since the ion beams can heat matter in a collisionless way via volumetric heating, distinct experiments will be allowed to access WDM, allowing to evaluate both transport properties and equation of state independently. Moreover, the generated WDM state will present a high uniformity, large volumes necessary for diagnostic access and will give access to high entropy matter at high density.

A new exciting scenario emerges from what we have discussed, opening high expectations for warm dense matter studies.

# Appendix A

# Résumé en français

## A.1 Introduction

Le travail de ma thèse est dedié au développement de nouvelles techniques d'investigation de la matière dense et chaude, aussi connue sous l'acronyme WDM (pour Warm Dense Matter en anglais). Ce régime se situe à la frontière entre la physique de la matière condensé et la physique des plasmas. Il est characterisé par des densités comprises entre 0.1 et 100 fois la densité du solide et des températures dans l'intervalle 0.1-100 eV. Notre connaissance du comportement de la matére dans ce régime est peu précise bien que sa compréhension soit indispensable dans différents domaines de la physique. En particulier, la conaissance de la relation entre la pression, la densité et la température, qui définit l'équation détat (EOS) est un point clef dans des domaines aussi importants que la fusion par confinement inertiel (FCI), la géophysique, l'astrophysique, et la planétologie.

Dans chacun de ces contextes, la connaissance encore trop imprécise des propriétés de la matière est à la base de nombreux débats encore ouverts, notamment autour de l'hydrogène et du fer. C'est la raison pour laquelle beaucoup d'efforts sont engagés afin de développer de nouveaux diagnostiques pour l'investigation de la matière dense et chaude. L'état de matière dense et chaude ainsi que les outils pour le sonder peuvent être créés en laboratoire. L'approche expérimentale est indispensable car nous ne disposons pas encore d'une description théorique satisfaisante. Les mesures standard de l'EOS utilisées jusqu'à présent emploient des techniques optiques ou des méthodes basés sur l'utilisation de rayons X de faible énergie. Ces diagnostiques ont permis d'étudier le comportement de différents matériaux dans des conditions extrêmes; cependant elles présentent des limitations. En particulier, les informations sur les paramètres du plasma obtenues par ces techniques sont indirectes. Cela engendre des incertitudes très élevées qui empêchent de discriminer parmi les différents modèles théoriques. De

plus, l'investigation des matériaux à Z élevé avec ces techniques n'est possible qu'à faibles pressions, limitant ainsi leur caractérisation.
Le développement de nouveaux diagnostiques est donc nécessaire pour franchir une nouvelle étape dans la connaissance de la matière dense et chaude.

## A.2 WDM: comment la créer et comment la sonder

Ce chapitre se concentre sur la caractérisation de la matière dense et chaude et sur la façon de la générer expérimentalement : la compression par choc laser.

### A.2.1 WDM, plasma fortement couplés et dégénérés

Le régime de matière dense et chaude se situe à la frontière entre la physique de la matière condensé et la physique des plasmas. Même s'il n'y a pas de limites formelles, par convention on considère que la WDM occupe la partie de l'espace des phases caractérisée par des températures comprises entre 0.1 et 100 eV et des densités entre 0.1 et 100 fois la densité du solide.
La modélisation théorique de ces régimes est très complexe car dans ces conditions la matière se présente comme un plasma fortement couplé et dégénéré. La description en terme d'écrantage de Debye et d'expansion en petites perturbations, communément appliquée aux plasmas classiques, n'est donc plus possible. De plus, des effets dépendants de la densité, comme l'ionisation par pression, commencent à devenir très importants.

La différence entre un plasma classique et un plasma dégénéré repose sur le paramètre $\Lambda \equiv \lambda_{dB} n^{1/3}$, où $\lambda_{dB}^2 = \frac{\hbar}{2\pi m k_B T}$ est la longueur de de Broglie. Si $\Lambda \ll 1$ la distance entre les particules est supérieure à la longueur de de Broglie, alors le comportement du plasma est classique. Dans le cas contraire, le fluide devient dégénéré. La même condition peut être exprimé en terme d'énergie de Fermi $E_F = \frac{\hbar^2}{2m}(3\pi^2 n)^{2/3}$: dans ce cas, le plasma est dégénéré si $Te/T_F \ll 1$.

Un autre paramètre est utilisé pour distinguer les plasmas fortement ou faiblement corrélés: $\Gamma \equiv \frac{1}{4\pi n \lambda_S^3}$, ou $\lambda_S$ est la longueur typique d'écrantage, la longueur de Debye $\lambda_S = \lambda_D = \left(\frac{\epsilon_0 k_B T}{4\pi n e^2}\right)^{1/2}$ pour un plasma classique ou la longueur de Thomas-Fermi $\lambda_{TF} = \left(\frac{2\epsilon_0 E_F}{3ne^2}\right)^{1/2}$ pour l'analogue quantique. Lorsque $\Gamma \gtrsim 1$, l'énergie potentielle est dominante sur l'énergie thermique et le plasma est fortement corrélé. La relation inverse est valable dans le cas d'un plasma faiblement corrélé. Les corrélations entre différentes espèces de particules peuvent être considérées.

### A.2.2 Comment créer la WDM: l'onde de choc

Parmi les différentes méthodes possibles pour atteindre les conditions de mati ère dense et chaude, nous avons choisi d'utiliser la compression par une onde de choc, générée lors de l'interaction entre un laser intense et une cible solide. Ce choix était principalement motivé par le hautes pressions que l'on peut atteindre : jusqu'à 100 Mbar. De plus, de récents travaux expérimentaux ont démontré la validité de cette technique pour la mesure de l'équation d'état de matériaux sous conditions extrêmes.

Une onde de choc est généré lors de l'interaction entre un laser intense ($I > 10^{12} W/cm^2$) à impulsion longue ($\sim ns$) et une cible solide dans le "régime classique", quand l'absorption de l'énergie laser se fait par absorption collisionelle. Dans ce cas, la surface de la cible est tr ès vite ionisée et un plasma chaud est formé. Ce plasma se détend dans le vide et, en réaction, une onde de choc se propage vers l'intérieur de la cible en la comprimant. D'un point de vue plus formel, l'onde de choc est la conséquence du développement des effets non linéaires dans la dynamique du fluide qui déforme le profil des ondes acoustiques. On peut démontrer alors que le profil final est une discontinuité.

Dans le référentiel du laboratoire le choc se propage avec une vitesse $U_S$ tandis que le fluide choqué a une vitesse $U_P$. Les lois de conservation de part et d'autre de la discontinuité sont connues sous le nom de relations de Hugoniot-Rankine et s'expriment:

$$\rho_0 U_s = \rho_1 (U_s - U_P) \tag{A.1}$$

$$P_1 - P_0 = \rho_0 U_s U_P \tag{A.2}$$

$$E_1 - E_0 = \frac{U_P^2}{2} + \frac{P_0 U_P}{\rho_0 U_s} \tag{A.3}$$

### A.2.3 Comment sonder la WDM

Le syst ème d'équations de Hugoniot-Rankine que nous venons de décrire est composé de 3 équations à 5 param ètres: $U_S$, $U_P$, $\rho_1$, $P_1$, $E_1$. Ces grandeurs thermodynamiques ne sont pas indépendantes, mais reliées entre elles à travers l'équation d'état. Si celle-ci est connue, on dispose d'une équation en plus. La mesure d'un seul param ètre est alors suffisante pour connaître tous les autres et donc determiner l'état du plasma. En revanche, la mesure de deux param ètres est nécessaire si on ne connaît pas l'equation d'état et qu'on veut la déterminer. Si les deux param ètres sont mesurés dans le même matériau on obtient une "mesure absolue" de l'équation d'état. On peut aussi réaliser une mesure "relative" de l'équation d'état par rapport à celle d'un second matériau. Ce dernier,

bien connu, est utilisé comme référence. Cette technique est appelée “désadaptation d’impédance” et repose sur la mesure simultanée d’une seule grandeur dans les deux matériaux.

Les techniques utilisées jusqu’à présent reposent sur la mesure des vitesses du choc $U_S$ et du fluide $U_P$. Elles comprennent des techniques d’interférométrie optique comme le VISAR, des mesures d’émission propre résolue en temps, et lorsqu’on s’intéresse aux matériaux de faible Z, des mesures de radiographie X résolue en temps. Toutes ces méthodes ont permis d’obtenir la connaissance de la mati ère dense et chaude que nous avons actuellement. Cependant, elles présentent des limites que l’on doit surmonter pour franchir une nouvelle étape dans la compréhension de la WDM.
En particulier, la précision obtenue avec ces techniques “standard” n’est pas satisfaisante. A partir de la mesure de la vitesse nous avons une mesure indirecte des param ètres du plasma, qui doivent être déduits au travers des équations de Hugoniot-Rankine. Dans ce passage, les erreurs de mesure sont amplifiées. On, peut, par exemple, relier l’erreur sur la vitesse à celle sur la densité à partir de l’équation de la conservation de la masse; on obtient alors:

$$\frac{\delta\rho}{\rho} = \left(\frac{\rho}{\rho_0} - 1\right)\sqrt{\left(\frac{\delta U_S}{U_S}\right)^2 + \left(\frac{\delta U_P}{U_P}\right)^2} \tag{A.4}$$

On peut remarquer que l’imprécision sur la densité est tr ès sensible à celle sur les vitesses. En particulier, le facteur $\left(\frac{\rho}{\rho_0} - 1\right)$ peut causer une amplification de l’erreur tr ès importante pour les matériaux fortement compressibles, comme le deutérium. De plus, une mesure absolue de l’équation d’état pour les matériaux opaques de Z élevé, parmi lesquels le fer, n’est possible que dans des conditions restreintes, à faibles pressions. Ceci est principalement dû au fait que ces matériaux sont opaques aux sondes optiques et X habituellement utilisées. Dans ces cas, la seule possibilité est donc d’effectuer une mesure relative de l’équation d’état, ce qui, encore une fois, engendre des barres d’erreurs tr ès importantes. Enfin, une mesure simple et précise de la température n’est pas possible avec les techniques traditionnelles. La température est un des param ètres pour lesquels les mod èles théoriques différent le plus et c’est aussi une quantité clef dans la détection des changements de phases. Un mesure directe de la température pourrait éventuellement permettre de discriminer parmi les différents mod èles.
Le besoin de développer des nouveaux diagnostiques pour améliorer la connaissance de la WDM apparaît maintenant clair.

En particulier nous souhaitons augmenter la précision des mesures en accédant directement aux param ètres du plasma, notamment la densité et la température. De plus, nous avons besoin de développer et employer des sources beaucoup plus énergétiques

pour obtenir une mesure absolue de l'équation d'état pour les matériaux opaques de Z élevé.
Dans cette th èse, trois nouvelles techniques sont présentées: la radiographie par X durs (¿10 keV) et par protons énergétiques ($\sim$ 1-20 MeV) pour obtenir une mesure directe de la densité des matériaux comprimés par choc laser, et la diffusion Thomson X qui permet d'accéder à une mesure de la densité et de la température électronique des plasmas denses.

## A.3 Radiographie par X durs

Pour cette technique, un faisceaux X est généré et dirigé transversalement sur une cible choquée. Le faisceau transmis est collecté sur un détecteur. Cela permet d'avoir à la fois une image 2D de la cible comprimée et des informations sur la transmission. L'image est ensuite "inversée" pour obtenir directement la densité en chaque point de la cible.
L'expérience a été menée au Rutherford Appleton Laboratory (RAL) en Angleterre. Nous avons utilisé 3 des 6 faisceaux ns du laser Vulcan pour générer un choc dans une cible d'aluminium. Le choc a été généré dans un "pousseur" en CH/Al/CH puis transmis dans la partie de la cible appelé "sliver" en Al, le matériau à sonder. Le faisceau X a été généré par le faisceau ps du laser Vulcan, au cours de l'interaction avec avec une deuxième cible (backlighter) en Molybdène. Le rayonnement $K\alpha$ à 17.5 keV généré transversalement a ensuite été collecté sur des plaques radiographiques (imaging plates) aprés avoir traversé la cible choquée. La source K$\alpha$ est une bonne candidate pour cette mesure car elle est très énergétique, suffisamment brève ($\sim$ ps) pour permettre d'étudier un état bien défini du plasma (temps hydrodynamique $\sim$ 100 ps), et monochromatique ce qui permet de faciliter le procèssus d'inversion. Cependant, la source K$\alpha$ est généralement très étendue spatialement ($\gtrsim 50\ \mu m$), même lorsque le laser est focalisé dans une tache très réduite ($\sim 10\ \mu m$). Ceci est dû au fait que les électrons qui génèrent le rayonnement X peuvent recirculer sur la cible sur une surface beaucoup plus grande. Pour réduire la taille de la source X nous avons employé une nouvelle configuration du backlighter, où une faible épaisseur est utilisée pour restreindre la surface sur laquelle les électrons peuvent recirculer. Au cours de cette expérience nous avons utilisé une géométrie en "drapeau", qui nous a permit d'obtenir une bonne résolution ($\sim$ 20 $\mu$m) dans une direction, dans notre cas, celle coincidente avec la direction du propagation du choc.
La figure A.1 montre un des résultats obtenus, pour un retard de 8 ns entre le faisceau ps et les faisceaux ns. On observe une partie correspondant au vide, ou la transmission est de 100 %, la partie de la cible pas encore choquée, plus absorbante, et la partie comprimée, caractérisé par une transmission encore plus faible.
Pour remonter à la densité, nous supposons tout d'abord que le choc est symétrique

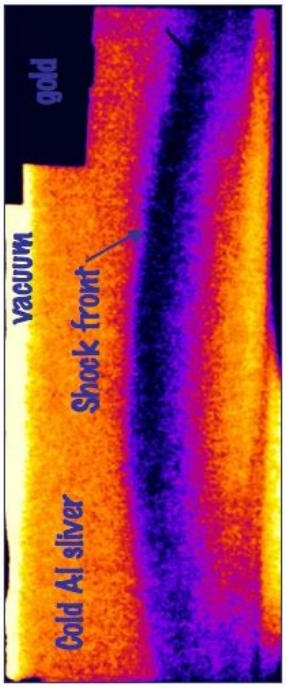


**Figure A.1:** *Radiographie X d'une cible d'Al choque. Le retard entre le faisceau ps et les faisceaux ns est de 8 ns.*

autour de l'axe de propagation du choc. On considère ensuite la transmission selon un axe perpendiculaire à l'axe de symétrie et on calcule l'inversion (inversion d'Abel) sur ce profil. En considérant plusieurs profils à différentes positions sur l'axe de symétrie, on peut reconstruire le profil du choc. Les résultats correspondants pour la densité sont présentés en figureA.2. On obtient une compression maximale de ∼1.65. Ces valeurs peuvent être comparés aux résultats donnés par les simulations hydrodynamiques qui ont étés bien calés sur les mesures de vitesses donnés par le diagnostic d'émission propre resolue en temps et implanté dans le dispositif experimental. Nous observons un bon accord qualitatif ; cependant les simulations hydrodynamiques predisent une compression maximale de ∼2, 25% plus importante que les résultats de la radiographie X.

Il existe deux principales sources d'erreur possible dans notre analyse:

- Imprécision sur le spectre du rayonnement X: la transmission par l'aluminium froid (390 $\mu m$ d'épaisseur) est de 75%, alors que l'on attend $\sim$ 61% pour un spectre monochromatique à 17.5 keV. Le spectre complet, nécessaire pour le calcul correct de la densité surfacique correspondant à chaque valeur de transmission, a dû être simulé à l'aide d'un code Monte-Carlo.

- La taille de la source : du fait de la géométrie du backlighter, la résolution ($\sim$ 70

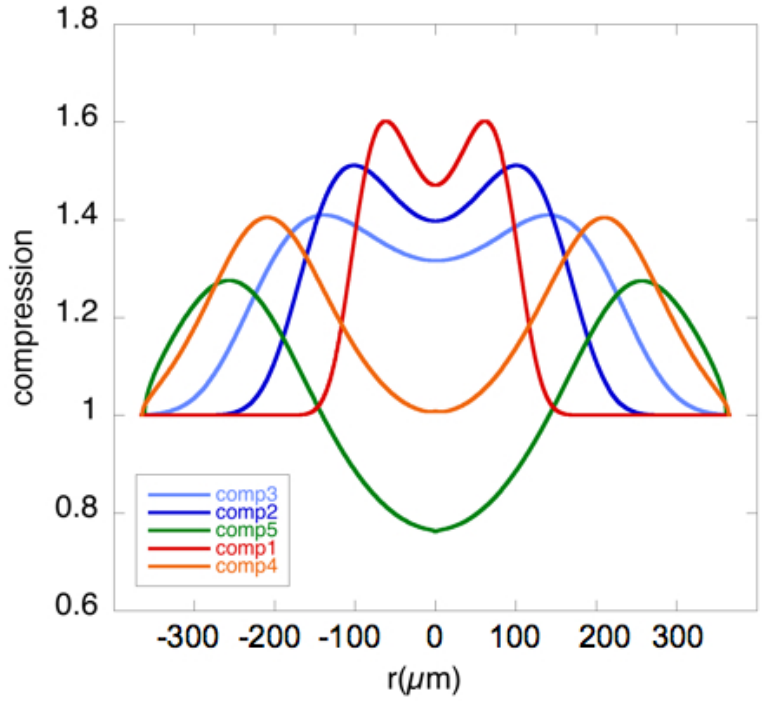


**Figure A.2:** *Valeurs de compression obtenues pour des profils différents sur l'axe de propagation du choc.*

$\mu m$) obtenue dans la direction utilisé par l'inversion d'Abel n'était pas suffisante. L'effet d'une source étendue est d'adoucir les gradients au détecteur, résultant en une sous-estimation de la densité.

En conclusion, nous avons obtenu une première mesure directe de la densité d'un matériau opaque de Z élevé. L'analyse conduite a permis de souligner les améliorations à apporter pour des futurs développements.

## A.4 Radiographie protonique

Des faisceaux de protons très énerg étiques ($\sim$ 800 MeV) générés par des accélérateurs ont déjà été utilisés pour sonder des objets de densités surfaciques de l'ordre de 50 $g/cm^2$. Cependant, les difficultés pratiques pour coupler ces sources de particules aux expériences de type laser-plasma sont nombreuses. De plus, les résolutions spatiales et temporelles atteintes avec ces sources sont typiquement de $\sim$ 200 $\mu m$ et 50 ns respectivement, ce qui n'est pas suffisant pour les besoins de la physique de l'interaction laser-plasma. En revanche, les protons générés par laser présentent des propriétés uniques qui les rendent particulièrement adaptés à l'investigation de plasmas denses et chauds. En particulier, grâce aux propriét és spécifiques de ces faisceaux, les hautes

résolutions spatiale et temporelle, nécessaires dans ces contextes, sont facilement accessibles.

Quand le faisceau de protons se propage dans un gradient de densité, il est perturbé par la diffusion àux petits angles et les pertes d'énergie. Le principe de la mesure est donc d'évaluer au niveau du détecteur les effets induits sur le faisceau par la propagation dans la cible choquée, pour ensuite remonter au profil de densité dans la cible même. Pour cela, nous avons développé un code Monte-Carlo qui reproduit la propagation des protons dans le gradient de densité dû à la compression par choc ; les protons sont ensuite propagés jusqu'au détecteur, ou ils sont arrêtés. Le profil du faisceau ainsi obtenu est comparé aux donnés expérimentales : si nous obtenons un accord, nous considèrons que le profil de densité utilisé dans le code est correct ; dans le cas contraire, nous le modifions jusqu'à obtenir l'accord recherché.

L'expérience a été menée pendant la même campagne expérimentale que celle de la radiographie X. Le dispositif expérimental est donc similaire. Les changements concernent la cible du backlighter qui cette fois-ci une cible en or permettant de produire les protons, le détecteur qui est maintenant un empilement de films radiochromiques. La cible principale est ici une mousse de carbone dont la faible densité (0.1 $g/cm^3$) a été choisie de manière à réduire les effets masquants associés à la diffusion àux petits angles.

La figure A.3 montre les résultats obtenus sur le huitième film radiochromique (correspondant à des protons de $\sim$10 MeV) pour un retard entre le faisceau ps et les faisceaux ns, générants l'onde du choc respectivement de 7 ns (a) et 11 ns (b) . Pour des protons de cette énergie et pour les valeurs de compression typiquement atteintes dans l'expérience, le pertes énergétiques ne sont pas observables sur le film. L'image obtenue est donc due principalement à la diffusion àux petits angles. La perturbation typique due au bord de la cible froide est très clairement visible et caractérisée par une zone d'accumulation de protons (une couleur bleue plus foncée sur le film), suivie par une zone de déplétion (une couleur plus claire sur le film). Plus à l'intérieur de la cible, nous pouvons aussi remarquer la modulation induite par le front du choc. Ses caractéristiques dépendent fortement des propriétés du gradient de densité associé à l'onde du choc. A' 11 ns (A.3 b), on peut aussi remarquer une modulation ultérieure, suivant celle du choc : il s'agit de l'effet du pousseur, qui pour ce retard beaucoup est plus éloigné du front du choc (la vitesse du front choc est supérieure à la vitesse des particules). Les effets dus au front du choc peuvent ainsi être distingués.
Nous avons comparé ces résultats aux donnés des simulations Monte-Carlo, obtenues en insérant les gradients de densités calculés par les simulations hydrodynamiques, encore une fois bien calés sur les mesures expérimentales de vitesses d'émission propre.

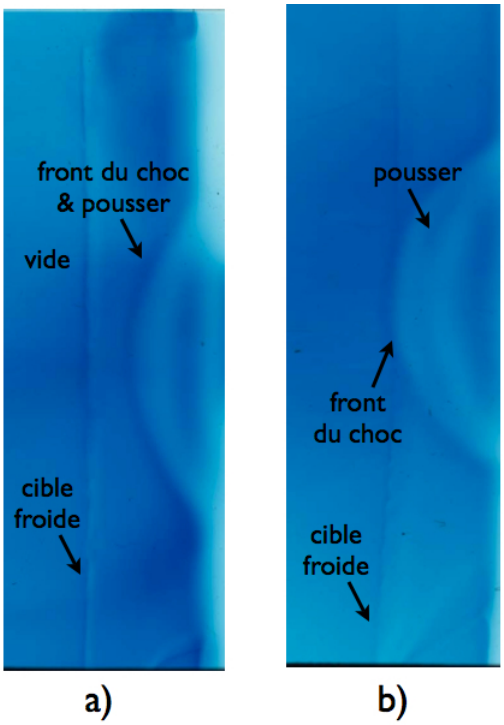


**Figure A.3:** *Radiographie protonique d'une cible choquée. Le retard entre le faisceau ps et les faisceaux ns est de 7 ns a) et 11 ns b).*

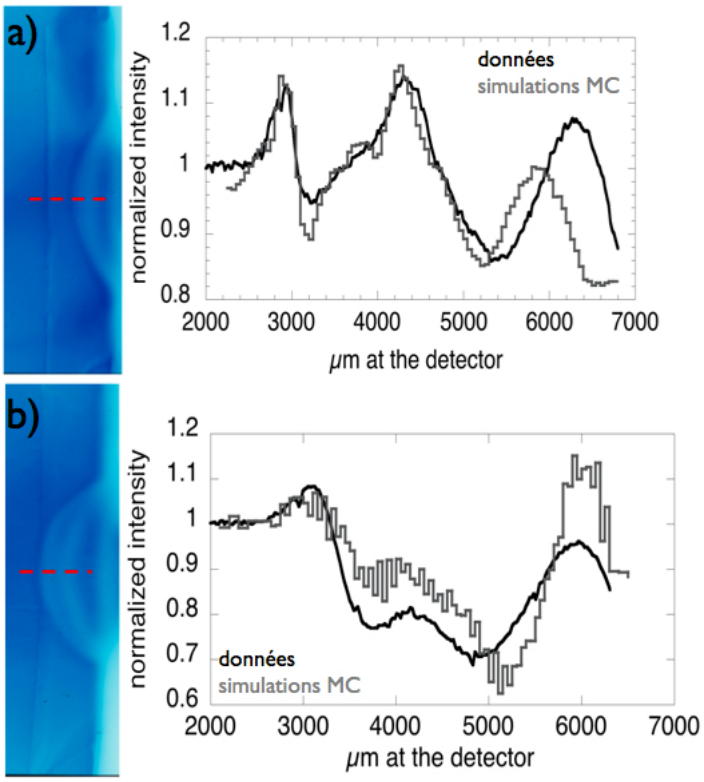


**Figure A.4:** *Profils expérimentaux simulés pour à 7 ns a) et 11 ns b).*

Pour les deux temps, nous obtenons un bon accord, en ce qui concerne soit les positions de modulations, soit leur intensité, comme le montre la figure A.4.

En conclusion, nous avons obtenu les premières radiographies d'une cible choquée en utilisant des faisceaux de protons générés par laser. Les résultats sont très prometteurs et notre analyse a permis de cibler les développements à venir. En particulier, des protons plus énergétiques sont nécessaires pour sonder des matériaux de densité plus élevé.

## A.5 Diffusion Thomson X

La diffusion Thomson résolue spectralement est couramment utilisée dans le domaine optique pour sonder les plasmas de faible densité ($Ne < 10^{23} cm^{-3}$). Très récemment cette technique a été étendue au domaine X, en donnant la possibilité d'étudier des plasmas plus denses et notamment à la densité du solide. Nous avons appliqué cette technique aux plasmas créés par choc laser, ce qui nous a permis de sonder des conditions différentes, de hautes densités et basses températures, correspondant à des plasmas fortement couplés et dégénérés.
Pour la mesure, on dirige un faisceau de rayonnement X sur le plasma. Soumis au champ électrique des photons, ses électrons oscillent en émettant des photons diffusés. En raison de l'importante énergie des photons incidents, il y a, durant le processus, un échange d'énergie et de moment qui fait que le rayonnement diffusé est décalé spectralement. En particulier, le spectre du rayonnement diffusé dépend des paramètres du plasma (température électronique Te, densité électronique Ne, et ionisation $Z^*$). Le principe de la technique repose alors sur la mesure du spectre diffusé pour caractériser l'état du plasma.
La section efficace du processus est proportionnelle au facteur de structure du plasma S(k, $\omega$). On peut démontrer que celui-ci s' écrit comme la somme de trois termes. Un premier terme est dû aux électrons fortement liés. Ceux-ci peuvent partager le moment transféré avec les ions beaucoup plus lourds et leur contribution à la diffusion est une composante à la même énergie que le rayonnement incident, appelé "diffusion élastique". En revanche, la diffusion par les électrons libres ou faiblement liés, génère une composante décalée en énergie, qui est appelée "diffusion inelastique". C'est en évaluant cette composante inélastique qu'on obtient les informations sur les paramètres du plasma.

On distingue deux régimes de diffusion, caractérisés par le paramètre de diffusion $\alpha = \lambda_P/\lambda_D$, où $\lambda_D$ est la longueur typique dÕécrantage et $\lambda_P = \lambda_0/(2sin(\theta/2))$ avec $\lambda_0$ la longueur dÕonde sonde. Si $\alpha < 1$, le régime est dit "non collectif" et la diffusion

a lieu sur les électrons individuels. Dans ce cas, nous avons accès à une mesure de température électronique et de l'ionisation moyenne à partir du spectre diffusé. Si, au contraire, $\alpha > 1$, le régime est dit "collectif", la longueur de la sonde est plus grande de la longueur d'écrantage et la diffusion a lieu sur les ondes du plasma (plasmons). A partir du spectre diffusé nous avons donc accès aux propriétés collectives du plasma. Plus précisément, en évaluant la composante inélastique on parvient à une mesure directe de la densité électronique.
L'expérience a été menée sur le laser LULI2000 du Laboratoire LULI de l'École Polytechnique. Il dispose de deux faisceaux capables de délivrer jusqu'à 400 J de lumière doublée en fréquence dans une impulsion de 1 ns. Nous avons utilisé un des deux faisceaux pour générer une onde de choc dans une cible principale en CH/Al/CH (4.5/6/4.5 $\mu m$). Les couches de plastique étaient nécessaires pour jouer le rôle d'ablateur en face avant (coté laser) et pour limiter l'expansion hydrodynamique de la face arrière de l'aluminium. Le deuxième faisceau a été focalisé sur une cible de titane pour générer une source X intense (radiation Ti He$\alpha$ et les satellites associés) dans la gamme 4.70-4.75 keV. Le rayonnement était envoyé sur la partie comprimée de la cible principale. La diffusion a 47¡ était collecté par un cristal courbé en LiF et focalisé sur une camera CCD. Un deuxième cristal plan en quartz a aussi été utilisé pour collecter le faisceau transmis par le plasma, ce qui nous a permis de contrôler l'émission de la source à chaque tir. Deux diagnostiques optiques de VISAR et d'émission propre résolue en temps, ont été ajoutés dans le dispositif expérimental pour mesurer la vitesse du choc et caractériser les paramètres du plasma de façon classique, afin de pouvoir valider le nouveau diagnostique. Les équations d'état du plastique et de l'aluminium sont bien connues dans le régime de pression atteinte lors de cette expérience et la mesure d'un seul paramètre est suffisante pour en déduire toutes les autres. Les mesures de vitesses nous ont permis de bien caler les simulations hydrodynamique pour connaître l'évolution du plasma d'Al dans le temps. Pour pouvoir sonder différentes conditions du plasma nous avons testé deux temps différents: 500 ps et 5 ns âpres que le faisceau créant l'onde de choc ait atteint l'intensité maximale. Pour $\Delta t = 500ps$, et pour la durée de la sonde ($\sim$ 1 ns), la couche d'Al est totalement comprimée et le plasma est très dense et relativement froid : les conditions de densité électronique, température et ionisation, moyennées sur la durée de la sonde ($\gtrsim$ 1ns) sont respectivement Ne$\sim 2.5 \cdot 10^{23} cm^{-3}$, Te$\sim$0.35 eV et $Z^* \sim 2.9$. Le spectre diffusé présente un signal très élevé à l'énergie de satellites, dont l'intensité est beaucoup plus importante que l'intensité de la composante élastique à la résonance, comme le montre la figure A.5 A l'énergie des satellites le signal est la somme de la composante élastique des satellites mêmes, très faible, et de la composante inélastique provenant de la résonance. On observe ainsi une diffusion inélastique plus importante que la diffusion élastique.
A 5 ns âpres le maximum d'intensité du faisceau générant le choc, les conditions du

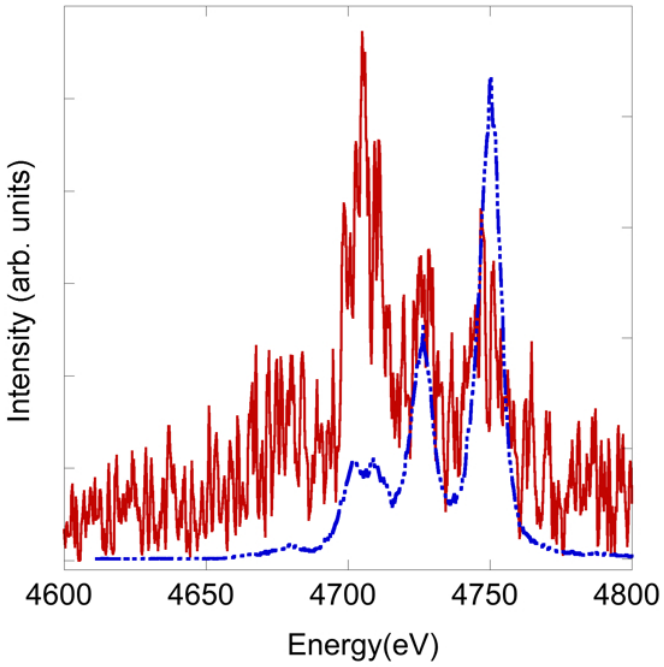


**Figure A.5:** *Spectre diffusé (courbe solide rouge) et transmis (courbe bleu pointillé) pour un retard de 500 ps entre les faisceaux qui génèrent le choc et la source X.*

plasma sont très différentes : à cet instant, le choc est sorti de la cible et une onde de détente la remonte. La densité électronique, la température et l'ionisation sont maintenant données par: Ne$\sim 8.5 \cdot 10^{22} cm^{-3}$, Te$\sim$0.25 eV et $Z^* \sim 2.1$. Le spectre diffusé a maintenant la même forme que le spectre incident, comme le montre la figure A.7, où on observe que la diffusion inélastique est de nouveau la composante la plus intense.

Pour interpréter les résultats et comprendre la différence observée entre les deux spectres diffusés il faut considérer les effets dus aux corrélations ioniques. Pour avoir une idée de l'influence de ceux-ci sur la diffusion dans un plasma fortement couplé, on peut considérer les cas extrêmes d'un solide et d'un plasma faiblement couplé. Un ordre bien défini est présent dans un solide (le réseau cristallin) et la diffusion élastique est possible seulement à des angles précis, donnés par la loi de Bragg. Dans le cas opposé d'un plasma non couplé, il n'y a pas de structure et la diffusion élastique est possible aussi en dehors des angles de Bragg. Un plasma fortement couplé se situe entre le deux cas, ce qui fait qu'il est encore possible d'observer la diffusion élastique en dehors de l'angle de Bragg, mais qu'elle peut être beaucoup plus faible qu'en l'absence de corrélations.
Si on considère le niveau de couplage pour les deux temps sondés, on observe deux régimes différents. Pour les conditions déduites à 500 ps, et pendant 1 ns, les ions sont fortement couplés, avec un paramètre de couplage $\Gamma_{ii} \sim 240$, alors que les électrons sont

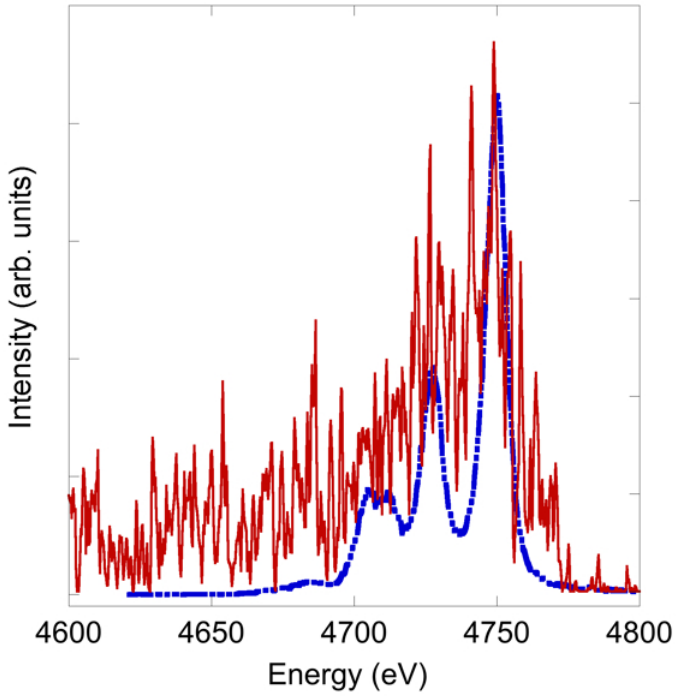


**Figure A.6:** *Spectre diffusé (courbe solide rouge) et transmis (courbe bleue pointillée) pour un retard de 5 ns entre les faisceaux qui génèrent le choc et la source X.*

fortement dégénérés, $T_e/T_F \sim 0.03$. L'écrantage électronique a pour effet de réduire les interactions électrostatiques et une expression plus appropriée du paramètre de couplage est alors donnée par : $\Gamma_s = \Gamma \exp(-k_s a) \sim 19$, où $1/k_s$ est la longueur d'écrantage à courte portée. Etant donné que $\Gamma$ et $\Gamma_s$ sont très importants, on s'attend à ce que le couplage ionique joue un rôle majeur dans ces conditions expérimentales. A 5 ns, le plasma est beaucoup moins dense et le paramètre de couplage ionique est baissé à $\Gamma_s \sim 5$. L'importance des corrélations ioniques est ainsi moindre.
Un traitement mathématique plus rigoureux des concepts qualitatifs décrits ci-dessus comprend une correction à la section efficace associée au facteur de Debye-Waller. Il décrit les vibrations collectives des ions, associées à l'ordre à longue portée qui apparaît dans le plasma.
Ce traitement a été inclus dans le calcul du spectre diffusé, de même que la correction à la masse effective des ions due à l'écrantage électronique. Les résultats pour les deux cas discutés sont présentés dans la figure A.7.

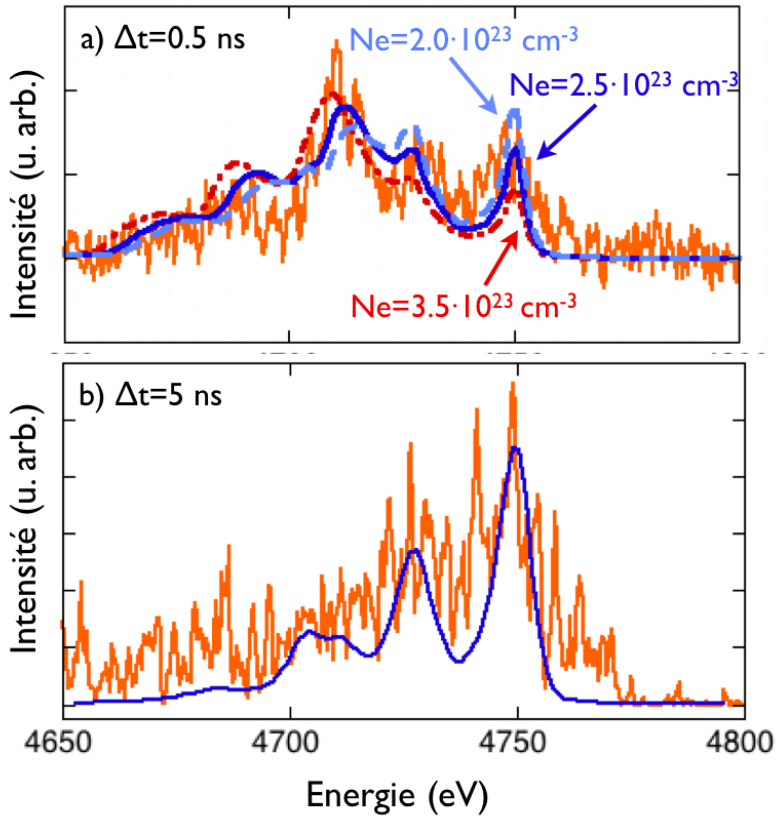


**Figure A.7:** *Spectres diffusés expérimentaux (courbes oranges) et théorique (courbes bleues) calculés pour les conditions du plasma obtenues à 500 ps (a) et 5 ns (b). La figure a) comprend aussi les calcules à différentes densités:* $2 \cdot 10^{23} cm^{-3}$ *(courbe azurre pointillé) et* $3.5 \cdot 10^{23} cm^{-3}$ *(courbe rouge pointillée).*

Les simulations et les résultats expérimentaux sont en bon accord. En particulier, le faible signal à l'énergie de la résonance observé pour le court délai temporel est bien reproduit, ainsi que le signal intense à l'énergie des satellites.
La sensibilité des calculs avec la température électronique (i.e. température ionique) et la densité électronique a aussi été testé. L'effet de la variation de la température est de changer l'importance des corrélations et donc l'intensité de la composante élastique. En changeant la densité, on observe encore un changement d'intensité de la composante élastique, et aussi un décalage spectral de la composante inélastique, (figure A.7a).

En conclusion, nous avons obtenu les premiers résultats de diffusion Thomson X par un plasma fortement couplé. Le régime collectif a été testé, ce qui a permis une mesure de la densité électronique. Les résultats obtenus sont très prometteurs et ont permis la première mise en évidence expérimentale de la dynamique des ions fortement couplés dans un plasma dense.

## A.6 Conclusion

En conclusion, nous avons développé des nouvelles techniques pour sonder la matière dense et chaude dans ce travail de thèse. Les résultats obtenus sont très prometteurs et permettent de cibler les prochains développements pour pouvoir franchir une nouvelle étape dans l'étude de plasma denses. En particulier, des possibilités nouvelles et excitantes sont ouvertes par le développement des systèmes laser comme PICO2000 au LULI ou OMEGA EP à Rochester, qui mettent à disposition un faisceau ns à haute énergie (kJ) et un faisceau PW à courte impulsion simultanément. On disposera ainsi de sources beaucoup plus énergétiques pour l'investigation de la matière comprimée par choc laser. Ces sources seront capables d'améliorer les techniques étudiées pendant cette thèse (source K$\alpha$ pour la radiographie X et diffusion Thomson X, protons énergétiques pour la radiographie protonique) en ouvrant un nouveau scénario dans la physique de la matière dense et chaude.